A study of binary star orbits using precise radial velocity measurements with the HERCULES spectrograph

A dissertation submitted in partial fulfilment
of the requirements for the degree of
Doctor of Philosophy in Astronomy
in the University of Canterbury

by

Siramas Komonjinda

University of Canterbury
New Zealand
2008

Acknowledgments

Before the start of this dissertation, I would like to spend these pages to express my gratitude to many individuals and organizations who provide assistance during my PhD study. This dissertation could not have been written without them.

Firstly, I would like to thank my supervisor, Prof. John Hearnshaw. John always gives me advice, guidance and suggestions, not only on my research work but also on how to live in New Zealand. He always patient in describing Astronomy to me as well as while he did the proof reading of this dissertation.

Many suggestions on my research came from my co-supervisor, Dr. David Ramm, whom I also thank. David gave me many technical advice, and ideas on binary star research. Further, I would like to deserve my acknowledgment to my associated supervisor, Dr. William Tobin, and my mentor, Dr. Richard Watts.

I would like to thank many people at Mt John University Observatory for all their help and support, including Alan, Pam, Maryrose, Nigel, Steve and Paul. I would like to acknowledge Alan and Pam, who helped me to solve problems during nights and observed all the photometric data in this research. I also thank David and Stuart for spectroscopic observations on the stars I studied in this research.

There are staffs and students at the Department of Physics and Astronomy who helped me on so many things, particularly Gill Evans for her help on the first few days I arrived in New Zealand. I would like to thank Duncan for his great contribution of his MATLAB code for measuring the rotational velocity of a star and broaden the stars' spectra.

This research gratefully acknowledges the efforts and work of the CDS and NASA. This research has made use of the SIMBAD database, operated at CDS, Strasbourg, France and the NASA's Astrophysics Data System Bibliographic Services.

I would like to thank my Thai friends and the Thai communities in Christchurch who made me feel like home here. Many special thanks to Jimmy and Wast, Fon, Vi, Puin, Pear, and others, for all the days we had together. Thanks for all your support, especially for the last few months when I tried to finish this dissertation.

During this research, I have financial support from a Thai Government Scholarship. I

would like to thank the director of National Astronomical Research Institute of Thailand Assoc. Prof. Boonrucksar Soonthornthum, my MSc supervisor who encouraged me to come to New Zealand, for all his help. I also would like to thank the staff at the Department of Physics at Chiang Mai University, the Royal Thai Embassy in Wellington, the Office of Civil Service Commission in Bangkok and the Office of Education Affair in Canberra.

Several trips to conferences and summer schools were supported by the D. W. Moore fund, the Frank Bradshaw & Elizabeth Pepper Wood fund, the IAU, the Vatican Observatory, RSNZ, RASNZ and the Department of Physics and Astronomy. During those trips, I met several people and had an opportunity to discuss my research.

Finally, I would like to thank my family for their understanding, unwavering support and belief that I would eventually finish this thesis. Many difficult times happened during this research, but they got me through to this day.

Abstract of the Dissertation

A study of binary star orbits using precise radial velocity measurements with the HERCULES spectrograph

by

Siramas Komonjinda

Doctor of Philosophy in Astronomy

University of Canterbury, 2008

Orbits of spectroscopic binary systems have been studied for more than a century. Over three thousand orbits of spectroscopic binary systems have been derived. These orbits are based on the radial velocities measured from the spectra recorded by a photographic plate to a high precision spectrum observed from a modern spectrograph. In many cases, the shape of the orbit was assumed to be circular, of hence the eccentricity is zero. This assumption is based on the fact that a small eccentricity ($e < 0.1$) measured from the observed data might be a result from the error of observations or from the intrinsic variation of a spectroscopic binary system.

Sixteen southern spectroscopic binary systems, including twelve single-lined binaries and four double-lined binaries, were selected to study in this research program. These systems were assumed to have circular orbits or have very nearly circular orbits ($e < 0.1$) from their previous published solutions. The HERCULES spectrograph was used in conjunction with the 1-m McLellan telescope at Mt John University Observatory to collect the spectra of these systems. The observations, taken from October 2004 to August 2007, comprised about 2000 high-resolution spectra of spectroscopic binary systems and standard radial-velocity stars. Radial velocities of spectroscopic binary systems were measured from these spectra and orbital solutions of the systems were derived from these radial velocities.

It was found that from HERCULES data, we are able to achieve high-precision orbital solutions of all the systems studied. The best-fit solutions can be improved as much as 70 times from the literature's orbital solutions. It has been found that the precision of

a system depends on the rotational velocities of the components as well as the level of their chromospheric activity.

We are able to confirm the eccentricity in the orbit of only one of the selected spectroscopic binary systems, HD 194215. Its eccentricity is $0.123\,29 \pm 0.000\,78$. The small eccentricities of other systems are not confirmed.

There are four systems; HD 22905, HD 38099, HD 85622 and HD 197649, that have circular orbital solutions from the large errors in their measured eccentricities. Two systems, HD 77258 and HD 124425, have too small eccentricities, $e = 0.000\,85 \pm 0.000\,19$ and $0.002\,60 \pm 0.000\,99$ to be acceptable.

An intrinsic variation is a presumed cause of the spurious eccentricities derived from the data of the other eight systems. Photometric data from Mt John University Observatory service photometry program, as well as the photometric data from the Hipparcos satellite and information of these systems from the literature, using various methods and instruments, give a wider view on the systems' behaviour.

It is possible that the spurious eccentricities derived for these systems result from the eclipsing behaviour of a system (HD 50337), or from the nature of the components, such as, the distortion of their shape (HD 352 and HD 136905), their chromospheric activity (HD 9053, HD 3405, HD 77137, HD 101379 and HD 155555), or stellar pulsation (HD 30021).

Models of the active chromosphere system, HD 101379, have been simulated. An analysis of synthetic radial velocity data shows that spots on the star's photosphere can cause a spurious eccentricity. The values of the spurious eccentricity and the longitude of periastron are dependent on the spot size, the spot temperature, and the position of the spots.

Table of Contents

List of Figures

List of Tables

CHAPTER 1

Introduction

A binary star system is a pair of stars in a bound orbit about their common centre of mass. This is different from an *optical double* which is an optical pair of stars that is in the same line of sight but not bound. An unresolved double star is one that cannot be visually resolve into two separate stars. Such a double has a small angular separation ($\theta 0.25''$). It may be a close binary or a wide binary at a great distance. The system called a *closed binary system* is one where the angular separation between the two stars is very small and there is a large tidal interaction between two stars. This is distinguished from another type of star system, a *visual binary star*, for which the observer can clearly resolve two components and measure their apparent relative motion.

The term *binary star* or *binary star system* includes a system of stars that is in a bound orbit. Many binary systems consist of two or three stars, and systems with four stars or more have been discovered. The components of a binary system complete one orbit in anything from a few hours to a month or many thousands of years, depending on the separation and masses of the stars.

1.1 The study of binary stars

Binary systems have been studied for a few centuries. It is credited to John Goodricke (1783) for his identification that Algol is an eclipsing binary with a two-magnitude variation with a period 68.8 hours. William Herschel published a report in 1802 and 1803 on his 40-year observing programme on double stars that he did with his sister Caroline. He demonstrated that some of the double stars they observed were in orbits that are in accordance with Newton's laws. These systems are now called visual binaries. Herschel (1802) first introduced the term *binary star* from this work. From the nineteenth century, many methods were used to study binary systems. The most commonly used

observational techniques are astrometry, photometry and spectroscopy.

The binary systems are as common as single stars in the universe, as about 50% of visible stars are members of binary or multiple systems (Kallath and Milone (1998) and Lada (2005)). As they are numerous, it is important to study their behaviour.

The binary system is also important because of the information it can provide. One of the most important fundamental properties of a star is its mass. The gravitational interaction between stars in a system causes the stars to orbit, which can be detected through the variation of their positions and velocities. Stellar masses can be determined directly from their gravitational interaction. It also provides information about the separation between stars in a system. Some binary systems have a variation in brightness that can inform us about the sizes of stars. Other fundamental properties of stars can be determined depending on the method of observation and analysis. The methods depend on the type of binary system.

The study of binary stars also helps us to find invisible celestial objects, since the gravitational interaction depends on the mass of stars. If there is any invisible celestial object in a system, with a proper observational method and instrument, one can detect that object by direct or indirect means. Occasionally, brown dwarfs or planets are detected as components of binary systems.

1.2 Classification of binary stars

Close binaries can be classified into various groups depending on the observational techniques employed. The techniques that are mainly used by astronomers to observe a binary star are astrometry, photometry and spectroscopy. The variation of a measurement from each technique can be analysed and shows that the spot of light we observed is a member of a binary system.

1.2.1 Visual binaries

A visual binary is a binary system that has a relatively large angular separation. By making careful observations with telescopes, observers can see the changing of the stars' relative positions. The angular separation between two stars is in the order of arcseconds.

The position angle ϕ is measured from north through east. The relative orbit of one component with respect to its companion can be determined from a set of observed position angles and angular separations using astrometry. The orbital periods range from hundred of days to as long as centuries, depending on the systems' separation. The important stellar property, mass, can be determined from Kepler's third law. This law relates the stars' orbital period P and the size of their orbit to the sum of the masses of the two stars

$$G(m_1 + m_2) = 4\pi^2 a^3 / P^2$$

where G is the universal gravitational constant and a is the system's semi-major axis.

For some visual binaries that have a large difference in their brightness, the light from the secondary component may be hidden in the glare of the primary component. This system will appear to an observer as one single star that has a periodic change in its position compared with the background stars. Such a binary is called an *astrometric binary.*

1.2.2 Spectroscopic binaries

Spectroscopic binaries are discovered by effects they produce in the combined spectrum of the binary system. There are two subgroups of spectroscopic binaries, the *single-lined spectroscopic binary* (SB1), where the spectrum of only one component is observed, and the *double-lined spectroscopic binary* (SB2) where both spectra are detected. The line-of-sight velocity or *radial velocity*, $V_{\rm rad}$ of a binary system is the projected velocity of a star onto the line of sight. This can be measured spectroscopically using the Doppler shift of absorption lines;

$$\frac{\lambda - \lambda_0}{\lambda_0} = \frac{\Delta\lambda}{\lambda_0} = \left[\frac{1 + (V_{\rm rad}/c)}{1 - (V_{\rm rad}/c)}\right]^{1/2} - 1 \approx \frac{V_{\rm rad}}{c} \tag{1.1}$$

where $V_{\rm rad}$ is the radial velocity relative to the observer, which is much less than c, the speed of light, λ is the observed wavelength of a line and λ_0 is the rest wavelength. For a receding star, the radial velocity is positive when the spectrum is redshifted. The radial velocity is negative when the star is approaching and the spectrum is blueshifted. The spectra will show a blue shift when the star is moving towards the observer and a red

shift will show when the star is moving away from the observer.

The orbit of a binary star can be determined from the variation of its radial velocity as

$$\begin{aligned} V_{\rm rad} = \dot{z} &= \sin i[\sin(\upsilon+\omega)\dot{r} + r\cos(\upsilon+\omega)\dot{\upsilon}] + \gamma \\ &= \frac{2\pi a \sin i}{P(1-e^2)^{1/2}}[\cos(\upsilon+\omega) + e\cos\omega] + \gamma \\ &= K[\cos(\upsilon+\omega) + e\cos\omega] + \gamma \end{aligned}$$

where a is the semi-major axis, i is the inclination of the system, e is the orbital eccentricity, υ is the true anomaly and ω is the longitude of periastron. The parameter $K = [2\pi a \sin i]/[P(1-e^2)^{1/2}]$ is called the *semiamplitude* of the radial velocity curve, and γ is the *systemic velocity* or the radial velocity of the centre of mass of the binary system.

The maximum or minimum radial velocity of a star will occur when the star is at the ascending node ($\upsilon + \omega = 0$) or at the descending node ($\upsilon + \omega = \pi$). If the star has a circular orbit, the radial velocity curve is a cosine curve.

If the inclination is known from another kind of observation, the mass ratio and the semi-major axis of a system can be determined. For SB2s the mass ratio can also be calculated from the ratio of the maximum radial velocities of the two stars.

1.2.3 Eclipsing binaries

Eclipsing binaries are binary systems which have a periodic variation in their brightness. These systems orbit approximately perpendicular to the sky plane. When one star is passing in front of the other from the observer's line of sight, an eclipse will happen. The photometric observation of this kind of system will show the characteristic light curve of an eclipsing system.

Eclipsing binaries can be categorized into three types following the shape of their light curves. These are *EA*, *EB*, and *EW*. The EA type is also known as the Algol type. The light curve of this type of binary star has a clearly defined eclipse with an almost flat top outside the eclipse. The first eclipsing binary star discovered, Algol, is a historical prototype of this type of eclipsing binary. The EB type or β Lyrae type is a binary system that has a continuously variable level of its light curve with a well

defined eclipse. Both EA and EB types have a large difference between two minima, which indicates the difference in surface brightness of the two components. Finally, the EW type or W UMa type is a binary star that is continuously variable in its light curve but with no distinction between the eclipse phase and out-of-eclipse phase. The depths of both minima are nearly the same.

The analysis of a light curve can provide the inclination of a system, the ratio of luminosities, the photometric mass ratio, and the information about the stellar shapes. The absolute parameters of an eclipsing binary can be determined from its photometric and spectroscopic observations.

1.2.4 Binary systems by other methods

Besides the main groups of binary stars we have mentioned, many other types of binary stars have been found. *X-ray binaries* such as Cen X-3 (Schreier *et al.* 1972) and Her X-1 (Tananbaum *et al.* 1972) are bright stars in X-ray wavelengths which pulsate in a period of seconds and sometimes show eclipses in a period of days. It was shown that this type of sometimes system consists of an ordinary star and a neutron star or, possibly, a black hole.

At radio wavelengths, *pulsar binaries* have been discovered in a compact region of globular clusters. There have been discoveries of compact binaries with a period as short as tens of minutes. These systems consist of two neutron stars.

1.3 The motivation and goal of this study

A study of a binary stars by various techniques delivers a solution for a system's fundamental parameters. Various catalogues of binary stars were compiled to collect the solutions of each method such as the *Aitken Double Star Catalogue* (ADS), the *Washington Double Star Catalogue*, the *Finding list for observers of interacting binary stars* or a series of the *Catalogue of Spectroscopic Binary Orbits*. These catalogues collected orbital solutions from historical works. The development of instruments in astronomy has made the acquisition of data more effective.

We are interested in the orbital solutions of spectroscopic binaries. We investigated

the 9th Catalogue of Spectroscopic Binary Orbits (S_{B^9}, Pourbaix *et al.* 2004). There are in total 2770 spectroscopic binaries in the S_{B^9} main catalogue, with 3308 orbital solutions (February, 2008). The orbital solutions reported in this catalogue are graded from 0 (poor) to 5 (definitive).

In 2001 the High Efficiency and Resolution Canterbury University Large Echelle Spectrograph (HERCULES, Hearnshaw *et al.* 2002) was built at Mt John University Observatory (MJUO), Lake Tekapo. This spectrograph was designed for an efficiency to achieve very precise radial velocities. To study binary stars with this spectrograph will help us to obtain better orbital solutions.

The orbits of some spectroscopic binaries that were reported as circular in the S_{B^9} catalogue were derived using the methodology of Lucy and Sweeney (1971). This is a statistical method to test the reality of an observed orbit being nearly circular. This test suggests that slightly non-circular orbits are all spurious, and arise from any proximity effects, or as a result of the error of measurements. Theoretical work on the circularization of orbits and the synchronization of stellar rotation periods and orbital periods of short-period binaries was done on these orbital solutions. These studies have been made by Zahn (1977) and Tassoul & Tassoul (1992), based on earlier work on tidal effects in binaries by Darwin (1879), Cowling (1941), Zahn (1975), Kopal (1978), and others. Data on late-type dwarfs by many observers show that solar-type stars can have maximum circular periods ranging from 4.3 to 18 days, depending on their ages (Abt, 2006).

The purpose of this research is to observe spectroscopic binary systems using the HERCULES spectrograph and analyse their orbits. One spectroscopic binary system, ζ TrA, was observed at MJUO during the years 2003-2004. Skuljan *et al.* (2004) reported the orbital eccentricity of this system as $e = 0.013\,98 \pm 0.000\,19$ with an orbital period of $P = 12.975780$ days and the root-mean-square scatter of radial velocities to be 14 m s^{-1}. The tests of Lucy and Sweeney (1971) and Lucy (2005) show that this small eccentricity is non-Keplerian and therefore spurious. The theoretical model of ζ TrA data shows that there is a possibility of starspots on the primary star surface (Komonjinda *et al.* 2006).

The aim of this research is to detect a small eccentricity in other systems and test for its reality. The theory of tidal circularization and synchronization can be improved from

any detectable eccentricity. Besides that, the nature of stellar activity can be investigated from theoretical models that fit with HERCULES high-precision radial-velocity data.

1.4 Thesis content

This thesis is divided into several chapters as follows:

- **Chapter 2.** The simple way to explain the physics of a binary star is to consider it as a system of two spherical stars. Newtonian mechanics, including Kepler's laws of motion, describe the motion of two point masses. In fact, in a binary star system, there may be perturbations and interactions that cause various phenomena in the system. These include apsidal motion and the circularization of the orbits and the synchronization of the stellar rotation period and orbital period.

- **Chapter 3.** Twenty spectroscopic binary systems were selected from the S_{B^9} catalogue. High resolution spectra of these systems were obtained from Mt John University Observatory (MJUO), Lake Tekapo, New Zealand using the HERCULES spectrograph. The instrument, method of data acquisition and reduction of the HERCULES spectra lead us to high precision radial velocities.

- **Chapter 4.** The method of cross-correlation was used to find the radial velocities of spectroscopic binaries from HERCULES spectra. One-dimensional cross-correlations on SB1s were done using the HRSP package. The TODCOR code (Zucker and Mazeh, 1994) is a program to calculate radial velocities of SB2s using 2-D cross-correlation techniques. The radial velocities of both components and their light ratio can be measured from HERCULES spectra.

- **Chapter 5.** The analysis of high precision radial velocities of SB1s from HERCULES spectra provides better orbital solutions of the selected binary systems than those that were reported in the S_{B^9} catalogue.

- **Chapter 6.** As in chapter 5, we now discuss the solutions of the SB2s.

- **Chapter 7.** The radial velocities observed from HERCULES of the quadruple system GT Mus were combined with MJUO photometry and data and information from a literature review to provide more information on the orbit of this system and the nature of the components.

- **Chapter 8.** The radial velocities and orbital solutions we obtained from HERCULES spectra for SB1s and SB2s are much more precise than those that were reported in the S_{B^9} catalogue. It was found that some of these systems have detectable non-circular orbits. The rotational velocities of these systems were also measured. The circularization of the orbit and the synchronization of the stellar rotation period and orbital period of these systems was investigated.

CHAPTER 2

Binary Star Systems

The main properties of binary star systems were introduced in chapter 1. Here we will discuss the physics of these systems. The orbit of the system and the physical properties of the stars can be determined from the observational data, according to the Newtonian mechanics of point masses. For close binary systems, we shall consider that the stars are spherical bodies with an interaction between them. This interaction explains apsidal motion, the circularization of orbits and the synchronization of the stellar rotation period and orbital period. For some binary systems, the star itself has a non-spherical shape and has a variation in its brightness as an interacting binary star.

2.1 Geometry of binary systems

We shall first consider that a binary system consists of two point masses m_1 and m_2 which orbit their common centre of mass in their mutual gravitational field. The mass m_1 is the more massive star and it is called a primary star. Its component is called the secondary star, m_2. The separation between these masses is $\vec{r} = \vec{r_1} - \vec{r_2}$, as shown in figure 2.1. The acting gravitational forces on these masses are equal but of opposite direction, $\vec{F_1} = -\vec{F_2}$, with a magnitude $F = Gm_1m_2/r^2$ where G is the gravitational constant.

The motion of each body can be considered in two ways, relative to each other or relative to their common centre of mass. The relative motion is a motion of one body relative to its companion. This motion is in its *relative orbit*. The moving mass has a reduced mass, $\mu = m_1m_2/(m_1 + m_2)$ and it orbits around the central fixed body of mass $m = m_1 + m_2$.

The *absolute* or *barycentric orbit* is an orbit of each body relative to the common centre of mass or the barycentre, B. Each body has its own barycentric orbit. Subscript

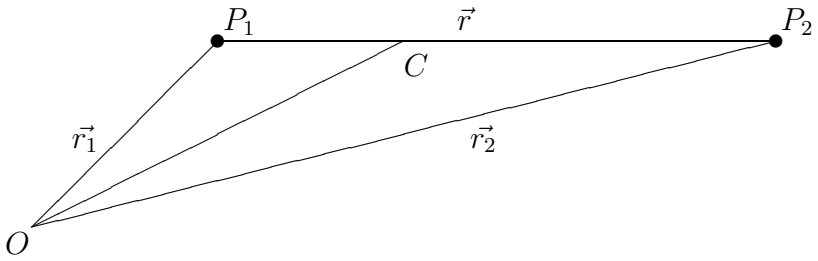

Figure 2.1: A diagram of the two point masses, m_1 and m_2 at positions P_1 and P_2. The centre of mass is at C and the reference point is at O

'1' is used for the primary component's barycentric orbit and subscript '2' is used for the secondary component's. The observed radial-velocity variation of spectroscopic binaries is due to the barycentric orbital motion in a binary system.

The orbit of a star in a system can be described using *Kepler's equation* as the position and velocity of a star are functions of time. For the general case, the shape of a star's orbit is eccentric. The motion of a star is considered in polar coordinates (r, θ) where r is the radius vector from the focus of the ellipse, and θ is the position angle.

2.1.1 The equation of motion

The gravitational force plays the most important role in the motion of stars in a binary system. This force is a central force and it is a conservative force.

For the barycentric orbits, it is assumed that the stars have a position vector $\vec{r_1}$ and $\vec{r_2}$. The unit vector from the secondary star to primary star is $\hat{r} = (\vec{r_1} - \vec{r_2})/|(\vec{r_1} - \vec{r_2})|$. We can write the equations of motion for the two stars as

$$m_1 \ddot{\vec{r_1}} = -\frac{Gm_1m_2}{r^2}\hat{r} \qquad ; \qquad m_2 \ddot{\vec{r_2}} = -\frac{Gm_1m_2}{r^2}(-\hat{r}). \tag{2.1}$$

The relative motion is found though a reduced mass, $\mu = m_1m_2/(m_1 + m_2)$, which orbits on its relative orbit around the $m_1 + m_2$ central fixed body. The relative motion of the reduced mass is

$$\ddot{\vec{r}} = \ddot{\vec{r_1}} - \ddot{\vec{r_2}} = -\frac{G(m_1 + m_2)}{r^2}\hat{r}, \tag{2.2}$$

so that the equation of motion of this reduced mass is

$$\mu \ddot{\vec{r}} = -\frac{Gm_1m_2}{r^2}\hat{r}. \tag{2.3}$$

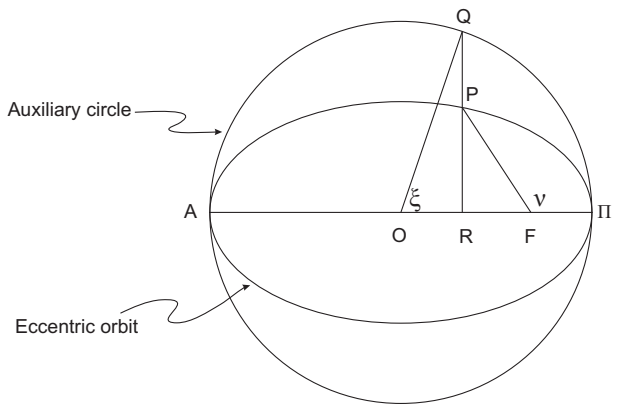

Figure 2.2: A model of an ellipse with a centre at O, and a focus at F. The position Π is the point closest to the ellipse's focus and A is the point farthest from the focus. They are called the periastron and the apastron, respectively for a star system. In this sketch, the star's position is at P. The auxiliary circle has a common centre with the ellipse and touches the ellipse at Π and A. The true anomaly is the angle $\Pi FP = \upsilon$ and the eccentric anomaly is $\Pi OQ = \xi$. The line RQ is perpendicular to the orbit's major axis

Kepler's second law determines that the radius vector sweeps out equal areas in equal interval of time which is the so-called *law of equal areas*. It can be concluded that for any star with a circular orbit, the speed of the star is constant. But for a star with an elliptical orbit, the speed is varying as a function of position and time.

The position angle of a star in orbit is called the *true anomaly*, υ. If the orbit is a circle, υ at a time t will be a simple function of time and it is equal to the *mean anomaly*, Φ. This can be derived from Kepler's laws, giving

$$\upsilon(t) = \Phi = \frac{2\pi}{P}(t - T) \tag{2.4}$$

where T is the time of periastron passage.

For a system with an elliptical orbit, the true anomaly is a complex function of time. This angle can be determined by defining the angle ξ or the *eccentric anomaly*. This anomaly is a projection angle of a star's position on an *auxiliary circle* as it is shown in figure 2.2. An auxiliary circle is a circle which has a radius equal to the semimajor axis of the ellipse and has a common centre with the ellipse.

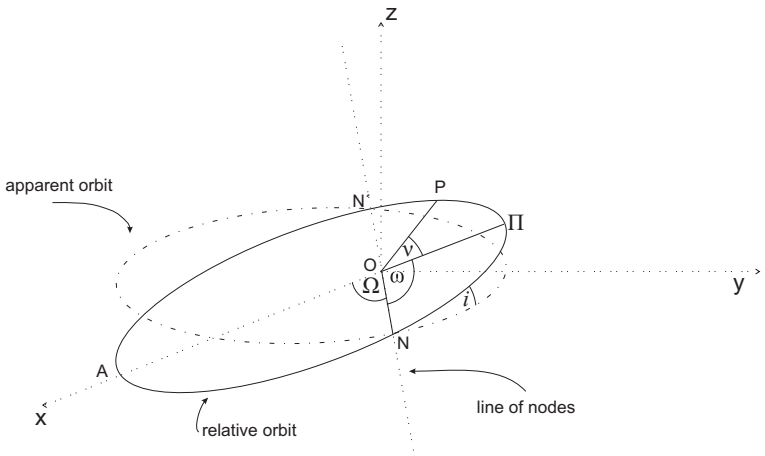

Figure 2.3: The orientation of a relative orbit and its projection on the sky plane (xy-plane). The observer's line of sight is along the z-axis. The primary component is at the origin O. The secondary component is at the relative position P at the time t.

The relationship between υ and ξ can be proven to be

$$\tan(\frac{\upsilon}{2}) = \sqrt{\frac{1+e}{1-e}}\tan(\frac{\xi}{2}) \tag{2.5}$$

where e is the eccentricity[1] of the system. Kepler's equation for an elliptical orbit will transform to

$$\xi - e\sin\xi = \frac{2\pi}{P}(t-T). \tag{2.6}$$

Figure 2.3 shows the orientation of a binary orbit presented in space related to the observer's line of sight (z-axis) and the tangent plane of the sky (xy-plane). The star's position in polar coordinates is $(r,\upsilon+\omega)$. This is the position $(r\cos(\upsilon+\omega), r\sin(\upsilon+\omega))$ on the sky plane and $r\sin(\upsilon+\omega)\sin i$ in the line of sight where i is the inclination of the orbit to the sky plane. For a system with $i = 90°$ the observed line of sight is on the orbital plane[2]. The orientation of the orbit can also be defined by the angles Ω, i, ω. The points N and N' are the intersection of the orbital plane with the sky plane. The point N is defined as the *ascending node* where the star is receding from the observer

[1]The eccentricity is a property of a conic section. It is defined by $e = (a-b)/(a+b)$, where a is the semi-major axis and b is the semi-minor axis. For a circle, e is equal to 0. An ellipse has e between 0 and 1. A parabola has e equal to 1 and a hyperbola has e greater than 1.

[2]An inclination $i \approx 70° - 90°$ is required as a condition for eclipse of a binary star system, depending on the stellar radii and separation of both components

most rapidly. The other side, N', is the *descending node* where the star is approaching the observer most rapidly. The line NON' is called the line of nodes and the angle $xON = \Omega$ is called the longitude of the ascending node. The angle $NO\Pi = \omega$ is called the *longitude of periastron.* In the figure, the secondary component is at the position P and its has a true anomaly $\Pi OP = \nu$. The observed radial velocity of a star is the star's orbital motion along the line of sight.

$$V_{\text{rad}} = \dot{z} = \sin i[\sin(\upsilon + \omega)\dot{r} + r\cos(\upsilon + \omega)\dot{\upsilon}]. \tag{2.7}$$

For an ellipse in polar coordinates, $r = a(1 - e^2)/(1 + e\cos\upsilon)$ and Kepler's second law, $r^2\dot{\upsilon} = 2\pi a^2(1 - e^2)^{(1/2)}/P$, and hence

$$V_{\text{rad}} = \frac{2\pi a \sin i}{P(1 - e^2)^{(1/2)}}[\cos(\upsilon + \omega) + e\cos\omega]. \tag{2.8}$$

If the centre of mass of a system has a radial velocity γ, then

$$V_{\text{rad}} = K[\cos(\upsilon + \omega) + e\cos\omega] + \gamma \tag{2.9}$$

where $K = \frac{2\pi a \sin i}{P(1-e^2)^{(1/2)}}$. γ is called the *systemic radial velocity* of the binary system.

2.1.2 Interpretation of spectroscopic binary radial velocity

As it is shown in equation 2.9, some fundamental parameters of a binary star orbit can be determined from the radial velocity curve of a companion. The radial velocity has a maximum or a minimum when $\upsilon + \omega$ is equal to 0 or π, respectively. These are the positions of star at the *ascending node* or the *descending node.* The systemic radial velocity γ can be determined from the shift of the curve and K is the semi-amplitude of the curve. The shape of the curve is defined by the eccentricity e. For $e = 0$, the curve is a cosine curve (a solid line in figure 2.4). If e is increased, the curve is increasingly skew-symmetric (dashed line and dotted line in 2.4 and 2.5). Other orbital fundamental parameters can also be determined from the curve, i.e., the time of periastron passage T and the orbital period P. For a steady system, these parameters are constant. For SB1, only one radial velocity curve can be determined. This gives one set of orbital parameters. For SB2, the radial velocities of each component are measured. Two sets

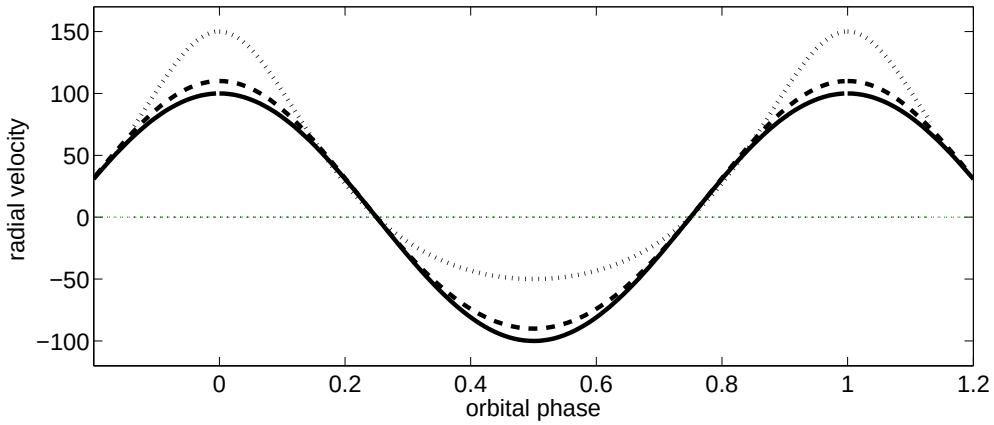

Figure 2.4: The radial-velocity curves of a circular orbit ($e = 0$, solid line), and elliptical orbits. The dashed line represents the curve of $e = 0.1$ and $\omega = 0°$ and the dotted line represents the curve of $e = 0.5$ and $\omega = 0°$. The semi-amplitude of all curves is $K = 100$ $\mathrm{km\,s^{-1}}$ where $\gamma = 0$ $\mathrm{km\,s^{-1}}$.

of quantities of K, a and ω will be determined for the primary star (with subscript '1') and for the secondary star (with subscript '2'). The longitudes of periastron ω of each component are different by 180°.

Besides from determining of the system's orbit, some fundamental characteristics of stars can be derived. For a binary system with masses m_1 and m_2, the total mass or the system mass is

$$M = m_1 + m_2 \tag{2.10}$$

and the ratio of the masses or the mass ratio is

$$q = \frac{m_2}{m_1} \leq 1. \tag{2.11}$$

Therefore

$$m_1 = \frac{1}{1+q} M \qquad ; \qquad m_2 = \frac{q}{1+q} M. \tag{2.12}$$

Using Kepler's third law, for a system with a semimajor axis a and an orbital period P, the system mass is given

$$M = m_1 + m_2 = \frac{4\pi^2 a^3}{GP^2}. \tag{2.13}$$

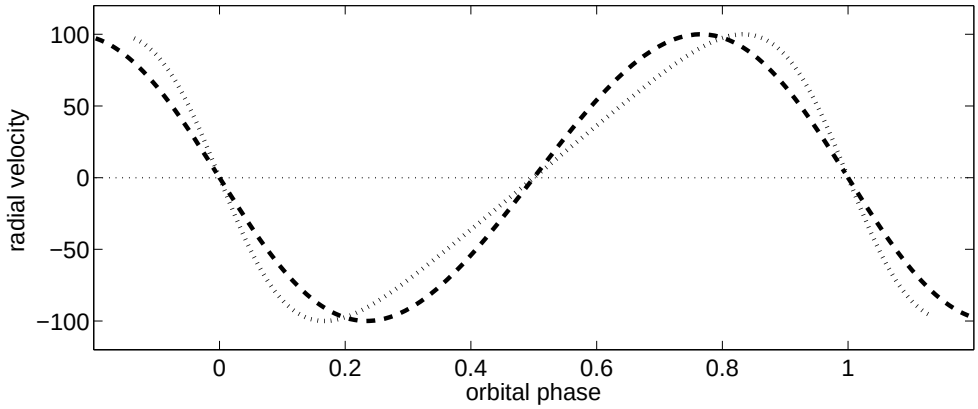

Figure 2.5: The radial-velocity curves of eccentric orbits as of figure 2.4 but with $\omega = 90°$.

For an SB2 system, the value measured from the radial velocity curve are the semiamplitude, K_1 and K_2. Form the definition of K, the *projected semimajor axis* $a_1 \sin i$ and $a_2 \sin i$ can be derived

$$a_{1,2} \sin i = \frac{(1 - e^2)^{1/2}}{2\pi} K_{1,2} P. \tag{2.14}$$

From equation 2.13 and $m_1 a_1 = m_2 a_2$, we can write

$$(m_1 + (a_1/a_2)m_1) = 4\pi^2 a^3 / GP^2 \tag{2.15}$$

which can be rewritten as

$$m_1 \sin^3 i = \frac{4\pi^2}{GP^2} \frac{a^3 \sin^3 i}{1 + (a_1 \sin i)/(a_2 \sin i)}. \tag{2.16}$$

Hence, the *minimum masses* for a binary system are

$$m_{1,2} \sin^3 i = \frac{1}{2\pi G} (1 - e^2)^{3/2} (K_1 + K_2)^2 K_{2,1} P. \tag{2.17}$$

These values are the true masses only for the orbits with $i = 90°$. For inclined orbits, these provide only the lower limit for the mass of each component. To determine the absolute masses, one should use another technique to determine the inclination of the orbit.

For an SB1, only K_1 can be determined from the radial velocity curve. Hence, only $a_1 \sin i$ can be determined. Direct measurement of the component masses is not possible;,

the quantity that can be obtained is a *mass function*, $f(m)$

$$f(m) = \frac{m_2^3 \sin^3 i}{(m_1 + m_2)^2} = (1.0361 \times 10^{-7})(1 - e^2)^{3/2} K_1^3 P \mathrm{M}_\odot \tag{2.18}$$

The mass of the primary star can be estimated roughly from the primary star's spectral type. With an assumption that $i = 90°$, the lower limit of the secondary star's mass can be determined from the mass function. Since the secondary star is undetectable, the upper limit of its luminosity can be calculated and its upper limit of mass can be estimated (Skuljan *et al.*, 2004).

2.2 General perturbation in binary systems

In the previous section, Newtonian mechanics was used to describe the motion of point-mass stars in a binary system. In fact, these stars have sizes and shapes. The general perturbation is due to the tidal force between the two stars[3]. This can make the system's characteristics change with time. Many continued observations of some systems may show the phenomenon of *apsidal motion*, the *circularization* of the orbit and the *synchronization* of the stellar rotation period and orbital period.

2.2.1 The Roche model and the classification of binary systems

The shape of a star in any binary system can be distorted by the tidal forces to an ellipsoidal shape. The problem of this tidal distortion was solved by Roche in the 1840s and it is called the *Roche model*. This model is based on a system with two point masses synchronously orbiting in circles around their common centre of mass and a third body of infinitesimal mass which moves in the gravitational field of the other two massive bodies. The total gravitational potential of the third mass is constant at a given value on a surface of constant gravitational potential or an *equipotential surface*. For a close binary system, this equipotential surface defines the stellar surfaces.

As it is seen in figure 2.6, the shapes of the equipotential surfaces near each mass point are spheres. Both stars have spherical shapes and the system is called a *detached binary system*. The further from each mass point, the surfaces are more distorted toward

[3]The other sources of perturbation are the general-relativity correction to Newtonian gravitational theory, the rotational potential of a spinning body or a third body.

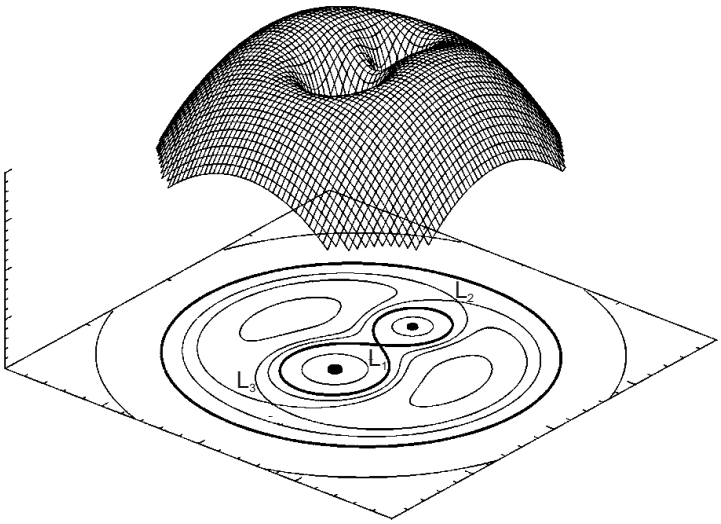

Figure 2.6: A three-dimensional representation of the equipotential surface in a binary star with $q = 0.5$, in the co-rotating frame. The droplet-shaped figures at the bottom of the figure are the Roche lobes of each star. L_1, L_2, and L_3 represent the inner and outer Lagrangian points. (diagram from van der Sluys, 2006).

the other stars. The equipotential surfaces around each of the point masses will touch each other at a point called the *inner Lagrangian point*, L_1. These touching surfaces are referred to as the *Roche limits* for the binary system and they enclose limiting volumes, the *Roche lobes*. The Roche lobe defines the maximum volume of a star that all of its matter comes under its gravitational field.

A *detached binary system* is a system in which both stars do not fill the Roche lobe. A system with both stars that just fill the Roche lobe is a *contact binary system*. If only one star fills the lobe, then it is called a *semi-detached binary system*. Beyond the Roche limit, the system is an *over-contact binary system*. The stars will then share a common envelope with mass exchange between the two stars. Figures 2.7 to 2.10 show the surface diagrams of each classification of binary systems with their radial velocity curves and light curves.

If the common envelope reaches an appropriate volume, it will reach the *outer Lagrangian point*, L_2. At this point, matter can escape from the gravitational field of the system. At the opposite side, L_3, is also a point where matter can escape from the im-

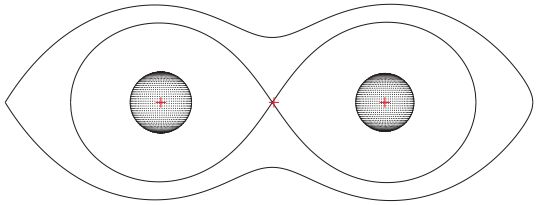

(a)

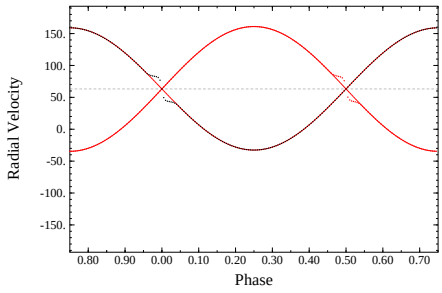

(b)

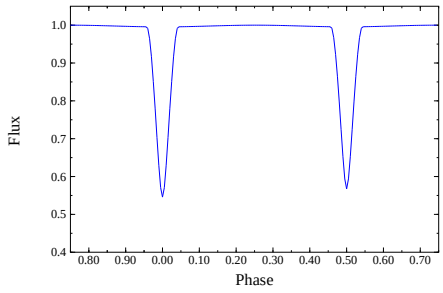

(c)

Figure 2.7: Diagrams of (a) surface outline with a Roche lobe, (b) radial velocity curve, and (c) V light curve of a detached binary system, TY Pyx, generated from Andersen *et al.* (1981) ($q = 0.98$, $i = 87.^{\circ}88$, $e = 0$, and $P = 3.198581$ days) using a program Binary Maker 3.0 (Bradstreet and Steelman 2002 . Note that the bumps in the radial velocity curves is from a Rossiter effect see section 4.3.1 page 55 for details.

mediate vicinity of the components. The points L_4 and L_5 are the points of maximum potential.

Extensive models for asynchronous systems were presented by Limber (1963). Avni (1976) presented a solution for an eccentric orbit. The combined problem for systems with asynchronous eccentric orbits was solved by Wilson (1979).

In this research, only detached binary systems are studied. A spectrum of a detached system consists of one or two sets of absorption lines from each component. Each set of lines belongs to each component. The star in a detached system is not distorted which results in the lack of an ellipsoidal effect. The stars do not fill the Roche lobe and mass do not transfer between the components. This causes a normal absorption-line spectrum which lessens the error in the radial-velocity measurement (see section 4.3.1 for more

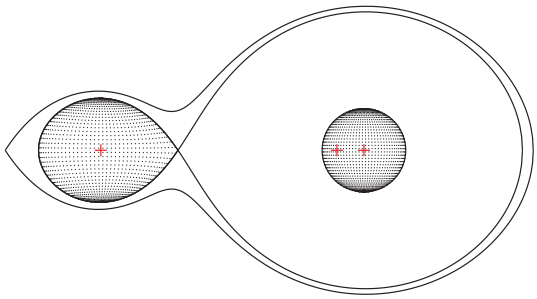

(a)

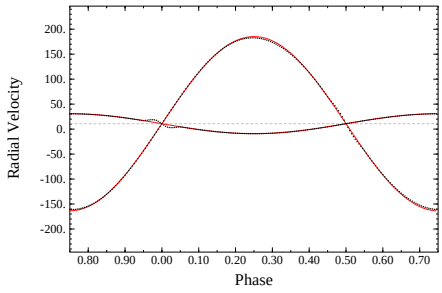

(b)

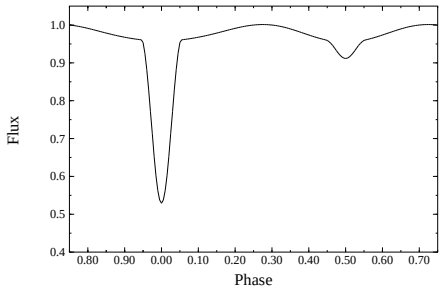

(c)

Figure 2.8: Diagrams of (a) surface outline with a Roche lobe, (b) radial velocity curve, and (c) V light curve of a semi-detached binary system, AS Eri, generated from Van Hamme & Wilson (1984) ($q = 0.1144$, $i = 80.^{\circ}018$, $e = 0$, and $P = 2.664152$ days) using a program Binary Maker 3.0.

detail).

2.2.2 Apsidal motion

The apsidal motion is the precession of the orbit in its own plane. It is observed by the changing of the observed longitude of periastron, $d\omega/dt \neq 0$, or, for an eclipsing system, which has the uneven interval of the times of minima. The apsidal rotation period, U, can be as short as a few years or as long as a few centuries. The theoretical problem of apsidal motion was presented by Sterne in 1939. At the position (r, ϕ) on the surface of the primary star, the total potential is

$$\Phi_t = \Phi_p + \Phi_{rot} + \Phi_d \tag{2.19}$$

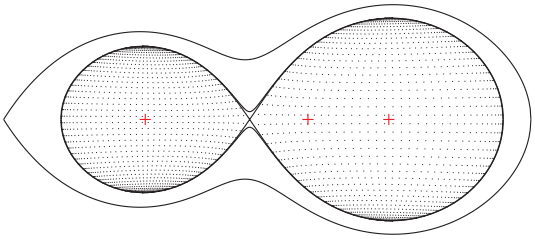

(a)

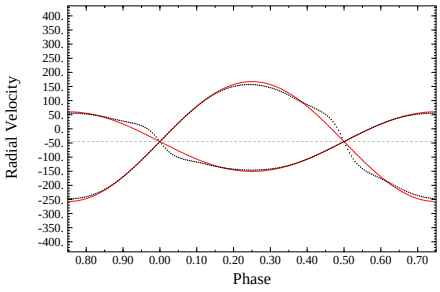

(b)

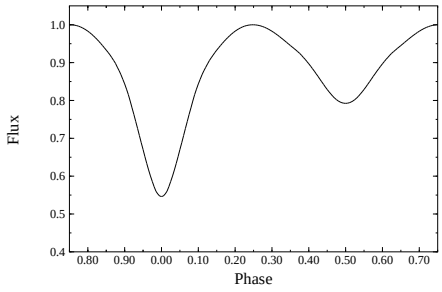

(c)

Figure 2.9: Diagrams of (a) surface outline with a Roche lobe, (b) radial velocity curve, and (c) V light curve of a contact binary system, BX And, generated from Samec *et al.* (1989b) ($q = 0.497$, $i = 75\overset{\circ}{.}5$, $e = 0$, and $P = 0.61011258$ days) using a program Binary Maker 3.0.

where $\Phi_t = -\frac{Gm_1}{r} - \frac{J_2 P_2(cos\phi)}{r^3}$ is the gravitational potential. The term $-\frac{J_2 P_2(cos\phi)}{r^3}$ is due to the non-spherical shape of the primary star where J_2 is the density distribution function of the stellar structure. Φ_{rot} is the rotational potential and it is equal to $-\frac{1}{2}\omega^2 r^2 \sin^2\phi'$. The tidal potential due to the point-mass secondary star at a distance d is $\Phi_d = -\frac{Gm_2}{d^3} r^2 P_2(\cos\phi)$. These give the perturbing potential for the primary star

$$S_p = -\frac{J_2 P_2(\cos\phi)}{r^3} + \Phi_{rot} + \Phi_d \tag{2.20}$$

and a similar equation for the secondary star. The detail of Sterne's work will not be discussed here. His final expression shows that the ratio of the apsidal period and the orbital period is a function of eccentricity, semimajor axis, mean radii of both stars, and the *apsidal constants* k_{12} and k_{22}. Improved models were discussed by many other authors, which improved the theoretical models so as to agree with the observed values,

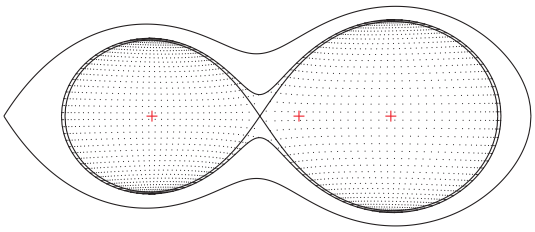

(a)

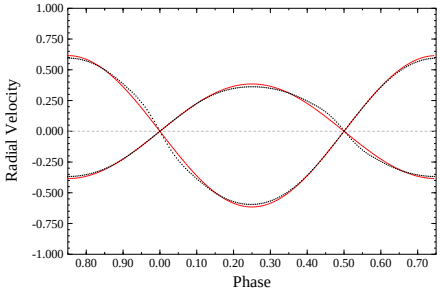

(b)

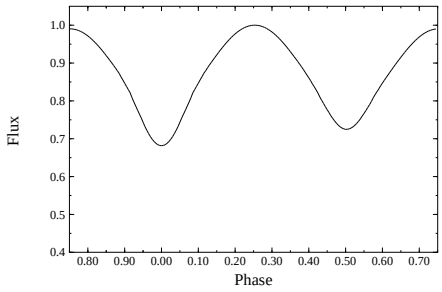

(c)

Figure 2.10: Diagrams of (a) surface outline with a Roche lobe, (b) radial velocity curve, and (c) V light curve of an overcontact binary system, AD Cnc, generated from Samec *et al.* (1989a) ($q = 1.6$, $i = 64\overset{\circ}{.}9$, $e = 0$, and $P = 3.198581$ days) using a program Binary Maker 3.0.

as of discussed by Claret (1995).

2.2.3 Circularization and synchronization

Tidal friction between the two stars in close binaries effects the circularization of the orbit as much as the synchronization between the stellar rotation period and orbital period. The theory of this process was developed by Zahn (1975, 1977, and 1978) and Zahn and Bouchet (1989). Later works, including Mayor and Mermilliod (1984), Jasniewicz and Mayor (1988), Latham *et al.* (1988), Mathieu and Mazeh (1988), Tassoul (1987, 1988), and Zahn (1992) have investigated the distribution of observed eccentricities versus orbital periods from various sample groups of binary systems and compared the results with those that are predicted from the theory.

The basic mechanism of tidal interaction is based on Newtonian mechanics as it is applied to the Earth-Moon system. The tidal perturbation is an effect from the superposition of the gravitational field of the secondary star on the gravity of the primary star. This produces a tidal bulge which causes the apsidal motion. The star itself has an inertia which affects its response to the forces between the stars, that gives rise to the *equilibrium tide* and the *dynamical tide*. The equilibrium tide is a hydrostatic adjustment of the star which occurs instantaneously in response to the changing tidal distortion. The dynamical tide is an effect including the oscillation of the star due to restoring forces such as the buoyancy and the Coriolis force, and the dispersion of energy from the compressed heated gases.

To study the tidal mechanism in binary systems, one should separate stars into two classes; stars with convective envelopes (CE) and stars with radiative envelopes (RE). For CE stars, the major role in the mechanism is played by the equilibrium tide which is the turbulent friction in the CE. For a star of mass M, radius R, and luminosity L, the friction timescale is

$$t_{\rm f} = t_{\rm conv} \approx (MR^2/L)^{1/3}. \tag{2.21}$$

For the Sun, this timescale is about 1 year. Zahn (1977) estimated the synchronization and circularization timescales for a late-type CE star with moment of inertia I, semi-major axis a and apsidal constant[4] k_2 as

$$t_{\rm sync} = \frac{1}{6q^2k_2}\left(\frac{MR^2}{L}\right)^{1/3}\frac{I}{MR^2}\left(\frac{a}{R}\right)^6 \tag{2.22}$$

$$\approx 10^4\left(\frac{1+q}{2q}\right)^2 P^4 \quad ; \tag{2.23}$$

$$t_{\rm circ} = \frac{1}{84q(1+q)k_2}\left(\frac{MR^2}{L}\right)^{1/3}\left(\frac{a}{R}\right)^8 \tag{2.24}$$

$$\approx 10^6 q^{-1}\left(\frac{1+q}{2}\right)^{5/3} P^{16/3} \tag{2.25}$$

where the orbital period P is in days and the timescales is in years.

[4]The *apsidal constant* can be derived from an apsidal motion in an eclipsing binary. It can also be computed from models of evolving main-sequence stars.

For RE stars, radiative damping is the most efficient process and the dynamical tide plays an important role for these stars. The radiation timescale is

$$t_{\rm f} = t_{\rm rad} \approx \frac{GM^2}{RL}. \tag{2.26}$$

The synchronization and circularization timescales for an early-type RE star was also derived by Zahn (1977) as

$$t_{\rm syn} = \frac{1}{5\times 2^{5/3}} \left(\frac{R^3}{GM}\right)^{1/2} \left(\frac{I}{MR^2}\right) \frac{1}{q^2(1+q)^{5/6}} \frac{1}{E_2} \left(\frac{a}{R}\right)^{17/2}; \tag{2.27}$$

$$t_{\rm cir} = \frac{2}{21} \left(\frac{R^3}{GM}\right)^{1/2} \frac{1}{q(1+q)^{11/6}} \frac{1}{E_2} \left(\frac{a}{R}\right)^{21/2}. \tag{2.28}$$

The constant E_2 is a tidal-torque constant which can be determined from stellar-structure theory (Zahn, 1975).

The circularization processes is a long-term process and it is not possible to follow any system that goes through the process. Surveys of the orbital eccentricities of binary systems in clusters have been done by many authors. These works presented the *circularization cutoff period* which is the shortest orbital period of a binary system with an eccentric orbit in a cluster[5], and compared it with the theoretical value. The observed cutoff periods increase with age[6]. For example, the Hyades (age $\approx$ 0.8 Gyr) sample has a cutoff period at 8.5 days (Duquennoy *et al.*, 1992), while M67 (age $\approx$ 4 Gyr) and halo stars (age $\approx$ 10 Gyr) have a cutoff period of 12.4 days and 18.7 days, respectively (Latham *et al.*, 1992 and Latham *et al.*, 1992b). This can be used as an indirect evidence of the circularization process.

2.2.4 Third body

Even though they are called binary systems, in some cases, they consist of more than two stars. A survey of 165 solar-type spectroscopic binaries with period from 1 to 30 days by Tokovinin *et al.* (2006) found that around 63% of spectroscopic binaries have additional companions. This number is increased to 96% for the sample systems with period less than 3 days. The extra companion can be a star or planet, in a close or distant orbit.

[5]In some literature, the $P_{\rm cutoff}$ is defined as the longest orbital period of a circular orbit.
[6]with an approximation that the ages of stars in a cluster or group are equal.

The problem of a triple (or multi) system arises and it is questioned whether the system is dynamically stable. The system was first studied by Harrington (1968, 1969). It is now known that the third body exerts tidal forces on the whole binary system, which it effects in reverse way from the tidal friction between the two components, and can cause an eccentricity in the binary orbit. It is also affects the apsidal motion of the binary and the nodal precession of the binary orbit around the total angular momentum of the triple system.

Mazeh and Shaham (1979) discussed a long-term effect of the third component on the eccentricity of a close binary. They demonstrated that the eccentricity of a binary orbit is decreasing with a modulation in its value. This implies that the system will not be in a stable circular orbit but with eccentricity oscillations (Kozai cycles[7]). An evidence on this effect can be observed in a short-perriod system such as those that were published by Mazeh (1990). The frictional forces inside the two stars causes the decrease in the binary separation. The effect from the third component combined with the tidal friction of a close system was further investigated by many authors including Kiseleva *et al.* (1998), Eggleton & Kiseleva-Eggleton (2006), Eggleton (2006) and Fabrycky & Tremine (2007).

Bozkurt and Değirmenci (2007) investigated the apsidal motion in six triple systems. They found that the contributed effect from the third body is small and can be ignored. Mazeh (2008) suggested that the technique that is used in the discovery of the third body and the apsidal motion is the same, i.e. timing of the eclipsing minima and the light-travel time technique. Therefore, the orbital period of the third star is of the same order as the detected apsidal motion. The modulation time from the third body is dependent on the ratio of the period of the third component and the period of the close component which results in a longer apsidal period. Mazeh (2008) proposed that a system with a small period ratio should be investigated in order to study the effect of a third star on apsidal motion.

Mayor and Mazeh (1987) used the effect on the nodal precession of the orbital plane in their study to sample the frequency of multiple systems. The tidal interaction from the third component induces the precession of the companions' angular momentums,

[7]The oscillation of e and i in a triple system was introduced by Kozai (1962). In that paper, he studied the secular perturbation of asteroids under the attraction of the sun and Jupiter.

$L_{1,2}$ with the total angular momentum, L. The periodic change in the angle of $L_{1,2}$ with the line of sight can be detected as well as the periodic changes in the inclination, i, and the semi-amplitudes $K_{1,2}$.

CHAPTER 3

Observations and Data reductions

The sample binary systems that were studied in this research were selected from the S_{B^9} catalogue and observed using the HERCULES spectrograph at the Mt John University Observatory, Lake Tekapo, New Zealand (170°27.9′ E, 43°59.2′ S, 1029 m above sea level).

3.1 Instrument: the HERCULES spectrograph

3.1.1 Introduction to spectrographs

A spectrograph is an instrument that splits the light from a star or any objects of into its component wavelengths or spectrum. A simple spectrograph uses a prism or a diffraction grating to disperse the light. A diffraction grating is a glass substrate which has thousands of grooves ruled on the surface. The reflected light from the grating will be dispersed into a spectrum.

Most astronomical spectrographs have a slit. Only one point source in the telescope's field of view can enter and act as a point source. A collimator in a spectrograph makes the incoming light parallel before it falls on the diffraction grating. After the grating the camera optics converges the light rays so as to create an array of monochromatic slit images in the spectrograph's focal plane. Dispersed light from a grating will be recorded on the detector placed in the focal plane, such as a glass photographic plate or a CCD detector. Beside these optical instruments, a spectrograph needs to have a comparison lamp. This lamp is at rest with respect to the spectrograph and it emits known spectral lines. These spectral lines are used to calibrate any shift of the source spectra.

Table 3.1: Table of HERCULES fibres and their properties

Fibre #	core ⊘ (μm)	microslit (μm)	R
1	100	-	41 000
2	50	-	82 000
3	100	50	70 000

3.1.2 HERCULES spectrograph

The observational part of this research was conducted at Mt John University Observatory (MJUO) using the 1-m McLellan telescope and HERCULES spectrograph. The 1-m McLellan telescope is a Dall-Kirkham reflecting telescope built in 1986. There are two Cassegrain foci available at f/7.7 and f/13.5.

The HERCULES spectrograph, whose name stands for *High Efficiency and Resolution Canterbury University Large Échelle Spectrograph* (Hearnshaw *et al.* 2002), is one of the world's first vacuum échelle spectrographs. It sits in an insulated room inside a vacuum tank about 20 metres from the telescope. Light is fed to HERCULES along optical fibres from the fibre-feed module that is attached to the telescope at the f/13.5 Cassegrain focus.

Table 3.1 gives details of three optical fibres that are available for feeding light from the telescope with total length of fibres from the telescope's focal plane to the spectrograph of 22 m. These fibres are (i) a 100-micron core diameter (ii) a 50-micron core diameter and (iii) a 100-micron core diameter with a 50-micron slit. The resolving powers, R, of these fibres are 41 000, 82 000, and 70 000 respectively. The selection of fibres depends on the brightness of the star and the seeing conditions. Generally, in this research fibre #3 was used to observe stars brighter than 6^{th} magnitude and fibre #1 was used for the rest.

On the 4.5-m length optical bench inside HERCULES are housed the collimator, prism, échelle grating, Schmidt corrector plate, Schmidt camera, and fold mirror. The optical layout is shown here in figure 3.1. These optical components are housed inside the vacuum tank (2-3 torr) with a temperature control. The collimator used for HERCULES is a 210-mm diameter paraboloid with a focal length of 783 mm. The cross-dispersion

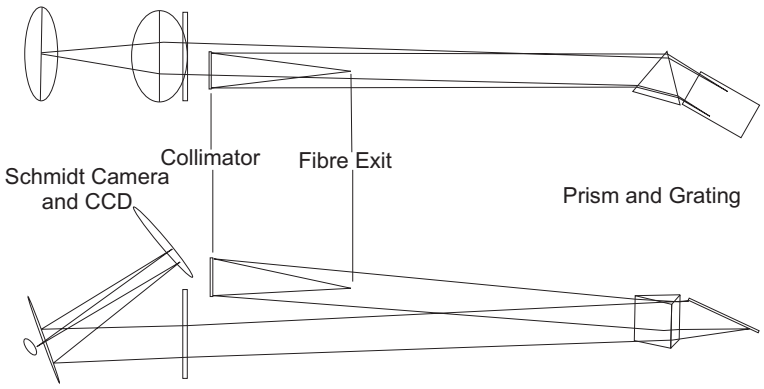

Figure 3.1: Optical design of the HERCULES spectrograph.

prism is a single BK7 prism. It dimensions are 276×258×255 mm with a mass of 23 kg. The R2 échelle grating has 31.6 groves per mm and its ruled area is 204 by 408 mm. The Littrow angle[1] is designed at 3°.0.

The Schmidt camera is set to correct any aberration. It consists of the BK7 Schmidt plate and a fold mirror is located inside the vacuum tank, the field-flatting lens which acts as a tank's window and a CCD detector. During the observation time of this research, the HERCULES detector was a SITe SI 003 1024×1024 thinned CCD chip with 23-micron square pixels. This chip cannot cover all the focal plane area of the dispersed spectrum. Later in 2006, the detector for HERCULES was changed to a SI-Fairchild 486 CCD which has 4096×4096 15-micron square pixels.

The dispersed spectrum is in the range from 380 - 880 nm in 86 orders. This is spread out over an approximately 50×50 mm square. At the time of this research, the dispersed area was separated into four regions to match the size of the SITe CCD. The CCD region that was mainly used in this research is called region 2, which covers a wavelength region around 450-700 nm, in approximately 48 orders. The CCD region 4 was also position used and is able to record the CaII H & K emission lines for the purpose of studying the star's atmospheric activities.

Inside the fibre-feed module of HERCULES, there are two standard lamps that can direct light into the fibres. These are a thorium-argon (Th-Ar) hollow cathode lamp and

[1]This is the angle between the échelle facet normals and the incident beam measured in the normal plane of the échelle. The smallest possible angle is needed in order to get the highest efficiency. A smaller angle requires a longer spectrograph as it is required to separate the incident and diffracted échelle beams.

a white smooth-field lamp. The Th-Ar spectra are used for the purpose of wavelength calibration. The white lamp spectrum is used for the order tracing and flat fielding.

Besides the principal optical components, there is a set of instruments that is used for measuring the amount of incoming signal. A 45° diagonal mirror is located in front of the Schmidt corrector plate. A few percent of the light is sent via relay lenses, that act as a small window in the tank wall, to a photomultiplier tube (PMT). The signal from the PMT is read by an exposure meter which has the purpose of metering the signal from the sources. This is useful for an observer to fine-tune the position of a star on the fibre's entrance during an exposure, metering the spectrograph's throughput to define more accurately the flux-weighted time of mid-exposure (which is required for a high precision radial velocity measurement), and providing an estimated total readout which can be used to predetermine the exposure time require for a desired signal-to-noise ratio (S/N).

3.2 The programme stars

To investigate the possibility of a detectable small eccentricity in binary systems, a sample group of binary systems was selected. The criteria of selection are described here.

Firstly, the system should have a known circular or nearly circular orbit, $e < 0.1$. It was suggested from the method of Lucy and Sweeney (1971) that these small eccentricities are spurious, and arise from proximity effects, or result from error of measurement. Many studies of the orbits of binary systems assumed that the orbits of those systems are circular and neglected the detectable small eccentricities. If those rejected non-zero eccentricities are the results from errors in historical data, then the observation of these systems using a high precision spectrograph will confirm the circularization of the system's orbit.

Secondly, the observed spectra should be those of late-type stars. From the theory of circularization and synchronization, the tidal perturbation on an early-type companion is mainly a radiative damping under an assumption that the star is behaving as a rigid body and co-rotation was assumed in the calculation (Zahn, 1992). It also ignores the pre-main sequence circularization (Zahn and Bouchet, 1989) and the main-sequence

evolution of the star. The most recent models of early-type stars are needed to continue the research on the circularization and synchronization theory.

The other criteria are on the limit of the instruments used in this research. The systems must be in the southern hemisphere, due to the position of MJUO. They should be systems that are brighter that magnitude 8.0. This is due to the limiting magnitude of the HERCULES spectrograph. In spectroscopic work, the usable spectra are those that have at least S/N $\approx$ 25. To obtain a precise radial velocity, S/N $\approx$ 100 is recommended (Hilditch 2001). If the seeing is 2″, HERCULES will take 5 minutes to reach a S/N of 100 for a 7th magnitude G0 star using fibre 1 and the exposure time can reach an hour for a 10th magnitude star (Hearnshaw 2002). The mean seeing at MJUO is 3″–4″ which will take a longer exposure time. One should be concerned that the spectroscopic observation of a binary system has a limit on the exposure time. During a long exposure, the components would have changed their radial velocities by some amount depending on their orbital period. To avoid this motion blur, it is suggested that the exposure time should not exceed 1-2% of the orbital period.

In conclusion, the selection of spectroscopic binary systems is under the conditions that:

1. The known orbit of a system has an eccentricity less than 0.1.
2. The primary component (for SB1) and also the secondary component (for SB2) is a star of a spectral type F1V - K9V.
3. The system is a southern star ($\delta < 0^\circ$) with an apparent magnitude brighter than $m_V = 8.0$.

The systems were selected from the ninth catalogue of spectroscopic binary orbits (S_{B^9} catalogue, Pourbaix *et al.*, 2004). This catalogue is the latest compilation of spectroscopic binary orbits. It is a work continued from the eighth catalogue of spectroscopic binary orbits (Batten *et al.*, 1989). As at February 2008, S_{B^9} catalogue contained 3308 orbits for 2770 systems. The catalogue is available on-line[2]. From the orbits reported in the S_{B^9} catalogue, it was found that around half of them (1600 orbits) have $e < 0.1$ and around one third (1090 orbits) are circular orbits. There are 220 orbits where e is

[2]http://sb9.astro.ulb.ac.be/

fixed to zero and around half of the orbits that are reported in the catalogue have no error bars on the eccentricities.

The total number of spectroscopic binaries selected from the criteria above is 23 systems. Four systems, i.e. HD 92214, HD 106516, HD 129903, and HD 210737, were under the selection criteria but they were not studied in this research because of their periods. HD 92214 and HD 106516 have too long periods (1200 d and 853.2 d, respectively) to be able to archive a good phase coverage during the time available for this research. HD 106516 and HD 210737 have short periods, 7.2 hours and 2.198 d. With the brightness of these systems, $m_V = 8.00$ and 7.55, HERCULES may take up to an hour on an average seeing to archive a 100-S/N spectrum which exceeds the limit of an observation time (2% of an orbital period). Later after the spectra analysis was begun, three systems were excluded from this research. They are HD 26337 (EI Eri), HD 81410 (IL Hya) and HD 88215. Radial velocities were not successfully measured from spectra for these systems, because the first two systems are very active chromosphere stars, while the last has very broad absorption lines.

A total of 16 systems were studied in this research as shown in table 3.2. This is including an interesting system that has no report in the S_{B^9} catalogue. It is the system HD 101379. HD 101379 is a single lined spectroscopic binary in a quadruple system, GT Muscae (Murdoch *et al.*, 1995). The record of photometric and spectroscopic observations of this system has been continued at MJUO for more than 25 years. This SB1 is in an orbit of around 60 days with e less than 0.1. It is also in a wide orbit with a 2.7-d eclipsing binary, HD 101380. The wide orbit of this system has not been solved. This system is also interesting because of the spot activity of the SB1 primary star.

3.3 Observational process and statistics

The observational part of this research was carried out at MJUO from October 2004 to August 2007. All observations were conducted from the 1-m telescope dataroom, using a computer to control the HERCULES fibre-feed module and guiding mode[3], and

[3]The HERCULES fibre-feed control software is running on the Windows system. This software not only controls all aspects of the fibre-feed module, including the shutter, the exposure meter, and auto-guiders but also monitors the temperature and pressure inside HERCULES.

Table 3.2: The 19 selected spectroscopic binaries studied in this research. The first part of the table is the systems that are listed in the S_{B^9} catalogue with their periods that are reported in the catalogue. The second part has an additional system that was included in this research. The question marks in the column *Spectral type* are for the unknown spectra of the systems' components.

HD	**RA(2000.0)**	**Dec(2000.0)**	m_V	**Spectral type**	P (days)
352	00 08 12.09	-02 26 51.7	6.08	K2III	96.439
3405	00 36 37.63	-49 07 55.2	6.78	G3V + G8V	3.7418
9053	01 28 21.94	-43 19 03.8	3.40	K5Ib	193.79
22905	03 40 11.44	-15 13 35.4	6.33	G8III	91.629
30021	04 43 34.73	-08 47 39.3	6.00	G8III	42.3279
38099	05 43 09.32	-01 36 47.4	6.31	K4III	143.03
50337	06 49 51.32	-53 37 21.0	4.39	G5	195.26
77137	08 59 42.75	-27 48 58.3	6.87	G2 + G2	3.1986
77258	09 00 05.44	-41 15 13.5	4.45	F8IV	74.1469
85622	09 51 40.69	-46 32 51.5	4.57	G5	329.3
124425	14 13 40.67	-00 50 42.4	5.93	F6IV	2.696
136905	15 23 26.06	-06 36 36.7	7.31	K1III	11.1345
155555	17 17 25.54	-66 57 02.5	6.67	G5IV + K0IV-V	1.6817
194215	20 25 26.82	-28 39 47.8	5.84	K3V	377.6
197649	20 46 18.58	-36 07 12.1	6.48	F6IV-V + G8V	18.0668
An additional system that is not included in the S_{B^9} catalogue.					
101379	11 39 29.59	-65 23 51.9	5.17	G2III	61.448

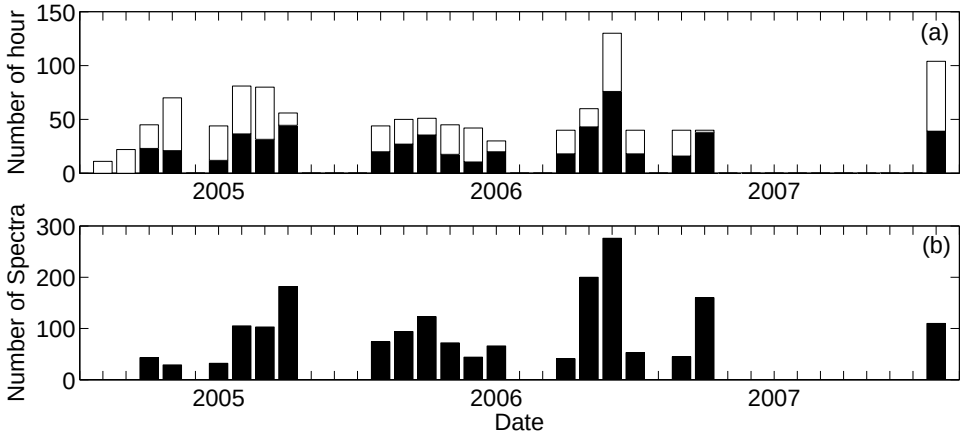

Figure 3.2: The distribution of observation hours at MJUO for each observation month is shown in panel (a). The usable hours are solid proportions and unusable hours are clear proportions. In panel (b) is the number of spectra obtained for each observation month.

a computer to control the observation sequence and the CCD camera[4].

The observation times were scheduled at MJUO approximately five nights per observing run. There are 22 observing runs inclusive[5]. The total number of scheduled hours are 1125 hours, of which 578 hours or 51.4% were unusable because of the weather. From the 547 observable hours, 1852 stellar spectra, including those of the binary systems, the standard radial-velocity stars and the Sun, were archived. These statistics of observation are presented in figure 3.2. It should be noted that during the period of observation, the HERCULES detector unit was changed. The last observation in August 2007 was done using the new SI 4k×4k CCD camera. The spectra obtained from this observation run have not been used for the radial velocity measurement in this research but they were helpful for the study of the activity in the stellar atmosphere.

[4]It is controlled by the Mount John CCD image acquisition software (MOJO), which runs on the Linux operating system

[5]There are two runs in August 2007

3.4 The reduction of HERCULES spectra

All archived HERCULES spectra were reduced using the *HERCULES Reduction Software Package* (HRSP) version 2.2 (Skuljan, 2003)[6]. HRSP is a C program which runs on the Linux operating system, processing standard FITS[7] files. The controlled parameters used in the reduction process are specified in various configuration files. These files are in ASCII format and can be edited by the user. In some cases, the basic keywords or descriptors of a FITS header may be incorrect or missing, such as star name, fibre used, or CCD position. These can also be edited using these configuration files.

For each stellar spectrum, the reduction process was done (following standard reduction steps, following the flow chart figure 3.3). Two final image files were created, one on a linear wavelength scale and one on a logarithmic scale. The latter form is suitable for a cross-correlation method to measure the radial velocity of the object. For each observing night, the reduction steps start with

1. *Preparation of all spectra.* Before the reduction can be processed, image rotation and flip will be done if it is necessary. The image should have the échelle orders appear horizontal and the wavelengths must increase from left to right. The image is then converted into the 32-bit floating point format (REAL) and the median bias is subtracted.

2. *Calculation of image transformation.* For each observation run, the CCD position may change and its plane can be tilted or not in focus. It is necessary to calculate the transformation coefficients between the absolute coordinates and pixel positions. It is performed by using one Th-Ar spectrum as a template with the Th-Ar calibration line table.

3. *Reduction of white lamp spectrum.* A white spectrum is reduced to locate the échelle orders. A Gaussian is fitted to every order profile to determine the position and width of each order.

4. *Creation of flat-field image.* A flat-field image is created to define the global curvature of the continuum level. This curvature is a result of the spectrograph blaze

[6]The latest version of HRSP is 3.0+ which supports the new SI 4k×4k CCD.
[7]Flexible Image Transport System

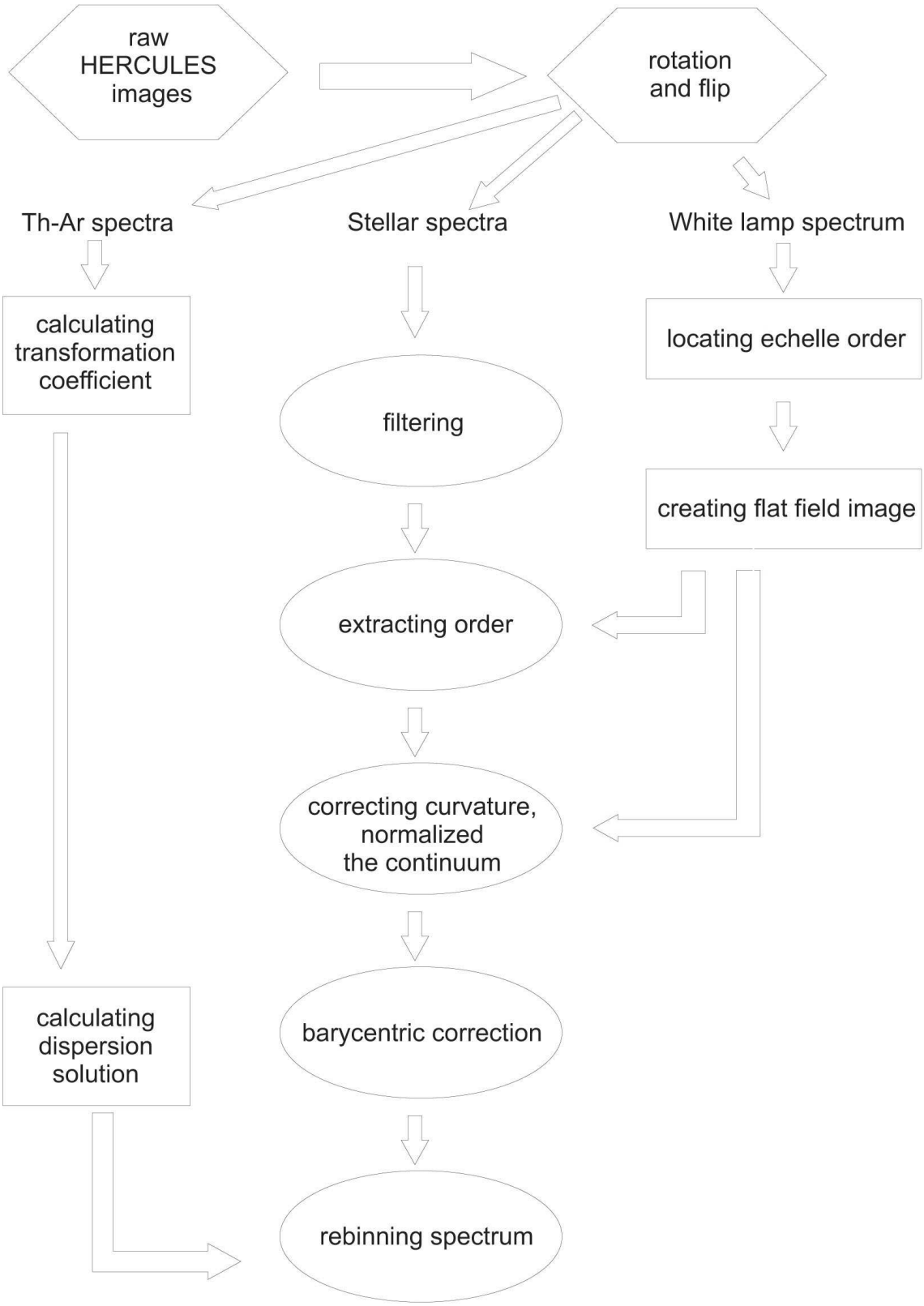

Figure 3.3: The reduction method of HERCULES spectra.

function.

The following reduction steps are applied to each stellar spectrum

1. *Filtering the image.* For each stellar image an interpolation between the neighbouring pixels was done to correct any bad pixels. A filtering box is constructed around every pixel and a median value is computed for all pixels in the box. If the actual value is above or below the median value by more than the given threshold, the value of that pixel will be replaced by the median value. The background light is computed and subtracted from the image, so that the order profiles have a zero base level. A normalized profile is calculated and a low-order polynomial is fitted to the pixel value in each row. Any pixel found too high above the fitted value is considered as a cosmic ray and replaced by the fit.

2. *Correction of the continuum curvature and normalization of the continuum level.* The clean image is extracted using the information and definitions from the reduced Th-Ar and white spectra. Each order spectrum is divided by the flat-field image. Each pixel row of a flat-field spectrum is divided by the maximum pixel value to normalize the continuum level.

3. *Calculate the dispersion solution.* Two Th-Ar spectra were archived just before and after each stellar spectrum. For each Th-Ar spectrum, thorium calibration spectral lines are located in pixel-space and the dispersion solution or a wavelength calibration with a pixel position is computed using a polynomial regression. The dispersion solutions from each pair of Th-Ar spectra are interpolated using the linear interpolation method.

4. *Barycentric correction.* For a given stellar image, a barycentric radial velocity correction and Julian day correction is computed from the flux-weighted mid-exposure time. HRSP uses its own table of the positions and velocities of the Earth which is precomputed using the DE200/LE200 ephemerides by the Jet Propulsion Laboratory (JPL). This table covers the data for every day at 0^h TDT[8] between 1 January 1980 and 1 January 2020. The precision of this correction is as small as $10^{-3}\ \mathrm{m\,s^{-1}}$.

[8]Terrestrial Dynamical Time.

5. *Rebinning of the échelle spectrum.* The final reduction step is to rebin a spectrum from pixel space to wavelength space. The process is done using a spline interpolation function. Two images are produced, one on a linear wavelength scale in Angstroms and one on a natural logarithmic wavelength scale. The latter image is in an appropriate form for the radial velocity measurement using the cross-correlation method.

CHAPTER 4

Methods of data analysis

The orbital parameters of a spectroscopic binary system can be determined from a set of radial velocities of the system's components. The cross-correlation method is used to measure the shift of absorption lines of the component's spectrum which can be transformed to a radial velocity. Applying the least-squares method to these radial velocities, the orbital parameters of a system can be derived.

4.1 Radial-velocity measurement

4.1.1 The cross-correlation method

The *cross-correlation method* is a standard method for estimating the degree to which two series are similar or correlated. The cross-correlation function (CCF) $c(x)$ of an independent variable x between two function $f(k)$ and $g(k)$ of an independent variable k is a convolution of the two functions $f(k)$ and $g(k)$. This is defined as

$$c(x) = f(x) * g(x) = \int_{-\infty}^{\infty} f(k)g(k-x)\,dk \tag{4.1}$$

when $f(k)$ and $g(k)$ are continuous functions and

$$c(x) = \sum_{k=1}^{N} f(k)g(k-x) \tag{4.2}$$

when $f(k)$ and $g(k)$ are discrete functions composed of N discrete bins at equal intervals, and where $*$ denotes the convolution.

The CCF $c(x)$ is evaluated point by point of x and is equal to the integral of the product of the two functions $f(k)$ and $g(k-x)$. The value of $c(x)$ is strongly dependent on the value of x and the forms of the functions $f(k)$ and $g(k)$.

The spectrum of a star has a pattern of absorption lines according to its spectral type. It can be assumed that the pattern of absorption lines is a mathematical function in wavelength space. This function is shifted according to the star's radial velocity. The shift is given by the Doppler effect which is expressed in equation (1.1) page 3. An analysis of each line shift can give information about the radial velocity of the star. In fact, each absorption lines of a stellar spectrum can give a different radial velocity. This is because each line is created at a different depth in the stellar atmosphere and they can have a different velocity.

To calculate a precise radial velocity, the integrated analysis of the whole set of lines is needed. From the Doppler effect, the shift at each wavelength is not only dependent on the velocity but also on the rest wavelength. This gives a pattern of moving spectrum different from the rest pattern. The logarithmic scale of wavelength is introduced to make the shifted pattern the same as the rest pattern. The Doppler shift in the natural logarithmic scale is

$$\begin{aligned} \Delta(\ln\lambda) &= \ln\lambda - \ln\lambda_0 = \ln\frac{\lambda}{\lambda_0} \\ &= \frac{1}{2}\ln\left(\frac{1+(V_{\rm rad}/c)}{1-(V_{\rm rad}/c)}\right) \\ &\approx \ln(1+(V_{\rm rad}/c)) \approx V_{\rm rad}/c \end{aligned} \tag{4.3}$$

for $V_{\rm rad} \ll c$. The shift of spectra in $\ln\lambda$ space is independent of wavelength. The absorption line pattern of a moving object is unchanged. The radial velocity of an object can be measured by applying the cross-correlation method to the whole spectrum.

The spectrum of a star is a discrete spectrum as it is a digital record with a CCD. The application of the cross-correlation to binary star research is considered by noting that the template profile is a function $f(\ln\lambda)$ and the spectral profile is a function $g(\ln\lambda)$, each with a measure of fractional flux density relative to the continuum level that is set to unity. The normalized CCF of these spectra is

$$c(x) = \frac{1}{N}\sigma_f\sigma_g\sum_{k=1}^{N} f(k)g(k-x) \tag{4.4}$$

where

$$\sigma_f^2 = \frac{1}{N}\left(\sum_{k=1}^{N} f(k)^2\right) \quad \text{and} \quad \sigma_g^2 = \frac{1}{N}\left(\sum_{k=1}^{N} g(k)^2\right) \tag{4.5}$$

are the rms of the spectra.

In an ideal situation, the $c(x)$ will have a maximum value when the template is coincident with the stellar spectrum. This occurs when the template has been shifted by $x = \ln(1 + (V_{\rm rel}/c)) \approx V_{\rm rel}/c$, where $V_{\rm rel}$ is the relative velocity between the star and the template.

4.1.2 Selection of spectral range

The spectra obtained from HERCULES in this research cover approximately 48 échelle orders, spread over the wavelength range of 450-700 nm. However, the whole spectral range cannot be used in the cross-correlation method because of a contamination. The Earth's atmosphere is not transparent. It contains atoms and molecules which interact with the starlight. A number of wavelengths of the starlight are absorbed from this interaction. These are called *telluric lines* and *telluric bands*. These bands and lines are superposed on stellar spectra. The telluric lines are mainly from water vapour (H_2O) and molecular oxygen (O_2). The water vapour lines are very numerous but weak at many wavelengths, especially in the yellow and red regions. The O_2 lines are very strong, especially at the A (≈770 nm) and B (≈690 nm) bands (figure 4.1). These lines should not be included in the cross-correlation method, because their radial velocities are those of the Earth's atmosphere.

The analysis of HERCULES spectra in this research had to avoid several orders that include telluric lines. Those orders are order numbers 82, 83, 85, 86, 90, 95–97, and 100.

4.1.3 Cross-correlation peak and the radial-velocity measurements

To have an efficient evaluation of the CCF $c(x)$, the fast-Fourier-transform (FFT) algorithm is used (Gray, 1992 and Press *et al.*, 1994). The requirement of this algorithm is that the spectra need to be as lacking as possible in any discontinuities. As the ends of each échelle order are sharp ends, the method called *apodizing* with a cosine bell should be used before applying the FFT. The following steps are performed.

The wavelength window of each order is defined by the number $m \times \lambda$ limits, where m is the order number. An HRSP command is used to trim both ends of each order

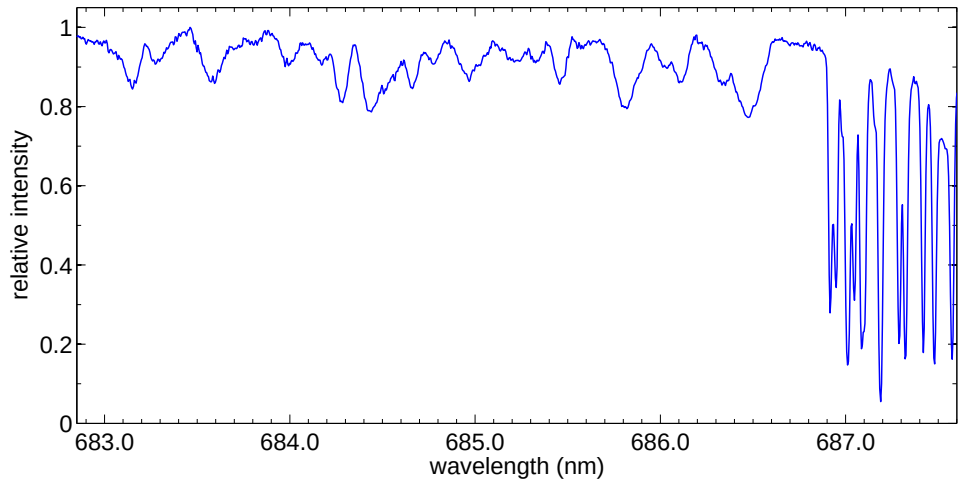

Figure 4.1: Part of a spectrum of an SB1 HD 38099. The sharp lines at the end of the spectrum are telluric lines from the oxygen molecules compared with weaker and broader lines of the star.

spectrum to have a particular wavelength window size $(m \times \lambda)_{min}$ to $(m \times \lambda)_{max}$. The arithmetic mean flux is calculated and subtracted from all datapoints to have a zero mean. The cosine-bell function is applied to the sharp edges of a window to smooth and taper the data to zero. The default size of the cosine window in HRSP is 64 bins which is equal to 6.25% of the HERCULES spectrum.

The cross-correlation between the stellar spectrum and the selected template spectrum can now be computed and the cross-correlation function generated. The selection of the template spectrum will be discussed in section 4.1.6. In HRSP, the cross-correlation must be performed at least twice for each pair of spectra in order to obtain the best determined radial velocity. The first cross-correlation estimates the relative radial velocity between the stellar spectrum and the template spectrum. The shift of radial velocity causes the difference in the spectral features of the two spectra. The wavelength window size, which is performed by the numbers $(m \times \lambda)_{\min}$ and $(m \times \lambda)_{\max}$, may need to be adjusted in the second cross-correlation for the best match of the spectral features of both images.

The CCF is produced with its shape depending on the matching of the spectra. For an SB1, the cross-correlation has one maximum which corresponds to the relative radial

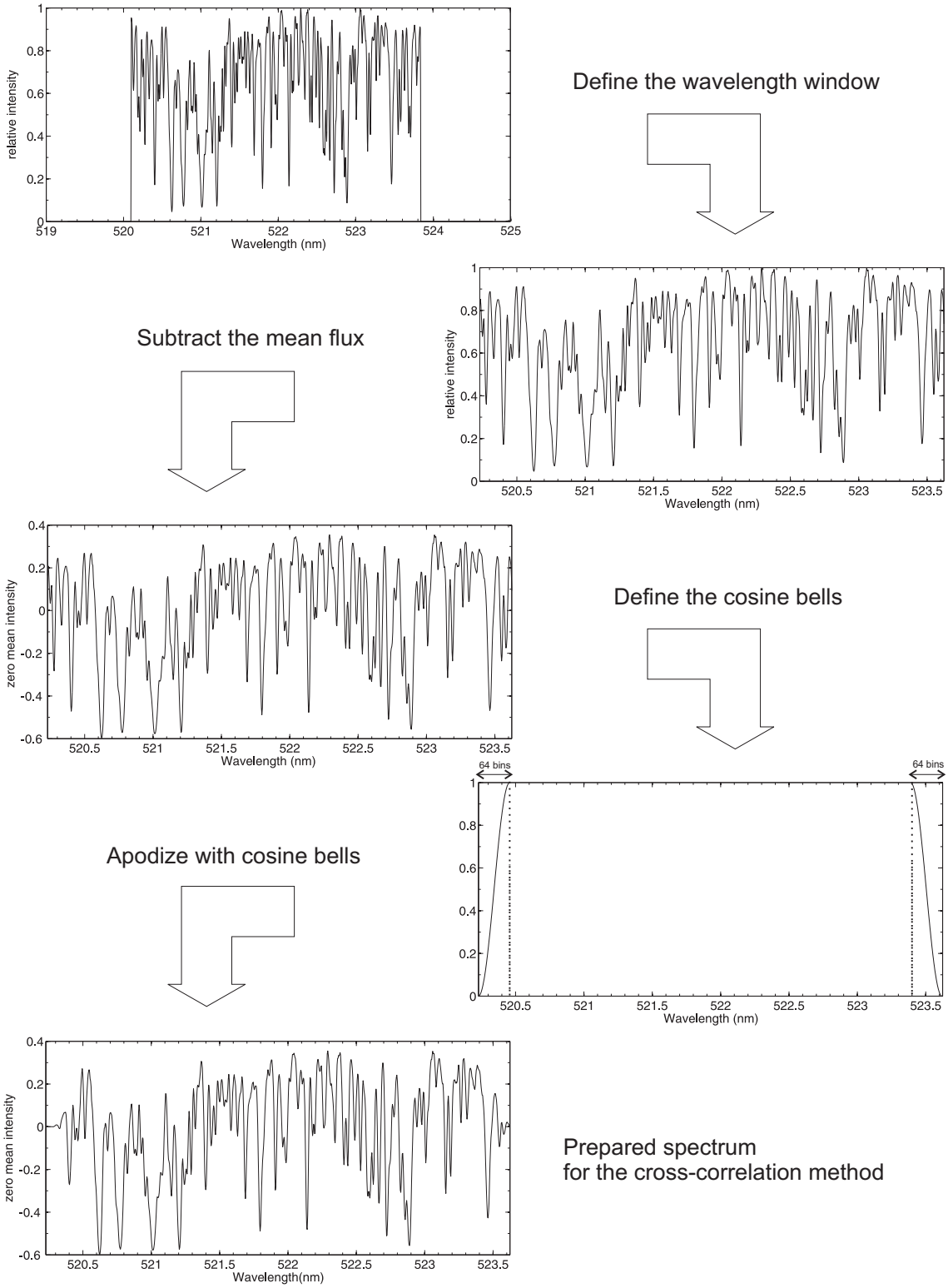

Figure 4.2: Diagrams of an apodizing method to prepare a spectrum for the cross-correlation. See text for details.

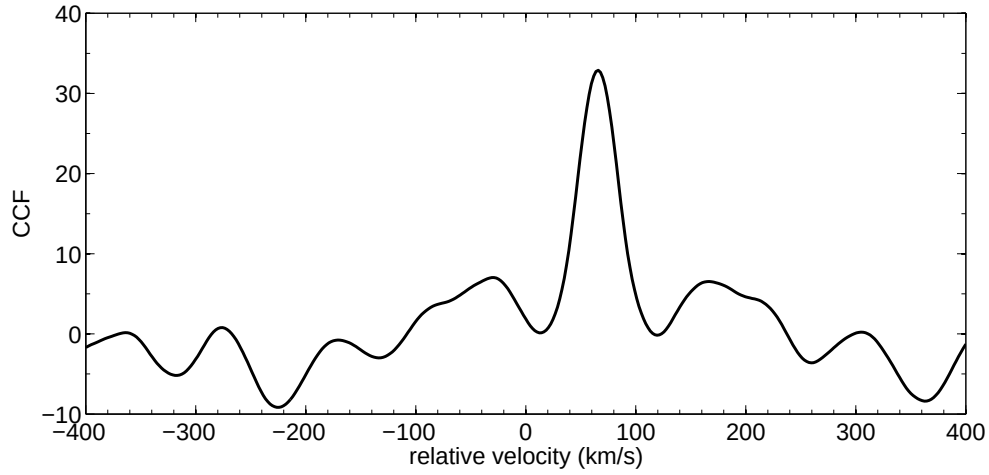

Figure 4.3: The CCF of an SB1 HD 352 spectrum with a spectrum of a standard star HD 150798 from the order 109 of HERCULES spectrum. The relative velocity measured from the peak position is $V_{\rm rel} = 63.290\ {\rm km\,s^{-1}}$. This velocity is not barycentric corrected.

velocity of the primary star. Figures 4.3 and 4.4 are CCF of spectra of systems HD 352 and HD 38099 both are cross-correlated with a standard star spectrum (HD 150798; $v \sin i = 6\ {\rm km\,s^{-1}}$). HD 352 has a broader CCF because of its rotational velocity, $v \sin i$, is 23 $\rm km\,s^{-1}$ while HD 38099 has $v \sin i = 3\ {\rm km\,s^{-1}}$. The cross-correlation maximum in every échelle order is calculated using the fitting method. The possible methods to measure the peak's position are spline interpolation, a Gaussian fit, and a parabolic fit, all of which are provided in HRSP. The spline method interpolates the CCF using all available points. The parabolic fit uses only three points around the maximum to fit the peak position. The Gaussian fit uses a least-squares method to fit a maximum profile with a selected number of points around the maximum profile. The Gaussian method was used in this research, as suggested by Ramm (2004). Typically eight data points in the peak of the CCF were used to fit a Gaussian by least-squares. However, for a few stars with rotationally broadened lines, this was increased to give good coverage of the peak.

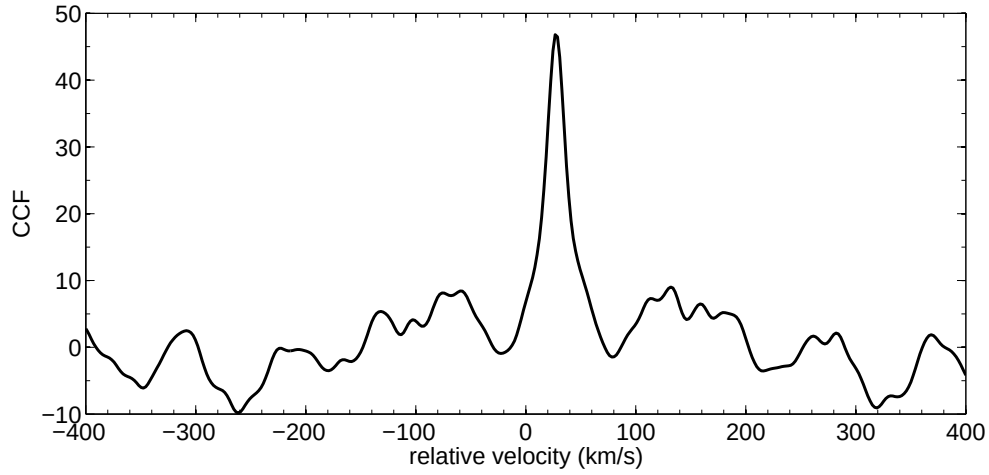

Figure 4.4: The CCF of an SB1 HD 38099 spectrum with a spectrum of a standard star HD 150798 from the order 109 of HERCULES spectrum. The relative velocity measured from the peak position is $V_{\rm rel} = 25.422\,{\rm km\,s^{-1}}$. This velocity is not barycentric corrected.

4.1.4 Two-dimensional cross-correlation

The cross-correlation of an SB2 system is calculated using the same process as described for an SB1. The cross-correlation of an SB2 spectrum with a single-lined template spectrum will cause a CCF with two peaks, i.e. figure 4.5, each peak corresponding to the relative radial velocity of each SB2 component.

A problem will occur if the radial velocities of both components are not much different, typically when the two components are crossing the line-of-sight and the velocities are transverse. Both spectral lines are then blended which results in an unresolvable peak of the CCF. It is possible to fit these peaks with a double Gaussian, but with a low precision.

The method of two-dimensional cross-correlation was introduced by Zucker and Mazeh (1994) with an algorithm they developed called TODCOR (TwO-Dimensional CORrelation). This technique can simultaneously obtain the Doppler shift of both components from the expansion of the cross-correlation technique to a two-dimensional velocity space. The principle of this technique is to replace the single template in the 1D-CCF by a combination of two templates with two different Doppler shifts, x_1 and

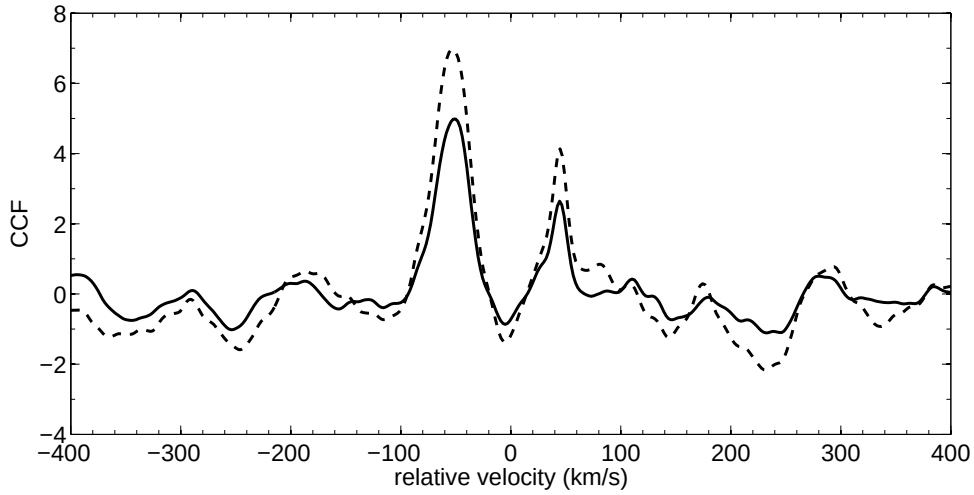

Figure 4.5: The CCF of an SB2 HD 197649 from the order 109 of HERCULES spectrum. The double peaks are related to each of the components. The spectrum is cross-correlated with two broadened spectra of standard stars, HD 203608 (solid line) and HD 20794 (dashed line). The average relative velocities measured from the peak positions are $V_{\mathrm{rel},1}$ $-57.49\ \mathrm{km\,s^{-1}}$, and $V_{\mathrm{rel},2}$ $39.85\ \mathrm{km\,s^{-1}}$.

x_2, with a flux-density ratio between the two stars, α. The equation 4.4 becomes

$$c(x_1, x_2, \alpha) = \frac{1}{N\sigma_f\sigma_g(x_1, x_2)} \sum_{k=1}^{N} f(k)(g_1(k - x_1) + g_2(k - x_2)) \tag{4.6}$$

where

$$\sigma_g^2(x_1, x_2) = \frac{1}{N} \left(\sum_{k=1}^{N} (g(k - x_1) + \alpha g(k - x_2))^2 \right). \tag{4.7}$$

Using TODCOR, the observed spectrum and two templates, each of which matches the spectrum of each of the components, are rebinned to have a constant pixel size in $\ln\lambda$ space. The mean value of each spectrum is calculated and subtracted from the spectrum in order to have a zero mean. The spectra are apodized with a cosine bell and the 2D-CCF is calculated. The algorithm searches over a grid of values of the two shifts to find the position of maximum correlation and it is also possible to find the light ratio of the components ($\alpha = L_2/L_1$ usually less than 1).

An application on the cross-correlation method is now extended to multi-dimensional space. The algorithm TODCOR has been successfully developed into three-dimensional

(Zucker *et al.*, 1995) and four-dimensional (Torres *et al.*, 2007) cross-correlations.

4.1.5 Weighted-mean radial velocities

The cross-correlation method generated the CCF for each order of spectrum. The characteristics of each order can give a different result in a measured radial velocity. The impurity of the spectrum, mainly from the telluric lines, was discussed in section 4.1.2. Besides that, the number of sharp and broad lines in each order also can have an effect, as the shape of a cross-correlation peak is dependent on the sharpness of the lines. The measured radial velocity will be less precise when broad lines such as those of hydrogen are included. These broad lines can also be avoided by the setting of the window size.

Besides the impurity of the spectral profile, the number of lines and their strength also affects the precision of the measured radial velocities from each order. The weighting factor should be considered in the determination of the final weighted-mean radial velocities. For each template spectrum, a number of copied spectra were generated which simulated the effect of random photon noise (with the same S/N as the original). Each image was cross-correlated with the original spectrum. The weights, $w_n = 1/\sigma_k^2$ were computed from the standard deviation, σ_k of the radial velocity for a given order, n.

4.1.6 Standard radial-velocity stars

As discussed in the previous sections, the cross-correlation method needs a template spectrum to calculate the shift of an observed spectrum. This template spectrum is a spectrum that has a known radial velocity on the standard system. Typically, it is a synthetic spectrum or a spectrum of a standard radial-velocity star. The standard radial-velocity stars are stars whose radial velocities have been monitored and found constant to within ± 1 km s^{-1} over decades. These stars typically are of spectral type F–K. The commission 30 of the IAU[1] takes responsibility to update and monitor the radial velocity of these stars. This can be found from their triennial publication in the *Reports on Astronomy* by the IAU.

In order to obtain the best results from the cross-correlation method, a template

[1]International Astronomical Union

spectrum which has the most similar characteristics as of the component is needed. An appropriate model of a stellar atmosphere is required for a synthetic template. In this research, the choice of stellar template is selected. A suitable template spectrum needs to be observed using the same instrument as the stellar spectra. For the SB1, the template spectrum can be one of the spectra of the system. But the proper standard star spectrum is still needed in order to convert the relative radial velocities from the cross-correlation to absolute values on a standard system. For the SB2, the template spectrum is a spectrum of a selected standard star. The spectral types of the template standard stars should match the spectral type of each SB2 component. The rotational velocity of the star should be small in order to have sharp lines which can be convolved with a rotational profile to match the line-broadening with that of the component's spectrum.

For this research, the other conditions of the selection are (i) it is a southern star, and (ii) it is brighter than $m_V = 5.0$ which allows a high S/N observation to be done using the HERCULES fibre#3. All the standard stars needed could not be found only from the stars listed in the IAU radial-velocity standard stars published by Stefanik *et al.* (1999), because of the lack of southern standard radial-velocity stars in that list. The other stars were selected from the list of standard stars observed with HERCULES by previous observers (Skuljan, 1999 and Ramm, 2004) and also from the *Bibliographic catalogue of stellar radial velocity* by Malaroda *et al.* (2006) and the *Bright Star Catalogue* 5th revised edition by Hoffleit *et al.* (1991). The total number of nine single stars were selected. These stars are listed with their basic data and reference catalogues in table 4.1. These stars were observed at least once using HERCULES with its fibre#3 during the time of this research.

The best S/N spectrum of each standard star was selected and used as a template for the cross-correlation method with the matched binary star spectra. The MJUO archived numbers, the published radial velocities from the references $V_{\rm pub}$, and the relative radial velocities with the sky $V_{\rm sky}$ of these templates are shown in table 4.2. Note that the standard radial-velocity stars used by Skuljan (1999) have no report on the measured radial velocity from that work, and in the standard radial-velocity star list by Stefanik *et al.* (1999), the velocity of HD 109379 is not reported in that list[2].

[2]HD 109379 has a velocity of -7.0 ± 0.0 km s^{-1} in the 2008 Astronomical Almanac. Also in the

Table 4.1: Basic data of standard radial-velocity stars observed in this research taken from various references.

HD	**R.A.(2000.0)**	**Dec (2000.0)**	m_V	**Spectral Type**	**Ref**
693	00 11 15.86	−15 28 04.7	4.89	F5V	1,3
11937	01 55 56.83	−51 36 34.5	3.69	G5IV	5
20794	03 19 53.22	−43 04 17.6	4.26	G8V	3
71701	08 20 38.89	−77 29 04.5	4.34	K0III-IV	5
109379	12 34 23.23	−23 23 48.3	2.65	G5II	1,2,3
114837	13 14 15.43	−59 06 10.3	4.92	F7IV	4
150798	16 48 39.89	−69 01 39.7	1.92	K2II-III	5

Reference
(1) Stefanik *et al.* (1999)
(2) Skuljan (1999)
(3) Ramm (2004)
(4) Malaroda *et al.* (2006)
(5) Hoffleit *et al.* (1991)

The $V_{\rm sky}$ are mean relative radial velocities calculated from the cross-correlation between each standard star spectrum and the blue-sky spectrum (HERCULES archived number 3405012). They are calculated for the purpose of converting the radial velocities of standard stars observed from HERCULES to a standard system. The blue-sky spectra were observed several times during observing runs using both fibre#1 and fibre#3. The rms scatter of their spectra is around 7 $\mathrm{m\,s^{-1}}$ for both fibres. The $V_{\rm sky}$ are used as zero-point radial velocities of G-type standard stars.

Figure 4.6 is a relative plot between the measured radial-velocities of template spectra and the published values. The difference between $V_{\rm sky}$ and $V_{\rm pub}$ of Ramm (2004) indicates the shift in the HERCULES measurements at around 160 $\mathrm{m\,s^{-1}}$. This shift is possibly because of the selection of the blue-sky spectrum used in the cross-correlation method. Even the blue-sky was used as a standard spectrum and its radial velocity was assumed to be zero, but the Sun itself is rotating and the radial-velocity difference between

almanac, the radial velocities of HD 693 and HD 150798 were reported as $+14.7 \pm 0.2$ $\mathrm{km\,s^{-1}}$ and -3.7 ± 0.2 $\mathrm{km\,s^{-1}}$ respectively.

Table 4.2: The standard-star template spectra used for the cross-correlation method with the programme binary stars in this research, with their radial velocities from the references (see the references code in table 4.1) and their radial velocities from cross–correlation with the sky spectrum.

HD	image	$V_{\rm pub}$ ($\rm km\,s^{-1}$)	Ref	$V_{\rm sky}$ ($\pm$ 0.007 $\rm km\,s^{-1}$)
693	3608097	+14.50	1	+15.108
		+14.933	3	
11937	3608094	−6	5	−6.016
20794	3301066	+87.812	3	+87.974
71701	3304051	+22	5	+21.619
109379	3489063	−7.390	3	−7.246
114837	3405089	−63.7	4	−63.721
150798	3487075	−3	5	−3.163

opposite limbs of the Sun is more than 4 $\rm km\,s^{-1}$. The position of the Sun and the pointing position of the telescope can make a difference in the measured velocities. The atmospheric turbulence, including the horizontal wind, are also factors that can influence the apparent velocity of the blue sky.

The differences in $V_{\rm sky}$ and $V_{\rm pub}$ of the other references are possibly because of the uncertainty in both values. Even these numbers are high precision and accuracy but one cannot expect these numbers to be strictly absolute radial velocities. Stefanik *et al.* (1999)'s report on the IAU standard radial-velocity stars which showed that the rms of the measured radial velocities of standard stars are at the level of uncertainty of 500 $\rm m\,s^{-1}$. The reasons for this result are that the star itself has an intrinsic variation in its radial velocity. Asymmetric line profiles from the convective motion on the stellar surface and asymmetric emissions of the stellar atmosphere can caused an inaccurate measurement. Giant and supergiant stars are variable, due to the activities of their photospheres, i.e. pulsation and spots, which cause a few tens of $\rm m\,s^{-1}$ variation in radial velocities (Hatzes, 2002). Udry *et al.* (1999) suggested that the high-precision standards should be dwarfs.

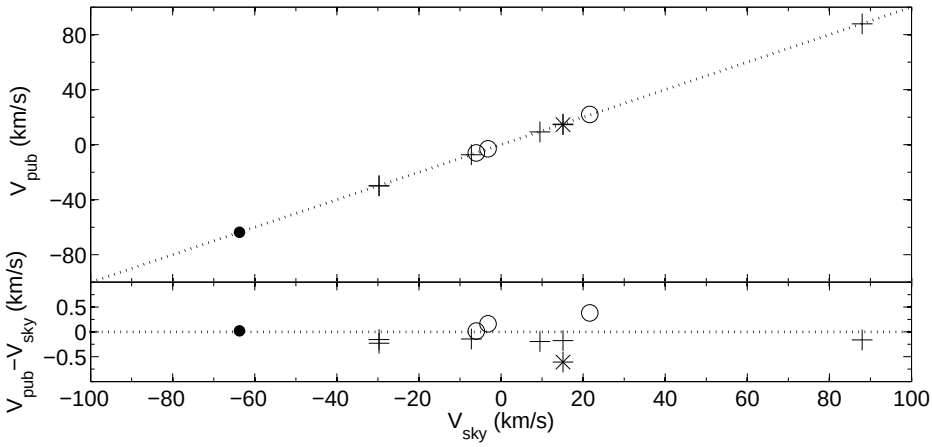

Figure 4.6: The radial velocities of standard radial-velocity stars measured from HERCULES compared with those from published data (Markers: $*$, Stefanik *et al.* (1999); $+$, Ramm (2004), $\bullet$, Malaroda *et al.* (2006), $\circ$, Hoffleit *et al.* (1991)). The dotted lines present $V_{\rm pub} = V_{\rm sky}$.

Besides that, many processes take part in the effect on radial velocities. These include an effect from the star's gravitational potential that causes the gravitational redshift, which varies from around 30 $\mathrm{m\,s^{-1}}$ for supergiants to around 30 $\mathrm{km\,s^{-1}}$ for white dwarfs, and an effect from exoplanets which may vary the measured radial velocities by 10–100 $\mathrm{m\,s^{-1}}$. Instrumental characteristics, i.e. the diffuse scattered light, the resolution, the selection of the template, etc., also affect the precision. A detailed discussion on the precision and absolute zero-point of standard radial-velocity stars can also be found in Lindegren & Dravins (2003).

4.2 Orbital analysis from radial velocities

Fundamental parameters of a system's orbit can be derived from a set of radial velocities of any spectroscopic binary system. The analysis of the radial velocities is based on the radial velocity equation

$$V_{\rm rad}(K, e, \omega, T, P, \gamma) = K[\cos(\upsilon + \omega) + e\cos\omega] + \gamma \tag{4.8}$$

where υ is a function of T and P. This equation and the graphical method to determine these parameters was first introduced by Lehmann-Filhés (1894). In the present day, the analytical method and differential methods are more generally used. The following discussion will be on the differential method as it is used in this research.

4.2.1 Least-squares differential correction

Six orbital elements of a particular binary system, $K, e, \omega, T, P, \gamma$, can be determined from a set of n observations of radial velocity $V_{\rm rad}(t)$. The best values of these elements can be found following an iterative least-squares analysis known as *differential corrections*.

From equation (4.8), a small change in any of the orbital elements has an impact on the radial velocity. Thus, equation (4.8) can be expanded as a first-order Taylor series as

$$\Delta V = \frac{\partial F}{\partial K}\Delta K + \frac{\partial F}{\partial e}\Delta e + \frac{\partial F}{\partial \omega}\Delta\omega + \frac{\partial F}{\partial T}\Delta T + \frac{\partial F}{\partial P}\Delta P + \frac{\partial F}{\partial \gamma}\Delta\gamma \tag{4.9}$$

The result of this partial derivative was first shown by Lehmann-Filhés (1894) as

$$\begin{aligned}\Delta V \;=\; & [\cos(\upsilon+\omega)+e\cos\omega]\Delta K \\ & +K\left[\cos\omega - \frac{\sin(\upsilon+\omega)\sin\upsilon(2+e\cos\upsilon)}{(1-e^2)}\right]\Delta e \\ & -K\left[\sin(\upsilon+\omega)+e\sin\omega\right]\Delta\omega \\ & +K\left[\sin(\upsilon+\omega)(1+e\cos\upsilon)^2\frac{2\pi}{P(1-e^2)^{3/2}}\right]\Delta T \\ & +K\left[\sin(\upsilon+\omega)(1+e\cos\upsilon)^2\frac{2\pi(t-T)}{P^2(1-e^2)^{3/2}}\right]\Delta P \\ & +\Delta\gamma. \end{aligned} \tag{4.10}$$

All the coefficients of the differential-correction terms can be calculated from the preliminary estimation of the orbital elements. The $(O-C)$ value or the difference between the observed velocity (O) and the calculated velocity (C) from the initial estimation was performed for the value ΔV at the time of observation t. For each observation of $V(t)$, equation (4.10) can be written. There will be a set of n simultaneous equations for n observations with six unknown differential-correction terms, which are overdetermined when n is greater than 6. The least-square iterations were performed to

find the differential-correction terms (ΔK, etc.) and this put the revised values back to the equation for a second iteration ($K_1 = K_0 + \Delta K$, etc.) and so on. If the initial estimation is close to the solution, which can be estimated using the graphical method, the subsequent iterations will converge to the best fit solution.

This method of Lehmann-Filhés will provide a reasonable result for a system with eccentricity $e > 0.15$. For a system with low eccentricity, such as those that we study in this research, the solution becomes more unstable. This is because the longitude of periastron ω and the time of periastron passage T are increasingly indeterminate when e approaches to zero.

To eliminate this problem, a new method of analysis was introduced by Sterne (1941). The time of periastron passage T is replaced by the *time of zero mean longitude* T_0 which is the time of ascending-node passage. The mean longitude, L is defined by

$$L = 2\pi(t - T)/P + \omega = \Phi + \omega \tag{4.11}$$

where Φ is the mean anomaly, which means that T_0 occurs when $\Phi = -\omega$. This approach is an advantage because T_0 is always defined regardless of the eccentricity, and to convert the T_0 to T is straightforward;

$$T = T_0 + \frac{\omega P}{2\pi}. \tag{4.12}$$

Replacing T_0 in equation (4.8), the differential-correction equation (4.10) is revised. The coefficients of two terms, $\Delta\omega$ and ΔP, are changed.

$$\begin{aligned}
\Delta V \;=\; & [\cos(\upsilon + \omega) + e\cos\omega]\Delta K \\
& + K\left[\cos\omega - \frac{\sin(\upsilon+\omega)\sin\upsilon(2 + e\cos\upsilon)}{(1-e^2)}\right]\Delta e \\
& - K\left[\sin(\upsilon+\omega) + e\sin\omega - \frac{\sin(\upsilon+\omega)(1+e\cos\upsilon)^2}{(1-e^2)^{3/2}}\right]\Delta\omega \\
& + K\left[\sin(\upsilon+\omega)(1+e\cos\upsilon)^2\frac{2\pi}{P(1-e^2)^{3/2}}\right]\Delta T_0 \\
& + K\left[\sin(\upsilon+\omega)(1+e\cos\upsilon)^2\frac{2\pi(t-T_0)}{P^2(1-e^2)^{3/2}}\right]\Delta P \\
& + \Delta\gamma.
\end{aligned} \tag{4.13}$$

For a system with e approaching to zero, equation (4.13) becomes

$$\begin{aligned}\Delta V &= \cos L\Delta K + Ke\cos\omega\cos 2L + Ke\sin\omega\sin 2L \\ &\quad + \frac{2\pi K\sin L}{P}\Delta T_0 + \frac{2\pi K(t-T_0)\sin L}{P^2}\Delta P + \Delta\gamma. \end{aligned} \tag{4.14}$$

For $e < 0.03$, L can be approximated as $L = \Phi + \omega \approx \upsilon + \omega$ (Andersen, 1983).

The radial velocity is assumed to have a normal distribution with its variance σ^2. Their residuals, or the difference between the observed and calculated best-fit values, are also expected to have a normal distribution. In this research, the radial velocities with their residuals larger than the rejection threshold of 3σ were rejected from the iteration of a least-squares method. This interval, $\pm 3\sigma$, covers 99.7% of normally distributed data.

4.2.2 Error estimation

The value of any measured parameter is greatly reduced without its error bar. The error determination is based on numerical simulations that are used in this research and assume that the best-fit solution is most probable estimate of the true value.

From an orbital solution, the error of the best fit and the error of individual observations, a number (usually 100) of random sets of observations were created by replacing every observed radial velocity by a random value assuming a Gaussian distribution. An orbital solution was derived for each random set. The standard deviations, σ, of each orbital parameter, which can be regarded as the rms errors of each parameter, were calculated from the distribution of N values.

4.2.3 Improvement of an orbital solution by fixing some elements and combining HERCULES data with historical data

In many cases, it is not necessary to find all six orbital elements from a set of radial velocities simultaneously. Also, in some cases, the data are not sufficient, in view of the size of data and the phase coverage, for an orbital solution to be achieved with the all variables free. Some orbital parameters may be independently estimated from the available data. For example, observations at the ascending-node passage (known as the time of zero mean longitude, T_0) and at the descending-node passage are necessary, in

order to provide information on the semi-amplitude K. The convergence to the orbital solution may not occur without a good prior estimation of the parameters, or after fixing some of the parameters.

To achieve the best solution, the information about a system usually comes from a combination set of data. Photometric observation of an eclipsing binary can provide a more accuracy orbital period of a system. It is also possible to use a combination of radial-velocity data sets to find a more precise solution. A long time span between the present HERCULES data and the historical published data, especially those that are referenced in the S_{B^9} catalogue, could be used to determine with more accuracy some orbital periods. This possibly results in an improvement in all the other orbital parameters as well.

Considering the precision of historical data, a decision is needed on how they could be combined with HERCULES data. The historical data usually have lower precisions than HERCULES data. This means that when the data are combined, they should have lower weights. These weights should be calculated properly. Also, there are sometimes systematic differences between the historical data and HERCULES data. Both data sets should be brought to the same velocity zero-point.

To avoid these obstacles, both sets of data are analysed separately. Two difference sets of orbital solution are obtained, which means that there are two values of T_0. In principle, the difference in these two T_0 values should be a number of complete orbital cycles. The time of zero mean longitude of each cycle between the two values is a simple linear ephemeris in the form

$$T_{0,n_c} = T_{0,\mathbf{hist}} + n_c\bar{P}, \tag{4.15}$$

$$T_{0,\mathbf{new}} = T_{0,\mathbf{hist}} + N_c\bar{P}, \tag{4.16}$$

where n_c is the number of orbital cycles that elapsed from the historical time of zero mean longitude $T_{0,hist}$, $T_{0,new}$ is the HERCULES time of zero mean longitude, and N_c is the total number of cycle between two epochs and $\bar{P}$ is the orbital period.

The orbital period $\bar{P}$ can be calculated from the above approach. The time interval $\Delta T_0 = T_{0,new} - T_{0,hist}$ is divided by the number of complete cycles N_c that the time

interval ΔT_0 contains. The mean orbital period is

$$\bar{P} = \frac{\Delta T_0}{N_c}, \tag{4.17}$$

and the corresponding uncertainty for $\bar{P}$ is

$$\sigma_{\bar{P}} = \frac{\sigma_{\Delta T}}{N_c} \tag{4.18}$$

where $\sigma^2_{\Delta T} = \sigma^2_{T,\mathrm{hist}} + \sigma^2_{T,\mathrm{new}}$.

It is also possible that other types of epoch that can be used for the $\bar{P}$ calculation rather that T_0 (Ramm, 2004). These are the time of periastron passage, the time of nodal passage and the time of ascending or descending radial velocity (where it reaches the systemic radial velocity). The latter two epochs can be determined from sufficient observations, with no orbital solution needed, for instance spline interpolation of the data or a fitting with a suitable function such as a sinusoidal. But T_0 should preferably be used as it is the most precise value.

A new orbital solution can be obtained after fixing the orbital period with this higher precision value $\bar{P}$, while the other five parameters are still free.

4.3 Problem of a small-detectable eccentricity

The detection of a small eccentricity in the work of Skuljan *et al.* (2004) motivated the study of this research. In that work, the orbit of an SB1, ζ TrA, was found to have a very precise $e = 0.013\,98 \pm 0.000\,19$ with an rms of the fit only about 14 $\mathrm{m\,s^{-1}}$. The question arises whether this detectable e comes from the eccentric orbit or whether it is a result from any intrinsic perturbation of the system.

4.3.1 Systematic errors in a measured radial velocity

As discussed in section 4.1.6, the measured radial velocity, even from a high precision spectrograph, can contain errors which result from both the intrinsic variation of the star's photosphere and the instrument's characteristics. Besides that, the characteristic and evolutionary state of a binary system can also have an effect on its measured radial velocity.

Proximity effects is the term used for an interaction between the stars in a close binary system. They include two important sources of errors in a measured radial velocity of a star. That are the ellipticity effects and the reflection effects. For a star with a non-spherical shape, such as those in a contact or semi-detached binary system, its surface gravity is a function of position on the surface which results in a differential brightness or so-called *gravity darkening*. This *ellipticity effect*[3] makes the facing hemisphere of a star, which is more distorted, radiate less than the other hemisphere. A review of the ellipticity effect in spectroscopic binary and eclipsing binary stars can be found in a series of papers by Beech (1985, 1986a, 1986b and 1989). The mathematical analysis of this effect was presented by Morris & Naftilan (1993) and this was applied to the photometric data of an SB1 system, HR 8427, to determine the properties of both components.

The consequences of the *reflection effect* arise when the temperatures of both components are different. This term is really a misuse of the word 'reflection', as this effect is the mutual irradiation of the facing hemispheres of the two stars. The radiant energy of the companion heats up the facing hemisphere of the star which in turn leads to an increase of its local flux. One should be aware that, for a system with two components, which have similar temperatures, multiple reflections are needed to treat the effect properly, since each reflection produces a higher temperature on both components. A theoretical review about this effect was discussed by Kopal (1988), and by Wilson (1990).

Both effects impact on the light curve and the shape of absorption lines. The centre of the integrated flux from a star may have a centre displaced from the centre of gravity into the direction of the illuminating source (i.e., depending on the orbital phase). This causes an asymmetry in the absorption lines, which results in an error in the measured velocity.

Beside proximity effects, other phenomena can also cause systematic errors in the measured radial velocity of a binary system. These include the mass transfer between the two components, and a gas stream that flows between the two stars. When a star fills the limiting surface of its Roche lobe, the mass from the filled component flows through the inner Lagrangian point, L_1 of the Roche lobe. This effect will not be discussed in this research as it occurs in a contact or semi-detached system.

[3]In some literature sources, a non-spherical star is called an ellipsoidal variable and this effect is so-called the ellipsoidal effect.

For a spectroscopic binary system that eclipses, the *Rossiter effect* can occur. Each section of the stellar disk has a different line-of-sight velocity which results in the stellar rotational broadening. In general, the total flux comes from the whole stellar disk and the observed velocity is centred at the centre of mass of the star. However, when the system is partially eclipsed, part of the stellar disk is hidden by the other star. The observed light comes from the visible part only. The measured radial velocity is therefore greater or smaller than the radial velocity of the star's centre of mass. This effect was studied by Rossiter (1924) and McLaughlin (1924) in the binary systems, β Lyrae and Algol, and it is sometimes called the Rossiter-McLaughlin effect[4]. An example of this effect in a binary system is shown in figure 2.7 on page 18. The sample system TY Pyx is a spectroscopic binary which is also an eclipsing binary. It consists of two solar-type stars which orbit at an inclination of $i = 87\overset{\circ}{.}88$.

4.3.2 Statistical test of low-eccentricity orbital solutions

The errors in the measured radial velocities, whether from observational errors, an intrinsic variation (sections 4.1.6), or from proximity effects (section 4.3.1) can cause a spurious eccentricity in an analysed orbit of a binary system. This issue was first pointed out by Carpenter (1930) from his study of the Algol-type system, U Cephei. Luyten (1936) discussed orbital elements of 77 spectroscopic binaries with small eccentricity and found that 33 orbital solutions should be adopted as circular orbits as the value of e is too small to be determined from the observations. The work by Sterne (1941a) showed that tidal distortion and darkening effects in binaries influence the observed radial velocity, which may leads to a spurious eccentricity. Savedoff (1951) investigated the eccentricty obtained independently from the light curve and the velocity curve and found them to be only weakly correlated.

The widely used method to investigate the reality of a detectable small-eccentricity orbit was proposed by Lucy and Sweeney (1971). This section will review a statistical method to test the significance of an orbital eccentricity, as proposed by Lucy & Sweeney (1971, hereinafter LS71), and by Lucy (2005, hereinafter L05).

If the orbit of a spectroscopic binary star is a pure Keplerian orbit, i.e. no perturba-

[4]In their papers, the effect is called a rotational effect.

tion from any sources, the radial velocity of a component can be shown to be given by equation (2.9);

$$V_{\rm rad} = K[\cos(\upsilon + \omega) + e\cos\omega] + \gamma. \tag{4.19}$$

Since $V_{\rm rad}$ is a periodic function of time, it can be expanded as a Fourier series

$$V_{\rm rad} = \frac{1}{2}C_0 + \sum_{j=1}^{\infty}[C_j \cos jL + S_j \sin jL], \tag{4.20}$$

where $L = 2\pi(t-T)/P + \omega = \Phi + \omega$ is the mean longitude and Φ is the phase. The Fourier coefficients, C_j and S_j are

$$C_j = \alpha c_j \cos j\omega + \beta s_j \sin j\omega, \quad \text{and} \quad S_j = \alpha c_j \cos j\omega - \beta s_j \sin j\omega, \tag{4.21}$$

where $\alpha = K(1-e^2)\cos\omega$ and $\beta = K\sqrt{1-e^2}\sin\omega$. The coeffcients c_j and s_j can be expressed in terms of Bessel functions as an expansion of the power series of e, which is given in Appendix A. The first three terms of the Fourier coefficients can be approximated as

$$\begin{aligned} C_0 = 2\gamma, \quad C_1 &= K, \quad C_2 = Ke\cos\omega, \quad C_3 = (9/8)Ke^2\cos 2\omega \\ S_1 &= 0, \quad S_2 = Ke\sin\omega, \quad S_3 = (9/8)Ke^2\sin 2\omega. \end{aligned} \tag{4.22}$$

If there is any perturbation in the radial velocity of a star, the coefficient of the Keplerian orbit will be affected by a non-Keplerian term. This means that the coefficients of equation (4.20) differ from the actual orbit and result in an error in the orbital parameters, including the eccentricity.

For each observed radial velocity, v_n, there is a relative weight w_n. The weights are in general equal for all observations of a given star. If the predicted radial velocity is V_n for a model of the system, the goodness-of-fit of a model k is

$$R_k = \sum_{n=1}^{N} w_n (v_n - V_n)^2. \tag{4.23}$$

The first model to be investigated is the model of a circular orbit with an observational error. We assume that the orbital solution set $k = 1$ is a solution from the least-squares method applied to the observed radial velocities with a constraint of a circular orbit, $e = 0$, and the orbital solution set $k = 2$ is a solution of the same data set

using the same method with no constraint. The first solution has four variables (P, T_0, γ, and K) while the second solution will have a better fit because it has two additional variables ($e\cos\omega$ and $e\sin\omega$). To test the significance of these two additional fitting parameters, a circular orbit is assumed and a null hypothesis is

$$e\cos\omega = 0, \quad e\sin\omega = 0. \tag{4.24}$$

The probability that a detected eccentric orbit is a result of the measurement errors of a circular orbit is

$$p_1 = \left(\frac{R_2}{R_1}\right)^{\beta_2} \tag{4.25}$$

where $\beta_2 = (1/2)(N - M_2)$ and M_2 is the number of variables for the $k = 2$ fit, i.e. there is no fixed parameter in the $k = 2$ model, and M_2 is equal to 6. LS71 suggested that the assumption of a circular orbit should be adopted at the 5% significance level;

$$e = 0 \quad \text{if} \quad p_1 \geq 0.05. \tag{4.26}$$

In that paper, orbits of 213 spectroscopic binary systems were recomputed from their low eccentricity orbits ($e \approx 0.1$) that were reported in the *Sixth catalogue of the orbital elements of spectroscopic binary systems* (Batten 1967). It was found that as many as 153 orbits have $p_1 \geq 0.05$ and hence circular orbits were adopted. Various papers by many authors have used this method to reject small e values and circular orbits have been adopted.

As present modern astronomical instruments lead to a higher precision in the measured radial velocity, so the error in the measurement is decreased. The probability that the detected e is a result from measurement errors is decreased and this leads to the possibility to detect either a perturbation in a system or a genuine small value of the eccentricity.

As show in equation (4.20), a function of eccentric radial velocities is a summation of various sinusoidal functions. These sine functions have their amplitudes that depend on the K, e and ω values (equation (4.22)) and their frequency is an integral multiple of the orbital frequency. If there is no perturbation in the orbit, an analysis of the higher harmonics in the observed data will show a correct amplitude and phase of these harmonics. A perturbation, on the other hand, will differ in phase and amplitude of the harmonics from the expected Keplerian harmonics.

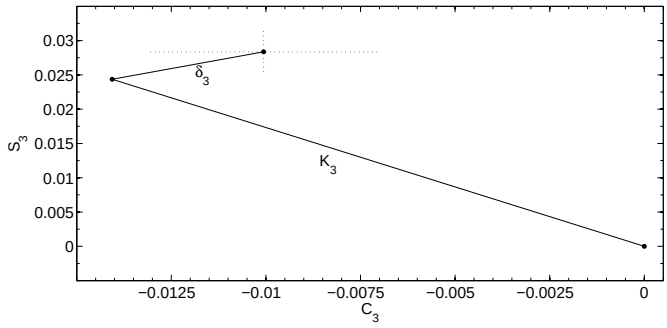

Figure 4.7: A phasor diagram of a perturbation system. The K_3 vector of a Keplerian eccentric orbit with $e = 0.05$, $\omega = 60^{\circ}$ and $K = 10\ \mathrm{km\,s^{-1}}$. The best-fit third harmonic perturbation is $\delta_3 = (0.004 \pm 0.003, 0.004 \pm 0.004)\ \mathrm{km\,s^{-1}}$.

First, assuming that the system has an elliptical orbit with a perturbation, the perturbed radial velocity can be written in the form

$$V_{\mathrm{rad}} = V_{\mathrm{ell}} + \Delta C_j \cos jL + \Delta S_j \sin jL. \tag{4.27}$$

The first term, V_{ell}, is the previously determined elliptical orbit ($k = 2$). The perturbation effects appear in the additional terms of the jth harmonic. L05 suggested that the third harmonic should be analysed and in some cases, extended to the fourth harmonic.

Let $K_3 = (C_3, S_3)$ be a vector of a third harmonic of a Keplerian eccentric orbit and $\Delta_3 = (\Delta C_3, \Delta S_3)$ is a vector of a perturbation in the third harmonic. The best-fit solution of a set of data with equation (4.27) for $j = 3$ will give a best-fit third harmonic perturbation $\delta_3 = (\delta C_3, \delta S_3)$ with its error. The system will be considered to have no perturbation if the observed third harmonic vector $H_3 = K_3 + \delta_3$ is in-phase with the K_3 vector and its amplitude is within the δ_3 error bar. For example, if a system has an eccentricity $e = 0.05$, $\omega = 60^{\circ}$ and a semi-amplitude $K = 10\ \mathrm{km\,s^{-1}}$, then $K_3 = (-0.0141, 0.0244)\ \mathrm{km\,s^{-1}}$ with an amplitude $1.125\ \mathrm{km\,s^{-1}}$ and phase 120°. If the best-fit third harmonic perturbation is $\delta_3 = (0.004 \pm 0.003, 0.004 \pm 0.004)\ \mathrm{km\,s^{-1}}$, the observed third harmonic is in-phase and its amplitude is comparable within the errors (figure 4.7). One can consider that there is no perturbation in this example.

To investigate the significance of the perturbation, two null hypotheses need to be tested. The first is to test the probability of detecting the perturbation. From equation

(4.27), if there is no perturbation, the null hypothesis is

$$\Delta C_j = 0, \quad \text{and} \quad \Delta S_j = 0 \tag{4.28}$$

and the probability that there is no perturbation is

$$p_2 = (\frac{R_3}{R_2})^{\beta_3}, \tag{4.29}$$

where $\beta_3 = (1/2)(N - M_3)$ and M_3 is the number of additional parameters for the unconstrained model, which is equal to two. The hypothesis is rejected when $p_2 \geq 0.05$, which means that there is no evidence of a perturbation.

The problem still arises in the case that the third harmonic is strong and detectable. Even though the perturbation may not be significant in the third harmonic but the detectable e may be due to the second harmonic perturbation. The test for the detection of the third harmonic is under two null hypotheses that neither the Keplerian harmonic ($K_3 = (C_3, S_3)$) nor the non-Keplerian harmonic ($H_3 = K_3 + \delta_3$ where δ_3 is a best-fit third harmonic) is detected;

$$K_3 = 0, \quad \text{and} \quad H_3 = 0. \tag{4.30}$$

The second null hypothesis is for a conclusion that the best-fit third harmonic δ_3 is cancelled with the Keplerian third harmonic K_3.

To test the first hypothesis, the third harmonic K_3 is removed from equation (4.27) in order to examine the significance of the Keplerian third harmonic in a solution. The constraints are

$$\Delta C_3 = \delta C_3 - C_3, \quad \text{and} \quad \Delta S_3 = \delta S_3 - S_3 \tag{4.31}$$

which gives a probability

$$q_1 = (\frac{R_3}{R_4})^{\beta_3}. \tag{4.32}$$

The second test on a non-Keplerian third harmonic H_3 has constraints

$$\Delta C_3 = -C_3, \quad \text{and} \quad \Delta S_3 = -S_3. \tag{4.33}$$

The probability of the model is then

$$q_2 = (\frac{R_3}{R_5})^{\beta_3}. \tag{4.34}$$

To consider the detection of K_3 both null hypotheses should be rejected. That means that the probability that K_3 is detected is examined from

$$p_3 = \max(q_1, q_2). \tag{4.35}$$

The third harmonic is regarded as detected only if $p_3 \leq 0.05$.

In conclusion, for a system with a small detectable eccentricity, it is suggested that the tests for the detection of the perturbation and a higher Keplerian harmonic are needed. The decision on the reality of the eccentricity follows the results of the tests as follows:

1. $p_1 \leq 0.05$: The fitted e is accepted for its reality, and random errors in the velocities do not explain the departure from the $k = 1$ ($e = 0$) model. The subsequent tests on p_2 and p_3 test whether the apparent eccentricity is Keplerian or caused by perturbations.

2. $p_2 \geq 0.05$; $p_3 \leq 0.05$: The eccentricity is strongly supported. The amplitude and phase of the first three Keplerian harmonics are consistent with the data. No evidence of perturbation.

3. $p_2 < 0.05$; $p_3 \leq 0.05$: The perturbation is detected as well as the third Keplerian harmonic. The eccentricity is uncertain.

4. $p_2 \geq 0.05$; $p_3 > 0.05$: The failure to detected the third Keplerian harmonic implies that even if the third harmonic perturbation is not detected but the detectable e may be due to a second harmonic perturbation.

5. $p_2 < 0.05$; $p_3 > 0.05$: The Keplerian third harmonic is not detected. The measured H_3 is all from a perturbed velocity curve. The amplitude and phase of the first three Keplerian harmonics are inconsistent with the data.

These statistical tests are designed only to test for the reality of a small measured e. More investigation is needed to determine the source of any detectable spurious eccentricity.

4.4 Inverse modelling of binary star systems

To solve a problem, it is not necessary to start from the problem and analyse the data to find the solution. For some sorts of problems, the best solution can be found inversely from a set of possible solutions and trying to match them with the data. In the data analysis, many possible models are generated to give a result that is the best match to the data, which represents an inverse modelling analysis. This method can be applied to the study of binary star systems. The models of a system are generated with various possible characteristics, including their masses, sizes, separation, surface temperatures, as well as their photospheric activities and tidal interaction. Theoretical light curves and radial velocity curves for these models will then confront with the observational data to find the best possible characteristics of a system.

The models and programs to analyse astrophysical data were significantly developed since the 1970s. The computing program is based on theoretical models and its ability has depend on the efficiency of the models and the power of computing machines, i.e. human, calculator and computer. The historical context for a binary star model has been reviewed by Wilson (1994). Many modelling programs were designed to analyse the light curves and radial velocity curves of binary systems, i.e. EBOP (Eclipsing Binary Orbit Program (Etzel, 1981)) , WINK (Wood, 1973), FOTEL (recent version FOTEL-4 Hadrava, 2004), WD (Wilson and Devinney, 1971), etc. The designing of each program is based on different models and techniques. Only the WD program will be discussed here, as it is used in this research. The detailed discussion on the other software packages can be found in Kallrath & Milone (1998).

The most widely used computer code in the analysis of binary system light curves and radial velocity curves is the Wilson-Devinney Program (WD). This program was first introduced in 1971 (Wilson and Devinney 1971) and has undergone continuous developments and several extensions. The most recent version of this program is the fourth version, WD03 (Van Hamme & Wilson 2003)[5]. The program consists of two main FORTRAN programs running under DOS, the **LC** code is for generating theoretical light curves and radial velocity curves, spectral line profiles, and images from any set of input parameters and the **DC** code is for light curve and radial velocity curve fitting using the

[5]During the time of this research, the latest extension was provided on the accurate radiative modeling (presented by Van Hamme & Wilson (2007)).

Table 4.3: Derived orbital parameters of ζ TrA, taken from table 2 of Skuljan *et al.* (2004). Note that the $\gamma_{\rm rel}$ is not barycentric corrected.

Parameter	**Skuljan *et al.* (2004)**
K	7.5001 ± 0.0017 km s^{-1}
e	$0.013\,98 \pm 0.000\,19$
ω	$252\overset{\circ}{.}30 \pm 0\overset{\circ}{.}87$
T_0	HJD $245\,2752.319\,45 \pm 0.000\,48$
P	12.975 780 d (fixed)
$\gamma_{\rm rel}$	6.3892 ± 0.0012 km s^{-1}

least-squares method, with ten subroutines used by the main programs.

4.4.1 Spot model of a binary system ζ Trianguli Australis

In a recent paper published by Skuljan *et al.* (2004), they derived precise elements of a Keplerian orbit for the F9V star ζ TrA ($m_V = 4.91$) in a single-line spectroscopic binary. They used 228 high-precision radial velocities from HERCULES. The orbital solution, as in table 4.3, indicated a nearly circular orbit with small but highly significant eccentricity ($e = 0.013\,98 \pm 0.000\,19$). King *et al.* (2003) assigned ζ TrA to the Ursa Major moving group and it must therefore be young (~ 500 Myr). Skuljan *et al.* (2004) concluded that, from the detectable small-eccentricity of ζ TrA, it should be considered a possibility that (i) the system may be older and not a member of the UMa moving group, (ii) it has sustained a near-circular orbit since its formation, or (iii) for late-type dwarfs, if the cut-off period of the circularization is 10 days, then the orbit of ζ TrA has circularized faster than the theoretically expected.

L05 re-analysed the solution of Skuljan *et al.* (2004) and criticized this orbital solution. He noted that for a system with $K = 7.5001$ km s^{-1} and $e = 0.013\,98$, the third harmonic of a Keplerian orbit is $(9/8)Ke^2 = 1.65$ m s^{-1}. However, he found that from the available HERCULES data of ζ TrA, the best-fitted third harmonic is 4.6 ± 2.0 m s^{-1} and it has a phase some 90° different from the expected value (figure 4.8). His

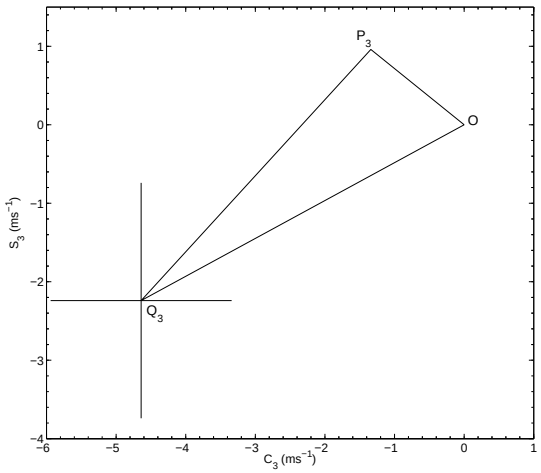

Figure 4.8: The 3rd harmonic components in the velocity curve of ζ TrA in a phasor diagram according to L05. $OP3$ is the expected Keplerian 3rd harmonic, while $OQ3$ is the observed 3rd harmonic with its error bars.

result gives the probability $p_2 = 0.0063$, and $p_3 = 0.47$ and it was pointed out that the Keplerian third harmonic should be undetectable with the precision of the data ($\sigma \approx 14$ $\mathrm{m\,s^{-1}}$ for one data point). Lucy instead preferred to ascribe a circular orbit to ζ TrA and all the second and higher harmonics are then attributed to proximity effects.

In a *Survey of Ca II H and K Chromospheric Emission in Southern Solar-Type Stars* (Henry *et al.* (1996)), ζ TrA is an active star from its H and K flux. The recent spectra from HERCULES (observed in 2006) show negligible chromospheric emission. However, it is possible that in 2006 ζ TrA activity was at its minimum.

Komonjinda *et al.* (2007) investigated the radial velocity perturbation on ζ TrA. The tidal distortion of the primary star, the reflection effect and the effect of starspots were included in their study. They generated models of ζ TrA from the WD03 code in order to match the observational data from Skuljan *et al.* (2004).

They found that the eccentric model of a system with tidal distortion and reflection effect shows no difference in radial velocities from the eccentric model without those proximity effects. Also, the radial velocities from the eccentric model with the proximity effects has a difference from those of the circular model by less than 1 $\mathrm{m\,s^{-1}}$. Such small perturbations would not affect the measured eccentricity, even if the true orbit is

circular. Thus it can be concluded that the proximity effects cannot cause the spurious eccentricity that was detected from the data of ζ TrA.

In that work, however, Komonjinda *et al.* (2007) found that the spotted models of a star in a circular orbit can deliver velocity perturbations as much as 140 $\mathrm{m\,s^{-1}}$ which is similar to the difference in radial velocities between the circular orbit and the observation. Moreover, the fictitious eccentricities from the spotted models are comparable with the observed value as well as the third harmonics. Hipparcos photometry shows constancy of light to 0.006 magnitude which is less than predicted from the spotted models, but more than the photometric precision, but the period analysis of these photometric data gave no detectable period near the 12.9-day orbital period.

Komonjinda *et al.* (2007) concluded that ζ TrA is a system showing a small eccentricity. However, the results from the test of L05 show that the system possibly has a small perturbation from an unknown source, which cannot be proximity effects. Spot variation can possibly be the source of the perturbation, but the photometric variation from Hipparcos data does not confirm that ζ TrA has spots.

CHAPTER 5

Orbital solutions of single-lined spectroscopic binaries

A total of twelve SB1s were observed and their spectra were analysed in this research. At least 50 spectra were obtained for each star during nearly three years of observation at MJUO. The standard reduction method was done using the HRSP package. For each star, at least one best spectrum was selected to be a template for the 1D cross-correlation of its own spectra. The list of these image numbers is shown in table 5.1. These templates were cross-correlated with standard radial-velocity stars' spectra in order to relate the measured radial velocities to a standard system (also in table 5.1). The radial velocities of these twelve systems are reported in Appendices B.1 – B.11. A successful analysis has been undertaken for the orbital solutions of these systems. The solutions for these SB1s are reported in this chapter, except for the system HD 101379 (GT Muscae), which will be reported in detail in section 7.1.

5.1 Photometric observations of binary systems

Even though they are spectroscopic binary systems that we study in this research, photometry of these systems should still be included in the analysis. It was found that some spectroscopic binary systems also have a photometric variation. This variation may due to an eclipse of the system, if it is an eclipsing binary system. Various perturbation effects which arise from the tidal interaction between the components may also cause an intrinsic variation. Such effects include photospheric activity, proximity effects, and mass transfer, etc. Pulsation may also present.

The data from the Hipparcos and TYCHO photometry are included in this investigation as well as photometric data of selected systems obtained at MJUO. The Hipparcos

Table 5.1: MJUO archived numbers of template spectra of SB1s ($\#_{\rm star}$) and the standard radial-velocity stars ($\#_{\rm standard}$) that were used for the cross-correlation method, the relative radial velocities between each SB1 and its matched standard star ($V_{\rm ref}$), and the relative radial velocities between the standard star and the blue-sky spectrum ($V_{\rm sky}$).

HD	**Spectral type**	$\#_{\rm star}$	**HD**$_{\rm Std}$	$\#_{\rm std}$	$V_{\rm sky}$ $\pm$ 0.007 km s^{-1}	$V_{\rm ref}$ km s^{-1}
352	K2III	3692014	150798	3487075	−3.163	+23.91827 ± 0.121
9053	K5Ib	3668029	150798	3487075	−3.163	+44.73884 ± 0.121
22905	G8III	3689056	20794	3301066	+87.974	−75.12328 ± 0.015
30021	G8III	3742007	11937	3608094	−6.016	+28.01975 ± 0.045
38099	K4III	3689071	150798	3487075	−3.168	+25.29155 ± 0.121
50337	G5	3741037	11937	3608094	−6.016	+21.37894 ± 0.045
77258	F8IV	3741044	114837	3405089	−63.721	+41.51093 ± 0.039
85622	G5	3741051	109379	3489063	−7.246	+10.15235 ± 0.024
124425	F6IV	3405112	114837	3405089	−63.721	+57.44433 ± 0.039
136905	K1III	3452076	71701	3304051	+21.619	+50.19470 ± 0.070
194215	K3V	3667010	150798	3487075	−3.163	+7.25364 ± 0.121

satellite was operated from November 1989 to March 1993 to make precise measurements of the positions, parallaxes and proper motions of many thousands of stars. It included a high accuracy photometric system in both Hipparcos and Tycho photometers. The main Hipparcos instrument observed in a broad-band system (≈ 500 nm) to optimize the astrometric signal. The system has a specific configuration and called H_p. This single-colour photometry cannot give much information about the physical characteristics of a star but it has a very high precision from which information on the small amplitude light variations can be obtained. It has an average of some 110 observations for each of the 118000 programme stars. The Tycho data are two-colour photometric data. These two bands are close to the Johnson B and V magnitudes and they are referred to as B_T and V_T respectively. The average number of observations from Tycho is 130. This number is larger because the Tycho mission is to map the sky.

The Hipparcos and Tycho data were obtained from the online catalogue (Perryman, & ESA, 1997) available online at the VizieR service (Ochsenbein *et al.*, 2000). Table 5.2 shows the photometric data from the Hipparcos and Tycho catalogues of the spectroscopic binary systems that are studied in this research. The column *Type* is a note from the Hipparcos catalogue on the variation of a system; C: constant, P: periodic, M: micro-variable ($< 0\overset{\mathrm{m}}{.}03$), U: unsolved variable (no category), D: duplicity-induced variability, and a blank entry signifies that the entry could not be classified either as variable or constant, as the data are not sufficient.

It is useful to transform the Hipparcos and Tycho photometric data to the standard Johnson system, which is used in ground-based photometry. The H_p, B_T, and V_T systems are all designed to link to and be normalized with the standard Johnson system. The zero points are set according to the following criteria:

$$\begin{aligned} H_p &\equiv 0 \quad \text{for} \quad V_\mathrm{J} = 0 \quad \text{and} \quad B - V = 0 \\ V_T &\equiv 0 \quad \text{for} \quad V_\mathrm{J} = 0 \quad \text{and} \quad B - V = 0 \\ B_T &\equiv 0 \quad \text{for} \quad B_\mathrm{J} = 0 \quad \text{and} \quad B - V = 0. \end{aligned}$$

It is possible to convert H_p to a standard Johnson system, as well as to convert the value of V_T and B_T. This is better done by using a transformation table available with the Hipparcos and Tycho catalogues. But there is an approximate linear transformation

Table 5.2: Photometric data of spectroscopic binary stars from the Hipparcos and TYCHO catalogues, including TYCHO $B_{\rm T}$ and $V_{\rm T}$ magnitudes, the Hipparcos magnitude $H_{\rm p}$, and its scatter, and trigonometric parallax, π. The period of variation is presented for those systems with a periodic photometric variation.

HD	$B_{\rm T}$ (mag)	$V_{\rm T}$ (mag)	$H_{\rm p}$ (mag)	$H_{\rm p,scat}$ (mag)	**P** (d)	*Type*	π (mas)
352	7.967	6.362	6.3245	0.075	48.34	P	3.25
	± 0.014	± 0.008	± 0.0130				± 0.96
3196			5.3209	0.005		D	47.51
			± 0.0007				± 1.15
3405	7.553	6.861	6.9204	0.013		M	22.79
	± 0.004	± 0.003	± 0.0011				± 0.73
9053	5.491	3.624	3.5329	0.037	97.50	P	13.94
	± 0.005	± 0.004	± 0.0041				± 0.64
10800	6.626	5.950	6.0069	0.008			36.86
	± 0.004	± 0.003	± 0.0008				± 0.52
22905	7.452	6.437	6.5037	0.008		C	5.06
	± 0.009	± 0.006	± 0.0007				± 0.84
30021	6.748	6.048	6.1193	0.018		U	8.04
	± 0.006	± 0.006	± 0.0020				± 1.39
38099	8.234	6.483	6.4428	0.012		U	4.80
	± 0.012	± 0.005	± 0.0021				± 0.95
50337	5.564	4.513	4.5681	0.004		C	5.9
	± 0.003	± 0.002	± 0.0006				± 0.51
77137	7.748	6.966	7.0155	0.028		P	17.91
	± 0.008	± 0.005	± 0.0019				± 0.74
77258	5.245	4.532	4.5767	0.006		C	16.91
	± 0.003	± 0.002	± 0.0005				± 0.53
85622	6.112	4.713	4.7497	0.007		M	3.10
	± 0.003	± 0.002	± 0.0007				± 0.56
101379	6.043	5.174	5.1796	0.033		U	5.81
	± 0.004	± 0.004	± 0.0029				± 0.64
124424	6.457	5.948	5.9996	0.006			17.94
	± 0.004	± 0.004	± 0.0006				± 0.81
136905	8.690	7.474	7.4899	0.061	11.12	P	10.51
	± 0.018	± 0.012	± 0.0069				± 1
155555	7.877	6.960	7.0114	0.037		U	31.83
	± 0.008	± 0.005	± 0.0036				± 0.74
194215	7.266	5.975	6.0227	0.006		C	6.03
	± 0.005	± 0.003	± 0.0007				± 0.86
197649	6.981	6.537	6.5843	0.007			14.42
	± 0.003	± 0.003	± 0.0007				± 0.84

between ($V_{\rm J}$, $(B-V)_{\rm J}$), and (V_T, B_T) for the range $-0.2 < (B-V)_T < 1.8$, namely

$$V_{\rm J} = V_T - 0.090(B-V)_T$$

and

$$(B-V)_{\rm J} = 0.850(B-V)_T.$$

These equations cannot be applied to M-type stars.

Selected variable stars were observed photometrically at MJUO. These included the eclipsing binary systems (HD 50337 and HD 77137), ellipsoidal variables (HD 352 and HD 136905), RS CVn-type stars[1] (HD 38099, HD 155555, and also HD 77137 and HD 136905) and an active-chromosphere quadruple system (HD 101379/80). The observations were conducted under the MJUO service photometry program using the f/16 0.6-m Optical Craftsmen telescope during the same period as the spectroscopic observations. An exception was for HD 101379, as this system has had continuous photometric observations from MJUO since the 1980s. The instrument used was a single-channel photoelectric photometer with EMI 9202B photomultiplier tube and with $UBV(RI)_{\rm C}$ filters. The time series of this absolute photometry, as well as the Hipparcos data, will be shown later when the systems are discussed in this chapter (for SB1s) or the next chapter (for SB2s).

Radial velocity curves of single-lined spectroscopic binaries

A radial velocity curve of each of the eleven single-lined spectroscopic binaries that are reported in this chapter is shown when the system is discussed. Each plot contains relative radial velocities from HERCULES observations. These radial velocities were measured as relative radial velocities with a selected binary star spectrum. The radial velocity curves were calculated from the orbital solutions with no fixed orbital period, and the residuals in the second panel are also from that solution. An orbital phase is calculated from the period of that solution. The time of periastron passage, $T = T_0 + \omega/2\pi$ was used to define the zero phase. The absolute systemic radial velocity, γ

[1] An RS CVn system is one type of *chromospherically active binaries* (CABs). They are detached binary systems with late-type companions. At least one component is very active and its photosphere is covered by spots. They are in rapid axial rotation and have deep convective envelopes. The system emits UV, soft x-ray and radio waves.

is calculated from the correction of $\gamma_{\rm rad}$ using the relative radial velocity between the binary star template and the standard radial-velocity spectrum.

5.2 HD 352

HD 352 (5 Ceti, AP Piscium, HR 14; $00^{\rm h}08^{\rm m}12^{\rm s}, -02°26'52''$) is an SB1 with a light variation like an EB-type eclipsing binary. This system was studied by Eaton & Barden (1986). They proposed that the system consists of an evolved K giant and an F-type star. The spectrum of this system is dominated by its K giant primary which nearly fills its Roche lobe and almost transfers its matter to its companion. The ultraviolet observation of this system showed that the hot secondary is immersed in the relatively dense lower atmosphere of the K giant (Eaton and Barden, 1988).

Hipparcos photometry presents a 48.34-day period variation of this system. This variation is from the fact that the primary star is an ellipsoidal variable. This period is about a half of the rotational period of the primary star. Figure 5.1(a) is a light curve of this system in the $H_{\rm p}$ magnitude with orbital phases calculated from the S_{B^9} orbital period. The photometric observation from MJUO, figure 5.1(b), also shows a similar periodic variation. The parallax from Hipparcos is 3.25 ± 0.96 milliarcsec. This implies that the distance to this system is about 310 ± 90 pc.

Radial velocity orbit

The radial velocity of this system was first found to be variable by Adams (1914). Christie (1933) investigated the orbit of this system from 36 spectra obtained from Mt Wilson Observatory. In that analysis, the orbital solution was computed from 12 grouped radial velocities at every 0.1 phase. This solution had an rms scatter of 1.33 $\mathrm{km\,s^{-1}}$. The solution has been recalculated in this research from all the reported data and it was found that the rms is 600 $\mathrm{m\,s^{-1}}$.

More radial velocities were observed at the Fick Observatory during 1977-1982. These radial velocities and an orbital solution were published by Beavers and Salzer (1985). This is the orbit that is in the S_{B^9} catalogue. Their solution was compared with the recalculated solution and with those from Christie (1933), and is shown in table 5.3.

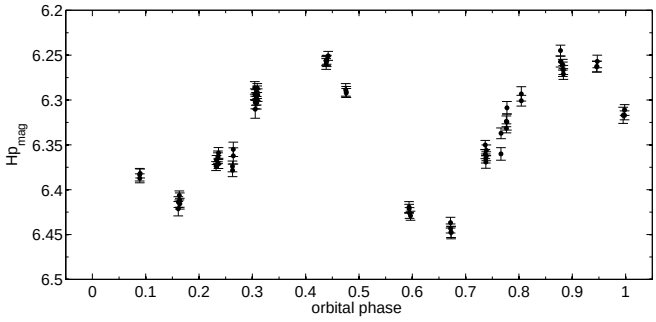

(a)

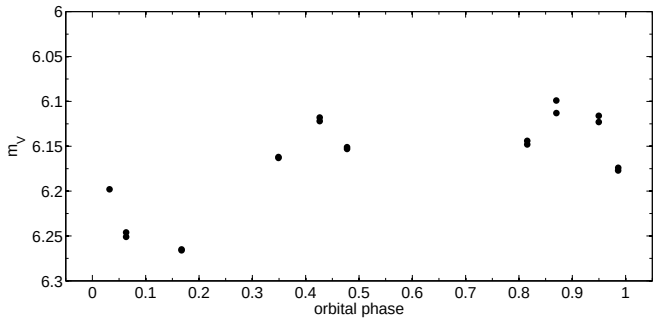

(b)

Figure 5.1: $H_{\rm p}$ and m_V light curves of HD 352 from Hipparcos and MJUO photometry. The orbital phases are calculated from an S_{B^9} catalogue orbital period, $P = 96.439$ days.

The HERCULES spectrograph was used to observe the spectra of HD 352 using a resolving power of 42 000. In total, 67 spectra were obtained. The radial velocities measured from these spectra were fitted and their orbital solution is shown in table 5.4. A correction for the measured radial velocities was calculated from the relative radial velocity between the star template and a standard star. The absolute systemic radial velocity of this system is -0.529 ± 0.156 km s^{-1}.

Figure 5.2(a) is a plot of HD 352 radial velocities measured from HERCULES spectra versus orbital phase. This orbital phase is calculated from $P = 96.414$ days and phase zero is defined by the time of periastron passage $T = T_0 + \omega/2\pi =$ JD 245 3726.2 $\pm$ 1.2. The radial velocities are plotted versus Julian date in figure 5.2(b). The residuals of the fit are plotted in the lower panels of both figures.

When combining the HERCULES data set and those of Christie (1933) and Beavers and Salzer (1985), the times of zero mean longitude, T_0, are used. The time intervals

Table 5.3: The archived orbital solutions of SB1 HD 352 (K2III) from the literature and from the recalculations.

Parameter	**Christie (1933)**		**Beavers and Salzer (1985)**	
	published	recalculated	published	recalculated
K ($\mathrm{km\,s^{-1}}$)	23.88 ± 0.90	23.08 ± 0.72	24.29 ± 0.40	24.24 ± 0.34
e	0.124 ± 0.034	0.099 ± 0.040	0.037 ± 0.016	0.037 ± 0.016
ω ($^\circ$)	222.1 ± 9.2	211 ± 25	152 ± 25	165.32 ± 31
T_0 (HJD)	242 0006.84	242 0929.68	244 4288.7	244 4344.44
		$\pm$ 0.51	$\pm$ 6.7	$\pm$ 0.27
P (days)	96.14	96.393 ± 0.026	96.439 ± 0.003	96.413 ± 0.035
γ ($\mathrm{km\,s^{-1}}$)	1.11	1.25 ± 0.56	-0.43 ± 0.27	-0.41 ± 0.27
$\#_{obs}$	12	40	35	35
$\#_{rej}$	0	6	0	0
σ ($\mathrm{km\,s^{-1}}$)	1.33	0.600	1.46	0.631

were calculated between the HERCULES $T_{0,new} = 245\,3602.117 \pm 0.039$ and the recalculated value of Christie (1933) $T_{0,C} = 242\,0929.68 \pm 0.51$ and the recalculated value of Beavers and Salzer (1985) $T_{0,BS} = 244\,4344.44 \pm 0.27$. These give $N_{c,C} \approx 339$ and $N_{c,BS} \approx 96$ when $P \approx 96.4$ d. The orbital period obtained from these combined data is 96.3910 ± 0.0016 days. Even the period is ten times more precise than the solution from HERCULES radial velocities only, but the final HERCULES solution, as shown in table 5.4, has no significant change.

It should be note here that the large rms ($\approx 245\ \mathrm{m\,s^{-1}}$) in the HERCULES solution is possible from the fact that this system is an ellipsoidal variable. More investigation on the perturbation of this effect is needed before the final eccentric solution is accepted. The discussion on this will be in section 8.2.

5.3 HD 9053

The third magnitude star HD 9053 (γ Phoenicis, HR 429; $01^{\mathrm{h}}28^{\mathrm{m}}22^{\mathrm{s}}$, $-43^\circ19'06''$) was first reported as a binary star by H. K. Palmer in 1905 (Wright, 1905). This star was

Table 5.4: The orbital parameters of SB1 HD 352 (K2III) from the HERCULES radial velocities.

Parameter	**New value from this analysis**	
	with all free parameters	with fixed period
K ($\mathrm{km\,s^{-1}}$)	24.070 ± 0.054	24.088 ± 0.061
e	0.0296 ± 0.0020	0.0300 ± 0.0020
ω ($^\circ$)	103.3 ± 4.5	106.2 ± 5.1
T_0 (HJD)	$245\,3602.117 \pm 0.039$	$245\,3602.154 \pm 0.033$
P (days)	96.414 ± 0.017	96.3910 (fixed)
γ_{rel} ($\mathrm{km\,s^{-1}}$)	-21.248 ± 0.035	-21.227 ± 0.033
γ ($\mathrm{km\,s^{-1}}$)	-0.53 ± 0.16	-0.51 ± 0.15
$\#_{obs}$	68	68
$\#_{rej}$	1	1
σ ($\mathrm{km\,s^{-1}}$)	0.244	0.245

first classified as K5M by Pickering (1897). Landi Dessy and Keenan (1966) classified the system as K5+ IIb-IIIa from their spectrograms. Later, the spectral type of this system was classified as M0- IIIa from the Revised MK system program at the Perkins Observatory (Keenan 1983). The Hipparcos input catalogue refers to Landi Dessy and Keenan (1966) for the spectral type of this system.

In the catalogue of astrometric orbits of S_{B^9} stars by Jancart *et al.* (2005), they concluded that HD 9053 has a circular orbit with an astrometric period of 193.8 days. The inclination of the orbital plane was reported as 46°.30.

The Hipparcos and Tycho observations show that this system has a variation in its brightness with a period of 97.50 days, as shown in figure 5.3. This variation is about a half of the orbital period. It is not possible for a system to have an eclipse at a low inclination. As this system is an X-ray source (Reimers *et al.* 1996), the periodic variation in its brightness could be the result of starspots. The possibility is that there are two groups of spots on the surface of the primary component of HD 9053. These two groups are on a different side of the stellar surface and make double spot waves which results in the observed variation in the system's brightness. The scatter in photometric

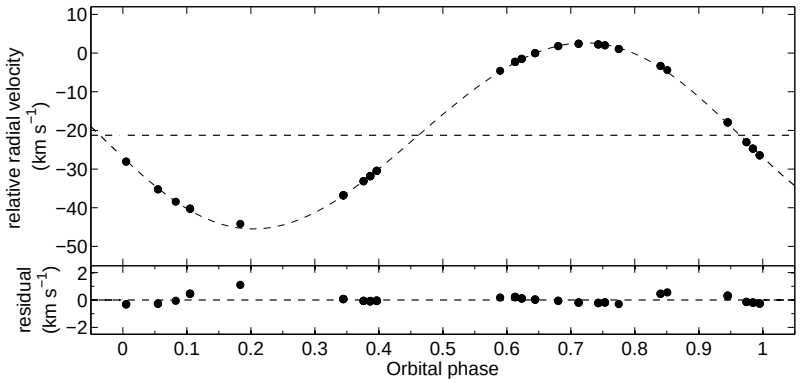

(a) Phase plot of HD 352 radial velocities.

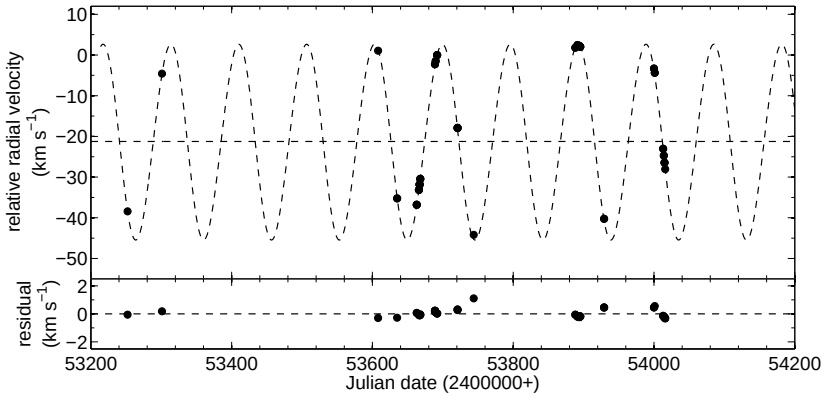

(b) Measured radial velocities of HD 352 versus Julian date.

Figure 5.2: Sixty-eight radial-velocity observations of HD 352 (K2III) measured from HERCULES spectra. This solution has $e = 0.0296 \pm 0.0020$ and $P = 96.414 \pm 0.017$ with an rms scatter of the fit of 244 m s^{-1}.

magnitude is in agreement with the typical amplitude of a spot wave. It is also possible that this system is an ellipsoidal variable.

The parallax of this star from the Hipparcos catalogue is 13.94 ± 0.64 mas, indicating that the distance to this system is about 70 ± 3 pc.

Radial velocity orbit

The radial velocity of HD 9053 was first measured by Palmer from the D. O. Mills Expedition at Lick Observatory. His five measured radial velocities were reported by Wright

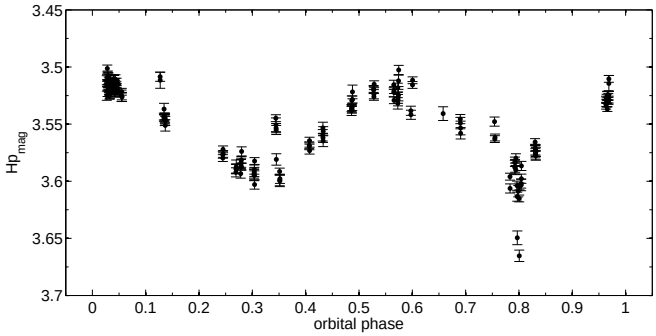

Figure 5.3: Phase plot of the Hipparcos magnitude of HD 9053. The period of variation is half of the orbital period. In this figure, phase is calculated from the orbital period, $P = 194.056$ days.

(1905). Wilson and Huffer(1918) analysed the orbit of HD 9053 from 31 spectrograms observed from 1903 to 1917, including those that were reported by Wright (1905). His orbital solution had a slightly non-circular orbit ($e = 0.005$). This solution was re-analysed and fixed to a circular orbit by Luyten (1936). The S_{B^9} catalogue reported Luyten's solution, which is shown in table 5.5. The radial velocities of HD 9053 were observed in a few other programs, i.e. Lunt (1919) and Buscombe and Kennedy (1968).

During this research, the HERCULES spectrograph was used to observe HD 9053, using a resolving power of 70 000. One hundred and twenty-six spectra were obtained. The radial velocities measured from the cross-correlation method and the orbital solution calculated from this set of radial velocities are shown in table 5.6 with their residuals plotted in figure 5.4. The plot of HD 9053 radial velocities measured from HERCULES spectra versus orbital phase is shown in figure 5.4(a) and versus Julian date is shown in figure 5.4(b). The curves in both fits are calculated from the orbital solution with all free parameters. The rms scatter of this fit is 159 $\mathrm{m\,s^{-1}}$ and the residual of this fit is shown in the lower panel of both figures. The orbital phase is calculated with a definition of zero phase at $T = \mathrm{JD}\,245\,3541.2 \pm 2.3$.

In table 5.6 is also shown an orbital solution when the orbital period is fixed. This period is calculated from $T_{0,hist} = \mathrm{JD}\,241\,7800.311 \pm 0.030$ from table 5.5 and $T_{0,new} = \mathrm{JD}\,245\,3477.021 \pm 0.069$ in table 5.6. These give $N_c \approx 184$ and $\bar{P} = 193.89516 \pm 0.00041$ days. Even though the period is at a very high precision (nearly a hundred

Table 5.5: The orbital parameters of SB1 HD 9053 (K5II) analysed from the data of Luyten (1936). The first column is the solution reported in that paper and also in the S_{B^9} catalogue. The recalculated solution is in the second column.

Parameter	**Luyten (1936)**	
	published	recalculated
K ($\mathrm{km\,s^{-1}}$)	16.0 ± 0.28	15.779 ± 0.010 $\mathrm{km\,s^{-1}}$
e	0	0.0048 ± 0.00067
ω (°)	-	$249.^{\circ}0 \pm 8.^{\circ}8$
T_0 (HJD)	241 9544.92 ± 0.05	241 7800.311 ± 0.030
P (days)	193.79 d	193.7891 ± 0.0022
γ ($\mathrm{km\,s^{-1}}$)	26 ± 0.20	25.6118 ± 0.0071
$\#_{obs}$	31	31
$\#_{rej}$	0	1
σ ($\mathrm{km\,s^{-1}}$)	1.00	0.040

times better), the orbital solution is not improved.

It is clearly seen that the period has changed from 193.7891 ± 0.0022 d from the literature's data to 194.056 ± 0.037 d from HERCULES data. The other remarkable point is the rms scatter of HERCULES fit with this period is large (159 $\mathrm{m\,s^{-1}}$) compared with those of the literature (40 $\mathrm{m\,s^{-1}}$). It is possible to be explained from the fact that the primary component of HD 9053 is a magnetically active star. The number of spots can affect the symmetry of stellar absorption lines, which can cause errors in the observed radial velocities. It is possible that, during this research, HD 9053 was more active than in the past.

5.4 HD 22905

HD 22905 (HR 1120; $03^{\mathrm{h}}40^{\mathrm{m}}11^{\mathrm{s}}$, $-15^{\circ}13'35''$) is a binary system consisting of a late G giant and an undetectable component. The spectral type of this system listed in the *Bright Star Catalogue* is G5 with an apparent magnitude of 6.33 and a colour index

Table 5.6: The orbital solutions of SB1 HD 9053 (K5II) analysed from HERCULES observations.

Parameter	**New value from this analysis**	
	with all free parameters	with fixed period
K ($\mathrm{km\,s^{-1}}$)	16.220 ± 0.037	16.911 ± 0.038
e	0.0228 ± 0.0013	0.0211 ± 0.0013
ω (°)	119.0 ± 4.4	114.9 ± 5.2
T_0 (HJD)	245 3477.021 ± 0.069	245 3477.270 ± 0.043
P (days)	194.056 ± 0.037	193.89516 (fixed)
γ_{rel} ($\mathrm{km\,s^{-1}}$)	−15.830 ± 0.022	−15.808 ± 0.022
γ ($\mathrm{km\,s^{-1}}$)	25.609 ± 0.143	25.587 ± 0.143
$\#_{obs}$	126	126
$\#_{rej}$	0	0
σ ($\mathrm{km\,s^{-1}}$)	0.159	0.172

$(B-V) = 0\overset{\mathrm{m}}{.}88$. The spectral type of this system as presented in Salzer and Beavers (1985) from their discussion with Houk, N. in 1984 is G8III and they called this a composite spectrum, because of the strength of the Hβ line being higher than normal. Salzer and Beavers (1985) indicated that there was no evidence of the secondary from their radial-velocity measurements. They suggested that the secondary is hotter than the primary star from the evidence in the system's strong Balmer lines. The fact that they could not find other evidence of the secondary in the radial-velocity measurements or in the observed spectrogram suggested that the secondary is not a giant. They concluded that this system consists of a G8III star and an early F dwarf. Recent speckle observations done by Sowell *et al.* (2001) showed that no light was detected from the secondary star.

Photometric observations from the Hipparcos and Tycho satellite indicated that this system has no variation in its brightness. Salzer and Beavers (1985) estimated the distance to HD 22905 from its spectral type as about 150 pc. The parallax of this star from the Hipparcos catalogue is 5.06 ±0.84 mas, indicating that the distance to this system is about 198 ± 33 pc.

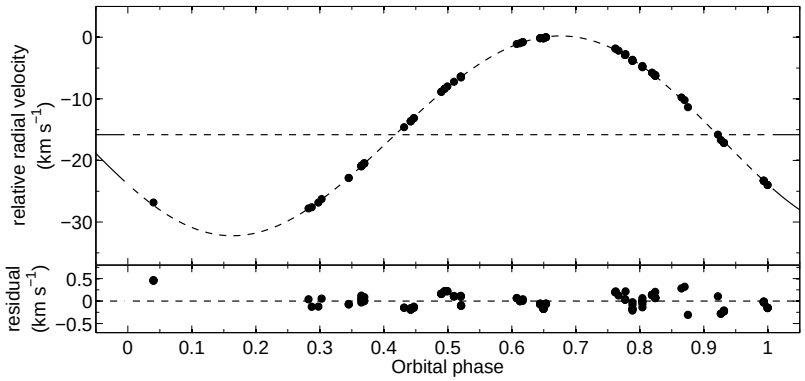

(a) Phase plot of HD 9053 radial velocities.

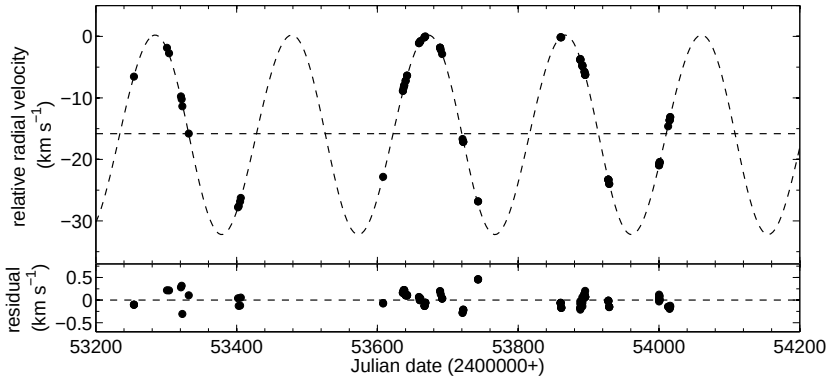

(b) Measured radial velocities of HD 9053 versus Julian date.

Figure 5.4: Radial velocities of HD 9053 measured from HERCULES spectra. The plotted curves are calculated from the orbital solution with all free parameters. The lower panels of both figures are the residuals from this fit.

Radial velocity orbit

The radial velocity orbit of HD 22905 that is reported in the S_{B^9} catalogue is that which was reported by Salzer & Beavers (1985). They were the first to report the variation in velocity of this system. They derived the orbit of this system from 25 spectroscopic observations obtained from the Fick Observatory spectrometer during October 1978 to January 1984. They adopted a circular orbit since their derived eccentricity was 0.01 ± 0.02. The rms error of their solution is 1.7 km s^{-1} and the published orbital solution is shown in table 5.7.

Table 5.7: The orbital parameters of SB1 HD 22905 (G8/K0III) reported in S_{B^9} catalogue.

Parameter	Salzer & Beavers (1985)	
	published	recalculated
K ($\mathrm{km\,s^{-1}}$)	26.02 ± 0.52	25.69 ± 0.46
e	0	0.012 ± 0.017
ω ($^\circ$)	-	140 ± 64
T_0 (HJD)	$244\,4990.37 \pm 0.26$	$244\,4990.49 \pm 0.27$
P (days)	91.629 ± 0.039	91.648 ± 0.044
γ ($\mathrm{km\,s^{-1}}$)	-9.10 ± 0.35	-8.72 ± 0.36
$\#_{obs}$	25	25
$\#_{rej}$	0	0
σ ($\mathrm{km\,s^{-1}}$)	1.7	1.6

A result from the recalculating of these historical data shows a large uncertainty in the eccentricity, $e = 0.012 \pm 0.017$. This possibly confirmed the decision to adopt the circular orbit of HD 22905 from these data.

Sixty-seven spectra were archived from the HERCULES spectrograph using a resolving power of 41 000. A standard fitting method were applied to these radial velocities with all free parameters, including e, as shown in table 5.8. The eccentric orbital solution has an indeterminate eccentricity, $e = 0.0011 \pm 0.0011$ with an rms scatter of 72 $\mathrm{m\,s^{-1}}$. This eccentricity was then fixed to zero and a circular orbit was adopted. This circular orbit solution has an rms scatter of 46 $\mathrm{m\,s^{-1}}$. The measured radial velocities were plotted in figure 5.5 with a radial velocity curve of a circular orbit and the residuals from fitting a circular orbit. The zero phase is defined by the time $T = \mathrm{JD}\,245\,3605.5125 \pm 0.0043$.

Combining the historical data and the HERCULES data, the period of $\bar{P} = 91.6492 \pm 0.0029$ days was obtained. The recalculation of the circular orbit with this new fixed period is shown in table 5.9.

HD 22905 is a star in a group of young disk stars as described by Eggen (1994). This indicated that the system HD 22905 has an age $\approx 1 - 2 \times 10^9$ years. The cutoff period

Table 5.8: The orbital solution of SB1 HD 22905 (G8/K0III) from HERCULES radial velocities.

Parameter	**New value from this analysis**	
	with all free parameters	adopted circular orbit
K ($\mathrm{km\,s^{-1}}$)	24.779 ± 0.018	24.7973 ± 0.0097
e	0.0011 ± 0.0011	0 (adopted)
ω ($^\circ$)	92 ± 78	-
T_0 HJD	$245\,3605.5265 \pm 0.0078$	$245\,3605.5125 \pm 0.0043$
P (days)	91.6534 ± 0.0045	91.6456 ± 0.0025
$\gamma_{\rm rel}$ ($\mathrm{km\,s^{-1}}$)	-21.1156 ± 0.0098	-21.0965 ± 0.0063
γ ($\mathrm{km\,s^{-1}}$)	-9.539 ± 0.025	-9.520 ± 0.021
$\#_{obs}$	67	67
$\#_{rej}$	1	4
σ ($\mathrm{km\,s^{-1}}$)	0.072	0.046

Table 5.9: The orbital parameters of SB1 HD 22905 when fixing $e = 0$, and $P = 91.6492$ days.

Parameter	adopted circular orbit with fixed P
K ($\mathrm{km\,s^{-1}}$)	24.7984 ± 0.0097
e	0 (adopted)
ω ($^\circ$)	-
T_0 HJD	$245\,3605.5127 \pm 0.0043$
P (days)	91.6492 (fixed)
$\gamma_{\rm rel}$ ($\mathrm{km\,s^{-1}}$)	-21.0994 ± 0.0065
γ ($\mathrm{km\,s^{-1}}$)	-9.523 ± 0.022
$\#_{obs}$	67
$\#_{rej}$	4
σ ($\mathrm{km\,s^{-1}}$)	0.046

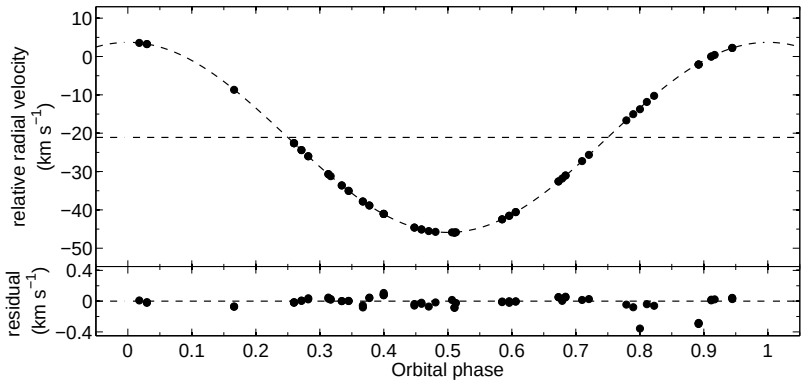

(a) Phase plot of HD 22905 radial velocities.

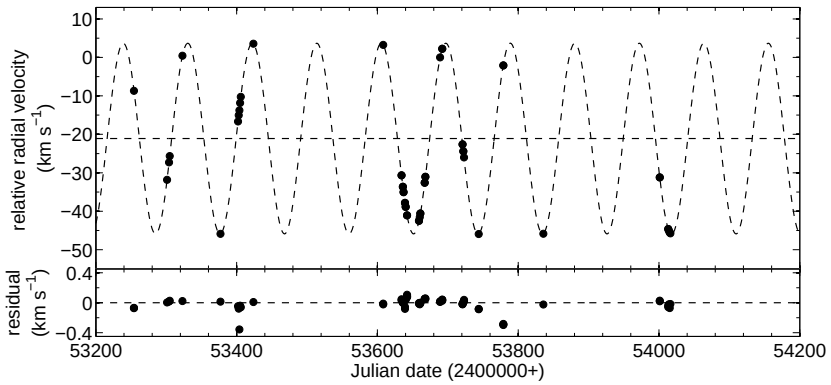

(b) Measured radial velocities of HD 22905 versus Julian date.

Figure 5.5: Radial velocities of HD 22905 measured from the HERCULES spectra. The plotted curves are calculated from the circular orbital solution. The lower panels shown the residuals from this fit.

for a G-star system with this age is around 16 days (Meibom and Mathieu, 2005). This star is not expected to have an exactly circular orbit.

5.5 HD 30021

55 Eri (HIP 21986; $04^{\rm h}43^{\rm m}35^{\rm s}$, $-08°47'40''$) is a visual binary system. It consists of two stars HD 30020 and HD 30021. The combined standard Johnson V magnitude as reported in the Hipparcos input catalogue is $5^{\rm m}.98$ with a colour index $(B-V) = 0^{\rm m}.645$. The Hipparcos catalogue reported the separation between this optical pair as 9.287 ±

0.003 arcsec. It measured a combined Hipparcos magnitude $6^{\mathrm{m}}.1193 \pm 0^{\mathrm{m}}.0020$ with an intrinsic variability of $0^{\mathrm{m}}.018$. In the *Multiple star catalogue* (MSC) by Tokovinin (1997), it was reported that the system 55 Eri consists of four stars, but no orbital solution was reported. The star HD 30020 (55 Eri B, DW Eri, HR 1505) is an F4IIp(Sr) ACVO[2] variable. This star has a mean V magnitude of $6^{\mathrm{m}}.820$, with a $0^{\mathrm{m}}.09$ variation (Adelman *et al.*, 2000).

In this research, we are interested just in the HD 30021 (55 Eri A, HR 1506) system. This system is an SB1 with a G8III primary star. There is no report of the variation of its brightness. The parallax of this system from the Hipparcos catalogue is 8.04 ± 1.39 mas, indicating that the distance to this system is about 124 ± 22 pc.

Radial velocity orbit

Lucke and Mayor (1982) reported 26 radial velocities of HD 30021 from the photoelectric measurements they made with the CORAVEL radial velocity scanner at the Observatoire de Haute Provence (CORAVEL-OHP) in 1977-1980. They combined their data with three measurements from Mount Wilson Observatory in 1927-1928 (Abt 1970) to find the orbital period of the system. In their solution, which used only CORAVEL-OHP data, the derived eccentricity was not significant and was fixed to zero. Their orbital solution is shown in table 5.10. This circular solution has an rms scatter of 0.53 $\mathrm{km\,s^{-1}}$.

The recalculation of their radial velocities also shows a non-significant eccentricity, $e = 0.0079 \pm 0.0086$.

Radial velocities of HD 30021 were measured from 48 HERCULES spectra. These spectra were archived using a resolving power of 41 000. The orbital solutions are reported in table 5.11. Even though the solution from the literature shows that the orbit should be adopted as a circle, the result from HERCULES data shows that a small eccentricity is detected with an eccentricity $e = 0.001\,73 \pm 0.000\,34$. Also, the eccentric orbit has a higher precision than the circular orbit, $\sigma_e = 45.91$ $\mathrm{m\,s^{-1}}$ and $\sigma_c = 59.92$ $\mathrm{m\,s^{-1}}$. Figure 5.6 is a plot of the radial velocities versus (a) orbital phase and (b) Julian

[2]Rapidly oscillating α^2 CVn variables. These are nonradially pulsating, rotating magnetic variables of Ap spectral type (DO Eri). Pulsation periods are in the range 0.004-0.01 days. The amplitudes of light variation caused by the pulsation are about $0^{\mathrm{m}}.01$ in V. The pulsational variations are superposed on those caused by rotation. (Combined General Catalogue of Variable Stars, Samus *et al.* (2004))

Table 5.10: Orbital solutions of HD 30021 from the data obtained from Lucke and Mayor (1982). The first column is the data from the literature and reported in the S_{B^9} catalogue. The data was recalculated and reported in the second column.

Parameter	**Lucke and Mayor (1982)**		
	published	recalculated	recalculated with $e = 0$
K ($\mathrm{km\,s^{-1}}$)	27.5 ± 0.33	27.43 ± 0.26	27.49 ± 0.17
e	0 (fixed)	0.0079 ± 0.0086	0 (fixed)
ω (°)	-	68 ± 53	-
T_0 (HJD)	244 3778.178	244 3778.206	244 3778.206
	± 0.063	± 0.036	± 0.038
P (days)	42.3279 ± 0.0073	42.3377 ± 0.0059	42.3354 ± 0.0061
γ ($\mathrm{km\,s^{-1}}$)	39.8 ± 0.21	39.82 ± 0.12	39.77 ± 0.11
$\#_{obs}$	26	26	26
$\#_{rej}$	0	0	0
σ ($\mathrm{km\,s^{-1}}$)	0.53	0.512	0.507

date. The zero phase is defined by the time T = JD 245 3308.6 ± 1.2. The curves are calculated from an eccentric solution and the residuals are also from an eccentric solution. The rms scatter of this eccentric fit is 46 $\mathrm{m\,s^{-1}}$.

5.6 HD 38099

HD 38099 (V1197 Orionis, HR 1970; $05^{\mathrm{h}}43^{\mathrm{m}}09^{\mathrm{s}}$, $-01°36'48''$) is an active chromosphere single-lined binary. This system is also known as an ellipsoidal variable from its light curve (Hall *et al.*, 1986 and Strassmeier *et al.*, 1989) with a photometric period of 70.09 ± 0.81 days. The Hipparcos magnitude of this system is $6\overset{\mathrm{m}}{.}4428 \pm 0\overset{\mathrm{m}}{.}0021$ with a $0\overset{\mathrm{m}}{.}012$ intrinsic variability of unclassified type. It can be seen from the plot between H_p magnitudes and orbital phase in figure 5.7 that this system has a periodic variation in brightness which is consistent with the characteristic of an ellipsoidal variable. The scatter in the light curve possibly comes from the activity of the primary component.

Table 5.11: The orbital parameters of SB1 HD 30021 (G8III) calculated from HERCULES observations.

Parameter	**New value from this analysis**	
	with all free parameters	with $e = 0$
K ($\mathrm{km\,s^{-1}}$)	27.2938 ± 0.0079	27.284 ± 0.010
e	0.001 73 ± 0.000 34	0 (fixed)
ω (°)	45 ± 10	-
T_0 (HJD)	245 3303.2937 ± 0.0045	245 3303.2834 ± 0.0057
P (days)	42.334 03 ± 0.000 45 d	42.335 07 ± 0.000 57
γ_{rel} ($\mathrm{km\,s^{-1}}$)	17.7222 ± 0.0066	17.7256 ± 0.0082
γ ($\mathrm{km\,s^{-1}}$)	39.442 ± 0.052	39.445 ± 0.053
$\#_{obs}$	56	56
$\#_{rej}$	1	0
σ ($\mathrm{km\,s^{-1}}$)	0.046	0.060

This system's primary component is a K4III giant. Hall (1990) suggested that the primary component has a mass $0.90M_{\odot}$ and a radius $51.3R_{\odot}$ while the secondary has a mass $1.14M_{\odot}$. The Hipparcos trigonometric parallax of this system is 4.80 ± 0.95 mas, which implies that the distance is approximately 208 ± 41 pc.

Radial velocity orbit

Griffin reported the variation in the radial velocity of this system in 1972. The first radial velocity analysis of this system by Radford and Griffin (1975) showed that the system has a circular orbit with $\sigma = 0.75$ $\mathrm{km\,s^{-1}}$. Bassett (1978) reanalysed the same 35 radial velocities and tested the orbital solution with the maximum likelihood method to show that the system has a slightly non-circular orbit with $e = 0.06 \pm 0.02$. The recalculated solution from these data also give the same eccentricity, as seen in table 5.12.

Fifty-five spectra of HD 38099 were archived using the HERCULES spectrograph. The orbital solution of this system was calculated. It is found that the solution with an

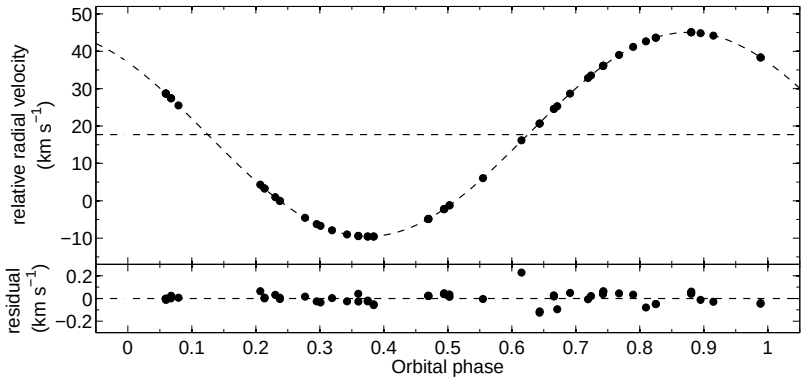

(a) Phase plot of HD 30021 radial velocities.

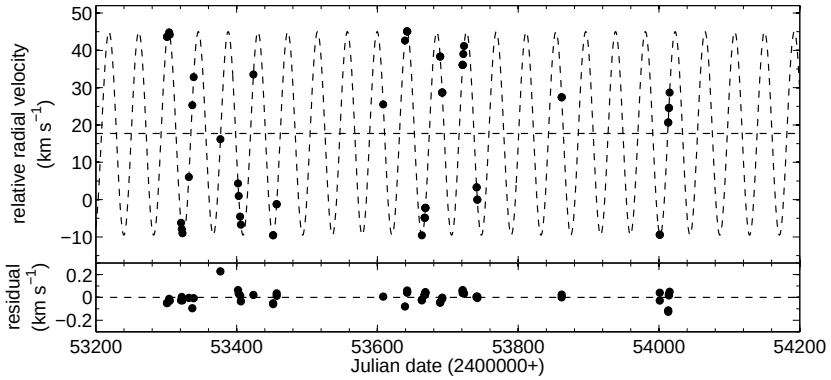

(b) Measured radial velocities of HD 30021 versus Julian date.

Figure 5.6: Radial velocities of HD 30021 measured from the HERCULES spectra. The plotted curves are calculated from the orbital solution calculated from these radial velocities. The second panel shows the residuals from this fit.

eccentric orbit should be rejected because of its large error in the calculated eccentricity $e = 0.0067 \pm 0.0060$. The circular orbit is therefore adopted. The eccentric orbit and circular orbit solutions are shown in table 5.13. The radial velocities measured for HD 38099 are plotted in figure 5.8 with (a) orbital phase and (b) Julian date. The orbital phase is calculated with a reference time for the zero phase as $T = \mathrm{JD}\,245\,3481.04 \pm 0.19$. The radial velocity curves in figure 5.8 are calculated from a circular orbital solution. The residual from this fit is shown in the lower panel of the same figure. Its rms scatter is 248 $\mathrm{m\,s^{-1}}$.

It should be noted here that the orbital solutions of this system has a large error

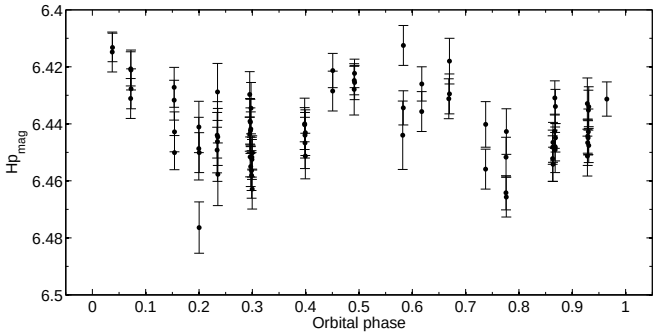

(a)

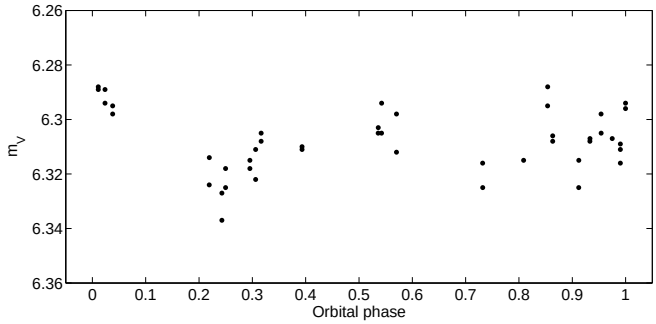

(b)

Figure 5.7: The light curves of the ellipsoidal variable HD 38099 from the Hipparcos satellite and from MJUO. The orbital phase was calculated from the HERCULES solution (table 5.13). The photometric variation of this system is due to the ellipsoidal effect from the primary component. The activity of the primary component causes an additional scatter in its light curve.

bar ($\approx 250\ \mathrm{m\,s^{-1}}$). This should be a result from the variation of lines from the star's chromospheric activities and the distortion of the primary component.

The orbital period was calculated from the combined data set of Radford and Griffin (1975) and HERCULES data with the decision that the system has a circular orbit. The period $\bar{P} = 143.2955 \pm 0.0072$ days was obtained. This value has ten times higher precision than the period from HERCULES data only. The orbital solution of a circular orbit with fixed period has no significant change from the previous solution, as shown in table 5.14.

Table 5.12: The orbital parameters of SB1 HD 38099 (K4III) analysed from the data of Radford and Griffin (1975). The first column is the solution analysed by Bassett (1978) and also reported in the S_{B^9} catalogue. The recalculated solution is in the second column.

Parameter	**Radford and Griffin (1975)**		
	Bassett (1978)	recalculated	recalculated $e = 0$
K ($\mathrm{km\,s^{-1}}$)	9.03 ± 0.18	9.05 ± 0.21	9.09 ± 0.23
e	0.06 ± 0.02	0.06 ± 0.021	0 (fixed)
ω ($^\circ$)	290 ± 17	293 ± 19	-
T_0 (HJD)	$244\,2016 \pm 7$	$244\,204361 \pm 0.49$	$244\,2043.28 \pm 0.54$
P (days)	143.03 ± 0.13	143.05 ± 0.14	143.06 ± 0.14
γ ($\mathrm{km\,s^{-1}}$)	32.10 ± 0.12	32.06 ± 0.14	32.03 ± 0.16
$\#_{obs}$	35	35	35
$\#_{rej}$	0	0	0
σ ($\mathrm{km\,s^{-1}}$)	14.94*	0.764	0.853

*reported as a weighted sum of squares

5.7 HD 50337

The spectroscopic binary star HD 50337 (A Carinae, V415 Carinae, HR 2554; $06^{\mathrm{h}}49^{\mathrm{m}}51^{\mathrm{s}}$, $-53^\circ 37' 21''$) is an eclipsing binary of the Algol type. Hagen and Stencel (1985) reported CaII H and K lines emission from the spectrum of this system. Ake and Parsons (1987) analysed data of this system from IUE[3] observations. From the G6II spectral type of the primary star reported in the 1975 *Michigan southern all-sky survey* by Houk and Cowley (1975), they found that the secondary is an A0V star about three V magnitudes fainter than the primary star. They also found that the spectrum of the secondary star was overlaid by many sharp, low-level FeII absorption components from the outer atmosphere of the primary star. They classified this binary system as a ζ Aur-type[4] of binary star. This was later confirmed from an IUE observation during the system's eclipse in

[3] *International Ultraviolet Explorer*

[4] This is an interacting binary system with a G-M giant primary and a A-B dwarf secondary, in which the hot component is eclipsed by the extended atmosphere of the cool component.

Table 5.13: The orbital parameters of SB1 HD 38099 (K4III) derived from HERCULES spectra.

Parameter	**New value from this analysis**	
	with all free parameters	with $e = 0$
K ($\mathrm{km\,s^{-1}}$)	9.147 ± 0.056	9.160 ± 0.051
e	0.0067 ± 0.0060	0 (adopted)
ω ($^\circ$)	166 ± 49	-
T_0 (HJD)	$245\,3481.00 \pm 0.18$	$245\,3481.04 \pm 0.19$
P (days)	143.29 ± 0.11	143.248 ± 0.098
γ_{rel}	9.063 ± 0.036	9.060 ± 0.037
γ ($\mathrm{km\,s^{-1}}$)	31.05 ± 0.16	31.05 ± 0.16
$\#_{obs}$	55	55
$\#_{rej}$	0	0
σ ($\mathrm{km\,s^{-1}}$)	0.251	0.248

Table 5.14: The orbital parameters of SB1 HD 38099 when fixing $e = 0$, and $P = 143.2955$ days.

Parameter	adopted circular orbit with fixed P
K ($\mathrm{km\,s^{-1}}$)	9.154 ± 0.048
e	0 (adopted)
ω ($^\circ$)	-
T_0 HJD	$245\,3480.97 \pm 0.11$
P (days)	143.2955 (fixed)
γ_{rel} ($\mathrm{km\,s^{-1}}$)	9.062 ± 0.037
γ ($\mathrm{km\,s^{-1}}$)	31.05 ± 0.16
$\#_{obs}$	55
$\#_{rej}$	0
σ ($\mathrm{km\,s^{-1}}$)	0.247

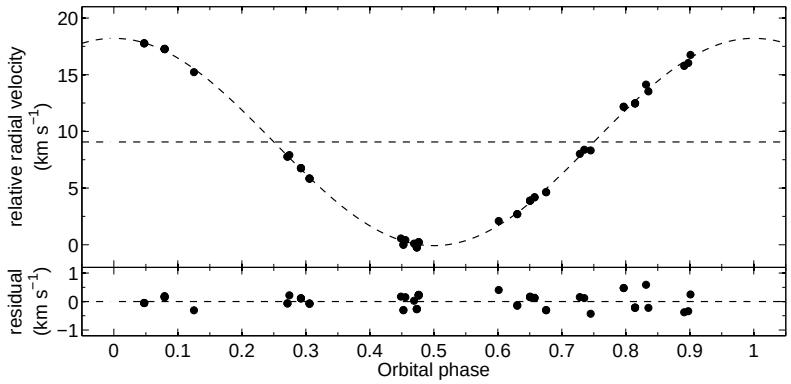

(a) Phase plot of HD 38099 radial velocities.

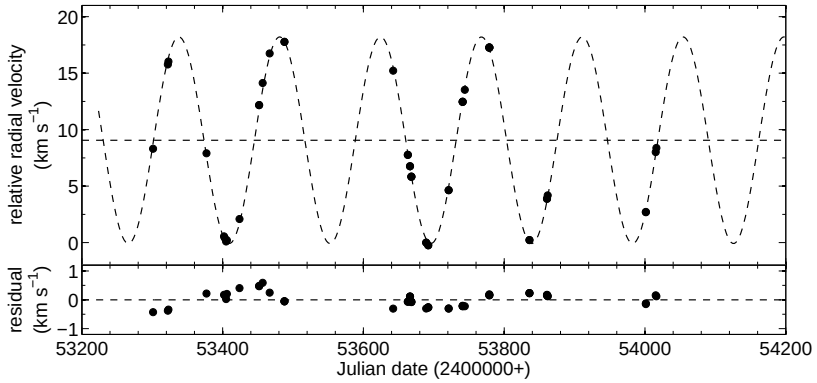

(b) Measured radial velocities of HD 38099 versus Julian date.

Figure 5.8: Radial velocities of HD 38099 measured from HERCULES spectra. The plotted curves are calculated from the circular orbital solution calculated from these radial velocities. The second panel shows the residuals from this fit.

November 1987 (Ake and Parsons, 1988). The following researches by Schröder (1990) and Schröder and Hünsch (1992) indicated that the primary component has a depleted chromosphere. They analysed the C IV and Si IV absorption lines and determined that the extended hot plasma from the primary star has a temperature around 8×10^4 K.

The Hipparcos catalogue indicated that this system has a constant brightness. However, the phase plot of Hipparcos photometry should demonstrate the periodic variation as the system is an eclipsing binary. This may be because the variation is small compared to the error bars. Photometric data of MJUO also shows the same periodic variation. These photometric data are plotted in figure 5.9. The system has a deeper eclipse in V

magnitude ($\approx 0^{\rm m}.05$) than in the H_p magnitude ($\approx 0^{\rm m}.01$), as expected from a ζ Aur-type system.

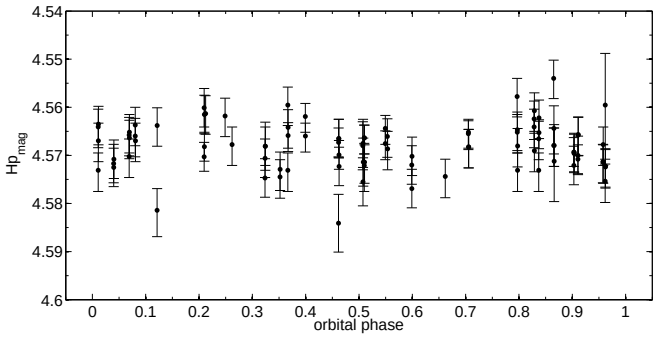

(a)

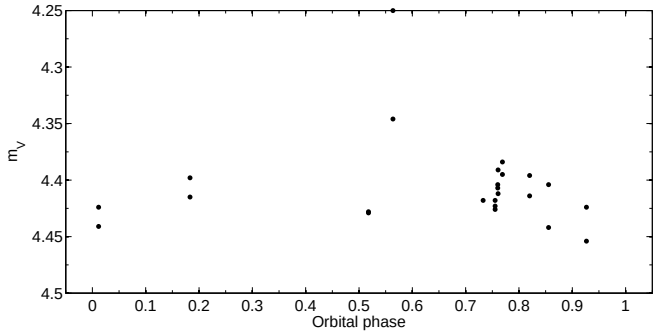

(b)

Figure 5.9: The light curves of the ellipsoidal variable HD 50337 from the Hipparcos satellite and from MJUO. The orbital phase is calculated from the HERCULES solution (table 5.16). The H_p photometry shows a periodic variation as of an EA-type binary.

The trignometric parallax of this system from the Hipparcos catalogue is 5.9 ± 0.51, which is implied to a distance 169 ± 14 pc.

Radial velocity orbit

The radial velocity of HD 50337 was first measured by Palmer in 1904–1905 (Wright 1905). Wilson and Huffer (1918) were the first who analysed the radial velocities of this system from observations in 1904-1918. They derived an orbital solution by the graphical method and adopted a circular orbit with a probable error of 0.87 $\mathrm{km\,s^{-1}}$. LS71 used

their statistical test to confirm that a circular orbit should be adopted for this system. A recent orbit of HD 50337 was analysed by Brown *et al.* (2001) from a combination of the earlier data and spectra obtained from the ESO 1.4-m coudé auxiliary telescope (ESO CAT). They applied the test of LS71 to these data and a circular orbit was adopted with an rms scatter for the ESO CAT radial velocity of 63 $\mathrm{m\,s^{-1}}$. They were able to measure the radial velocity of the secondary star from their HST/GHRS[5] observations in the ultraviolet region. They found that the secondary star is an A1V star with a stellar mass ratio of 1.59 ± 0.05. The U and B photometry of this eclipsing system was analysed and gave an inclination $i = 82\overset{\circ}{.}7 \pm 0\overset{\circ}{.}2$, $a = 244 \pm 4\ R_\odot$, $R_1 = 31.3 \pm 0.9\ R_\odot$ and $R_2 = 1.9 \pm 0.1\ R_\odot$ which gives $M_1 = 3.14 \pm 0.17\ M_\odot$ and $M_2 = 1.98 \pm 0.11\ M_\odot$. These orbital solutions from the radial velocities in the literature are shown in table 5.15.

Table 5.15: Orbital solutions of HD 50337 from the work by Wilson and Huffer (1918) and Brown *et al.* (2001). In both papers, circular orbits were adopted following the test of LS71.

Parameter	**Wilson & Huffer (1918)**	**Brown *et al.* (2001)**
K_1 ($\mathrm{km\,s^{-1}}$)	24.8	24.29 ± 0.03
K_2 ($\mathrm{km\,s^{-1}}$)	-	38.6 ± 1.1
e	0	0
ω (°)	-	-
T_0 (HJD)	242 1344	245 1022.68 ± 0.05
P (days)	195.32	195.258 ± 0.003
γ ($\mathrm{km\,s^{-1}}$)	25.4	25.4 ± 0.3
$\#_{obs}$	23	-
$\#_{rej}$	0	-
σ ($\mathrm{km\,s^{-1}}$)	0.87	0.063

In this research we obtained a hundred spectra of HD 50337 from HERCULES. Radial velocities were measured from the cross-correlation of these spectra with a template. The orbital solution of this system was calculated without a constraint on a circular orbit. This gives a solution with an eccentricity 0.00436 ± 0.00051 and an rms of 84 m $\mathrm{s^{-1}}$.

[5]The Hubble Space Telescope's Goddard High Resolution Spectrograph.

Other orbital parameters are shown in table 5.16 as well as the solution for a circular orbit. The radial velocities from the HERCULES spectra are plotted in figure 5.10 against (a) orbital phase and (b) Julian date. The time of periastron passage for the eccentric orbit is $T = \mathrm{JD}245\,3656.9 \pm 3.5$. This time is used for the definition of the zero phase.

Table 5.16: The orbital solutions of SB1 HD 50337 analysed from HERCULES data.

Parameter	HERCULES orbital solutions		
	eccentric solution	with $e = 0$	with $P = \bar{P}$
K_1 ($\mathrm{km\,s^{-1}}$)	24.323 ± 0.013	24.341 ± 0.017	24.322 ± 0.012
e	0.004 36 ± 0.000 51	0	0.004 67 ± 0.000 48
ω (°)	86.6 ± 6.5	-	81.4 ± 5.7
T_0 (HJD)	245 3609.878 ± 0.018	245 3609.850 ± 0.023	245 3609.911 ± 0.014
P (days)	195.295 ± 0.019	195.298 ± 0.026	195.2581 (fixed)
γ_{rel} ($\mathrm{km\,s^{-1}}$)	11.2912 ± 0.0094	11.286 ± 0.013	11.2861 ± 0.0089
γ ($\mathrm{km\,s^{-1}}$)	26.370 ± 0.054	26.365 ± 0.058	26.365 ± 0.054
$\#_{obs}$	100	100	100
$\#_{rej}$	0	0	1
σ ($\mathrm{km\,s^{-1}}$)	0.084	0.111	0.079

In order to improve the precision in the orbital period, the difference between T_0 of Brown *et al.* (2001) and T_0 of the HERCULES circular solution was calculated and also the $\bar{P}$. It was found that the $\bar{P}$ is 195.2581 ± 0.0042 days which is close to the value of Brown *et al.* (2001). This period was then fixed to the recalculation of the orbit from the HERCULES data. This orbital solution has a slightly better precision with an rms of the scatter of 79 $\mathrm{m\,s^{-1}}$, as shown in table 5.16, but one data point was rejected.

5.8 HD 77258

The bright star HD 77258 (w Velorum, HR 3591; $09^{\mathrm{h}}00^{\mathrm{m}}05^{\mathrm{s}}$, $-41°15'13''$) was first observed to have a variation in radial velocity by H. K. Palmer, as reported in the Lick Observatory Bulletin in 1904 (Wright 1904).

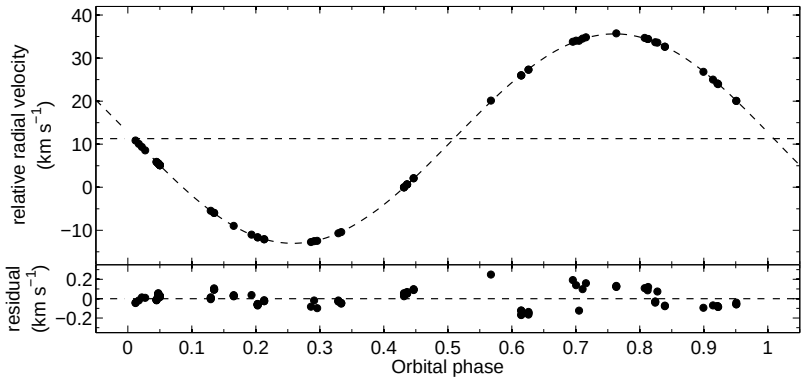

(a) Phase plot of HD 50337 radial velocities.

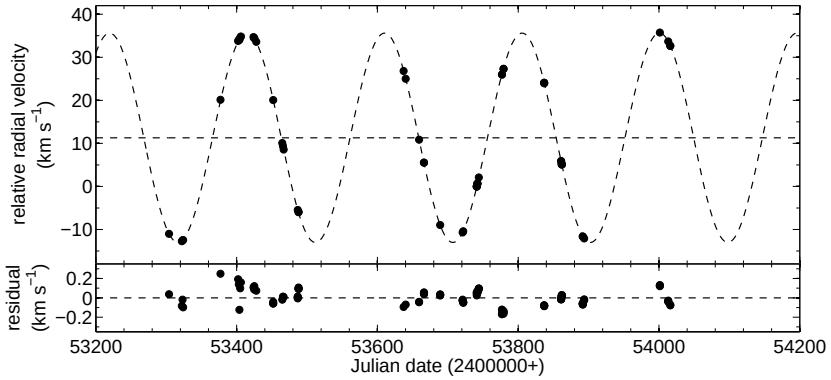

(b) Measured radial velocities of HD 50337 versus Julian date.

Figure 5.10: Radial velocities of HD 50337 measured from the HERCULES spectra. The plotted curves are calculated from the eccentric solution with the residuals from this fit in the second panel.

The spectral type of this star system was classified as F8IV by de Vaucouleurs (1957). Malaroda (1973) made a note on the hydrogen lines that correspond to an F5 spectral type, the metallic lines to F8, the K line to F0, and a very strong G band that matches to F8. Heck and Mersch (1980) predicted that this star has a spectral type of G1 from the photometric data. Davidson *et al.* (1987) classified this star in a group of stars with a blended or composite spectrum and it has a spectral type G8-K1III+A. This is the spectral type used in the fifth revised edition of the Bright Star Catalogue (Hoffleit *et al.* 1991). The SIMBAD database classifies this star as K0III+, while the Hipparcos and Tycho catalogue classifies it as an Fp star.

The Hipparcos type of photometric variation of this system is constant. The parallax of this system in the Hipparcos main catalogue is 16.19 ± 0.53 mas, which implies a distance of 61.8 ± 2.0 pc.

In the *Catalogue of Stellar Diameters* (CADARS) (Pasinetti-Fracassini *et al.* 2001), an apparent stellar diameter of the primary component of HD 77258 of $\phi = 1.2$ mas was reported. The absolute radius of the primary component was hence determined as $R = 5.3R_{\odot}$. This was calculated using the relation between the surface brightness and colour, with a spectral type F8II, as introduced by Wesselink (1969).

Radial velocity orbit

Wright found the variation in radial velocity of HD 77258 from three spectra observed by the D. O. Mills expedition in 1904 (Wright, 1904). Lunt (1919) observed five spectra of this star at the Cape during 1914-1916. He showed that the star has a range in radial velocity of 34.2 $\mathrm{km\,s^{-1}}$. During February and May 1921, 38 spectra of this star were observed and the radial velocities were measured as reported by Lunt (1924). He also derived the orbital solution of this star as shown in table 5.17. This solution has an error of 1.23 $\mathrm{km\,s^{-1}}$.

HD 77258 was observed using the HERCULES spectrograph with the resolving power of 70 000. The radial velocities were measured from 91 spectra. The orbital solution was analysed and it has an rms scatter of the fit of 19 $\mathrm{m\,s^{-1}}$, which is the lowest scatter in radial velocities of this research. The orbital parameters of the fit are presented in table 5.18. Figure 5.11 is a plot of these radial velocities as a function of (a) orbital phase and (b) Julian Date. The orbital phase is calculated from the period of 74.13715 days and the zero phase is defined by $T = \mathrm{JD}\,245\,3647.4 \pm 2.7$. The radial velocity curves of the eccentric orbital solution are also plotted in that figure with the corresponding residuals.

The period calculated from the T_0 of Lunt (1924) data and of HERCULES data is $\bar{P} = 74.1368 \pm 0.0023$ days. This period has a lower precision than the period that was calculated from HERCULES data alone, and the orbital solution that was calculated with this fixed period have no significant change from the previous solution.

Table 5.17: The orbital parameters of SB1 HD 77258 (F8IV) from the data published by Lunt (1924).

Parameter	**Lunt (1924)**	
	published	recalculated
K (km s^{-1})	17.8	17.61 ± 0.43
e	0.05	0.054 ± 0.023
ω (°)	90	102 ± 28
T_0 (HJD)	242 2709.904	242 2710.46 ± 0.97
P (days)	74.1469	74.091 ± 0.040
γ (km s^{-1})	−7.4	−7.44 ± 0.35
$\#_{obs}$	38	38
$\#_{rej}$	0	0
σ (km s^{-1})	1.23	1.9

Table 5.18: The orbital parameters of SB1 HD 77258 (F8IV) as obtained from HERCULES data.

Parameter	**HERCULES orbital solutions**	
	no fixed parameter	when $P = \bar{P}$
K (km s^{-1})	19.6744 ± 0.0041	19.6747 ± 0.0039
e	0.000 85 ± 0.000 19	0.000 87 ± 0.000 19
ω (°)	106 ± 13	106 ± 12
T_0 (HJD)	245 3625.5112± 0.0017	245 3625.5113 ± 0.0017
P (days)	74.137 15 ± 0.000 73	74.1368 (fixed)
$\gamma_{\rm rel}$ (km s^{-1})	18.2758 ± 0.0027	18.2757 ± 0.0027
γ (km s^{-1})	−5.0133 ± 0.042	−5.0134 ± 0.042
$\#_{obs}$	91	91
$\#_{rej}$	0	0
σ (km s^{-1})	0.019	0.019

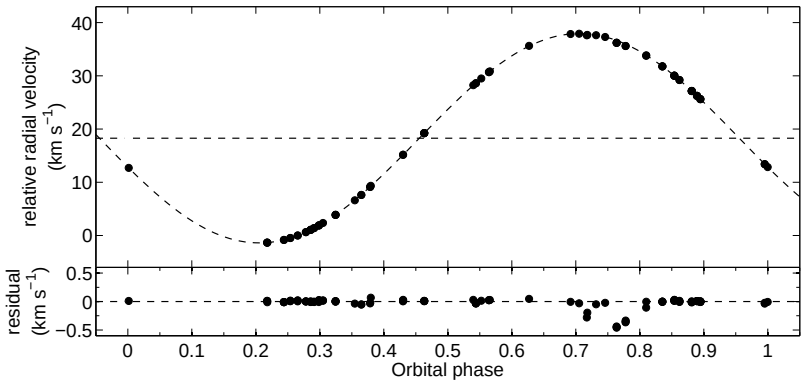

(a) Phase plot of HD 77258 radial velocities.

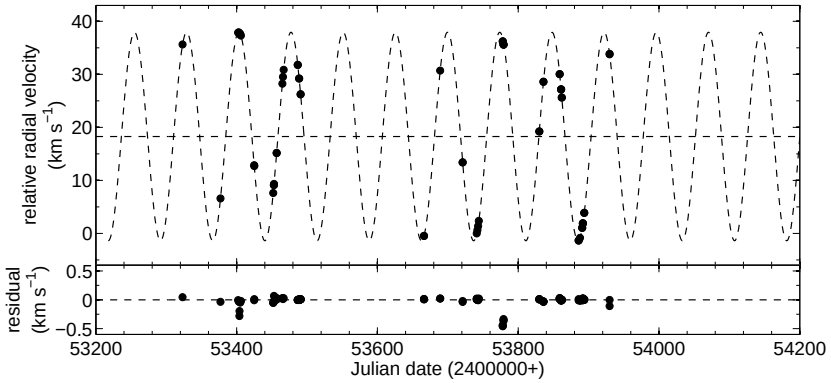

(b) Measured radial velocities of HD 77258 versus Julian date.

Figure 5.11: Radial velocities of HD 77258 measured from the HERCULES spectra. The plotted curves are calculated from the orbital solution calculated from these radial velocitieswith all free parameters. The second panel shows the residuals from the fit.

5.9 HD 85622

HD 85622 (m Velorum, HR 3912; $09^{\rm h}51^{\rm m}40^{\rm s}$, $-46°32'51''$) is a system with a supergiant primary star. It was first found to have variable radial velocity in 1905 during the D. O. Mills Expedition (Wright, 1907). It was classified as a supergiant star of a spectral type G5Ib by MacConnell & Bidelman (1976). The rotational velocity, $v \sin i$ of the supergiant component was measured by de Medeiros *et al.* (2002) as 19.3 ± 1.0 km s^{-1}.

Platais *et al.* (1998) surveyed the proper motion and space velocity from the Hipparcos data to find a possible star cluster. They found that HD 85622 is a member

of an association amongst 12 other stars, around HD 91590. They studied the colour-magnitude diagram of this association and matched it with an isochrone of an age of 100 Myr.

The Hipparcos and Tycho photometry indicated that this system has a micro-variability in its brightness with $0^{\rm m}.007$ scatter in $H_p = 4^{\rm m}.749 \pm 0^{\rm m}.0007$ and $0^{\rm m}.023$ scatter in $V_T = 4^{\rm m}.713 \pm 0^{\rm m}.002$.

Radial velocity orbit

Luyten (1936) collected 56 radial velocity observations of HD 85622 from the papers by Lunt (1919) and Jones (1928).He adopted a circular orbit for this system with an rms of 1.4 km s^{-1} (table 5.19). The orbital solution was recalculated from these data, including five radial velocities measured by Wright (1907).

Table 5.19: The orbital parameters of SB1 HD 85622 from the data collected by Luyten (1936).

Parameter	**Luyten (1936)**		**Luyten (1936) & Wright (1907)**	
	published	recalculated	recalculated	with $e = 0$
K (km s^{-1})	14.1	14.36 ± 0.32	14.25 ± 0.26	14.20 ± 0.23
e	0	0.044 ± 0.027	0.033 ± 0.023	0 (fixed)
ω (°)	-	16 ± 35	12 ± 44	-
T_0 (HJD)	242 3596.5	242 3595.2 ± 2.3	242 3596.2 ± 2.5	242 3598.2 ± 1.3
P (days)	329.3	328.65 ± 0.43	329.10 ± 0.16	329.12 ± 0.16
γ (km s^{-1})	11	10.55 ± 0.38	10.77 ± 0.37	11.09 ± 0.23
$\#_{obs}$	56	56	61	61
$\#_{rej}$	0	0	0	0
σ (km s^{-1})	1.4	1.4	1.3	1.3

Seventy-nine radial velocities were measured from the HERCULES spectra obtained with the resolving power 70 000. It is found that the calculated eccentricity has a large error bar, $e = 0.0026 \pm 0.0016$. A circular orbit should be adopted from these data with a precision of 61 m s^{-1}. These two solutions can be compared in table 5.20. The radial

velocities of this system and the residuals of this solution are plotted versus orbital phase in figure 5.12(a) and versus Julian date in figure 5.12(b). The zero phase is at the time $T = T_0 = \mathrm{JD}\,245\,3860.281 \pm 0.074$.

Table 5.20: The orbital parameters of SB1 HD 85622 analysed from HERCULES data.

Parameter	**New value from this analysis**	
	eccentric orbit	circular orbit
K ($\mathrm{km\,s^{-1}}$)	13.028 ± 0.013	13.021 ± 0.012
e	0.0026 ± 0.0016	0 (adopted)
ω ($^\circ$)	188 ± 46	-
T_0 (HJD)	$245\,3860.261 \pm 0.078$	$245\,3860.281 \pm 0.074$
P (days)	329.126 ± 0.093	329.266 ± 0.085
γ_{rel} ($\mathrm{km\,s^{-1}}$)	-11.516 ± 0.013	-11.531 ± 0.010
γ ($\mathrm{km\,s^{-1}}$)	11.510 ± 0.037	11.495 ± 0.034
$\#_{obs}$	86	86
$\#_{rej}$	7	7
σ ($\mathrm{km\,s^{-1}}$)	0.060	0.061

To improve the measurement in the orbital period, the number of epochs between the circular orbit T_0 in the last column of table 5.19 and table 5.20 was calculated. This gives the passed number of orbital cycles, $N_c = 92$, and the calculated $\bar{P}$ is 328.935 ± 0.014 days. It should be noted here that this $\bar{P}$ has a higher precision than P in table 5.20 (approximately 6 times better) but the solution for the other orbital elements with $\bar{P}$ is not improved.

5.10 HD 124425

The solar neighbourhood star HD 124425 (HR 5317; $14^{\mathrm{h}}13^{\mathrm{m}}40^{\mathrm{s}}$, $-00^\circ50'43''$) is a short period spectroscopic binary system ($P \approx 2.69$ days). It was found to have a variation in its radial velocity by Brayton in early 1920 (Duncan, 1921). Kondo and McCluskey (1969) investigated the spectrum of this system and found that the metallic elements are overabundant. This star was classified as a metallic-line star by Conti (1970). The

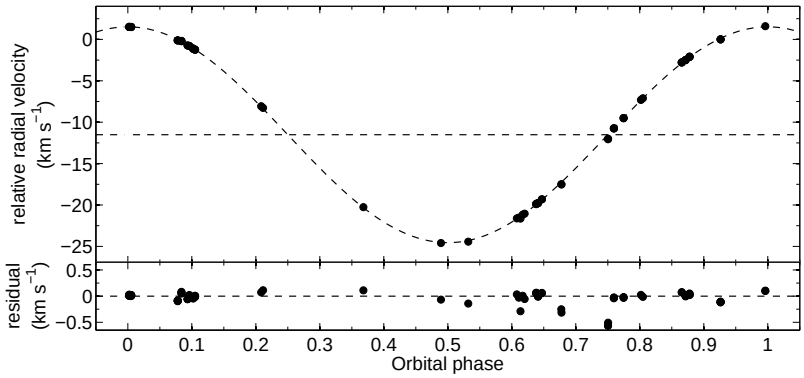

(a) Phase plot of HD 85622 radial velocities.

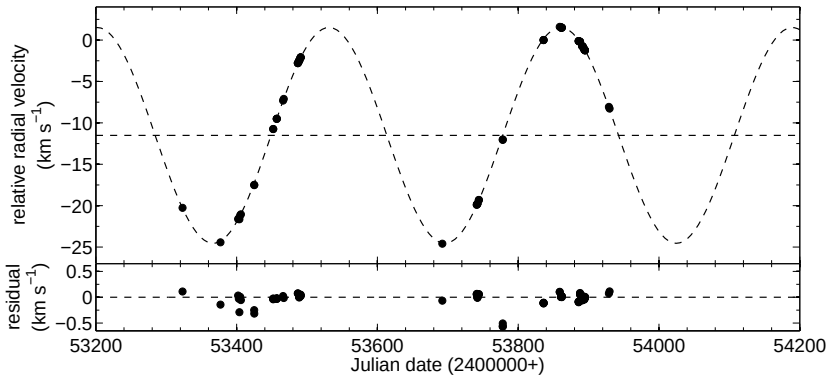

(b) Measured radial velocities of HD 85622 versus Julian date.

Figure 5.12: Radial velocities of HD 85622 measured from the HERCULES spectra. The plotted curves are calculated from the circular orbital solution. The second panel shown the residuals from this fit.

revised spectral type by Barry (1970) is F7Vw where w indicates weak lines in the spectrum.

The *Geneva-Copenhagen Survey of the Solar neighbourhood* (Nordström *et al.* 2004) reported that this system is at a distance of 56 pc with a parallax 17.9 ± 0.8 mas. Its absolute V magnitude is $2^{\mathrm{m}}.17$. The age of this system is 1.6-1.9 Gyr. The primary star has a mass of $1.60 M_{\odot}$ with a metallicity [Fe/H] $= -0.16$ and the temperature is $\log T_{\mathrm{e}} = 3.802$ K. Masana *et al.* (2006) analysed V and 2-MASS[6] IR photometric data of this system and fitting this data with the synthetic photometry computed from Kurucz

[6]The Two Micron All Sky Survey

Table 5.21: The orbital parameters of SB1 HD 85622 when fixing $e = 0$, and $P = 328.935$ days.

Parameter	adopted circular orbit with fixed P
K ($\mathrm{km\,s^{-1}}$)	13.031 ± 0.014
e	0 (fixed)
ω ($^\circ$)	-
T_0 HJD	$245\,3860.091 \pm 0.054$
P (days)	328.935 (fixed)
$\gamma_{\rm rel}$ ($\mathrm{km\,s^{-1}}$)	-11.518 ± 0.010
γ ($\mathrm{km\,s^{-1}}$)	11.508 ± 0.047
$\#_{obs}$	86
$\#_{rej}$	6
σ ($\mathrm{km\,s^{-1}}$)	0.070

atmosphere model. They obtained a result that the primary star has a temperature 6435 ± 58 K, its angular semi-diameter is 0.224 ± 0.003 mas, and its radius is $2.681 \pm 0.126 R_\odot$.

The Hipparcos satellite photometry measured a $5\overset{\mathrm{m}}{.}9996 \pm 0\overset{\mathrm{m}}{.}006$ for this system and indicated that no variability was detected. The V magnitude from the TYCHO satellite is $5\overset{\mathrm{m}}{.}948 \pm 0\overset{\mathrm{m}}{.}004$.

Radial velocity orbit

Duncan (1921) reported that HD 124425 has a variation in its radial velocity from radial velocities measured by Brayton from observations at Mt Wilson observatory in 1920. He analysed those radial velocities with his later observations in 1921 and adopted a circular orbit for this system with a 2.6960-day period. The probable error of a single observation is $3.18\ \mathrm{km\,s^{-1}}$. This orbital solution is shown in table 5.22. When these data were reanalysed, it is found that for an eccentric orbit e is 0.042 ± 0.046. Therefore, e was fixed to zero for the reanalysed solution in table 5.22.

This system was later observed by Mayor and Mazeh (1987) with the CORAVEL

radial velocity scanner at Haute-Provence Observatory between 1980 and 1982. They analysed 16 radial velocities with an assumed circular orbit and a fixed orbital period. The scatter of their radial velocities is 1.4 $\mathrm{km\,s^{-1}}$. The recomputed orbital solution from these data indicated that e should be fixed to zero, because of the large error bar in an eccentric solution, $e = 0.013 \pm 0.018$. The orbital solution of Mayor and Mazeh (1987) and the recalculated solution are shown in table 5.22.

Table 5.22: The orbital parameters of SB1 HD 124425 (F6IV) taken from the literature and the recalculated solutions from those data.

Parameter	**Duncan (1921)**		**Mayor and Mazeh (1987)**	
	published	recalculated	published	recalculated
K ($\mathrm{km\,s^{-1}}$)	24.34 ± 1.08	24.0 ± 1.3	26.0 ± 0.4	25.95 ± 0.45
e	0	0	0	0
ω	-	-	-	-
T_0 (HJD)	242 2744.103 ± 0.023	242 2744.100 ± 0.028	244 4600.744 ± 0.009	244 4600.777 ±0.011
P (days)	2.6960	2.696 54 ± 0.000 58	2.697 023 ± 0.000 004	2.697 018 ± 0.000 087
γ ($\mathrm{km\,s^{-1}}$)	17.6 ± 0.85	17.6 ± 1.1	18.1 ± 0.3	18.10 ± 0.41
$\#_{obs}$	20	20	16	16
$\#_{rej}$	0	0	0	0
σ ($\mathrm{km\,s^{-1}}$)	0.159	0.145	-	0.152

In this research, 64 spectra of HD 124425 were obtained using HERCULES with the resolving power 70 000. Radial velocities were measured from these spectra from a cross-correlation function with a template spectrum. Table 5.23 is the orbital solution analysed from these velocities. These radial velocities are plotted versus orbital phase in figure 5.13(a) and versus Julian Date in figure 5.13(b). The time of periastron passage, $T = \mathrm{JD}\,245\,3802.51 \pm 0.14$. The lower panels of these are residual plots from the fit of these radial velocities. The rms of this fit is 121 $\mathrm{m\,s^{-1}}$.

In order to get a higher precision for the orbital period, the number of orbital cycles was calculated from the difference in T_0 of the recalculated solution of Duncan (1921)

Table 5.23: The new orbital parameters of SB1 HD 124425 (F6IV) analysed from HERCULES spectra.

Parameter	**New value from this analysis**	
	with all free parameters	with fixed P
K ($\mathrm{km\,s^{-1}}$)	26.094 ± 0.023	26.107 ± 0.023
e	0.002 60 ± 0.000 99	0.0027 ± 0.000 94
ω (°)	294 ± 26	306 ± 21
T_0 (HJD)	245 3800.308 08	245 3800.307 52
	± 0.000 47	± 0.000 40
P (days)	2.697 0329	2.697 0220 (fixed)
	± 0.000 0050	
γ_{rel} ($\mathrm{km\,s^{-1}}$)	26.040 ± 0.015	26.035 ± 0.016
γ ($\mathrm{km\,s^{-1}}$)	18.684 ± 0.054	18.679 ± 0.055
$\#_{obs}$	64	64
$\#_{rej}$	1	1
σ ($\mathrm{km\,s^{-1}}$)	0.121	0.126

and the HERCULES solution. This gave $\bar{P} = 2.697\,0220 \pm 0.000\,0024$ or a precision of 0.2 second. This is half of the error in the orbital period of Mayor and Mazeh (1987), which they calculated using the same method. The orbital solution was recalculated with this fixed $\bar{P}$ and is shown in table 5.23.

5.11 HD 136905

The binary star HD 136905 (GX Librae; $15^{\mathrm{h}}23^{\mathrm{m}}26^{\mathrm{s}}$, $-06°36'36''$) is an ellipsoidal variable with an active K giant. This star was first reported as a star with H and K emission in a paper by Bidelman and MacConnell (1973). They classified this star as a K1III + F system with an uncertain emission. Burke *et al.* (1982) concluded from their spectroscopic and UBV photometric observations that this system is an RS CVn-type binary of a spectral type K0III-IV and with a moderate emission at H and K.

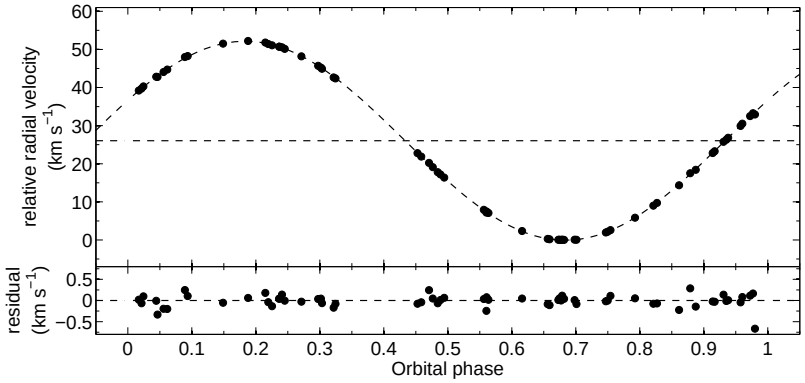

(a) Phase plot of HD 124425 radial velocities.

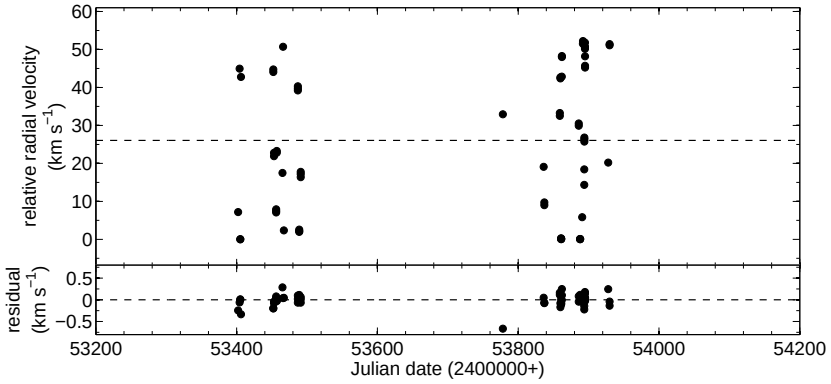

(b) Measured radial velocities of HD 124425 versus Julian date.

Figure 5.13: Radial velocities of HD 124425 measured from HERCULES spectra. The second panels show the residuals from the fit with all free parameters as in table 5.23.

A study by Fekel *et al.* (1985) reported that this system has moderate strength Ca II H and K and ultraviolet emission features and has a strong Hα absorption. They assumed that the primary star has a K1III spectral type with a mass of 1.2-1.8 $M_{\odot}$ and there is no evidence of any eclipses. They suggested that the secondary star is a G or K dwarf and that the inclination of this system is 58° ± 17°. They also suggested that the primary star has a minimum radius of 7.0 ± 0.4 $R_{\odot}$ and indicated that this system is an ellipsoidal variable. They pointed out that the light curve of HD 136905 has a variation in the amplitude and suggested that this could be the result of spot activity of this system.

Kaye *et al.* (1995) studied starspots on K giants in ellipsoidal RS CVn-type binaries.

They found a variability characteristic of starspots in HD 136905. As this system is an active binary star, it is interesting to study its emission in many wavelength regions. Busso *et al.* (1990) collected and analysed the near-IR data of this system to study its IR emission. They found no IR excess from HD 136905, from which can be concluded that there is no circumstellar shell around the primary star. Emission fluxes of this system, as well as other chromospherically active stars, have been published in survey programs in other wavelengths, including radio wavelengths (Morris and Mutel, 1988, Costa and Layola, 1990), IR (Verma *et al.*, 1987), UV (Simon and Fekel, 1987), X-ray (Fleming *et al.*, 1989, Gioia *et al.*, 1990), microwaves (Slee *et al.*, 1987) and in various other papers.

The Hipparcos photometry indicated that this system has an 11.12-day periodic variability of amplitude of $0\overset{\mathrm{m}}{.}061$, as well as the Tycho photometry. These variations are in agreement that the system is an ellipsoidal variable. The H_p magnitude as well as the V magnitude observed from MJUO are plotted in figure 5.14.

Pasinetti-Fracassini *et al.* (2001) calculated the absolute diameter of HD 136905 as $R = 6.3R_\odot$ from its K1III spectral type. The distance to this system is 95.1 ±9.1 parsec is calculated from the Hipparcos parallax $\pi = 10.5 \pm 1$ mas.

Radial velocity orbit

A study of the orbit of this system was done by Fekel *et al.* (1985). They assumed that this system has a circular orbit. Their orbital solution has a 1.3 $\mathrm{km\,s^{-1}}$ rms scatter. Balona (1987) measured 25 radial velocities of this system and reported an orbital solution of this system with an rms scatter of 3.5 $\mathrm{km\,s^{-1}}$. Kaye *et al.* (1995) analysed these historical radial velocities, including two from Beavers & Eitter (1986) and one from Lloyd Evans (1986), and reported a circular orbit with an rms scatter of 2.51 $\mathrm{km\,s^{-1}}$. This was done under their assumption that the system was circularized, from its large stellar radius relative to the orbital semimajor axis. These orbital solutions from the literature are shown in table 5.24. The epoch that is reported by Kaye *et al.* (1995) is at the time of conjunction when the primary component is behind, at JD 244 5061.901 ± 0.022, which is earlier than the T_0 by three quarter of an orbital period.

The radial-velocity data, as collected by Kaye *et al.* (1995), were reanalysed again in

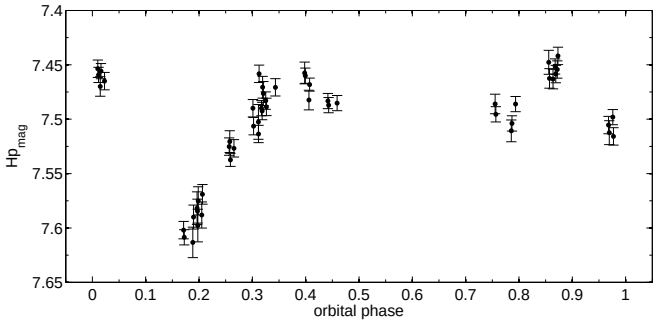

(a)

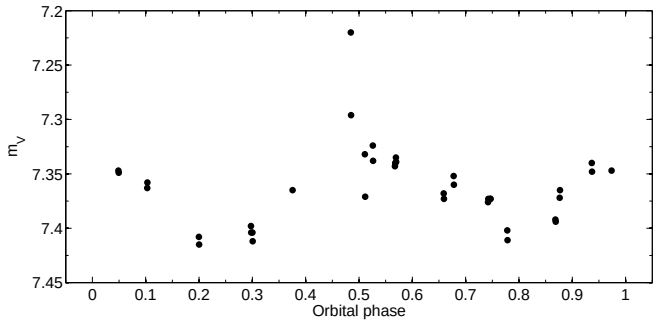

(b)

Figure 5.14: The light curves of the active ellipsoidal variable HD 136905 from the Hipparcos satellite and from MJUO. The orbital phase was calculated from the HERCULES eccentric solution (table 5.26).

this work. The solutions, for an eccentric orbit and a circular orbit, are shown in table 5.25.

Our recent spectroscopic observations with HERCULES archived 42 spectra of HD 136905 with the resolving power 41 000. The radial velocities of this system were measured using the cross-correlation method. The orbital solution is shown in table 5.26. The plot of the radial velocities and the radial velocity curve from this solution are shown in figure 5.15 versus (a) orbital phase and (b) Julian date. The orbital phase is calculated from the period of an eccentric solution and define the time of zero phase as $T = \mathrm{JD}\,245\,3611.02 \pm 0.66$. The lower panel of this figure shows the residuals of this fit. The rms scatter of this fit is 326 $\mathrm{km\,s^{-1}}$, which is high, as can be expected for an ellipsoidal RS CVn-type binary system.

Table 5.24: The orbital parameters of SB1 HD 136905 (K1III) as reported in the literature.

Parameter	**Published**		
	Fekel *et al.* (1985)	Balona (1987)	Kaye *et al.* (1995)
K ($\mathrm{km\,s^{-1}}$)	38.6 ± 0.4	39.7 ± 1.0	38.74 ± 0.50
e	0	0.06 ± 0.03	0
ω (°)	-	63.3 ± 19	-
T_0 (HJD)	244 5070.222	244 4136.9	244 5070.251
	± 0.017	± 0.6	± 0.022
P (days)	11.1345	11.130	11.134 48
	± 0.0005	± 0.003	± 0.000 37
γ ($\mathrm{km\,s^{-1}}$)	61.8 ± 0.3	59.7 ± 0.7	61.28 ± 0.35
$\#_{obs}$	29	25	57
$\#_{rej}$	0	1	1
σ ($\mathrm{km\,s^{-1}}$)	1.3	3.5	2.51

The long timespan between the historical dataset and the recent HERCULES spectra allows us to determine the orbital period of this system with a higher precision. The orbital period calculated from the T_0 of the eccentric solutions in table 5.25 and table 5.26 is $\bar{P} = 11.134\,396 \pm 0.000\,031$ days.

5.12 HD 194215

HD 194215 (HR 7801; $20^{\mathrm{h}}25^{\mathrm{m}}26^{\mathrm{s}}$, $-28°39'47''$) is a system with a K3V primary star. This system was noted for a variation in its radial velocity by Buscombe and Morris (1958) with a classification of this system as a K0 star. Bopp *et al.* (1970) measured 28 radial velocities of this system and analysed its orbit.

The separation between the components in this system was estimated from the spectral type and minimum mass ratio of 0.5 by Halbwachs (1981) as 0.170 arcsec. Later speckle observations by McAlister *et al.* (1987) was the first resolved observation of the system. It is found that indicated that the separation between the components is

Table 5.25: The orbital solutions of SB1 HD 136905 (K1III) analysed from the historical data.

Parameter	**recalculated**	
	eccentric solution	circular solution
K ($\mathrm{km\,s^{-1}}$)	38.85 ± 0.48	38.67 ± 0.39
e	0.026 ± 0.010	0 (fixed)
ω (°)	47 ± 26	-
T_0 (HJD)	244 5070.227 ± 0.023	244 5070.242 ± 0.018
P (days)	11.134 26 ± 0.000 32	11.13389 ± 0.00027
γ ($\mathrm{km\,s^{-1}}$)	61.21± 0.32	61.47 ± 0.27
$\#_{obs}$	57	57
$\#_{rej}$	2	4
σ ($\mathrm{km\,s^{-1}}$)	2.29	1.87

0.121 arcsec. From the CADARS catalogue (Pasinetti Francassini *et al.*, 2001), the disc diameter of the primary star is 1.3 mas and its absolute radius is $0.85\mathrm{R}_{\odot}$.

This system was studied for any evidence of a magnetic field by Saar and Osten (1997). They found that HD 194215 is an active chromosphere star from the system's high Ca II H and K flux, but indicated that there is no evidence for any magnetic flux on this star. They also measured the rotation of the primary star. They found that the primary component has a rotational period of 7.4 days as calculated from the model with $v \sin i = 3.7 \pm 1.0$ $\mathrm{km\,s^{-1}}$.

There is no evidence of a photometric variation from the Hipparcos photometry. This system has a proper motion in RA of 12.1 ± 0.5 mas/yr and in declination of 6.6 ± 0.7 mas/yr (Gontcharov *et al.*, 2001) at a distance of 166 ± 24 pc.

Radial velocity orbit

The orbital solution of this system as analysed by Bopp *et al.* (1970) is an eccentric orbit with $e = 0.0687 \pm 0.0138$ and $P = 377.60 \pm 0.25$ days. The other orbital parameters from their analysis can be found in table 5.27. The rms scatter of their measurement

Table 5.26: The orbital parameters of SB1 HD 136905 (K1III) analysed from HERCULES radial velocities.

Parameter	**HERCULES data**		
	eccentric orbit	with $e = 0$	with $P = \bar{P}$
K (km s^{-1})	39.029 ± 0.078	38.989 ± 0.82	39.040 ± 0.077
e	0.0079 ± 0.0026	0 (fixed)	0.0081 ± 0.0019
ω (°)	23 ± 24	-	33 ± 17
T_0 (HJD)	245 3599.1743	245 3599.1715	245 3599.1717
	± 0.0055	± 0.0067	± 0.0049
P (days)	11.134 14	11.134 13	11.134396 (fixed)
	± 0.000 30	± 0.00029	
$\gamma_{\rm rel}$ (km s^{-1})	−10.116 ± 0.065	−10.055 ± 0.062	−10.095 ± 0.060
γ (km s^{-1})	61.78 ± 0.14	61.72 ± 0.13	61.76 ± 0.13
$\#_{obs}$	42	42	42
$\#_{rej}$	0	0	0
σ (km s^{-1})	0.326	0.385	0.325

is 2.2594 km s^{-1}. These data was reanalysed and it was found that the orbital solution was different from the published solution, especially for the orbital period. This should be compared with the solution from the HERCULES data, table 5.28 which will be discussed later.

In total, there are 73 HERCULES spectra of HD 194215 using the 70 000 resolving power during this research. An eccentric orbital solution was calculated from the radial velocities measured from these spectra. This solution is shown in table 5.28. The radial velocities are shown in the plot of figure 5.16 versus (a) orbital phase and (b) Julian date. This eccentric solution has an rms scatter of the fit of 27 m s^{-1} and the residuals from the fit are plotted in the lower panel of both figures. The time of periastron passage is T = JD 245 3918.52 ± 0.65.

This orbital solution gives an orbital period of 374.88 ± 0.18 d which is consistent with the reanalysed solution from the Bopp *et al.* (1970) data. It should be questioned here why the published orbital period is different from our analysis. The other orbital

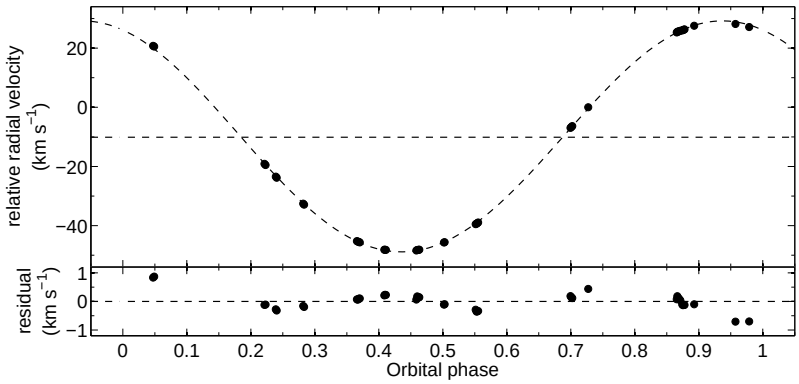

(a) Phase plot of HD 136905 radial velocities.

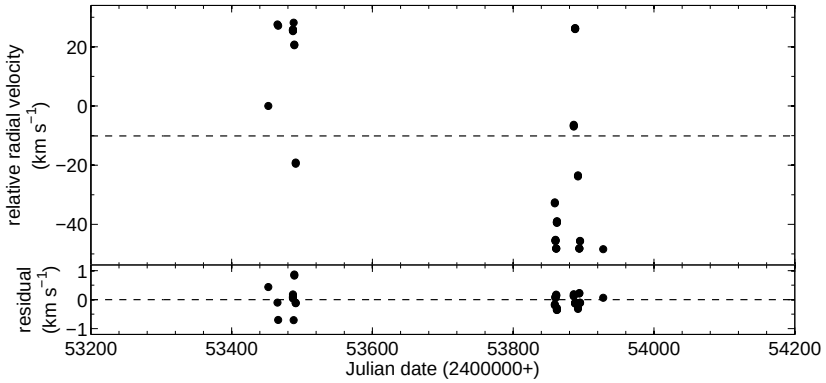

(b) Measured radial velocities of HD 136905 versus Julian date.

Figure 5.15: Radial velocities of HD 136905 measured from the HERCULES spectra. The second panels show the residuals from that fit.

parameters from both data sets are agree within their error bar.

Table 5.27: The orbital solutions of SB1 HD 194215 (K3V) from the data of Bopp *et al.* (1970).

Parameter	**Bopp *et al.* (1970)**	
	published	recalculated
K ($\mathrm{km\,s^{-1}}$)	11.19 ± 0.28	13.4 ± 3.9
e	0.0687 ± 0.0138	0.047 ± 0.071
ω ($^\circ$)	0 ± 9.46	219 ± 76
T_0 (HJD)	$243\,0279.9 \pm 10.8$	$243\,0350 \pm 37$
P (days)	377.6 ± 0.25	374.6 ± 1.8
γ ($\mathrm{km\,s^{-1}}$)	-7.25 ± 0.20	-8.3 ± 2.0
$\#_{obs}$	28	28
$\#_{rej}$	0	0
σ ($\mathrm{km\,s^{-1}}$)	2.2594	2.32

Table 5.28: The orbital parameters of SB1 HD 194215 (K3V) analysed from HERCULES radial velocities.

Parameter	**HERCULES solutions**
	all free parameters
K ($\mathrm{km\,s^{-1}}$)	14.1155 ± 0.0056
e	$0.123\,29 \pm 0.000\,78$
ω ($^\circ$)	258.14 ± 0.77
T_0 (HJD)	$245\,3649.711 \pm 0.074$
P (days)	374.88 ± 0.18
γ_{rel} ($\mathrm{km\,s^{-1}}$)	
γ ($\mathrm{km\,s^{-1}}$)	-8.14 ± 0.14
$\#_{obs}$	97
$\#_{rej}$	1
σ ($\mathrm{km\,s^{-1}}$)	0.047

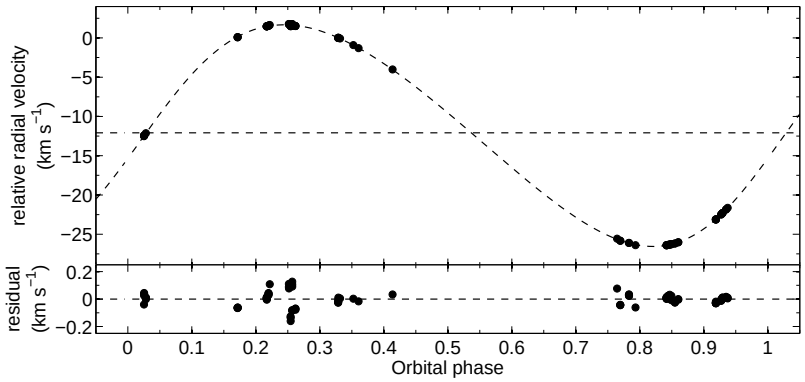

(a) Phase plot of HD 194215 radial velocities.

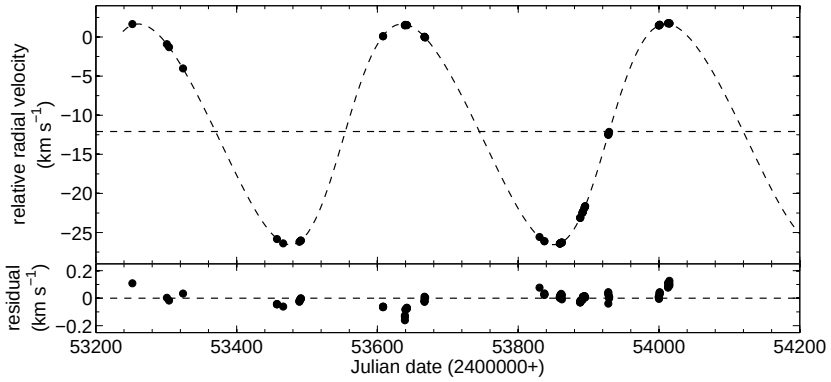

(b) Measured radial velocities of HD 194215 versus Julian date.

Figure 5.16: Radial velocities of HD 194215 measured from the HERCULES spectra. The plotted curves are calculated from the orbital solution calculated from these radial velocities. The second panel shown the residuals from this fit.

Summary of chapter 5

The analysis of eleven single-lined spectroscopic binaries from the HERCULES radial velocities found that there are five SB1s that have eccentric orbits which were rather reported as being eccentric (HD 352, HD 9053, HD 50337, HD 77258 and HD 194215) and three systems where circular orbits should be adopted (HD 22905, HD 38099, and HD 85622). For the other three systems, HD 30021, HD 124425, and HD 136905, it is found that the analysis from HERCULES data gave eccentric solutions which are inconsistent with the literature, as a circular orbit had previously been adopted.

However, these results should not be concluded until the eccentric solutions have been analysed for its reality. In section 8.2 page 161, The tests of LS71 and L05 will be applied to these results.

CHAPTER 6

Orbital solutions of double-lined spectroscopic binaries

Four double-lined spectroscopic binary systems have been analysed in this research. The cross-correlation method was done under the computer code TODCOR (TwO-Dimensional CORrelation algorithm) (Zucker and Mazeh 1994). The templates for this cross-correlation are broadened spectra of standard radial-velocity stars (table 4.1). These standards have the same or very close spectral type and luminosity class as each component of these binary systems and their observed HERCULES spectra were broadened with a gaussian to fit each binary star component's line profile. The radial velocities measured from the HERCULES spectra of these double-lined spectroscopic binary systems are reported in Appendices C.1 – C.4.

6.1 The stellar rotational velocity

Stars are rotating and each single point on their surface radiates. This rotation has an effect on the absorption lines of a star, as the light coming from different parts of the stellar disc has a different Doppler shift. The line profile can therefore be broadened depending on the rotation of the star, and corresponding to the rotational velocity and the orientation of the rotational axis. The spectral line profile can be employed as a one-dimensional map of the stellar disk. A star with a perpendicular rotational axis with the line-of-sight will have a maximum line broadening. On the other hand, a star with a parallel rotational axis will have a zero effect.

Rotational velocity, $v \sin i$, is defined as the projected equatorial velocity of a star. At the same rotational axis orientation, a star with a higher $v \sin i$ will have a greater difference between the velocity of the blue-shifted approaching limb and the red-shifted

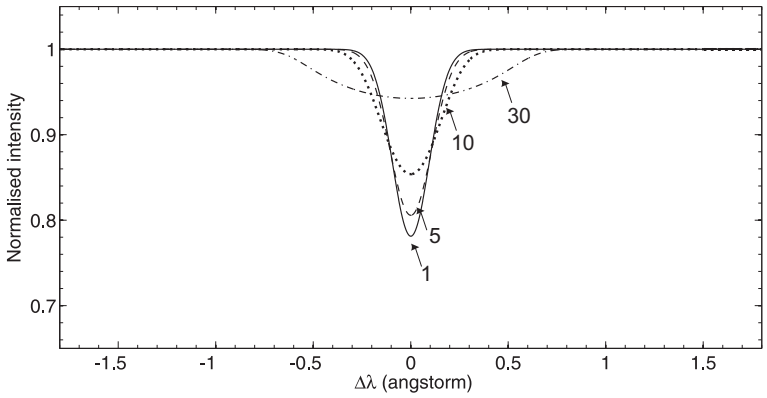

Figure 6.1: The computed line profiles as broadened from the rotation of a star. The labels are the value of $v \sin i$ in $\mathrm{km\,s^{-1}}$. These theoretical line profiles are computed at a wavelength 612.223 nm and $\epsilon = 0.6$.

receding limb, and more so than a star with a lower $v \sin i$. Indeed, the star with a higher $v \sin i$ will have a broader and shallower line profile.

To measure the $v \sin i$ value, it is necessary to compare the stellar line profile with a computed model. As described in Gray (1992), the rotational broadening function is

$$G(\Delta\lambda) = \frac{2(1-\epsilon)[1-(\Delta\lambda/\Delta\lambda_L)^2]^{1/2} + \frac{1}{2}\pi\epsilon[1-(\Delta\lambda/\Delta\lambda_L)^2]}{\pi\Delta\lambda_L(1-\epsilon/3)}, \tag{6.1}$$

where λ is the rest wavelength of the absorption line, $\Delta\lambda$ is the Doppler shift in this wavelength, $\Delta\lambda_L$ is the maximum Doppler shift at the limb, and ϵ is the limb darkening coefficient. This is function is proved by assuming a limb-darkening law of the form

$$I_c/I_c^0 = 1 - \epsilon + \epsilon\cos\theta \tag{6.2}$$

where I_c and I_c^0 are the intensity at a point on the surface and at the centre of the disk, respectively, and θ is the angle between the local normal and the line-of-sight.

The effect of stellar rotation on the line broadening profile is illustrated in figure 6.1. In this figure, are shown theoretical line profiles as a function of $v \sin i$ at a wavelength 612.223 nm and $\epsilon = 0.6$. The line becomes broad and shallow with the larger rotational velocity.

All SB2s studied in this research have had their $v \sin i$ measured by fitting the theoretical profiles with the stellar profiles. Two spectra, which have a maximum separation

between the two sets of absorption lines, were selected from each SB2's data. The absorption lines of each component were measured at the wavelengths 626.4275, 612.223, 604.2201, 605.5130 and 606.5306 nm. The measured $v \sin i$ of each of the SB2s is shown in table 6.1.

Table 6.1: The measured $v \sin i$ of SB2 components, which are noted by number '1' or '2' in the column '#', that are studied in this research. The number in the column 'spectrum' is the MJUO archived number of the selected spectrum. λ_1 to λ_5 are the selected wavelength that were used for the $v \sin i$ measurements (see text for details). All measurement are in $\mathrm{km\,s^{-1}}$. Mean $v \sin i$ for all ten measurements of each component and their error bar are shown in the column '$v \sin i$'.

HD	**#**	**spectrum**	λ_1	λ_2	λ_3	λ_4	λ_5	$v \sin i$ ($\mathrm{km\,s^{-1}}$)
3405	1	3663026	17	17	16	18	17.5	
		3721020	17	17	16.2	17	17	17.0 ± 0.5
	2	3663026	17	18.5	18	18	18	
		3721020	18	18.5	18	18	18	18.0 ± 0.4
77137	1	3406015	27	28	27	27	30	
		3488033	27	27	28	25	28	27.4 ± 1.3
	2	3406015	27	28	30	30	30	
		3488033	24	27	30	26	30	28.2 ± 2.1
155555	1	3642015	37	38	40	35	30	
		3668013	43	43	40	40	37	38.3 ± 3.9
	2	3642015	38	40	38.5	41	38.5	
		3668013	45	45	45	47	40	41.8 ± 3.4
197649	1	3636028	7	5.5	5.5	7	6.5	
		3663021	6	6.5	6	6.8	6.5	6.3 ± 0.6
	2	3636028	24	22	22	22	25	
		3663021	22.5	25	23	21.5	24	23.1 ± 1.3

These numbers are important for the cross-correlation method. The standard star template spectra that were used for the cross-correlation method using the TODCOR

program are needed to have the broadening with the same $v \sin i$ as the binary components, in order to obtain the best radial velocity measurements from the binary program. These standard stars' template spectra are listed with their radial velocities in table 6.2.

Table 6.2: MJUO archived numbers of template spectra of standard radial-velocity stars ($\#_{\rm standard}$) that were used for the cross-correlation method with spectra of each SB2 component, the relative radial velocities between the standard star and the blue-sky spectrum ($V_{\rm sky}$), and the $v \sin i$ value that was used to broaden the standard-star spectra.

HD	#	**Spectral type**	**HD**$_{\rm Std}$	$\#_{\rm std}$	$V_{\rm sky}$ ($\pm$ 0.007 km s^{-1})	$v \sin i$ (km s^{-1})
3405	1	G3V	sun	3405012	0.000	17.0
	2	G8V	20794	3301066	+87.974	18.0
77137	1	G2V	sun	3405012	0.000	27.0
	2	G2V	sun	3405012	0.000	28.0
155555	1	G5IV	11937	3608094	−6.016	38.0
	2	K0IV	71701	3304051	+21.619	42.0
197649	1	F6IV	203608	3859109	−29.733	6.0
	2	G8V	20794	3301066	+87.974	23.0

6.2 Simultaneous orbital solution

For a binary system, its mass ratio is defined by

$$q \equiv \frac{m_2}{m_1} = \frac{K_1}{K_2} = \frac{a_1}{a_2} \leq 1.$$

The radial velocities of each component can be measured relative to their common centre-of-mass,

$$v_{1,2} = K_{1,2}[\cos(\upsilon + \omega) + e \cos \omega]. \tag{6.3}$$

The linear momentum in this moving frame must sum to zero, therefore

$$m_1 v_1 = m_2 v_2, \tag{6.4}$$

which gives

$$q = \frac{m_2}{m_1} = -\frac{v_1}{v_2}. \tag{6.5}$$

This gives a relative ratio of the masses, semi-amplitude of the radial velocity curves, semi-major axis and relative radial velocities between the components as

$$\begin{aligned} 1 : q : (1+q) &= m_1 : m_2 : M = K_2 : K_1 : K_1 + K_2 = a_1 : a_2 : a_1 + a_2 \\ &= -v_1 : v_2 : v_2 - v_1. \end{aligned} \tag{6.6}$$

Thus, the relationship between the radial velocities of the primary component, $V_{\rm rad,1}$ and the secondary component $V_{\rm rad,2}$ can be written as

$$\begin{aligned} V_{\rm rad,1} &= v_1 + \gamma \\ &= -qv_2 + \gamma \\ &= -qV_{\rm rad,2} + (1+q)\gamma. \end{aligned} \tag{6.7}$$

This implies that there is a linear relationship between $V_{\rm rad,1}$ and $V_{\rm rad,2}$. Theoretically, the plot of SB2 data in $V_{\rm rad,2}$-$V_{\rm rad,1}$ space will be a straight line with a slope which equals to $-q$ and the y-intercept is equal to $(1+q)\gamma$.

In the analysis of the radial velocities of SB2, it will be possible to combine the two data sets, one for each component, into one data set using the relation of equation 6.7. This method, as we use in this research, will give a simultaneous solution for the system.

6.3 HD 3405

The nearby star system GJ 24 is a pair of common proper-motion stars. It consists of a single-lined spectroscopic binary, HD 3359, and a double-line spectroscopic binary star, HD 3405. The separation between the two binary systems is 329.9 mas at a position angle 272.°6 as derived by Gould and Chanamé (2004) using the Hipparcos parallaxes. These values were later derived by Tokovinin *et al.* (2006) in their survey of SB third components. They found that the separation between the two systems is 329.600 mas and the two systems orbit around each other at a period of 1080.012 kyr. In the same paper, they derived the orbital period of HD 3359 as $P = 22.400$ days with components' masses of $0.81M_\odot$ and $0.32M_\odot$ while HD 3405 consists of $0.98M_\odot$ and $0.83M_\odot$ components, orbiting at a period of 3.741 days.

The system HD 3405 ($00^{\rm h}36^{\rm m}38^{\rm s}$, $-49°07'56''$) is of interest in this research. The components' mass that was published by Tokovinin *et al.* were estimated from the spectral types of the components, G3V and G8V, that were reported by Bennett *et al.* (1962). This system has an angular size of 1.311 mas (Tokovinin *et al.* 2006). In the *Geneva-Copenhagen Survey of the Solar neighbourhood* (Nordström *et al.* 2004), the properties of the primary component were derived, including its age of 6.1 Gyr (under a range of 5.4 - 6.9 Gyr).

Cutispoto *et al.* (2002) derived the $v \sin i$ of both components as 17 ± 2 and 15 ± 2 km s^{-1} from their ESO-CAT spectra. Our measured values, 17.0 ± 0.5 km s^{-1} and 18.0 ± 0.4 km s^{-1}, consistent with their published data.

The Hipparcos variability classification of this system is 'M' with a $H_p = 6^{\rm m}\!.9204 \pm 0^{\rm m}\!.0011$ and a $0^{\rm m}\!.013$ scattering. This variation may be because of the chromospheric emission of the components as they are moderately active stars (Henry *et al.* 1996). The system has a Hipparcos trigonometric parallax $\pi = 22.79 \pm 0.73$ mas which can be converted to a distance of 43.9 ± 1.4 pc.

Radial velocity orbit

The orbit of HD 3405 was studied by Bennett *et al.* (1962) from only 12 observations that were done at the Cape Observatory using the Radcliffe Cassegrain and coudé spectrographs. They also commented that the absorption lines from both components' spectra are narrow and there are also strong metallic lines. The published orbital solution, as shown in table 6.3, was analysed from the radial velocities of the primary component. The secondary radial velocities was used only for the calculation of the K_2.

From their data, the linear correlation between primary and secondary star's radial velocities indicated that this system has a mass ratio $q = 0.937 \pm 0.036$ and a systemic radial velocity $\gamma = -2.33 \pm 1.4$ km s^{-1}. The reanalysis of the data, excluding three data points where two lines were blended, is shown in table 6.3. The solution adopted is a circular orbit, since there is a large error bar in the eccentricity of the recalculated eccentric solution, $e = 0.0096 \pm 0.0089$.

In total 65 spectra of the system HD 3405 were archived from HERCULES with a 42 000 resolving power over two years of observation. As the spectral types of the

Table 6.3: The orbital solution of the SB2 system HD 3405 as published by Bennett *et al.* (1962) and the reanalysed solution from their radial velocities.

Parameter	**Bennett *et al.* (1962)**	
	published	recalculated
K_1 ($\mathrm{km\,s^{-1}}$)	84.88 ± 1.02	84.08 ± 0.40
K_2 ($\mathrm{km\,s^{-1}}$)	86.77 ± 0.80	89.72 ± 0.38
e	0.0096 ± 0.0089	0 (fixed)
ω (°)	12.77 ± 28.62	-
T_0 (HJD)	243 0001.444	243 7548.5454 ± 0.0031
P (days)	3.7418	3.742 29 ± 0.000 12
γ ($\mathrm{km\,s^{-1}}$)	−2.97 ± 1.12	−2.33 ± 1.4
q	0.978	0.937 ± 0.036
$\#_{obs}$	12	9
$\#_{rej}$	0	0
σ ($\mathrm{km\,s^{-1}}$)	-	7.8

system's companions are G3V and G8V, the templates for the cross-correlation method for this system are a broadened spectrum of a standard radial-velocity star, HD 20794 (G8V), and a broadened solar spectrum. These broadened spectra have $v \sin i = 17$ and 18 $\mathrm{km\,s^{-1}}$, respectively.

The mass ratio and the systemic radial velocity can be computed from a plot between the primary and the secondary's radial velocities of each observation as in figure 6.2. The linear fit of this plot indicates that the system has a mass ratio $q = 0.947\,67 \pm 0.000\,99$ and a systemic radial velocity $\gamma = -4.285 \pm 0.038$ $\mathrm{km\,s^{-1}}$. This new derived mass ratio is compatible with the value derived from Bennett *et al.* (1962) data but higher than the ratio from the estimated masses of Tokovnin *et al.* (2006) of $q = 0.85$. The systemic velocity from the data of Bennett *et al.* is around 2 $\mathrm{km\,s^{-1}}$ different from the value of the HERCULES data. This changing value of γ may in part be due to the orbital motion between HD 3405 and HD 3359.

The orbital solution can be computed simultaneously from the combined data of

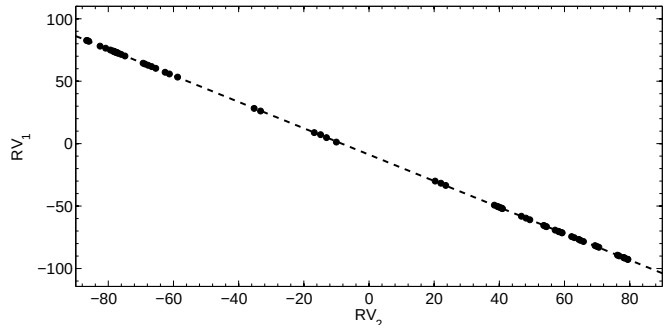

Figure 6.2: The linear correlation between the measured radial velocities of HD3405 primary and secondary star. The linear model is $V_{\mathrm{rad},1} = -0.94767 V_{\mathrm{rad},2} - 8.80662$ km s^{-1}. This model has a standard deviation of 0.14 km s^{-1}.

both components. This solution is presented in table 6.4. The longitude of periastron of the secondary component is $\omega_2 = \omega_1 + 180^\circ = 29\overset{\circ}{.}5 \pm 5\overset{\circ}{.}7$.

Table 6.4: Orbital parameters of HD 3405 as derived from HERCULES spectra. The γ is calculated from the linear relation between $V_{\mathrm{rad},1}$ and $V_{\mathrm{rad},1}$.

Parameter	**HERCULES solution**
K_1 (km s^{-1})	83.922 ± 0.016
K_2 (km s^{-1})	88.556 ± 0.016
e	0.001 91 ± 0.000 24
ω_1 ($^\circ$)	$209\overset{\circ}{.}5 \pm 5.7$
$T_{0,1}$ (HJD)	245 3771.268 87 ± 0.000 15
P (days)	3.742 2560 ± 0.000 0026
γ (km s^{-1})	−4.285 ± 0.038
$\#_{obs}$	65
$\#_{rej}$	2+1
σ (km s^{-1})	0.131

Figure 6.3 are plots of radial velocities of each component versus (a) orbital phase and (b) Julian date. The orbital phase is calculated from the period of $P = 3.742\,256$

days and the definition of the zero phase at the time of perioastron passage,

$$T = T_0 + \frac{\omega P}{2\Pi} \tag{6.8}$$

$$= \text{JD } 245\,3773.447 \pm 0.059. \tag{6.9}$$

The closed circles are radial velocities of the primary star and the crosses are radial velocities of the secondary star. The residuals from the fit are presented in the lower panel.

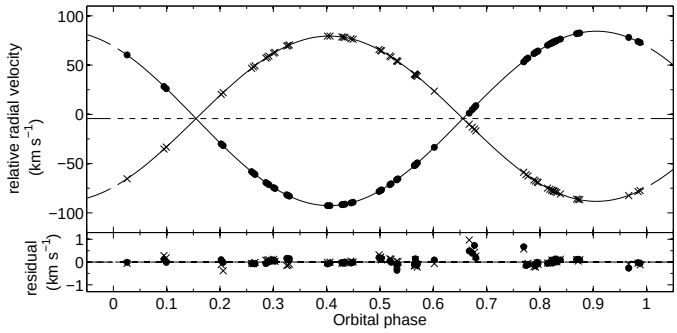

(a) Phase plot of HD 3405 radial velocities.

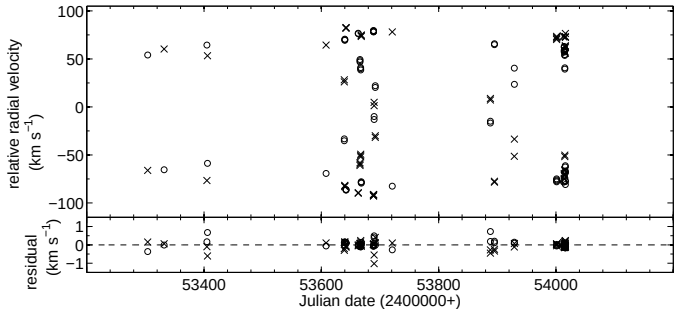

(b) Observed radial velocities of HD 3405 versus Julian date.

Figure 6.3: Radial velocities of HD 3405 measured from HERCULES spectra. In figure (a) is a plot and a best-fit curve as a function of orbital phase as calculated from the solution in table 6.7. The lower panel is the residual from this fit. Figure (b) is a plot of radial velocities versus observation time with the residual from the fit in the lower panel. In all figures, the primary star's radial velocities are presented as open circles and the secondary star's radial velocities are presented as crosses.

6.4 HD 77137

The SB2, HD77137 (TY Pyx; $08^{\rm h}59^{\rm m}43^{\rm s}$, $-27°48'59''$) is an active-chromosphere eclipsing binary star. It consists of two nearly identical G stars with an orbital period around 3.2 days and an orbital inclination, $i = 87\overset{\circ}{.}88 \pm 0\overset{\circ}{.}05$ (Andersen *et al.* 1981). A study by Tokovinin *et al.* (2006) indicated that this system consists of three stars; two identical $1.20M_{\odot}$ stars with a 3.199-days close orbit and a $0.12M_{\odot}$ dwarf in 680-year orbit. The wide orbit has a separation of $1.855''$ which was observed using adaptive optics.

HD 77137 is a famous member of the RS CVn-type of binary star. Its behaviour is well studied in many wavelengths. It was first discovered to be an eclipsing variable by Strohmeier (1967). Popper (1969) studied the photometric variation of this system and indicated its eclipsing behaviour with an ephemeris $\mathrm{JD_{min}} = \mathrm{JD}\ \ 242\,7154.325 + 1.599\,292\ E$, where E indicates the number of cycles from the reference time of minima. Later photometric data analysis by Andersen and Popper (1975) showed that Popper's period is only a half of the true orbital period, and the ephemeris is

$$\mathrm{JD_{min}} = \mathrm{JD}\ \ 242\,7154.325 + 3.198584\ E. \tag{6.10}$$

The photometric observations from the Hipparcos satellite show this periodic variation, as do also the observations from MJUO. These observations are shown in figure 6.4(a) and (b). The orbital phase in these plots is calculated from the ephemeris of equation 6.10.

Later studies in visual wavelengths were done by many authors including Hoffman (1978), Andersen *et al.* (1981), Vivekanande Rao and Sarma (1981) and Allen *et al.* (1993). The photometric result from these researches, including from Hipparcos photometry and MJUO photometry, indicated that there is no change in the orbital period of HD 77137. Andersen *et al.* (1981) derived absolute dimensions of both companions, as shown in table 6.5.

Antonopoulou (1983) studied the variability in the infrared (J, H and K filters) of this system. The sinusoidal light variations were detected outside eclipse, with approximately the same period as the orbital period, with the minimum at the phase of 0.409 ± 0.013. The amplitude of this variation decreases with increasing wavelength. This variation is proposed to be due to starspots. An IUE spectrum of HD 77137 was observed in

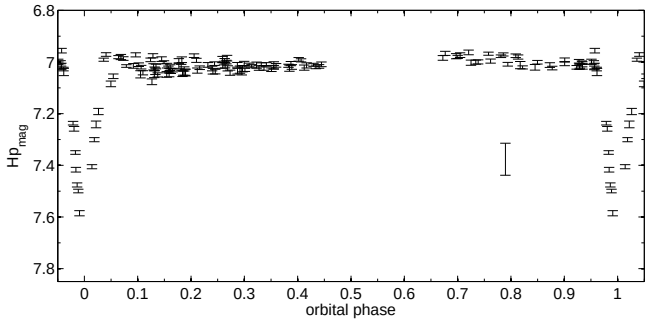

(a) H_p of HD 77137

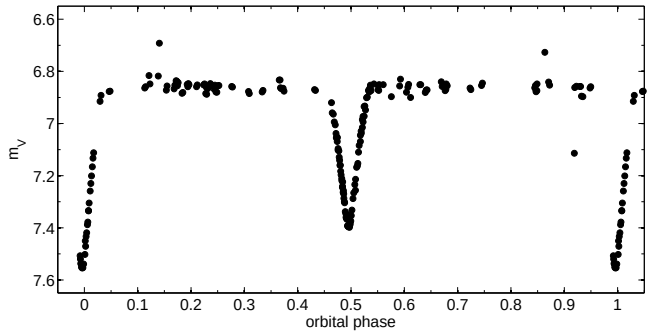

(b) m_V of HD 77137

Figure 6.4: $H_{\rm p}$ and m_V light curves of HD 77137 from Hipparcos and MJUO photometry. The orbital phases are calculated from Andersen and Popper's ephemeris with $P = 3.198\,584$ days.

Table 6.5: Absolute dimensions of HD 77137 as derived by Andersen *et al.* (1981).

	HD 77137A	HD 77137B
Inclination	$87\overset{\circ}{.}88 \pm 0\overset{\circ}{.}05$	$87\overset{\circ}{.}88 \pm 0\overset{\circ}{.}05$
Radius	$1.59 \pm 0.04 R_\odot$	$1.68 \pm 0.04 R_\odot$
Mass	$1.22 \pm 0.02 M_\odot$	$1.20 \pm 0.02 M_\odot$
$T_{\rm eff}$	5400 K	5340 K
$M_{\rm bol}$	$4\overset{\rm m}{.}03 \pm 0\overset{\rm m}{.}10$	$3\overset{\rm m}{.}96 \pm 0\overset{\rm m}{.}10$
$M_{\rm v}$	$4\overset{\rm m}{.}17 \pm 0\overset{\rm m}{.}10$	$4\overset{\rm m}{.}11 \pm 0\overset{\rm m}{.}10$
Distance	50 pc	50 pc

1983. The emission lines originated in the transition region, C IV, Si IV, and N V, and were analysed by Fernández-Figueroa *et al.* (1985), indicating a very high activity of this system. Fox *et al.* (1994) studied this system at radio frequencies and found no evidence of radio flares on a timescale of a few hours or less. A few X-ray observations using EXOSAT (Culhane *et al.*, 1990 and Preś *et al.*, 1995) and BeppoSAX (Franciosini *et al.*, 2002, 2003) indicated the emission of this system arose from different components, including an extended atmosphere, an interstellar loop, flares, and also from a quiescent emission component.

Spectroscopic observations by Gunn *et al.* (1997) indicated that HD 77137 has an excess emission in the Balmer lines and Ca II H and K lines. They found that the secondary component[1] is the more active star from the excess in Hβ which is in agreement with the study of Hα excess by Montes *et al.* (1995) and suggested the existence of prominence-like material in the system.

Radial velocity orbits

The spectroscopic orbit of HD 77137 was first studied by Andersen and Popper (1975) using the coudé spectrographs at Mt Wilson observatory (2.5-m telescope), Lick observatory (3-m telescope) and ESO (1.5-m telescope). The orbital parameters were calculated from these 40 spectra. They adopted a circular orbit for this system as shown here in table 6.6. The mean error of a single velocity is $\sim 2.6\ \mathrm{km\,s^{-1}}$. We have reanalysed these historical data as shown in table 6.6. The circular orbit was also adopted from these reanalysed data because of the large uncertainty in the observational data.

Radial velocities of HD 77137 was also observed by Gunn *et al.* (1996). No orbital solution was reported in their paper. The analysed orbital solution from their eleven data points has a very high rms error bar $\sim 6\ \mathrm{km\,s^{-1}}$.

Sixty-six spectra of HD 77137 were archived using HERCULES with a 41 000 resolving power. The rotational velocities of $v \sin i = 27.4 \pm 1.3\ \mathrm{km\,s^{-1}}$ and $28.2 \pm 2.1\ \mathrm{km\,s^{-1}}$ were measured from each component. The radial velocities of HD 77137 were measured from the cross-correlation function between the star's spectra and a broadened solar

[1]This was indicated as a primary component in the literature as they gave $m_1 = 1.20 M_\odot$ and $m_2 = 1.22 M_\odot$.

Table 6.6: The orbital element of HD 77137 as derived by Andersen and Popper (1975) and the recalculated solution analysed from their data.

Parameter	**Andersen and Popper (1975)**	
	published	recalculation
K_1 ($\mathrm{km\,s^{-1}}$)	96.2 ± 0.5	95.98 ± 0.49
K_2 ($\mathrm{km\,s^{-1}}$)	97.5 ± 0.8	97.47 ± 0.58
e	0 (adopted)	0 (fixed)
ω ($^\circ$)	-	-
T_0 (HJD)	242 7154.325	$242\,7135.858 \pm 0.076$
P (days)	3.198584	$3.198\,603 \pm 0.000\,017$
γ ($\mathrm{km\,s^{-1}}$)	63.2 ± 1.0	63.79 ± 0.45
$\#_{obs}$	40	40
$\#_{rej}$	0	0
σ ($\mathrm{km\,s^{-1}}$)	2.9	2.7

spectrum.

The plot of the primary star's radial velocities versus the secondary's radial velocities is shown in figure 6.5. A linear fitting method was applied to this correlation. From this fit, it has been found that the mass ratio of this system is $q = 0.9986 \pm 0.0025$ and the systemic velocity is $\gamma = 61.25 \pm 0.26$ $\mathrm{km\,s^{-1}}$.

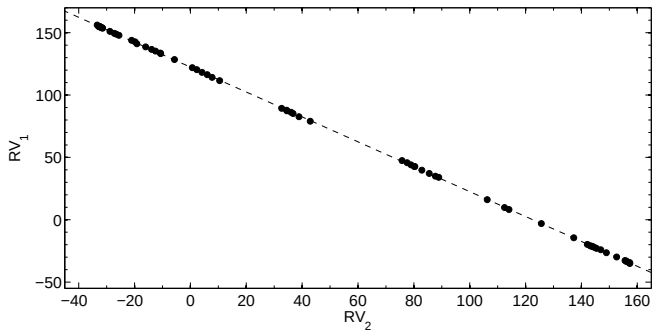

Figure 6.5: Relative plot between radial velocities of both components of HD 77137. The linear fitted model is $V_{\mathrm{rad},1} = -0.9986 V_{\mathrm{rad},2} + 122.4$ $\mathrm{km\,s^{-1}}$.

The orbital solution was derived from the radial velocities of both components, as shown in table 6.7. There are seven data points rejected from the fitting (six of the primary radial velocities and one secondary radial velocity). These data points are approximately 20 $\mathrm{km\,s^{-1}}$ different from the systemic radial velocity (at around an orbital phase 0.3 and 0.8). There are two possible reasons for this rejection. First, the two sets of absorption lines from each component are very close and blended together, which can cause an error in the measurement of the radial velocities of each component. Secondly, HD 77137 is an eclipsing binary, and the radial velocity measured around this point can be different from the star's centre-of-mass radial velocity as a result of the Rossiter effect.

Table 6.7: Orbital parameters of HD 77137 as derived from HERCULES data. Six primary star's radial velocities and one secondary star's radial velocities were excluded in this fit.

Parameter	**HERCULES solution**
K_1 ($\mathrm{km\,s^{-1}}$)	96.582 ± 0.051
K_2 ($\mathrm{km\,s^{-1}}$)	96.722 ± 0.052
e	0.003 01 ± 0.000 51
ω_1 (°)	$164\overset{\circ}{.}3$ ± 8.6
$T_{0,1}$ (HJD)	245 3700.160 36 ± 0.000 29
P (days)	3.198 6024 ± 0.000 0038
γ ($\mathrm{km\,s^{-1}}$)	61.25 ± 0.26
$\#_{obs}$	64
$\#_{rej}$	6+1
σ ($\mathrm{km\,s^{-1}}$)	0.386

Figure 6.6(a) shows a radial velocity plot of HD 77137 versus orbital phase and also the residual plot from the fit. The orbital phase is calculated from the solution of table 6.7. The zero phase is defined by the time of periastron passage, T = JD 245 3701.620 ± 0.076. In figure 6.6(b) the observed radial velocities as a function of Julian date are shown.

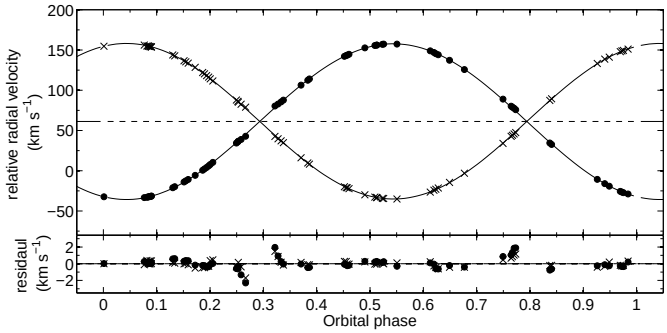

(a) Phase plot of HD 77137 radial velocities.

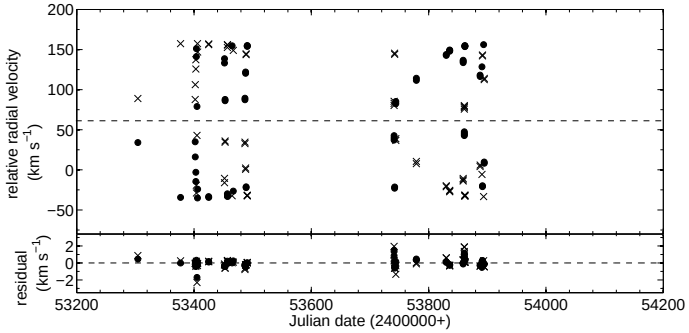

(b) Observed radial velocities of HD 77137 versus Julian date.

Figure 6.6: Radial velocities of HD 77137 measured from HERCULES spectra. In figure (a) is a plot and a best-fit curve as a function of orbital phase as calculated from the solution in table 6.7. The lower panel is the residual from this fit which indicates the large error in the radial velocities measured around the systemic radial velocity. Figure (b) is a plot of radial velocities versus observation time with the residual from the fit in the lower panel. In all figures, the primary star's radial velocities are presented as closed circles and the secondary star's radial velocities are presented as crosses.

6.5 HD 155555

The star HD 155555 (V824 Ara, LDS 587 A; $17^{\rm h}17^{\rm m}26^{\rm s}$, $-66°57'03''$) is an active binary system of the RS CVn-type. It was found to be a double-lined spectroscopic binary star with a short period of $P = 1.6817$ days by Bennett *et al.* (1962). It consists of a G5IV primary star and a K0IV-V secondary star. Both components have active chromospheres which show strong and nearly equal Ca II H and K emission. This system has a visual

binary M-star companion LDS 587 B ($V = 12.82$) with a 33″ separation.

An intrinsic light variation of this system was first reported by Collier (1982) and by Udalski and Geyer (1984). This variation is due to the rotation of the active G5IV star. The variation was also shown in the Hipparcos photometry as $H_p = 7\overset{\text{m}}{.}0114 \pm 0\overset{\text{m}}{.}0036$ with a scatter of $0\overset{\text{m}}{.}037$. Figures 6.7(a) and (b) present plots of the photometric variation in H_p from Hipparcos photometry and m_V from MJUO versus Julian date. There are two timescales of variation. The first one, as suggested previously, is from the rotation of the active primary. This variation is a periodic variation with the same period as the star's rotation period. The second longer timescale is of a period of several years, which may be a spot cycle. The plot of figure 6.7(c) and (d) are plots of photometric variations as a function of phase from selected observational periods to demonstrate the rotational variation.

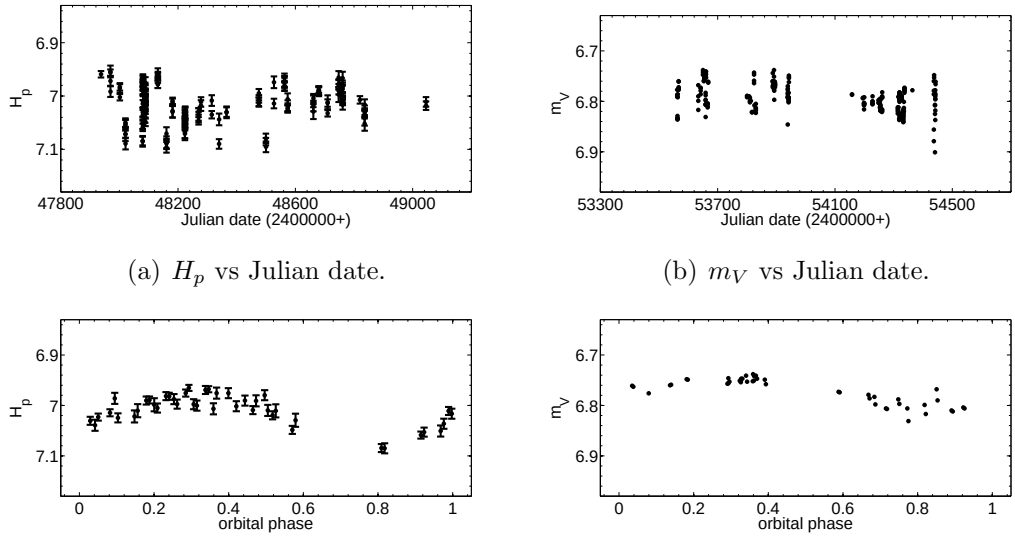

(a) H_p vs Julian date.

(b) m_V vs Julian date.

(c) H_p vs orbital phase.

(d) m_V vs orbital phase.

Figure 6.7: The photometric variation in H_p and m_V magnitude of HD 155555 as observed from the Hipparcos satellite and from MJUO. The data in figure (c) are from Julian date 244 8079 - 244 8089 and figure (d) are from Julian date 245 3633 - 245 3367. The orbital phase is calculated from the spectroscopic orbital phase $P = 1.681\,640$ days.

Hatzes and Kürster (1999) studied the spot distribution on HD 155555 from its Doppler images. They found that both components have slightly decentered polar spots with large spots or bands of spots at around 30° latitude. They noticed that the spot

distributions on both components have mirror symmetry which concentrated on the hemispheres turned away from each other. A later study of this system using the same technique by Strassmeier and Rice (2000) showed that the primary component has an asymmetric polar cap-like spot and a band or group of spots near the star's equator. Their surface map of the secondary star shows a high-latitude spot that just touched the pole and several low latitude spots. Both studies are mainly in agreement, except for the direction of the primary's polar spot asymmetry. Strassmeier and Rice (2000) concluded that this was possibly due to a cyclic behaviour of the RS CVn-type binary system.

Pasquini *et al.* (1991) studied the ESO/CORAVEL spectra of this system. They concluded that the components of HD 155555 are pre-main sequence objects with ages around $\approx 10^7$ years from their extremly high lithium abundances and the activity level of the visual component, LDS 578 B. The inclination of the binary system was derived from the fact that this system do not show any eclipses, the limits of mass and radius of the components, and the assumption that the stars are pre-main sequence stars. This gives the system inclination, $i = 50^\circ \pm 5^\circ$. The absolute dimension of both components were also derived as shown in table 6.8.

Table 6.8: The absolute dimension of HD 155555 as derived by Pasquini *et al.* (1991) from the assumption of pre-main sequence stars.

	HD 1555555A	HD 155555B
Inclination	$50^\circ \pm 5^\circ$	$50^\circ \pm 5^\circ$
Radius	$1.61 \pm 0.24 R_\odot$	$1.26 \pm 0.31 R_\odot$
Mass	$1.16 \pm 0.25 M_\odot$	$1.08 \pm 0.23 M_\odot$
T_{eff}	5500 ± 100 K	5050 ± 150 K
M_{Bol}	$3^m.83 \pm 0^m.$	$4^m.80 \pm 0^m.55$
M_v	$4^m.00 \pm 0^m.3$	$5^m.1 \pm 0^m.55$
Distance	39 ± 9 pc	39 ± 9 pc

HD 155555 is a soft x-ray source (Walter *et al.*, 1980, Barstow, 1987 and Dempsey *et al.*, 1993). Multiwavelength observations of HD 155555 were conducted by Dempsey *et al.* (2001). Their simultaneous observations were done in May 1996 using the GHRS/HST,

the EUVE[2], the ATCA[3], the 1.5-m telescope at CTIO[4], the 1.4-m coudé auxiliary telesope at ESO and optical observations from four further southern observatories[5]. They were able to detect a complicated variation in all wavelengths, including several flares which are well distributed over the star and a 0.075-magnitude variation in H_p photometry.

Radial velocity orbit

The spectroscopic orbit of HD 155555 was first studied by Bennett *et al.* (1962). Their solution was derived from 33 observations at the Cape Observatory in the late 1950s under an assumption of a circular orbit (column 2 of table 6.9).

Later orbital analyses were published by Pasquini *et al.* (1991) and Strassmeier and Rice (2000). Pasquini *et al.* (1991) analysed the solution from 13 CORAVEL radial velocities combined with previous published data by Bennett *et al.* (1962). Strassmeier and Rice (2000) examined 47 radial velocities observed in May 1996 from ESO-CAT and radial velocities from both previous published data sets. These orbital solutions adopted a circular orbit and are shown here in columns 3 and 4 of table 6.9, respectively.

The published solution of Strassmeier and Rice (2000) is different from the others in the literature in two ways. Their semi-amplitude ratio, K_1/K_2, is less than the previous values and the systemic radial velocity γ is 3 $\mathrm{km\,s^{-1}}$ higher with a comment that there is no systematic zero-point shift. They gave a reason that this is because of a higher precision of their data.

During the observation period of this research, 124 spectra of HD 155555 were archived using HERCULES with a 41 000 resolving power. The rotational velocities, $v \sin i$, of each component were measured from these spectra and they are 38.3 ± 3.9 $\mathrm{km\,s^{-1}}$ and 41.8 ± 3.4 $\mathrm{km\,s^{-1}}$. The standard radial-velocity stars for which their spectral type are matched with the components' spectral types reported in the S_{B^9} catalogue, and that were selected for the cross-correlation, are HD 11937 (G5IV) and HD 71701 (K0IV). After broadening these standard stars' spectra, the cross-correlation between the star's

[2]Extreme Ultraviolet Explorer spacecraft
[3]Australia Telescope Compact Array
[4]Cerro Tololo Inter-American Observatory
[5]These are from SAAO, MJUO, Auckland (NZ) and Waiharara (NZ).

Table 6.9: Circular orbital solutions of HD 155555 as derived by the literature.

Parameters	Bennett *et al.* (1962)	Pasquini *et al.* (1991)	Strassmeier & Rice (2000)
K_1 ($\mathrm{km\,s^{-1}}$)	84.92 ± 0.6	85.20 ± 1.20	86.0 ± 0.4
K_2 ($\mathrm{km\,s^{-1}}$)	90.92 ± 1.72	91.56 ± 1.88	94.6 ± 0.7
e	0 (adopted)	0 (adopted)	0 (adopted)
ω	-	-	-
T_0 (HJD)	243 7515.567	244 6998.4102	244 6998.4102 (adopted)
P (days)	1.6817	1.681 652	1.681 6463
		± 0.000 001	± 0.000 0003
γ ($\mathrm{km\,s^{-1}}$)	2.3 ± 0.42	2.74 ± 0.73	5.9 ± 0.2
$\#_{obs}$	33	46	93
$\#_{rej}$	0	0	0
σ ($\mathrm{km\,s^{-1}}$)	-	-	2.37

spectra and the broadened standard spectra was done by TODCOR.

The mass ratio and the systemic radial velocity of this system were calculated from the linear relation between the two components' radial velocities. This relation is shown in figure 6.8. This gave $q = 0.9382 \pm 0.0057$ and $\gamma = 2.04 \pm 0.21$ $\mathrm{km\,s^{-1}}$.

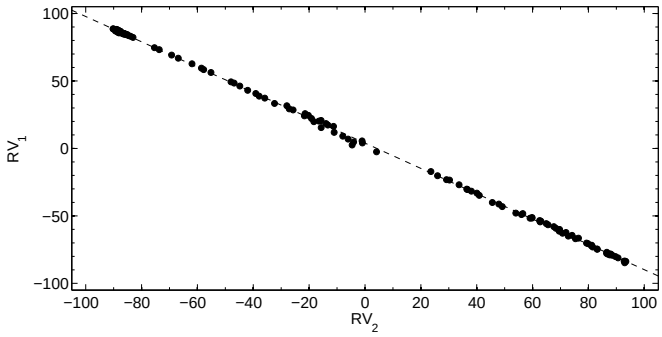

Figure 6.8: The relative plot of radial velocities of the primary component and the secondary component of HD 155555. This plot has a linear relation $V_{\mathrm{rad},1} = -0.9382 V_{\mathrm{rad},2} + 3.959$ $\mathrm{km\,s^{-1}}$.

The orbital solution was derived simultaneously from both components' radial velocities. This solution is presented in table 6.10. Even though the value of e is acceptable from its small error bar, a circular orbital solution is also presented here in order to compare with the published solutions. Both solution is agree with the solutions of Bennett *et al.* (1962) and Pasquini *et al.* (1991) by the means of the mass ratio and the systemic radial velocity.

Table 6.10: Orbital parameters of HD 155555 as derived from HERCULES spectra

Parameter	**HERCULES data**	
	eccentric orbit	circular orbit
K_1 ($\mathrm{km\,s^{-1}}$)	86.322 ± 0.059	86.392 ± 0.063
K_2 ($\mathrm{km\,s^{-1}}$)	92.010 ± 0.062	92.082 ± 0.067
e	0.003 89 ± 0.000 61	0 (fixed)
ω_1 (°)	12 ± 10	-
$T_{0,1}$ (HJD)	245 3518.147 39	245 3518.147 54
	± 0.000 25	± 0.000 27
P (days)	1.681 6404	1.681 6403
	± 0.000 0013	± 0.000 0013
γ ($\mathrm{km\,s^{-1}}$)	2.04 ± 0.21	2.04 ± 0.21
$\#_{obs}$	124	124
$\#_{rej}$	3+3	3+2
σ ($\mathrm{km\,s^{-1}}$)	0.620	0.670

The radial velocities of HD 155555 are plotted in figure 6.9. In this figure are plots of the radial velocities of each component and their residuals from the eccentric solution as a function of (a) orbital phase and (b) Julian date. The orbital phase and the radial velocity curve are also calculated from the eccentric solution using the zero-mean longitude time, T = JD 245 3518.202 ± 0.049 as a time of zero phase.

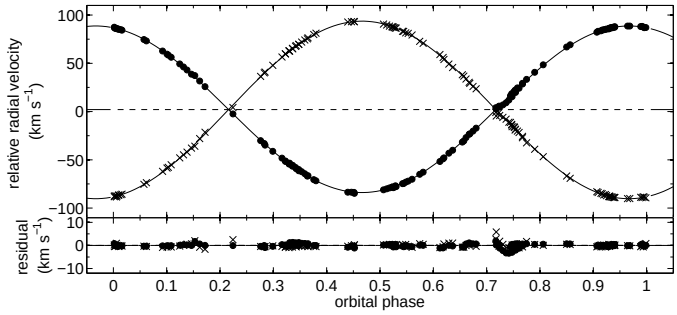

(a) Phase plot of HD 155555 radial velocities.

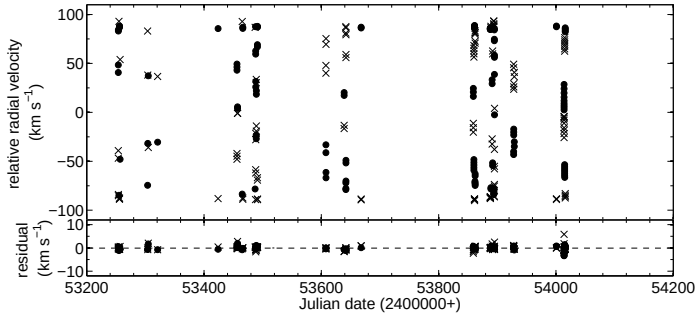

(b) Observaed radial velocities of HD 155555 versus Julian date.

Figure 6.9: Radial velocities of HD 155555 measured from HERCULES spectra. The orbital phase, the radial velocity curve and the residual are all calculated using the eccentric orbital solution. The zero phase is defined by $T = \text{JD } 245\,3518.202 \pm 0.049$.

6.6 HD 197649

The system HD 197649 (HR 7935; $20^{\text{h}}46^{\text{m}}19^{\text{s}}$, $-36°07'13''$) is a binary system which is a member of the solar neighbourhood thin disc (Ibukiyama and Arimoto, 2002). The primary star is earlier in spectral type and brighter. Bennett *et al.* (1963) suggested that the system consists of an F5/6 IV-V star and a fainter G8V star. Ibukiyama and Arimoto (2002) derived the age of this system as 1.72 ± 0.12 Gyr from the relationship between brightness, colour, metallicity and age. This was later derived by Nordström *et al.* (2004) in the Geneva-Copenhagen Survey of Solar neighbourhood, as 1.5 ± 0.2 Gyr.

The works by others reported only one spectral type for the whole system, i.e., Stokes (1972) as dF3; Malaroda (1975) as F3IV; Ibukiyama and Arimoto (2002) as F3/F5V. A

calculation by Vansina and de Grève (1982) showed that the components have masses $M_1 = 1.23M_\odot$ and $M_2 = 0.81M_\odot$ with luminosities, log $L/L_\odot$, 0.46 and 0.12 for the primary and secondary star, respectively. An observation of this system was reported in the 2MASS All-sky Catalogue of Point Sources (Cutri *et al.* 2003). The components of HD 197649 were successfully resolved using the NACO adaptive optics system (Tokovinin *et al.* 2006). The separation of the companions is 1.467 mas.

There is no record of a photometric variation of this system, nor of a variation in other wavelengths. The Hipparcos magnitude of this system is $6\overset{\mathrm{m}}{.}5843 \pm 0\overset{\mathrm{m}}{.}0007$. The ROSAT data of this system was published in the survey by Huensch *et al.* (1998). The X-ray source is at a 31-arcsec distance from the optical position of the system with an apparent X-ray flux of 41.7×10^{-17} W/m^2.

The distance to this system is 69.3 ± 4.0 pc as derived from the Hipparcos trigonometric parallax of $\pi = 14.42 \pm 0.84$ mas.

Radial velocity orbit

The orbit of HD 197649 in the S_{B^9} catalogue is a solution that was reported by Bennett *et al.* (1963). They analysed 24 spectra obtained in 1960–1962 made with the Radcliffe Cassegrain and coudé spectrographs. Their solution, calculated from the primary star's radial velocities, gave an rms error in the measurement of the radial velocities of 1.2 km s^{-1} for the primary star and 13.2 km s^{-1} for the secondary star. This solution is shown in table 6.11.

The data of Bennett *et al.* (1963) have been reanalysed in this research. Due to the large error bar in the $V_{\mathrm{rad},2}$, only the $V_{\mathrm{rad},1}$ were included in the orbital parameters calculation. The K_2 was calculated from the best fit of the $V_{\mathrm{rad},2}$ with all other parameters fixed to the primary star's solution. The circular orbit was adopted from these data because of a large error bar in $e = 0.020 \pm 0.028$ of an eccentric orbit.

In this research, 104 spectra of HD 197649 were archived using HERCULES with a 41 000 resolving power. The measured $v \sin i$ of the primary star is 6.3 ± 0.6 km s^{-1} and that of the secondary star is 23.1 ± 1.3 km s^{-1}. The selected standard radial-velocity stars were HD 203608 (F6V) and HD 20794 (G8V). These spectra were broadened in $v \sin i$ so as to have the same profile as the primary and the secondary stars respectively.

Table 6.11: Orbital parameters of SB2 HD 197649 from the S_{B^9} catalogue.

Parameter	**Bennett *et al.* (1963)**	
	published	recalculated
K_1 ($\mathrm{km\,s^{-1}}$)	44.81 ± 0.89	44.0 ± 1.2
K_2 ($\mathrm{km\,s^{-1}}$)	66.20 ± 2.52	65.0 ± 3.8
e	0.0910 ± 0.0018	0 (fixed)
ω_1 (°)	345.43 ± 6.38	-
T_0 (HJD)	243 7847.322	243 7847.53 ± 0.11
P (days)	18.0668	18.0479 ± 0.0056
γ ($\mathrm{km\,s^{-1}}$)	−14.07 ± 0.54	−10.8 ± 1.2
$\#_{obs}$	24	24
$\#_{rej}$	0	0
σ ($\mathrm{km\,s^{-1}}$)	1.2	3.8

The cross-correlation between these broadened standard star spectra and the observed HERCULES spectra gave the radial velocities for both components, using the TODCOR program.

Figure 6.10 is a plot of these radial velocities in the radial-velocity space. It is found that the linear relationship between the radial velocity of both components is $V_{\mathrm{rad},1} = -0.782 V_{\mathrm{rad},2} - 26.471\ \mathrm{km\,s^{-1}}$. This relation give the system mass ratio $q = 0.7820 \pm 0.0019$ and the systemic radial velocity $\gamma = -14.855 \pm 0.013\ \mathrm{km\,s^{-1}}$.

An orbital solution of HD 197649 was derived from the radial velocities of both components using their relation in q and γ. A circular orbit was adopted from the HERCULES data, since the eccentric solution has an indeterminate eccentricity, $e = 0.000\,28 \pm 0.000\,20$. The circular solution is shown in table 6.12. The number of rejected points is 11 for the primary star radial velocities and none for the secondary star radial velocities.

The radial velocities of HD 197649 and the best-fit curve, from table 6.12, are shown in figure 6.11. These are plotted versus (a) orbital phase and (b) Julian date. The residuals from the fit are also shown in each plot. The time of zero-phase is the time of zero-mean longitude, $T_0 = \mathrm{JD}\,245\,3871.063\,56 \pm 0.000\,54$.

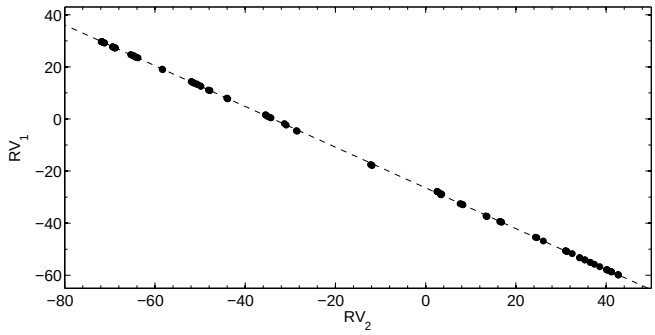

Figure 6.10: The plot of the primary star radial velocities versus the secondary star radial velocities of the system HD 197649. The linear correlation of this plot is $V_{\rm rad,1} = -0.782 V_{\rm rad,2} - 26.471$ km s^{-1}. This plot has a standard deviation of 0.25 km s^{-1}.

Table 6.12: Orbital parameters of HD 197649 as derived from HERCULES spectra

Parameter	**HERCULES data**
	circular orbit
K_1 (km s^{-1})	45.0837 ± 0.0070
K_2 (km s^{-1})	57.6587 ± 0.0087
e	0 (fixed)
ω	-
T_0 (HJD)	245 3871.063 56 ± 0.000 54
P (days)	18.044 527 ± 0.000 038
γ (km s^{-1})	−14.8255 ± 0.0070
$\#_{obs}$	107
$\#_{rej}$	11+0
σ (km s^{-1})	0.070

All the earlier literature on this system has used the mass ratio based on the solution of Bennett *et al.* (1963) as $q = 0.677 \pm 0.039$. The solution from HERCULES data gave a different value, $q = 0.7820 \pm 0.0019$. This gives a spectral type of the secondary component one or two decimal subtypes earlier.

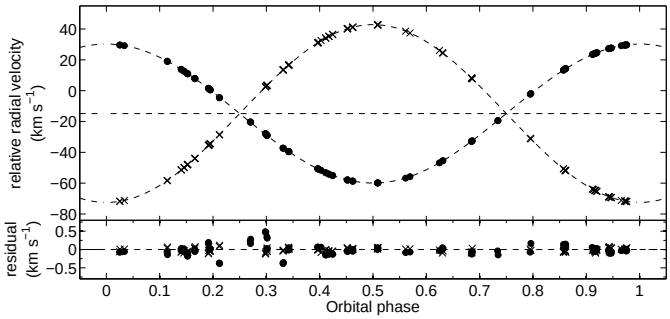

(a) Phase plot of HD 197649 radial velocities.

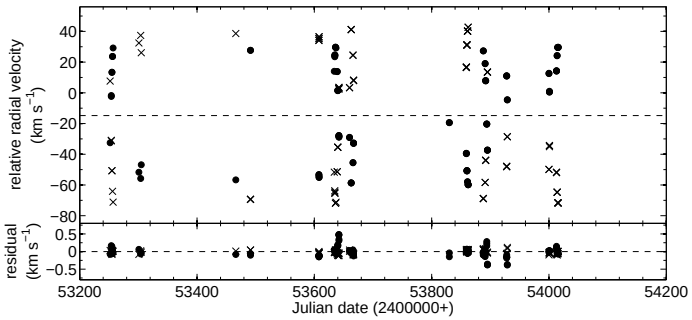

(b) Observed radial velocities of HD 197649 versus Julian date.

Figure 6.11: Radial velocities of HD 197649 measured from HERCULES spectra. These are plotted versus (a) orbital phase and (b) Julian date. An orbital phase is calculated from $P = 18.044\,527$ days with a zero-phase defined at $T_0 = \mathrm{JD}\,245\,3871.063\,56$. The lower panel of each plot shows the residuals from the circular orbit fit. In all figures, the primary star's radial velocities are presented as filled circles and the secondary star's radial velocities are presented as crosses.

CHAPTER 7

A detailed analysis of GT Muscae

In this chapter, the detailed analysis of the binary system GT Muscae will be presented. This system is a quadruple system which consists of the SB1, HD 101379 and the detached eclipsing binary, HD 101380. Both spectroscopic and photometric data of this system have been continuously recorded from MJUO since the 1980s.

7.1 The system GT Muscae

GT Muscae ($11^{\rm h}39^{\rm m}30^{\rm s}, -65°23'52''$) is a quadruple system. The brightness of this system varies because it comprises the RS CVn-type single-line spectroscopic binary, HD 101379 (orbital period $\sim$ 61.4 d) and the eclipsing binary, HD 101380 (eclipsing period $\sim$ 2.75459 d). McAlister, Hartkopf & Franz (1990) reported the separation between the two components as 0.23 arcsec. The Hipparcos and Tycho catalogues (Perryman & ESA, 1997) record the separation as 0.217 ± 0.004 arcsec with a rate of change of -0.014 arcsec yr^{-1} and a rate of change in position angle of $3\overset{\circ}{.}000$ yr^{-1}.

The spectral types of the stars in this system have been classified by many authors. Houk & Cowley (1975) have classified HD 101379 as G5/G8III and HD 101380 as A0/1V. Collier (1982a) determined the spectral types of HD 101379 as K4III and of the components of the eclipsing system as A0V and A2V from his photometric analysis. Murdoch *et al.* (1995) found that HD 101379 was redder than expected for a normal G giant and proposed the correction for this colour excess as a result of the interstellar extinction of $A_V = 0.15$ mag to the whole GT Mus system and a circumstellar extinction of $A_V = 0.45$ mag for HD 101379.

The RS CVn-type system HD 101379 shows a strong CaII H and K emission and a variable Hα line (Collier *et al.* 1982). This system is also a hard X-ray source (Garcia *et al.* 1980). Strong radio flares were detected with a 70 mJy flux at 5 GHz (Collier

et al. 1982). Jones *et al.* (1995) reported a flare with a 30 mJy flux at 8.64 GHz which corresponds to the model of large magnetic loops that extend to about four stellar radii from the star's centre, and a flare with 40 mJy flux at 4.8 GHz. No acceptable extreme ultraviolet flux in filters Lex/B (50–180 Å) and Al/Ti/C (160–240 Å) was detected from the EUVE all-sky survey (Mitrou *et al.* 1997).

Karatas *et al.* (2004) determined that GT Mus is a possible member of the local association moving group, from the criteria on the proper motion of the system. This moving group has a range of age 20–150 Myr.

7.2 Spectroscopic analysis

7.2.1 Orbit of the system

An analysis of GT Mus spectra was done by Murdoch *et al.* (1995). In that paper, the orbital solution of the system HD 101379 was analysed from the 17 spectra that were obtained from the MJUO's Cassegrain échelle spectrograph linked with the McLellan 1-m telescope combined with other radial velocities reported by Balona (1987), Collier Cameron (1987) and MacQueen (1986). This orbital solution is shown in table 7.1.

Table 7.1: The orbital parameters of SB1 HD 101379 (G2III) as published by Murdoch *et al.* (1995).

Parameter	**Murdoch *et al.* (1995)**
K ($\mathrm{km\,s^{-1}}$)	12.7 ± 0.2
e	0.032 ± 0.013
ω ($^\circ$)	238 ± 24
T_0 (HJD)	$244\,4888 \pm 6$
P (days)	61.448 ± 0.007

In this study 76 high resolution spectra of GT Mus at a wavelength 450–720 nm were obtained from the HERCULES spectrograph at the resolving power of 70 000. These spectra, which are dominated by HD 101379, were archived over a period of two years

(October 2004 – June 2006) with a signal-to-noise ratio of typically 70. Relative radial velocities of these spectra were calculated using the HRSP package with the MJUO archived spectrum number F3489055.FIT as a template for the cross correlations.

These relative radial velocities of HD 101379 can be converted into absolute radial velocities using the relative radial velocity of the template spectrum with respect to the standard star spectrum. The spectrum of the standard star HD 109379 was used for this purpose. The relative radial velocity of the template with respect to the standard star is $21.110 \pm 0.024\,\mathrm{km\,s^{-1}}$. The standard star absolute velocity is $-7.246 \pm 0.024\,\mathrm{km\,s^{-1}}$.

The orbital solution was calculated using the above radial velocities. The solution, as in table 7.2, has an rms of $518\,\mathrm{m\,s^{-1}}$. This is three times better than the precision of the Murdoch *et al.* (1995) radial velocities, for the reasons discussed below.

Table 7.2: The orbital parameters of SB1 HD 101379 (G2III) derived from HERCULES radial velocities

Parameter	**New analysed value**
K ($\mathrm{km\,s^{-1}}$)	12.911 ± 0.078
e	0.012 ± 0.010
ω ($^\circ$)	$237 \pm 51^\circ$
T_0 (HJD)	2453736.00 ± 0.10
P (days)	61.408 ± 0.027
γ ($\mathrm{km\,s^{-1}}$)	1.02 ± 0.11
$\#_{obs}$	76
$\#_{rej}$	0
σ ($\mathrm{km\,s^{-1}}$)	0.518

Figure 7.1a and b show the relative radial velocities measured from the HERCULES spectra with their residuals in the second panel. It is clearly seen that the residuals from this fit have a positive value during the first observation period and have a negative value during the second period. This should be due to the fact that the system GT Mus is a quadruple system and the radial velocity measured from the HERCULES spectra is a radial velocity of only the G star in the SB system. This star orbits around the centre-of-mass of the SB system, HD 101379, which orbits around the centre-of-mass of

the whole GT Mus quadruple system. This longterm variation was not shown in the radial velocities of Murdoch *et al.* (1995) because of their shorter observation period (JD 244 8260 – 244 8479).

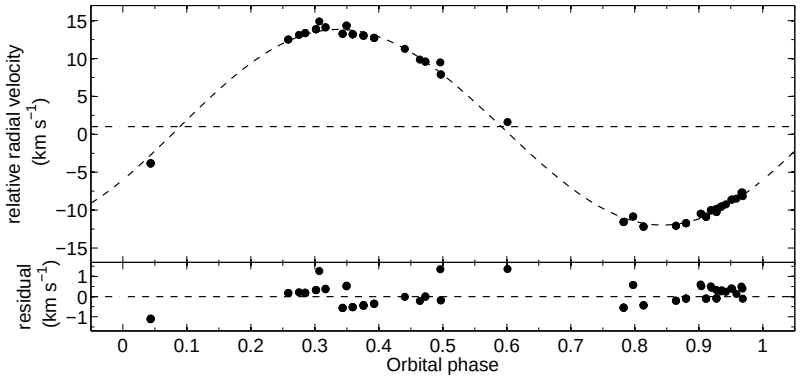

(a) Phase plot of HD 101379 radial velocities.

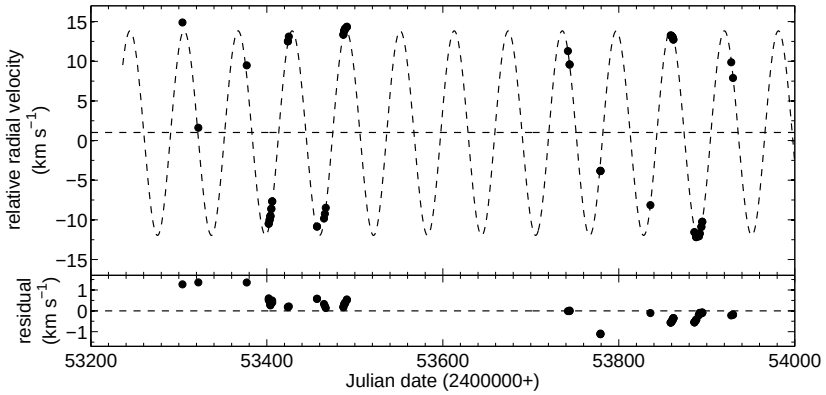

(b) Measured radial velocities of HD 101379 versus Julian date.

Figure 7.1: Radial-velocity observations of GT Mus measured from HERCULES spectra. The plotted curves are calculated from the orbital solution calculated from these radial velocities. The second panels shown the residuals from the fits.

When these data are separated into two groups by the observation time (October 2004 – May 2005 and November 2005 – June 2006), each data set gave a better solution with rms of 79 m s^{-1} and 54 m s^{-1}, as shown in table 7.3.

The orbital solutions from both data set do not change dramatically except the longitude of periastron ω and the systemic radial velocity γ. The value of ω changed

Table 7.3: The orbital parameters of HD 101379 derived from two data sets of HERCULES radial velocities, October 2004 - May 2005 and November 2005 - June 2006.

Parameter	**New analysed value**	
	October 2004 - May 2005	November 2005 - June 2006
K ($\mathrm{km\,s^{-1}}$)	12.948 ± 0.027	12.715 ± 0.011
e	0.0225 ± 0.0038	0.0331 ± 0.0027
ω ($^\circ$)	175.3 ± 6.9	61.8 ± 2.1
T_0 (HJD)	$245\,3429.478 \pm 0.036$	$245\,3797.763 \pm 0.018$
P (days)	61.516 ± 0.045	61.331 ± 0.017
γ ($\mathrm{km\,s^{-1}}$)	1.723 ± 0.035	0.287 ± 0.026
$\#_{obs}$	34	42
$\#_{rej}$	1	1
σ ($\mathrm{km\,s^{-1}}$)	0.079	0.054

from $175\overset{\circ}{.}3 \pm 6\overset{\circ}{.}9$ to $61\overset{\circ}{.}8 \pm 2\overset{\circ}{.}1$ and the value of γ changed from 1.723 ± 0.035 to 0.287 ± 0.26 $\mathrm{km\,s^{-1}}$. These changes could result from the motion of HD 101379 around the centre of mass of GT Mus.

The LS71 and L05 tests on the eccentricity of orbital solutions in table 7.3 indicate that these eccentric solutions have a detectable eccentricity like effect as well as a detectable perturbation in their Keplerian harmonic. This result agrees with the fact that the G star of HD 101379 is an active chromosphere star. Its spot activity can affect the measured radial velocities of the system.

To improve the solution, the historical radial velocities were analysed together with HERCULES radial velocities. The radial velocities of HD 101379 were observed at MJUO and reported by many observers using different instruments. These include MacQueen (1986), Collier Cameron (1987) and Murdoch *et al.* (1995). The other observations of HD 101379 that are included in this analysis are from Balona (1987). The data from MacQueen (1986) could not be combined into this analysis, due to the fact that his radial velocities showed an orbital period of around 54 days. The orbital solutions were calculated from all the other data sets.

Table 7.4: The systemic radial velocity γ of HD 101379 calculated from historical radial velocities and HERCULES radial velocities.

Radial velocity data	T_0 (HJD 2400000+)	γ ($\mathrm{km\,s^{-1}}$)
Balona (1987)	44 397.25 ± 0.63	9.12 ± 0.50
Collier Cameron (1987)	44 458.71 ± 0.59	8.13 ± 0.38
Murdoch (1995)	48 391.76 ± 0.42	0.53 ± 0.47
HERCULES data set 1	53 429.478 ± 0.036	1.723 ± 0.035
HERCULES data set 2	53 797.763 ± 0.018	0.287 ± 0.026

The systemic radial velocities γ of each data set are shown here in table 7.4. These γ values decrease during 30 years of observation. The orbital period of HD 101379 around the centre-of-mass of GT Mus can't be calculated from these few data. From the Hipparcos catalogue, $\pi = 5.81 \pm 0.64$ mas and the separation between the two stars is 0.217 ± 0.004 arcsec. The HIP photometry also measured the changing rate of the position angle between the two systems as $d\theta/dt = 3\overset{\circ}{.}0$ per year. This information gave a lower limit of the system total mass as $3.6M_{\odot}$. This value is about a half of the total mass calculated from the components' spectral types of G5III, M dwarf, A0V and A2V stars, of $7.4M_{\odot}$.

The radial velocities from each data set were shifted to the zero point of γ. The final orbital solution was calculated from a data set containing all relative velocities with the data weighted in the ratio Balona:Collier Cameron:Murdoch:this work 0.02:0.08:0.7:1.0 in accordance with the calculated rms scatter of each data set solution. The period of a solution from these combined data is 61.4370 ± 0.0012 days with an rms of 380 $\mathrm{m\,s^{-1}}$. This orbital solution is shown in table 7.5.

This orbital solution from table 7.5 gives a higher precision period $P = 61.4370 \pm 0.0012$ days. This period is then fixed in the calculation of HERCULES data to find the orbital solution as shown in table 7.6.

Table 7.5: The orbital parameters of HD 101379 calculated from HERCULES radial velocities and the previous published radial velocities.

Parameter	**Combined data**
K ($\mathrm{km\,s^{-1}}$)	12.823 ± 0.049
e	0.0053 ± 0.0034
ω ($^\circ$)	73 ± 51
T_0 (HJD)	$244\,4951.03 \pm 0.13$
P (days)	61.4370 ± 0.0012
$\#_{obs}$	183
$\#_{rej}$	1
σ ($\mathrm{km\,s^{-1}}$)	0.380

Table 7.6: The orbital parameters of HD 101379 derived from two data sets of HERCULES radial velocities, October 2004 - May 2005 and November 2005 - June 2006 when fixing the period to 61.4370 days.

Parameter	**New analysed value**	
	October 2004 - May 2005	November 2005 - June 2006
K ($\mathrm{km\,s^{-1}}$)	12.928 ± 0.027	12.698 ± 0.017
e	0.0182 ± 0.0031	0.0435 ± 0.0036
ω ($^\circ$)	173.3 ± 9.1	57.8 ± 2.4
T_0 (HJD)	$245\,3429.449 \pm 0.032$	$245\,3797.678 \pm 0.023$
P (days)	61.4370 (fixed)	61.4370 (fixed)
γ ($\mathrm{km\,s^{-1}}$)	1.673 ± 0.028	0.197 ± 0.035
$\#_{obs}$	34	42
$\#_{rej}$	1	1
σ ($\mathrm{km\,s^{-1}}$)	0.082	0.091

7.2.2 Variation of GT Mus spectra

The spectra of GT Mus also show that the system has a variation in the emission of Hβ. Figure 7.2 is a plot of selected GT Mus spectra versus orbital phase. It is clearly

seen that there is a variation in the depth of the Hβ line, which varies independently of the orbital phase. For a normal G-type star, the depth of the $H\beta$ line is approximately 70–80% of the continuum spectrum. For GT Mus, there are some observations that the depth is decreased to about 20%. This is due to the fact that the G star has an active chromosphere and the Hβ line was filled by the chromospheric emission of the star. The timescale of the emission is independent of its orbital period, as will be discussed in the next section, which results in the non-periodic variation of the depth of the Hβ line.

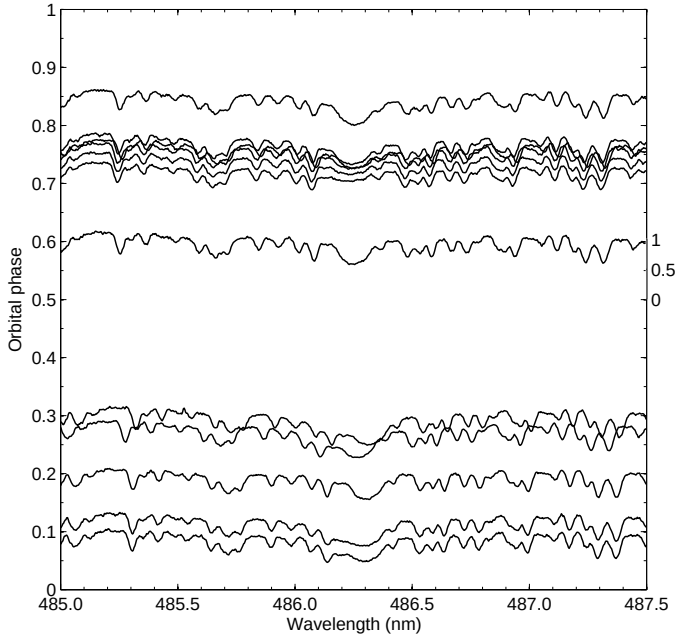

Figure 7.2: Hβ lines of GT Mus spectra. The spectra were plotted versus orbital phase of HD 101379. The right-hand scale is for the relative intensity.

A few HERCULES spectra were archived over a timespan of a month in August 2007 with the 4k×4k SI CCD. The Hα, Hβ, and CaII H and K lines from these spectra also have a variability in their emission as can be seen in figure 7.3. This may be due to phenomena related to the activity of the G star such as flares or prominences. These phenomena have strong emission lines but a short lifetime.

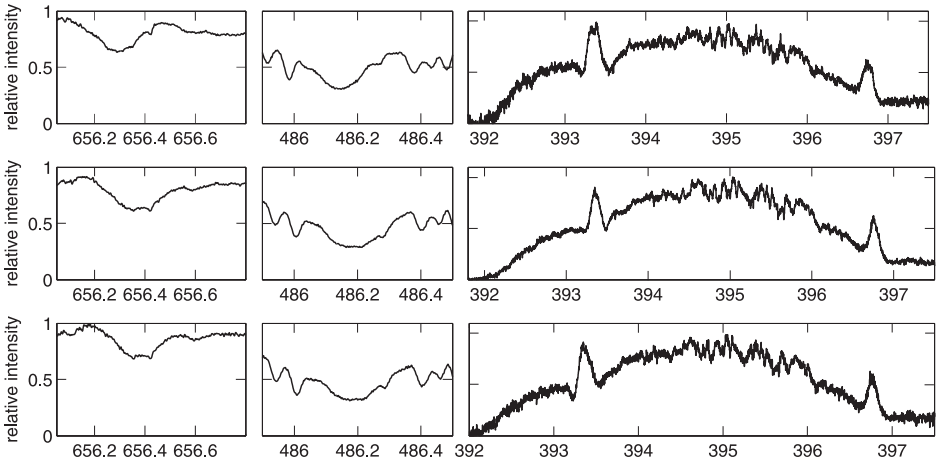

Figure 7.3: Parts of spectra of GT Mus as observed in August 2007 (HJD 2454315.77, 2454338.81 and 2454340.79). These spectra show a variation in the emission lines, Hα, Hβ and CaII H and K lines.

7.3 Photometric analysis

GT Mus is one of the variable stars that has been in a program of continued observations at MJUO. Differential $UBV(RI)_{\rm C}$ observations from the period of March 1987 – November 1993 were reported in Murdoch *et al.* (1995). From those observations, three timescales of brightness variation were shown. The first variation is the activity-cycle variations due to a starspot cycle on HD 101379. This effect varied around 0.18 mag over ten years. The second is the quasi-periodic variation due to the rotation of the spotted star. Murdoch *et al.* (1995) examined the periodogram of this variation and found that it is around 63.5 days and concluded that that this system was not fully tidally synchronized (which is also shown in their eccentricity, $e = 0.032 \pm 0.013$). They suggested that there may be a spot at the visible pole in combination with a spot or group of spots which formed at slow-rotating higher latitudes and moved to faster-rotating lower latitudes. A polar spot decreased in size during the time of their observation and the group of spots formed at the middle of their observations. The third timescale of variation is due to the eclipses of the HD 101380 system with a period of $P = 2.754\,59 \pm 0.000\,02$ d.

The new photometric data set from MJUO service photometry program is from

September 1997 to September 2006. These data and the data from Collier Cameron (1987) and Murdoch *et al.* (1995) are shown in figure 7.4. All three timescales of variation, as suggested by Murdoch *et al.* (1995), are clearly seen from these data. To analyse these variations, the light from the eclipsing system, HD 101380, needs to be removed from the total observed light.

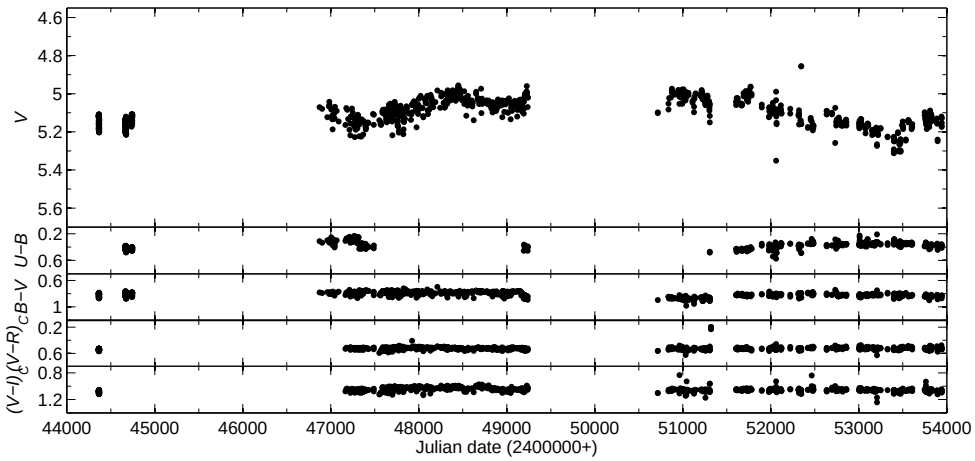

(a) Photometric observation of HD 101379 from MJUO

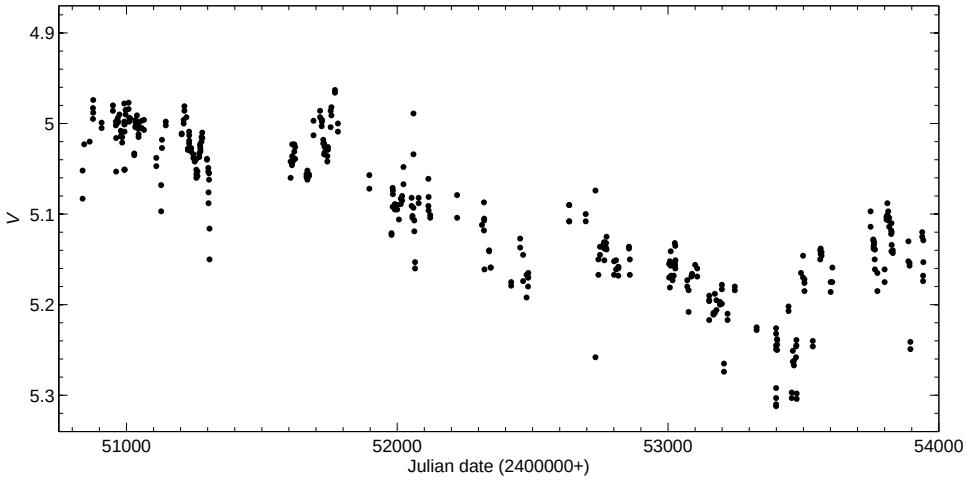

(b) An enlargement of figure (a). V of HD 101379 from MJUO during JD 245 0500 – JD 245 54000

Figure 7.4: Photometric data of GT Mus from MJUO. There are three timescales of variation visible in these data; 10-12 years variation in figure (a), and ∼60 days and ∼2 days variation in figure (b).

7.3.1 The model of the eclipsing system HD 101380

The model of the HD 101380 light curve was generated by considering that this system consists of A0V and A2V stars with an eclipsing period $P = 2.754\,59 \pm 0.000\,02$ days, as was determined by Murdoch *et al.* (1995). The program Binary Maker 3.0 was used to generate the light curve of the eclipsing system. The input radii were calculated from the calibrated physical parameters of A0V and A2V stars from Allen's Astrophysical Quantities (Cox eds. 2000), and they are $2.9M_{\odot}$ and $2.5M_{\odot}$, with a $14.562R_{\odot}$ separation. The third light, which is the light from HD 101379 system, was calculated from SIMBAD data; for HD 101379 $B = 5\overset{\mathrm{m}}{.}97$ and $V = 5\overset{\mathrm{m}}{.}17$, while for HD 101380 $B = 6\overset{\mathrm{m}}{.}3$ and $V = 6\overset{\mathrm{m}}{.}3$. These give a third light ratio for the B flux of 1.3553[1] and for the V flux of 2.8314.

The inclination and the orbital parameters (including the eccentricity) of the eclipsing system are free parameters in the model. The synthetic light curves were compared with normalized observed light curves. As the observed light varies because of the activity on the G-star, the data set was separated into small time intervals and was normalized by a data point at a non-eclipsing phase $\phi \approx 0.3$ of each interval. The normalized light curves in both B and V filters show a scatter due to the variation of brightness from the G-star. These normalized observational fluxes and the synthetic light curve are shown in figure 7.5

The best-fit model for both B light curve and V light curve are consistent. This gives the inclination of the eclipsing system as 84° and the eccentricity and longitude of periastron, as 0.05 and 290° respectively.

7.3.2 Timescales of photometric variation

The flux from this eclipsing model was removed from the observed flux, and hence only the flux from the G-star was left (figure 7.6). These new light curves show only the variation in brightness of the G-star due to its activity.

It is clearly seen that there are two timescales of variation left whose variation is due to the rotation of a spotted G star and a variation due to a starspot cycle. The Fourier analysis of the new MJUO photometric V band data set (from HJD 2450000+)

[1]The flux ratios are $f_{\mathrm{HD\,101379}}/f_{\mathrm{HD\,101380}}$. This is a difference from Murdoch (1995); in that paper, the B flux of HD 101379 was assumed to equal to that of HD 101380.

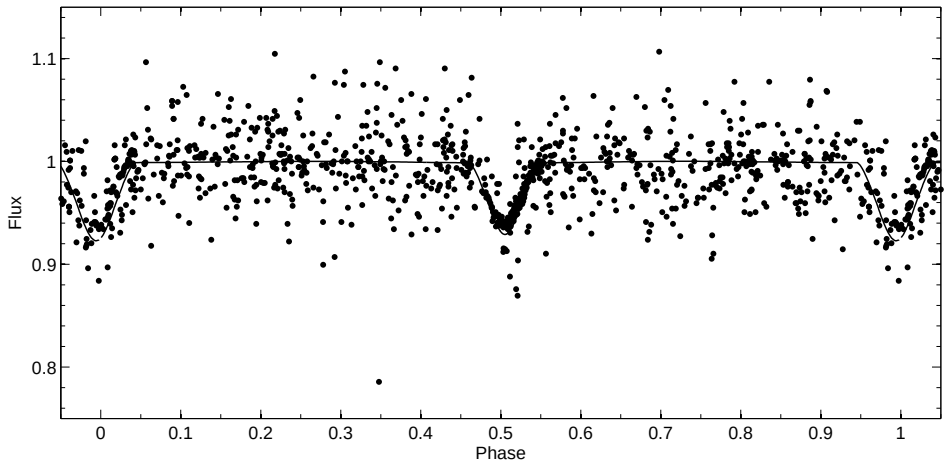

Figure 7.5: Synthetic light curve of the system HD 101380. The dots are normalized observational V fluxes of the system from MJUO.

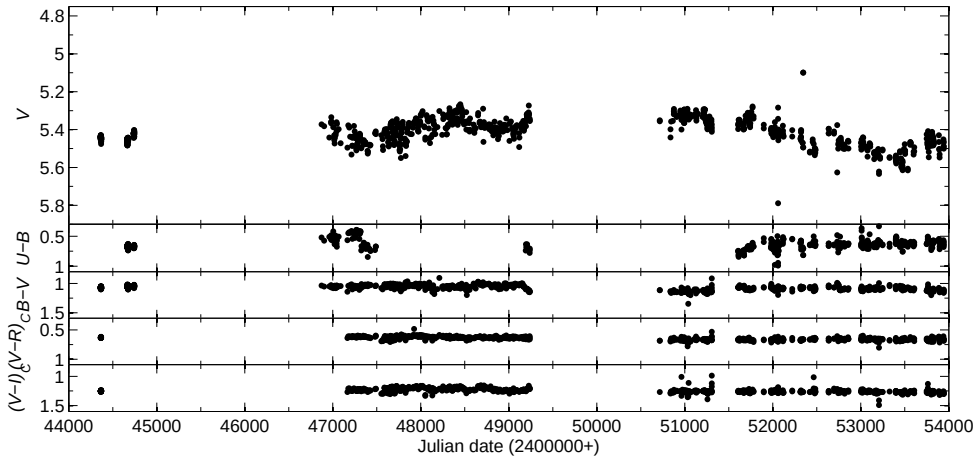

Figure 7.6: Calculated photometric data of HD 101379 after removing the photometry of the HD 101380 model from the GT Mus photometry

shows that the period of the starspot cycle is approximately 12 years. These V band data were separated into four equal subsets, i.e., HJD 245 0716.176 – 245 1306.983, HJD 245 1606.138 – 245 2345.119, HJD 245 2420.929 – 245 3107.979, and HJD 245 3151.922 – 245 3942.848, and these were examined using Fourier analysis to find the period of rotation of the spotted G star. The power spectra of each data set is shown in figure 7.7.

It is found that the periods of rotation are different in each subset, and are 65.75 ± 0.04 d, 66.87 ± 0.05 d, 65.98 ± 0.01 d and 63.60 ± 0.04 d respectively. On the same method of analysis, Murdoch *et al.* (1995) reported the rotation period of 63.5 ± 1.0 days and 68.5 ± 0.5 days from the data of HJD 244 6873 - 244 9332.

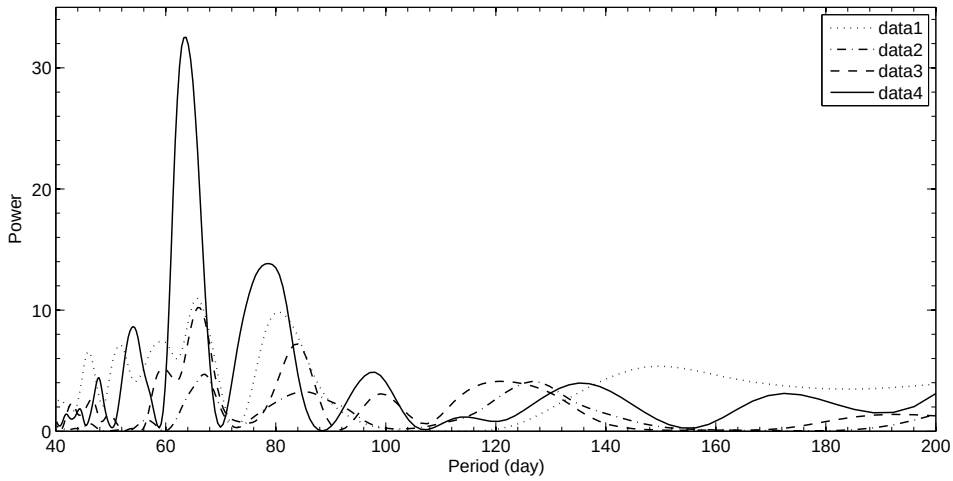

Figure 7.7: The power spectra of the V data of HD 101379. Each data set covers about one-quarter of the timespan of the whole data set. See text for details.

The changes in the rotational period are possibly due to the fact that the spots have migrated over the time of observation. The spots may have migrated from a slow-rotating latitude to a faster-rotating latitude in a differentially rotating star.

The percentage of a spotted area is changing during the observation period. This can be observed by the variation of the V magnitude in figure 7.6. The spotted area was increasing during the first three parts of the observation which is reflected in the decrease of the system's brightness. During the last part of the observation, the spotted area was decreasing, resulting in the brighter system.

The spot behaviour can also be observed from the variation in the star's colour as shown in figure 7.8a, b and c. When the star is dimmer, it is redder, due to the increase in the spotted area. The total flux of a spotted star, $F_{\rm star}$, is

$$F_{\rm star} = (1-\alpha) f_\star + \alpha f_\bullet \tag{7.1}$$

where $f_\star$ and $f_\bullet$ are fluxes per unit area of the unspotted star and of the spot, and α is

the ratio of the spotted area to the total surface area of the star. The colour index, CI, of the spotted star is

$$\mathrm{CI}_{\mathrm{star}} = -2.5 \log_{10} \left[\frac{F_{\mathrm{star},\lambda 1}}{F_{\mathrm{star},\lambda 2}} \right] + C_{\lambda 1} - C_{\lambda 2}. \tag{7.2}$$

The quantity $C_{\lambda i}$ are arbitrary constants defined by reference to standard stars.

In figure 7.8b, the $(V-R)_C$ data are plotted in four subsets, following each quarter of observation. The slopes of linear fits to each data set are 0.1988 ± 0.093, 0.1103 ± 0.068, 0.09 ± 0.11, and 0.151 ± 0.072. This indicates that the coverage and distribution of the spotted area increased during the first three quarters and decreased in the last quarter. These results are in agreement with the slopes from $(V-I)_C$ data in figure 7.8c, i.e. 0.327 ± 0.077, 0.178 ± 0.068, 0.23 ± 0.12 and 0.113 ± 0.062. The theoretical V, $(V-R)_C$ and $(V-I)_C$ of a spotted G5III star were calculated using equations 7.1 and 7.2 for different values of a spotted area and of a temperature difference, ΔT. The temperature of the primary star, G5III, is assumed to be $T = 5050$ K. The value of $\mathrm{d}(V-R)_C/\mathrm{d}(V)$ and $\mathrm{d}(V-I)_C/\mathrm{d}(V)$ for a different ΔT and α are plotted in figure 7.9.

When the reddening effect from the spots is calculated and compared with the star's observed colour, the most probable difference in temperature between the star's photosphere and spots ΔT is approximately 700 K with a possible spotted area varying from zero to 50%.

In order to investigate the spot temperature and its coverage area at each epoch, the observations of GT Mus using other techniques are needed. These include the Doppler technique and the analysis of the spectrum line-depth ratio (Frasca *et al.* 2005).

It is also noted that the colour of the system is redder than the expected value. From Allen's Astrophysical Quantities (Cox eds. 2000), the colour indices $(V-R)_C$ and $(V-I)_C$ of a G5III giant are 0.47 and 0.91, respectively. The observed values of HD 101379 are 0.67 ± 0.5 and 1.27 ± 0.5. It should be noted here that the data of HD 101380 from the SIMBAD database indicates no interstellar reddening on HD 101380 system as $(B-V) = 0.0$ and the model of HD 101380 in this research is based on these data. However, the reddening of HD 101379 may be a result of circumstellar reddening.

The large scatter in the $U-B$ data in figure 7.8a with its negative slope and the scatter in the first data set of $(V-I)_C$ in figure 7.8c might be a result from emission events of the star, i.e. flares. The I_C band data show a larger scatter than the first half

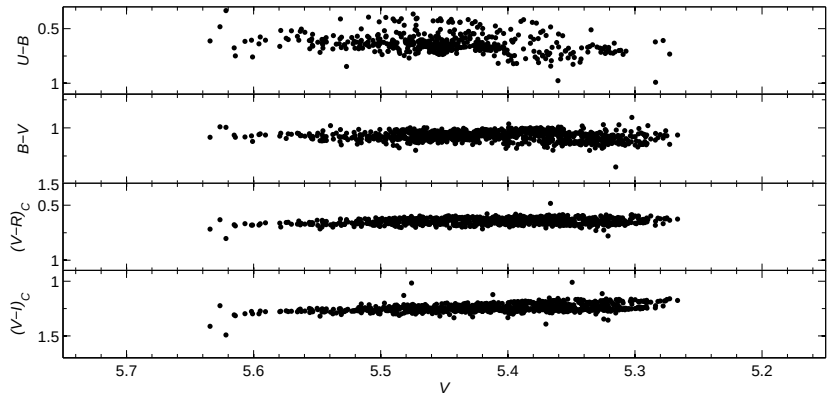

(a) Colour-magnitude diagram of HD 101379.

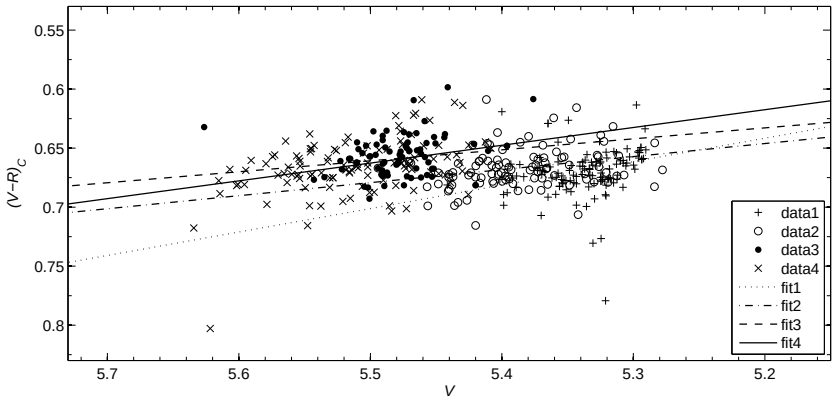

(b) Enlargement of figure (a), $(V-R)_C$ versus V of HD 101379 during each quarter of observation period.

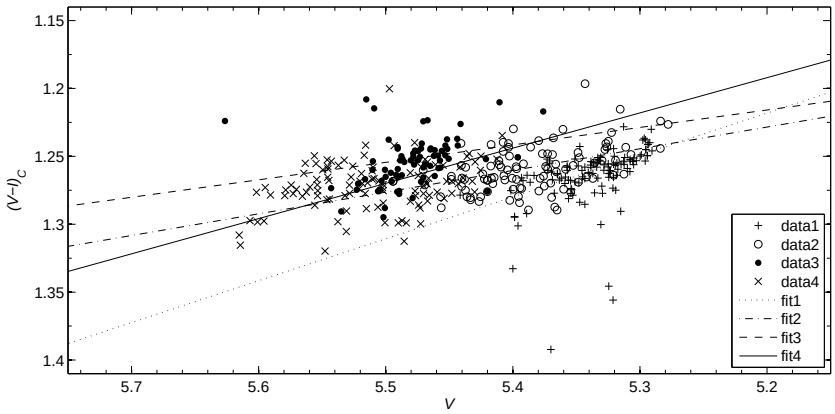

(c) Enlargement of figure (a), $(V-I)_C$ versus V of HD 101379 during each quarter of observation period.

Figure 7.8: The colour-magnitude diagram of HD 101379.

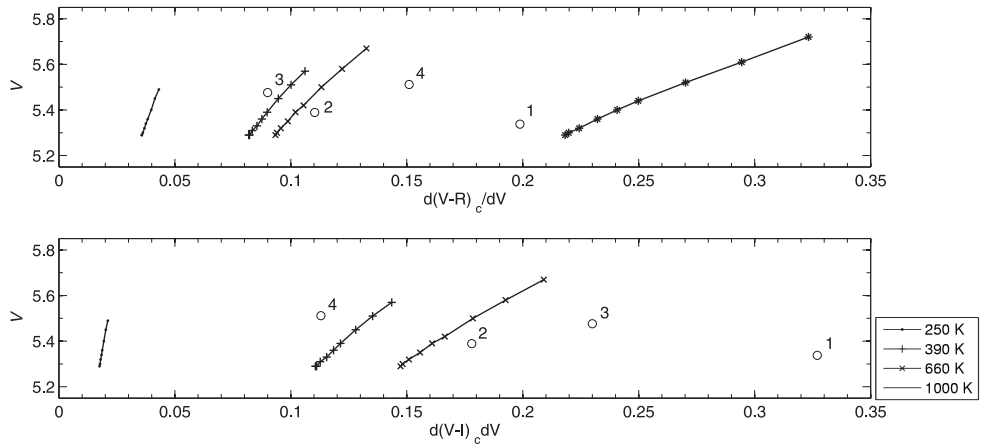

Figure 7.9: The variation in colour indices, $(V-R)_C$ and $(V-I)_C$ versus V magnitude when the star is spotted. The temperature differences, ΔT, are 250 K, 390 K, 660 K and 1000 K. The grid of spot area calculation, α, are 0.01, 0.02, 0.05, 0.10, 0.15, 0.30, 0.40 and 0.50. The $\mathrm{d}(V-I)_C/\mathrm{d}(V)$ for $\Delta T = 1000$ K is around 2.0 and is not plotted here. The open circles are slopes of linear fits to each quarter of observations.

of the data. This can be related to a young spot or a group of young spots that arose from the beginning of the observations.

7.4 The circularization and synchronization of the system

The test results on the orbital solutions of HD 101379 in table 7.6 page 146 indicate that the eccentricity of this system is measurable. The circularization and synchronization timescales of a system with an orbital period of 61.4370 days can be calculated (Zahn, 1977) as

$$\begin{aligned} T_{cir} &\approx 10^6 q^{-1} \left(\frac{1+q}{2}\right)^{5/3} P^{16/3} \\ &= 5.3 \times 10^{15} \text{ years} \qquad (7.3) \\ T_{syn} &\approx 10^4 \left(\frac{1+q}{2q}\right)^{2} P^{4} \\ &= 5.7 \times 10^{11} \text{ years.} \qquad (7.4) \end{aligned}$$

These timescales are very large compared to the age of the universe ($\sim 1.4 \times 10^{10}$

years). There is no doubt to conclude that any binary system with a period as long as HD 101379 is not tidally circularized.

However, the longitude of periastron, ω, and the eccentricity, e, calculated from each HERCULES data set are not certain. This cannot be used to conclude that these is apsidal motion from the tidal perturbation from the HD 101380 system, as the value for ω dramatically changed over a year. The period of apse-node perturbation from a third body is in the order of P_3^2/P_1 which is approximately 10^5 years for the tidal interaction between HD 101379 and HD 101380 systems.

The G star in HD 101379 is an active chromosphere star, and there is a detectable perturbation in the second and third harmonics of radial velocities, and hence the value of the HD 101379 eccentricity cannot be concluded from only the data analysed in this work. The rotational period of the G star, as analysed from the period of spot rotation, is always longer than the star's orbital period, $P_{\rm orb} = 61.4379$ d. This could be a result of the non-synchronized rotation of the star. Nevertheless, the star's chromosphere has a differential rotation. It is possible that the rotational period of the star at its equator is synchronized.

As was discussed by Komonjinda *et al.* (2007) in their analysis of the SB1 system ζ TrA (see also section 4.4.1 on page 64), spots on a stellar surface can deliver velocity perturbations which result in a fictitious eccentricity. The system HD 101379 may also have experienced the same effect from its spots. The program Binary Maker 3.0 was used to generate radial velocity curves for several different possible spot models related to the result in section 7.3.2. The result from these models are shown in table 7.7.

It is found that for a circular model with $\alpha = 0.2$, it is possible to achieve a spurious e of $0.013\,84 \pm 0.000\,33$ and ω of $269\overset{\circ}{.}8 \pm 1\overset{\circ}{.}1$ which is compatible with the observed eccentricity value of 0.0182 ± 0.0031 from the first data set. When there are two spots with the total area of 0.4, model 7, the spurious e can be as high as $0.031\,44 \pm 0.000\,67$ with ω of $68\overset{\circ}{.}72 \pm 0\overset{\circ}{.}96$. The values of e and ω are not only dependent on α but also on the spot positions and their distribution. From these results, it is possible that the system HD 101379 may already be circularized and that the eccentricity measured from all observed radial velocities may result from the starspots.

Table 7.7: Spurious eccentricities and longitude of periastron measured from synthetic radial velocities of a spotted G5III star. The models are generated using an assumption of a circular orbit. The spot temperature is 700 K cooler than the photosphere. The spot longitude is defined as zero from the line between the two stars and measured counterclockwise as seen from the upper pole.

Model	**Spot**	**latitude**	**longitude**	α	e	ω
1	1	18.°7 S	90.°0	0.01	$0.000\,017 \pm 0.000\,001$	$90.°2 \pm 1.°3$
2	1	2.°5 S	90.°0	0.10	$0.002\,11 \pm 0.000\,12$	$90.°3 \pm 2.°9$
3	1	15.°5 N	90.°0	0.20	$0.011\,82 \pm 0.000\,36$	$92.°1 \pm 1.°4$
4	1	15.°5 N	180.°0	0.20	$0.013\,84 \pm 0.000\,33$	$269.°8 \pm 1.°1$
5	1	15.°5 N	70.°0	0.20		
	2	15.°5 N	150.°0	0.20	$0.005\,05 \pm 0.000\,20$	$43.°09 \pm 2.°3$
6	1	2.°5 N	120.°0	0.10		
	2	33.°5 N	270.°0	0.30	$0.019\,27 \pm 0.000\,35$	$79.°97 \pm 0.°82$
7	1	15.°5 N	120.°0	0.20		
	2	15.°5 N	270.°0	0.20	$0.031\,44 \pm 0.000\,67$	$68.°72 \pm 0.°96$

CHAPTER 8

Summary of research

The radial velocities of 16 spectroscopic binary systems were observed using the HERCULES spectrograph. These radial velocities were analysed and the orbital solutions of these SB systems were presented in previous chapters. This chapter will summarize the results from this research following the aim of this study; on the precision of the orbital solutions and a comment on the possibility to detect a near-circular orbit of a system. The last section of this chapter is a recommendation for possible future research.

8.1 The precision of HERCULES velocities

The HERCULES spectrograph has been designed for the purpose of high precision radial velocity measurements of a celestial object. It is possible to achieve precision of less than 14 $\mathrm{m\,s^{-1}}$ for a star, i.e. Skuljan *et al.* (2004), or less than 4 $\mathrm{m\,s^{-1}}$ for the blue sky (Hearnshaw *et al.*, 2002). In this work, the radial velocities of 12 SB1s, 4 SB2s and 7 standard radial-velocity stars were measured.

During an observation, it has been found that there are many possible sources of measurement error that can affect the measured radial velocity. This is including the displacement of the stellar image on the fibre's entrance. As HERCULES is a fibre-fed spectrograph, light is fed along optical fibres from the telescope's f/13.5 Cassegrain focus. The field of view of the telescope is a lot larger than the diameter of a fibre. A spectrum that is obtained with a small misplacement of the stellar image on the fibre's entrance can result in a large measurement error in the radial velocity, as a result of an asymmetry in the absorption lines. For HERCULES, the exposure meter PMT was used for a fine-tuning of the star's position on the fibre's entrance. The seeing, and the mismatching between the driving rate of the telescope and the sky sidereal rate can cause a drift of the star's position on the fibre.

Apart from those problems, it has been found, as expected, that the precision of the radial velocities is dependent on the rotational velocity $v \sin i$ of a star. The precision of the best-fit orbital solution of SBs and the precision of standard stars' radial velocities are shown in table 8.1, as well as the measured $v \sin i$ from HERCULES spectra of each star.

Figure 8.1 is a plot of the relationship between precision of measured radial velocities from HERCULES and the rotational velocity. The open circles represent the data of standard radial-velocity stars and the closed circles represent the data of SBs. For an SB2, the data were plotted with the primary component's $v \sin i$.

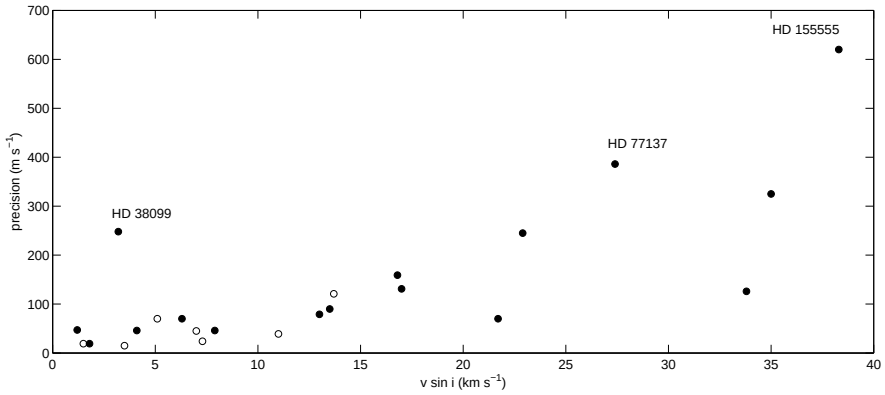

Figure 8.1: The plot of the precision of radial velocities measured from HERCULES versus the stars' $v \sin i$.

It is also shown in figure 8.1 that the precision of the radial velocities is also dependent on the activity level of a star. The systems HD 38099, HD 77137 and HD 155555 are active chromosphere stars. The measured radial velocities of these systems have higher rms scatters than the other stars.

The overall precisions of the best-fit orbital solution of SBs studied in this research are improved by 4–9 times for the S_{B^9} catalogue's grade 4 systems[1] and as much as 70 times for the S_{B^9} catalogue's grade 3 systems[2].

[1]Grade 4 orbit in the S_{B^9} catalogue is defined as a good orbit from its definitive orbital solution with some secular change in the orbital elements (Batten *et al.* 1989).

[2]Grade 3 orbit in the S_{B^9} catalogue is defined as an average orbit. The solution is believed to be reliable and unlikely to be much change from previous published value (Batten *et al.* 1989).

Table 8.1: Apparent magnitudes, spectral types, and measured $v \sin i$ of standard radial-velocity stars and spectroscopic binary systems observed in this research and the precision of their radial velocities from the HERCULES spectrograph.

HD	m_V	**Spectral type**	$v \sin i$ ($\mathrm{km\,s^{-1}}$)	**precision** ($\mathrm{m\,s^{-1}}$)
standard stars				
693	4.89	F5V	1.5 ± 0.5	19
11937	3.69	G5IV	7.0 ± 2.0	45
20794	4.26	G8V	3.5 ± 0.5	15
71701	4.34	K0III-IV	5.1 ± 1.0	70
109379	2.65	G5II	7.3 ± 0.3	24
114837	4.92	F7IV	11.0 ± 1.0	39
150798	1.92	K2II-III	13.7 ± 0.3	121
spectroscopic binaries				
352	6.08	K2III	22.9 ± 0.6	245
3405	6.78	G3V	17.0 ± 0.5	131
		G8V	18.0 ± 0.4	
9053	3.40	K5Ib	16.8 ± 0.5	159
22905	6.33	G8III	4.1 ± 0.4	46
30021	6.00	G8III	7.9 ± 0.5	46
38099	6.31	K4III	3.2 ± 0.5	248
50337	4.39	G5	13.0 ± 0.7	79
77137	6.87	G2	27.4 ± 1.3	386
		G2	28.2 ± 2.1	
77258	4.45	F8IV	1.8 ± 1.0	19
85622	4.57	G5	21.7 ± 1.3	70
101379	5.17	G2III	13.5 ± 0.8	80
124425	5.93	F6IV	33.8 ± 3.0	126
136905	7.31	K1III	35.0 ± 3.2	325
155555	6.67	G5IV	38.3 ± 3.9	620
		K0IV-V	41.8 ± 3.4	
194215	5.84	K3V	1.2 ± 1.0	47
197649	6.48	F6IV-V	6.3 ± 0.6	70
		G8V	23.1 ± 1.3	

8.2 The tests on the reality of small eccentricities

The aims of this research were to obtain precise radial velocities of SBs, analyse their orbits, and to find the possibility to detect a small eccentricity and test for its reality. It has been found that the first three aims of this research were successful, as was discussed in previous sections. The test on the reality of small eccentricities reported in chapter 5 and 6 was done and the results are discussed here.

In table 8.2 are orbital solutions of the SBs studied in this research, excluding HD 101379. Four systems; HD 22905, HD 38099, HD 85622 and HD 197649 have circular orbital solutions from the large errors in their measured eccentricities.

The statistical methods of Lucy and Sweeney (1971) and Lucy (2005) were applied to the eccentric orbital solutions to test for the reality of a small detectable eccentricity of a system. It was found that only the orbital solution of HD 194215 passes all the tests. Its eccentricity of $0.123\,29 \pm 0.000\,78$ is therefore acceptable.

The small eccentricity of the systems HD 77258 and HD 124425 failed the test of LS71 and they probably arise from measurement errors. There is little doubt for HD 124425, as this system is expected to be circularized from its short orbital period. The eccentricity of HD 77258 is too small to be acceptable, even though the fit has an rms as small as 19 $\mathrm{m\,s^{-1}}$ for its error bar.

Perturbations in the Keplerian third harmonic were detected in the other four systems, HD 352, HD 9053, HD 50337 and HD 136905. These results suggest that the systems' intrinsic variations may cause spurious eccentricities. It should be noted here that the system HD 352 is an ellipsoidal variable from its Hipparcos photometric data as well as HD 136905 (Fekel *et al.* 1985); Hipparcos photometric data of HD 9053 show a variation, as it has two groups of spots; and HD 50337 is an EA-type binary system from the eclipse of a hot component in an extended chromosphere of a cool component (Houk and Cowley, 1975).

One system, HD 30021, has no detectable Keplerian third harmonic and there is no evidence for any perturbation. The small eccentricity of this system may come from the perturbation in the other harmonic, as this system is a nonradially pulsating variable. It is also possible that the number of observations (56 observations) is not enough to confirm the nearly-circular orbit of this system.

Table 8.2: The orbital solutions of SBs studied in this research analysed from HERCULES data (not including HD 101379).

HD	P (day)	e	ω_1 (°)	K_1 (km s^{-1})	γ (km s^{-1})
352	96.414	0.0296	103.3	24.070	-0.53
	± 0.017	± 0.0020	± 4.5	± 0.054	± 0.16
3405	3.742 2560	0.001 91	209.5	83.922	-4.285
	± 0.000 0026	± 0.000 24	± 5.7	± 0.016	± 0.038
9053	194.056	0.0228	119.0	16.220	25.609
	± 0.037	± 0.0013	± 4.4	± 0.037	± 0.143
22905	91.6456	0	-	24.7973	-9.520
	± 0.0025	-	-	± 0.0097	± 0.021
30021	42.334 03	0.001 73	45	27.2938	39.442
	± 0.000 45	± 0.000 34	± 10	± 0.0079	± 0.052
38099	143.248	0	-	9.160	31.05
	± 0.098	-	-	± 0.051	± 0.16
50337	195.295	0.004 36	86.6	24.323	26.370
	± 0.019	± 0.000 51	± 6.5	± 0.013	± 0.054
77137	3.198 6024	0.003 01	164.3	96.582	61.25
	± 0.000 0038	± 0.000 51	± 8.6	± 0.051	± 0.26
77258	74.137 15	0.000 85	106	19.6744	-5.013
	± 0.000 73	± 0.000 19	± 13	± 0.0041	± 0.042
85622	329.266	0	-	13.021	11.495
	± 0.085	-	-	± 0.012	± 0.034
124425	2.697 0329	0.002 60	294	26.094	18.684
	± 0.000 0050	± 0.000 99	± 26	± 0.023	± 0.054
136905	11.134 14	0.0079	23	39.029	61.78
	± 0.000 30	± 0.0026	± 24	± 0.078	± 0.14
155555	1.681 649	0.003 89	12	86.322	2.04
	± 0.000 0013	± 0.000 61	± 10	± 0.059	± 0.21
194215	374.88	0.123 29	258.14	14.1155	-8.134
	± 0.18	± 0.000 78	± 0.77	± 0.0056	± 0.14
197649	18.044 527	0	-	45.0837	-14.8255
	± 0.000 038	-	-	± 0.0070	± 0.0070

Three SB2 systems; HD 3405, HD 77137 and HD 155555 have a short orbital period ($\sim 1-4$ days). The eccentricity of all three systems was rejected with a detectable second

harmonic perturbation. These systems are active chromosphere stars. Chromospheric emission of HD 77137 was reported by many authors, as discussed in section 6.4 page 124. The Doppler image of HD 155555 was analysed by Hatzes and Kürster (1999), and Strassmeier and Rice (2000). They found that both components were spotted. This is evidence that spots can cause a spurious eccentricity in SBs, as was discussed in the case of HD 101379 (section 7.4, page 155).

At this stage, the circular orbits of fourteen systems should be adopted. These solutions are shown here in tables 8.3 and 8.4.

Even though most of the SBs studied in this research have longer periods than the cutoff period of their spectral types, it is possible that the systems are already circularized. At a period higher than the $P_{\rm cutoff}$, all eccentricities have the same probability of occurring (Abt, 2006 and 2007). The secondary mass, and the primordial eccentricity also have an effect on the tidal circularization timescale. The circularization timescale depends on the mass ratio (Zahn, 1977 and Mazeh, 2008). Mazeh (2008) showed that a binary with an initial eccentricity of 0.2 will take half the time needed by a system with an initial eccentricity of 0.75 to get to an eccentricity of 0.05.

8.3 Future work

The improvement in the precision of SB orbital solutions derived from HERCULES spectra is satisfied. Apart from that, there is an opportunity for future work continuing from the work conducted in this research.

The proximity effect, the Rossiter effect, mass transfer, and also chromospheric activity of a star are examples of the possible phenomena that effect the measured radial velocity of a star. The difference of the measured radial velocity from the centre-of-mass radial velocity can be very small, nevertheless it results in the spurious eccentricity of a system's orbit.

By using only the cross-correlation technique applied to stellar spectra, it may not be possible to measured the centre-of-mass radial velocity of a star. The shape of an absorption line should be considered. Any asymmetry in line shape can give information on the distribution of flux on the stellar disk, as well as the convective motion on the

Table 8.3: Adopted circular orbits of SB1s studied in this research as a result from the tests of LS71 and L05 (not including HD 101379).

HD	P	K	γ	T_0	σ
	(day)	($\mathrm{km\,s^{-1}}$)	($\mathrm{km\,s^{-1}}$)	(HJD 2450000+)	($\mathrm{m\,s^{-1}}$)
352	96.454	23.794	-0.48	3650.189	549
	± 0.039	± 0.094	± 0.22	± 0.081	
9053	193.918	16.099	25.65	3477.42	291
	± 0.065	± 0.048	± 0.16	± 0.12	
22905	91.6456	24.7973	-9.520	3605.5125	46
	± 0.0025	± 0.0097	± 0.021	± 0.0043	
30021	42.335 07	27.284	39.445	3303.2834	60
	± 0.000 57	± 0.010	± 0.053	± 0.0057	
38099	143.248	9.160	31.05	3481.04	248
	± 0.098	± 0.051	± 0.16	± 0.19	
50337	195.298	24.341	26.365	3609.850	111
	± 0.026	± 0.017	± 0.058	± 0.023	
77258	74.137 60	19.6685	-5.021	3625.5154	21
	± 0.000 78	± 0.0037	± 0.048	± 0.0018	
85622	329.266	13.021	11.495	3860.281	61
	± 0.085	± 0.012	± 0.034	± 0.074	
124425	2.697 0329	26.089	18.682	3800.308 14	127
	± 0.000 0052	± 0.023	± 0.062	± 0.000 47	
136905	11.134 13	38.989	61.72	3599.1715	385
	± 0.000 29	± 0.082	± 0.13	± 0.0067	

stellar surface and the emission of the stellar chromosphere. The technique of line bisectors may applied to each absorption line. The time variation in line bisectors can give out some information on the star's atmospheric activities.

The photometric variation of systems can also give more information. In this research, photometric observations were undertaken at MJUO only to confirm the light variation and its type during the observation period, as well as at previous times using

Table 8.4: Adopted circular orbits of SB2s studied in this research as a result from the tests of LS71 and L05.

HD	P	K_1	K_2	γ	T_0	σ
	(day)	($\mathrm{km\,s^{-1}}$)	($\mathrm{km\,s^{-1}}$)	($\mathrm{km\,s^{-1}}$)	(HJD 2450000+)	($\mathrm{m\,s^{-1}}$)
3405	3.742 2600	83.894	88.527	-4.285	3769.397	137
	± 0.000 0027	± 0.016	± 0.017	± 0.038	± 0.000 15	
77137	3.198 5974	96.582	96.722	61.25	3700.160 34	469
	± 0.000 0044	± 0.060	± 0.062	± 0.26	± 0.000 35	
155555	1.681 6400	86.392	92.081	2.04	3518.147 54	670
	± 0.000 0013	± 0.063	± 0.067	± 0.21	± 0.000 27	
197649	18.044 527	45.0837	57.6587	-14.8255	3871.063 56	70
	± 0.000 038	± 0.0070	± 0.0087	± 0.013	± 0.000 54	

observations from the Hipparcos Satellite. In order to study the activity of a system, a specific programme to observe these systems photometrically may need to be established.

In order to study the activity of an active chromosphere star, other techniques may also be needed. In this research, the spot activity of GT Muscae's G star was studied by the inverse modelling technique to make a possible model of a spotted area on the star's surface. More observations of Balmer lines and Ca II H & K lines as well as Doppler imaging of the system may also be needed in order to map the spot position and size on the star's photosphere, and its temperature.

To improve the theory on the circularization and synchronization timescales, a larger number of SBs need to be studied. The timescales, as was discussed, are dependent on the initial eccentricity, and the mass ratio. For an SB1, only the value of the mass function can be quantified. The study also has a limitation because of the difficulty of the age determination, especially if the studied system is an isolated binary. For a system in a cluster, the reddening and the intrinsic uncertainties of the stellar models can still cause some uncertainty in the age determination (Claret, 2005).

APPENDIX A

Fourier expansion of a Keplerian velocity

The Keplerian velocity of a binary system can written in the form,

$$V_{\rm rad} = K[\cos(\upsilon + \omega) + e\cos\omega] + \gamma. \tag{A.1}$$

This term can be expanded as

$$V_{\rm rad} = K\left[(1-e^2)\cos\omega\sum_{j=1}^{\infty} c_j \cos jL - \sqrt{(1-e^2)}\sin\omega\sum_{j=1}^{\infty} s_j \sin jL\right] + \gamma, \tag{A.2}$$

where $M = 2\pi(t-T)/P$ and the coefficients c_j and s_j are functions of a Bessel's function of order j;

$$c_j = 2e^{-1}J_j(je) \quad ; \tag{A.3}$$

$$s_j = 2\frac{dJ_j(je)}{d(je)}. \tag{A.4}$$

The Bessel's function of order j is

$$J_j(x) = \frac{x^j}{2^j j!}\left[1 - \frac{x^2}{2(2j+2)} + \frac{x^4}{2\times 4(2j+2)(2j+4)} - ...\right]. \tag{A.5}$$

Hence, the coefficients c_j and s_j can be expressed (to e^7) as

$$\begin{aligned}
c_1 &= 1 - \frac{1}{8}e^2 + \frac{1}{192}e^4 - \frac{1}{9216}e^6 & \qquad s_1 &= 1 - \frac{3}{8}e^2 + \frac{5}{192}e^4 - \frac{7}{9216}e^6 \\
c_2 &= e\left[1 - \frac{1}{3}e^2 + \frac{1}{24}e^4 - \frac{1}{360}e^6\right] & \qquad s_2 &= e\left[1 - \frac{2}{3}e^2 + \frac{1}{8}e^4 - \frac{1}{90}e^6\right] \\
c_3 &= \frac{9}{8}e^2\left[1 - \frac{9}{16}e^2 + \frac{81}{640}e^4\right] & \qquad s_3 &= \frac{9}{8}e^2\left[1 - \frac{15}{16}e^2 + \frac{189}{640}e^4\right]
\end{aligned} \tag{A.6}$$

In term of Fourier series, this function can be expanded as

$$V = \frac{1}{2}C_0 + \sum_{j=1}^{\infty}[C_j \cos jL + S_j \sin jL], \tag{A.7}$$

where $L = 2\pi(t-T)/P + \omega = \Phi + \omega$ is the mean longitude. Comparing with equation A.2, the Fourier coefficients, C_j and S_j can be written in terms of c_j and s_j as

$$C_j = \alpha c_j \cos j\omega + \beta s_j \sin j\omega \qquad S_j = \alpha c_j \cos j\omega - \beta s_j \sin j\omega \tag{A.8}$$

where $\alpha = K(1-e^2)\cos\omega$ and $\beta = K\sqrt{1-e^2}\sin\omega$.

This gives the first three terms of the coefficients to be estimated as

$$\begin{aligned} C_0 &= 2\gamma \\ C_1 &= K \qquad & S_1 &= 0 \\ C_2 &= Ke\cos\omega \qquad & S_2 &= Ke\sin\omega \\ C_3 &= \frac{9}{8}Ke^2\cos 2\omega \qquad & S_3 &= \frac{9}{8}Ke^2\sin 2\omega. \end{aligned} \tag{A.9}$$

APPENDIX B

Radial velocities of single-lined spectroscopic binaries

B.1 HD 352

Table B.1: Radial velocities of HD 352 relative to the image number 3692 014.

HJD (2400000+)	$V_{\rm rad}$ ($\rm km\,s^{-1}$)	**HJD** (2400000+)	$V_{\rm rad}$ ($\rm km\,s^{-1}$)	**HJD** (2400000+)	$V_{\rm rad}$ ($\rm km\,s^{-1}$)
53252.1015	−38.432	53667.0703	−31.777	53720.9179	−17.930
53300.9648	−4.580	53668.0195	−30.456	53720.9257	−17.981
53608.0859	1.064	53668.0273	−30.449	53743.8945	−44.175
53608.0898	1.060	53668.0351	−30.424	53888.2031	1.806
53635.0664	−35.224	53668.0468	−30.444	53888.2109	1.801
53635.0820	−35.242	53688.8671	−2.284	53891.2695	2.408
53662.9804	−36.814	53688.8789	−2.263	53891.2773	2.438
53662.9921	−36.799	53688.8906	−2.263	53891.2890	2.430
53663.0000	−36.788	53688.9062	−2.264	53894.2304	2.253
53663.0117	−36.774	53689.8632	−1.499	53894.2382	2.247
53663.0195	−36.761	53689.8828	−1.494	53894.2421	2.218
53666.0351	−33.153	53689.9023	−1.469	53895.2304	2.025
53666.0468	−33.142	53691.8867	−0.009	53895.2421	2.019
53666.0585	−33.123	53691.8945	−0.016	53895.2500	2.027
53667.0312	−31.858	53691.9023	−0.012	53895.2578	2.029
53667.0429	−31.842	53691.9101	0.000	53929.1406	−40.234
53667.0507	−31.811	53720.8945	−17.882	53929.1523	−40.254
53667.0625	−31.827	53720.9062	−17.899	53929.1640	−40.254

Continued on next page

Table B.1 – continued from previous page

HJD (2400000+)	$V_{\rm rad}$ ($\rm km\,s^{-1}$)	**HJD** (2400000+)	$V_{\rm rad}$ ($\rm km\,s^{-1}$)	**HJD** (2400000+)	$V_{\rm rad}$ ($\rm km\,s^{-1}$)
54000.0312	−3.307	54012.9843	−23.069	54014.9687	−26.466
54000.0468	−3.338	54013.9414	−24.684	54014.9765	−26.448
54001.0468	−4.372	54013.9492	−24.697	54015.9218	−28.062
54001.0585	−4.385	54013.9609	−24.749	54015.9375	−28.058
54012.9687	−23.024	54014.9609	−26.431		

B.2 HD 9053

Table B.2: Radial velocities of HD 352 relative to the image number 3668 029.

HJD (2400000+)	$V_{\rm rad}$ ($\rm km\,s^{-1}$)	**HJD** (2400000+)	$V_{\rm rad}$ ($\rm km\,s^{-1}$)	**HJD** (2400000+)	$V_{\rm rad}$ ($\rm km\,s^{-1}$)
53254.1093	−6.542	53608.1367	−22.846	53642.1093	−6.381
53254.1132	−6.544	53636.2109	−8.869	53642.1132	−6.370
53254.1132	−6.547	53636.2187	−8.862	53659.0898	−1.109
53301.0117	−1.870	53636.2226	−8.867	53659.0898	−1.103
53303.9921	−2.741	53636.2265	−8.859	53660.1015	−0.976
53320.9453	−9.772	53637.1796	−8.375	53660.1015	−0.973
53321.8828	−10.211	53637.1835	−8.379	53660.8984	−0.821
53322.9179	−11.366	53638.0625	−7.985	53660.9531	−0.776
53331.9804	−15.809	53638.0703	−7.983	53666.9531	−0.143
53401.9062	−27.795	53638.0703	−7.978	53666.9531	−0.152
53402.8867	−27.607	53640.0664	−7.225	53666.9570	−0.145
53404.8828	−26.848	53640.0703	−7.225	53666.9609	−0.151
53405.8789	−26.279	53640.0742	−7.227	53667.9453	−0.002
53608.1289	−22.840	53640.0781	−7.232	53667.9453	0.000
53608.1289	−22.840	53642.1054	−6.390	53667.9492	−0.009
53608.1328	−22.837	53642.1054	−6.387	53667.9492	−0.003

Continued on next page

Table B.2 – continued from previous page

HJD (2400000+)	$V_{\rm rad}$ ($\rm km\,s^{-1}$)	**HJD** (2400000+)	$V_{\rm rad}$ ($\rm km\,s^{-1}$)	**HJD** (2400000+)	$V_{\rm rad}$ ($\rm km\,s^{-1}$)
53688.9570	−1.846	53861.2539	−0.169	53928.0429	−23.286
53688.9570	−1.846	53861.2539	−0.163	53928.0546	−23.312
53688.9609	−1.842	53861.2578	−0.173	53928.0664	−23.297
53688.9648	−1.843	53888.2421	−3.824	53928.0742	−23.308
53689.9843	−2.198	53888.2421	−3.818	53928.0898	−23.308
53691.9453	−2.870	53888.2460	−3.806	53929.2109	−23.986
53691.9492	−2.874	53888.2500	−3.853	53929.2148	−23.995
53691.9531	−2.869	53888.2539	−3.725	53929.2187	−23.996
53691.9531	−2.877	53888.2539	−3.671	53929.2226	−23.993
53720.9921	−16.690	53891.2421	−4.738	53929.2226	−24.001
53720.9960	−16.689	53891.2460	−4.736	54000.0664	−20.892
53721.9296	−17.151	53891.2500	−4.740	54000.0742	−20.927
53721.9335	−17.138	53891.2539	−4.672	54000.0781	−20.979
53721.9375	−17.133	53891.2578	−4.875	54000.0859	−20.824
53721.9414	−17.149	53891.2578	−4.800	54000.9609	−20.520
53742.9765	−26.825	53894.1796	−5.765	54000.9648	−20.507
53742.9843	−26.838	53894.1835	−5.777	54000.9687	−20.428
53742.9921	−26.832	53894.1835	−5.775	54013.0390	−14.616
53860.2500	−0.155	53895.1484	−6.248	54013.0429	−14.615
53860.2500	−0.158	53895.1484	−6.251	54013.0468	−14.614
53860.2539	−0.154	53895.1523	−6.248	54015.0429	−13.627
53860.2578	−0.147	53895.1562	−6.254	54015.0468	−13.636
53860.2617	−0.154	53895.1601	−6.254	54015.0468	−13.661
53861.2460	−0.174	53895.1601	−6.249	54015.0507	−13.647
53861.2500	−0.174	53894.1875	−5.781	54016.0000	−13.145
53861.2500	−0.170	53895.1601	−6.119	54016.0039	−13.118

B.3 HD 22905

Table B.3: Radial velocities of HD 22905 relative to the image number 3689 056.

HJD (2400000+)	$V_{\rm rad}$ ($\rm km\,s^{-1}$)	**HJD** (2400000+)	$V_{\rm rad}$ ($\rm km\,s^{-1}$)	**HJD** (2400000+)	$V_{\rm rad}$ ($\rm km\,s^{-1}$)
53254.1406	−8.678	53640.0976	−38.851	53720.9492	−22.613
53254.1484	−8.685	53640.1093	−38.859	53720.9570	−22.62
53301.1289	−31.836	53642.1445	−41.056	53720.9648	−22.631
53303.9804	−27.278	53642.1562	−41.037	553722.0156	−24.388
53304.9531	−25.653	53642.1601	−41.058	53722.0273	−24.411
53322.9648	0.423	53642.1679	−41.078	53722.9882	−26.003
53377.0000	−45.859	53659.1054	−42.471	53723.0000	−26.008
53401.9687	−16.647	53659.1132	−42.456	53743.9218	−45.926
53402.9531	−15.047	53660.1171	−41.536	53743.9414	−45.928
53403.9140	−13.756	53660.1328	−41.541	53778.8867	−2.111
53404.9101	−11.848	53661.0546	−40.596	53778.8984	−2.085
53405.9453	−10.261	53661.0742	−40.572	53778.9062	−2.083
53423.8593	3.553	53667.1757	−32.601	53835.7968	−45.839
53608.2343	3.248	53667.1835	−32.589	54001.1367	−31.196
53608.2421	3.255	53667.1914	−32.580	54001.1484	−31.206
53634.2265	−30.658	53668.1914	−31.050	54013.1289	−44.628
53634.2343	−30.684	53668.1992	−31.029	54013.1406	−44.613
53636.1445	−33.618	53689.0585	−0.016	54014.1445	−45.090
53636.1562	−33.634	53689.0664	0.000	54014.1523	−45.108
53637.1132	−35.007	53692.0625	2.244	54015.1835	−45.531
53637.1484	−35.059	53692.0664	2.243	54016.1640	−45.732
53639.1601	−37.800	53692.0742	2.235		
53639.1757	−37.847	53720.9414	−22.597		

B.4 HD 30021

Table B.4: Radial velocities of HD 30021 relative to the image number 3692 014.

HJD (2400000+)	$V_{\rm rad}$ ($\rm km\,s^{-1}$)	**HJD** (2400000+)	$V_{\rm rad}$ ($\rm km\,s^{-1}$)	**HJD** (2400000+)	$V_{\rm rad}$ ($\rm km\,s^{-1}$)
53301.1679	43.627	53456.8593	−1.229	53721.0156	36.065
53304.1289	44.834	53608.2656	25.508	53721.0273	36.119
53301.1679	43.627	53639.1875	42.647	53721.0390	36.161
53304.9765	44.185	53642.1757	45.085	53722.0742	39.020
53321.0664	−6.217	53642.1835	45.078	53723.0078	41.177
53322.0820	−7.881	53642.1914	45.096	53740.9531	3.309
53323.0742	−9.004	53663.1093	−9.564	53740.9648	3.276
53332.0664	6.048	53663.1210	−9.557	53741.9687	0.000
53336.9804	25.317	53667.1132	−4.879	53741.9765	−0.036
53339.0156	32.844	53667.1250	−4.852	53861.7656	27.443
53376.9492	16.184	53667.1367	−4.828	53861.7773	27.422
53402.0078	4.323	53668.1562	−2.258	54001.1601	−9.379
53402.9960	0.967	53668.1679	−2.218	54001.1718	−9.452
53404.9687	−4.536	53668.1796	−2.189	54013.1523	20.643
53405.9921	−6.708	53689.1015	38.365	54013.1640	20.702
53423.8828	33.537	53689.1132	38.339	54014.1015	24.567
53451.8359	−9.552	53692.0859	28.732	54014.1132	24.604
53451.8437	−9.542	53692.0976	28.688	54015.1718	28.680
53456.8515	−1.230	53692.1054	28.649		

B.5 HD 38099

Table B.5: Radial velocities of HD 38099 relative to the image number 3689 071.

HJD (2400000+)	$V_{\rm rad}$ ($\rm km\,s^{-1}$)	**HJD** (2400000+)	$V_{\rm rad}$ ($\rm km\,s^{-1}$)	**HJD** (2400000+)	$V_{\rm rad}$ ($\rm km\,s^{-1}$)
53301.1875	8.313	53663.1640	7.763	53743.9804	13.529
53322.1406	15.768	53666.1757	6.762	53778.9257	17.259
53323.0390	16.030	53666.1835	6.753	53778.9335	17.290
53377.0156	7.910	53666.1953	6.754	53778.9453	17.266
53401.9882	0.555	53668.0976	5.844	53778.9570	17.248
53402.9804	0.415	53668.1054	5.835	53835.8242	0.225
53404.9335	0.103	53668.1171	5.825	53835.8320	0.233
53405.9765	0.209	53689.1210	0.002	53835.8398	0.228
53423.8945	2.092	53689.1289	0.000	53860.7656	3.887
53451.8710	12.162	53689.1367	−0.003	53860.7734	3.879
53451.8789	12.175	53692.1171	−0.233	53860.7812	3.873
53456.8710	14.129	53692.1250	−0.237	53861.7851	4.186
53466.8281	16.747	53692.1328	−0.246	53861.7929	4.178
53487.7812	17.773	53721.0820	4.641	54001.1875	2.688
53487.7890	17.771	53721.0898	4.634	54001.1953	2.713
53487.8007	17.769	53740.9804	12.456	54015.2148	8.014
53487.8085	17.763	53740.9882	12.460	54016.2070	8.375
53642.2226	15.221	53741.0000	12.467		
53663.1484	7.777	53741.0117	12.483		

B.6 HD 50337

Table B.6: Radial velocities of HD 50337 relative to the image number 3741 037.

HJD (2400000+)	$V_{\rm rad}$ ($\rm km\,s^{-1}$)	**HJD** (2400000+)	$V_{\rm rad}$ ($\rm km\,s^{-1}$)	**HJD** (2400000+)	$V_{\rm rad}$ ($\rm km\,s^{-1}$)
53304.0273	−11.001	53487.8945	−5.963	53742.0898	0.652
53322.1562	−12.731	53637.2148	26.807	53744.0664	2.096
53323.1054	−12.525	53640.1445	24.992	53744.0742	2.099
53324.0390	−12.445	53659.1875	10.856	53744.0781	2.095
53377.0742	20.126	53659.1914	10.857	53776.8984	26.000
53402.0703	33.789	53666.0976	5.551	53776.9023	26.000
53403.0625	34.035	53666.1093	5.543	53776.9101	25.959
53403.9531	34.020	53666.1210	5.525	53776.9179	25.969
53405.0390	34.519	53666.1367	5.530	53779.1250	27.319
53406.0820	34.819	53666.1406	5.511	53779.1289	27.308
53424.0078	34.678	53666.1484	5.511	53779.1328	27.313
53424.9062	34.441	53689.1484	−8.968	53779.1367	27.299
53425.0390	34.442	53689.1523	−8.976	53836.8164	24.076
53427.8867	33.578	53689.1562	−8.973	53836.8203	24.074
53451.9531	20.061	53689.1640	−8.970	53836.9960	23.947
53451.9570	20.057	53721.1054	−10.692	53837.0039	23.944
53451.9648	20.069	53721.1093	−10.688	53860.8906	5.881
53464.9101	10.079	53721.1132	−10.678	53860.8945	5.869
53465.8437	9.376	53721.9609	−10.412	53860.8984	5.872
53466.8554	8.576	53721.9648	−10.417	53860.9023	5.865
53486.8398	−5.459	53721.9687	−10.409	53860.9062	5.864
53486.8398	−5.470	53741.1328	−0.037	53860.9101	5.865
53486.8437	−5.465	53741.1367	−0.013	53861.9179	5.131
53486.8476	−5.455	53741.1406	0.000	53861.9218	5.119
53487.8789	−5.955	53742.0742	0.644	53861.9257	5.112
53487.8828	−5.955	53742.0781	0.652	53861.9257	5.123
53487.8906	−5.948	53742.0820	0.664	53861.9296	5.112

Continued on next page

Table B.6 – continued from previous page

HJD (2400000+)	$V_{\rm rad}$ ($\rm km\,s^{-1}$)	**HJD** (2400000+)	$V_{\rm rad}$ ($\rm km\,s^{-1}$)	**HJD** (2400000+)	$V_{\rm rad}$ ($\rm km\,s^{-1}$)
53861.9335	5.112	53893.7500	−12.072	54013.1015	33.685
53891.7500	−11.624	53893.7578	−12.074	54013.1054	33.671
53891.7539	−11.625	53893.7617	−12.084	54013.1132	33.678
53891.7578	−11.633	53893.7695	−12.086	54016.0507	32.636
53891.7578	−11.634	54001.2109	35.750	54016.0585	32.639
53891.7656	−11.638	54001.2148	35.744		
53891.7656	−11.644	54001.2226	35.739		

B.7 HD 77258

Table B.7: Radial velocities of HD 77258 relative to the image number 3741 044.

HJD (2400000+)	$V_{\rm rad}$ ($\rm km\,s^{-1}$)	**HJD** (2400000+)	$V_{\rm rad}$ ($\rm km\,s^{-1}$)	**HJD** (2400000+)	$V_{\rm rad}$ ($\rm km\,s^{-1}$)
53323.1328	35.627	53453.0742	9.326	53488.8359	29.199
53377.0820	6.599	53456.8085	15.153	53488.8398	29.202
53402.0781	37.863	53456.8125	15.151	53490.8632	26.250
53403.0703	37.915	53456.8164	15.183	53490.8671	26.241
53403.9609	37.615	53456.8203	15.180	53490.8710	26.238
53404.0234	37.691	53464.9531	28.236	53490.8750	26.231
53405.0429	37.637	53465.8750	29.512	53490.8789	26.223
53406.0898	37.304	53466.8710	30.847	53666.1562	−0.491
53424.9179	12.859	53486.8515	31.786	53666.1601	−0.484
53425.0312	12.695	53486.8554	31.782	53666.1640	−0.478
53451.9726	7.615	53486.8593	31.777	53689.1718	30.698
53451.9765	7.625	53486.8632	31.770	53689.1757	30.705
53452.9960	9.111	53488.8320	29.220	53721.1210	13.401
53453.0078	9.138	53488.8320	29.203	53721.1250	13.380

Continued on next page

Table B.7 – continued from previous page

HJD (2400000+)	$V_{\rm rad}$ ($\rm km\,s^{-1}$)	**HJD** (2400000+)	$V_{\rm rad}$ ($\rm km\,s^{-1}$)	**HJD** (2400000+)	$V_{\rm rad}$ ($\rm km\,s^{-1}$)
53741.1484	0.002	53835.9335	28.593	53885.8906	−1.333
53741.1523	−0.014	53835.9375	28.602	53885.9023	−1.354
53741.1562	0.000	53835.9414	28.611	53887.8242	−0.842
53742.0976	0.623	53835.9453	28.608	53887.8281	−0.838
53742.1015	0.624	53858.9179	30.040	53887.8320	−0.838
53742.1054	0.631	53858.9218	30.032	53887.8359	−0.838
53743.0507	1.379	53858.9296	30.028	53890.9257	1.042
53743.0585	1.379	53858.9335	30.032	53890.9335	1.059
53744.0859	2.350	53858.9375	30.029	53890.9375	1.050
53744.0898	2.347	53860.9375	27.166	53891.8789	1.864
53778.0976	36.220	53860.9375	27.156	53891.8828	1.890
53778.1015	36.197	53860.9414	27.141	53891.8867	1.899
53778.1093	36.201	53860.9453	27.142	53891.8906	1.909
53779.1445	35.600	53861.9375	25.635	53893.8125	3.864
53779.1484	35.609	53861.9414	25.637	53893.8125	3.873
53779.1523	35.626	53861.9453	25.628	53893.8203	3.872
53829.9492	19.223	53861.9492	25.622	53893.8203	3.876
53829.9531	19.233	53861.9531	25.622	53929.8046	33.769
53829.9570	19.232	53861.9531	25.615	53929.8125	33.866
53829.9609	19.243	53885.8828	−1.333		

B.8 HD 85622

Table B.8: Radial velocities of HD 85622 relative to the image number 3741 051.

HJD (2400000+)	$V_{\rm rad}$ ($\rm km\,s^{-1}$)	**HJD** (2400000+)	$V_{\rm rad}$ ($\rm km\,s^{-1}$)	**HJD** (2400000+)	$V_{\rm rad}$ ($\rm km\,s^{-1}$)
53323.1523	−20.257	53490.9101	−2.112	53860.9609	1.512
53377.0898	−24.424	53490.9140	−2.119	53860.9648	1.493
53402.0859	−21.613	53490.9179	−2.090	53860.9687	1.493
53403.0781	−21.518	53490.9257	−2.098	53860.9726	1.497
53403.9687	−21.634	53692.1718	−24.592	53861.9804	1.484
53404.0351	−24.270	53692.1718	−24.592	53861.9843	1.500
53405.0507	−21.159	53741.1640	−19.888	53861.9882	1.498
53406.0976	−21.044	53741.1679	−19.882	53861.9882	1.502
53424.9375	−17.486	53741.1718	−19.875	53885.9101	−0.122
53425.0507	−17.526	53742.1132	−19.763	53885.9179	−0.135
53451.9843	−10.755	53742.1210	−19.770	53885.9218	−0.128
53451.9921	−10.747	53742.1289	−19.760	53885.9257	−0.123
53451.9960	−10.738	53744.0976	−19.312	53887.8437	−0.188
53456.9765	−9.511	53744.1054	−19.319	53887.8476	−0.201
53456.9804	−9.512	53778.1132	−12.055	53887.8515	−0.214
53456.9843	−9.500	53778.1210	−12.061	53887.8554	−0.222
53456.9882	−9.511	53778.1289	−11.999	53890.9687	−0.736
53465.9062	−7.308	53835.9726	0.000	53890.9765	−0.741
53466.9140	−7.111	53835.9804	0.008	53890.9843	−0.737
53486.8945	−2.785	53835.9843	0.006	53891.8945	−0.787
53486.8984	−2.783	53835.9882	0.001	53891.9023	−0.801
53486.9023	−2.783	53835.9960	−0.004	53891.9062	−0.807
53486.9023	−2.785	53858.9765	1.585	53893.8437	−1.116
53488.8476	−2.498	53858.9843	1.591	53893.8515	−1.124
53488.8515	−2.493	53858.9882	1.591	53893.8554	−1.139
53488.8554	−2.490	53860.9531	1.497	53893.8554	−1.127
53488.8593	−2.506	53860.9570	1.516	53894.8007	−1.250

Continued on next page

Table B.8 – continued from previous page

HJD (2400000+)	$V_{\rm rad}$ ($\rm km\,s^{-1}$)	**HJD** (2400000+)	$V_{\rm rad}$ ($\rm km\,s^{-1}$)	**HJD** (2400000+)	$V_{\rm rad}$ ($\rm km\,s^{-1}$)
53894.8046	−1.243	53894.8125	−1.230	53929.8242	−8.277
53894.8085	−1.234	53928.8359	−8.079		

B.9 HD 124425

Table B.9: Radial velocities of HD 124425 relative to the image number 3405 112.

HJD (2400000+)	$V_{\rm rad}$ ($\rm km\,s^{-1}$)	**HJD** (2400000+)	$V_{\rm rad}$ ($\rm km\,s^{-1}$)	**HJD** (2400000+)	$V_{\rm rad}$ ($\rm km\,s^{-1}$)
53402.1640	7.174	53487.0234	40.302	53861.9648	42.839
53404.1679	44.936	53488.9726	1.966	53862.0859	48.013
53405.1640	0.053	53488.9804	2.169	53862.0976	48.259
53405.1757	0.000	53488.9921	2.576	53886.0039	29.925
53406.1718	42.776	53490.9609	17.779	53886.0117	30.520
53452.0468	44.058	53490.9726	17.187	53887.9375	0.072
53452.0625	44.730	53490.9882	16.359	53887.9492	0.103
53453.1171	22.795	53778.1835	32.932	53887.9570	0.016
53453.1328	21.890	53836.1601	19.109	53890.9531	5.842
53456.0937	7.922	53837.0898	8.994	53891.9140	51.517
53456.1054	7.464	53837.1054	9.734	53892.0195	52.208
53456.1132	7.077	53859.0742	32.515	53893.8359	14.350
53457.0585	22.815	53859.0859	33.257	53893.9062	18.418
53457.0664	23.287	53860.0156	42.659	53894.0234	25.747
53465.0546	17.497	53860.0234	42.385	53894.0351	26.312
53466.0195	50.710	53860.9179	0.289	53894.0429	26.808
53467.0429	2.357	53860.9257	0.187	53894.7890	51.807
53487.0039	39.207	53861.0312	0.083	53894.8476	50.718
53487.0156	39.737	53861.0390	0.036	53894.8593	50.569

Continued on next page

Table B.9 – continued from previous page

HJD (2400000+)	$V_{\rm rad}$ ($\rm km\,s^{-1}$)	**HJD** (2400000+)	$V_{\rm rad}$ ($\rm km\,s^{-1}$)	**HJD** (2400000+)	$V_{\rm rad}$ ($\rm km\,s^{-1}$)
53894.8710	50.161	53895.0234	45.232	53929.8789	51.087
53894.9414	48.181	53927.8437	20.216		
53895.0117	45.699	53929.8632	51.420		

B.10 HD 136905

Table B.10: Radial velocities of HD 136905 relative to the image number 3452 076.

HJD (2400000+)	$V_{\rm rad}$ ($\rm km\,s^{-1}$)	**HJD** (2400000+)	$V_{\rm rad}$ ($\rm km\,s^{-1}$)	**HJD** (2400000+)	$V_{\rm rad}$ ($\rm km\,s^{-1}$)
53452.105	0.000	53859.125	−32.892	53886.043	−6.659
53465.082	27.549	53860.043	−45.228	53886.059	−6.344
53466.039	27.124	53860.059	−45.379	53887.973	26.000
53487.047	25.289	53860.078	−45.519	53887.984	26.078
53487.059	25.510	53860.094	−45.646	53888.000	26.227
53487.074	25.598	53861.094	−48.222	53888.012	26.314
53487.090	25.709	53861.105	−48.221	53892.035	−23.436
53487.109	25.846	53861.117	−48.171	53892.051	−23.800
53488.070	28.160	53861.129	−48.129	53893.922	−48.124
53489.070	20.775	53862.109	−39.495	53893.934	−48.146
53489.090	20.527	53862.125	−39.336	53893.949	−48.200
53491.008	−19.096	53862.137	−39.161	53894.961	−45.697
53491.027	−19.506	53862.152	−38.919	53894.973	−45.582
53859.109	−32.577	53886.027	−6.954	53927.883	−48.384

B.11 HD 194215

Table B.11: Radial velocities of HD 194215 relative to the image number 3667 010.

HJD (2400000+)	$V_{\rm rad}$ ($\rm km\,s^{-1}$)	**HJD** (2400000+)	$V_{\rm rad}$ ($\rm km\,s^{-1}$)	**HJD** (2400000+)	$V_{\rm rad}$ ($\rm km\,s^{-1}$)
53251.9062	1.647	53666.8398	0.004	53888.0976	−23.126
53300.8750	−0.920	53666.8515	0.000	53888.1093	−23.127
53303.8984	−1.299	53666.8593	−0.004	53888.1210	−23.113
53323.8671	−4.016	53666.9257	0.010	53888.1289	−23.121
53457.2148	−25.832	53666.9414	0.025	53888.1367	−23.119
53457.2265	−25.836	53667.9257	−0.077	53888.1484	−23.119
53457.2382	−25.837	53830.2382	−25.566	53891.1914	−22.494
53457.2460	−25.836	53837.1914	−26.104	53891.2031	−22.487
53466.1562	−26.392	53837.2070	−26.112	53891.2187	−22.487
53489.2148	−26.179	53837.2187	−26.111	53891.2343	−22.475
53489.2304	−26.185	53837.2343	−26.102	53891.9843	−22.310
53489.2421	−26.184	53859.2109	−26.405	53891.9960	−22.303
53491.2109	−26.029	53859.2187	−26.402	53892.0039	−22.300
53491.2226	−26.028	53859.2265	−26.400	53894.1093	−21.846
53491.2304	−26.023	53859.2343	−26.407	53894.1171	−21.839
53607.8906	0.083	53859.2421	−26.394	53894.1250	−21.840
53607.9023	0.087	53859.2539	−26.395	53894.1328	−21.840
53608.0117	0.099	53860.2109	−26.344	53895.0390	−21.640
53608.0195	0.102	53860.2226	−26.351	53895.0507	−21.642
53638.9843	1.517	53860.2304	−26.346	53928.0000	−12.513
53638.9921	1.507	53860.2382	−26.343	53928.0117	−12.426
53639.0000	1.483	53861.0546	−26.298	53928.0195	−12.442
53639.9101	1.544	53861.0625	−26.323	53928.0312	−12.428
53639.9218	1.548	53861.0742	−26.321	53929.0820	−12.134
53641.8085	1.518	53861.0820	−26.327	53929.0937	−12.133
53641.8203	1.520	53862.0585	−26.256	53929.1054	−12.139
53641.8281	1.511	53862.0664	−26.287	53999.8320	1.476

Continued on next page

Table B.11 – continued from previous page

HJD (2400000+)	$V_{\rm rad}$ ($\rm km\,s^{-1}$)	**HJD** (2400000+)	$V_{\rm rad}$ ($\rm km\,s^{-1}$)	**HJD** (2400000+)	$V_{\rm rad}$ ($\rm km\,s^{-1}$)
53999.8476	1.479	54000.9101	1.548	54012.8867	1.733
53999.8671	1.488	54000.9257	1.557	54014.8085	1.720
53999.8867	1.489	54000.9375	1.555	54014.8203	1.735
53999.9023	1.485	54000.9492	1.544	54014.8242	1.755
53999.9179	1.471	54012.8632	1.767		
53999.9335	1.478	54012.8750	1.744		

APPENDIX C

Radial velocities of double-lined spectroscopic binaries

C.1 HD 3405

Table C.1: Radial velocities of HD 3405.

HJD (2400000+)	$V_{\mathrm{rad},1}$ ($\mathrm{km\,s^{-1}}$)	$V_{\mathrm{rad},2}$ ($\mathrm{km\,s^{-1}}$)	**HJD** (2400000+)	$V_{\mathrm{rad},1}$ ($\mathrm{km\,s^{-1}}$)	$V_{\mathrm{rad},2}$ ($\mathrm{km\,s^{-1}}$)
53303.9603	−66.099	54.075	53667.0815	−51.997	40.963
53332.0043	60.304	−65.444	53667.0918	−50.701	39.774
53404.8934	−76.676	64.393	53667.1023	−49.277	38.472
53405.8908	53.270	−58.730	53668.0589	73.432	−77.911
53608.0733	64.373	−69.312	53668.0705	74.208	−78.604
53639.1278	28.216	−35.244	53668.0814	74.965	−79.378
53639.1436	26.082	−33.270	53688.9253	−92.653	79.395
53639.9895	−81.677	69.376	53688.9429	−92.686	79.454
53639.9986	−82.332	69.950	53689.0257	−91.686	78.564
53640.0083	−82.991	70.544	53689.0365	−91.465	78.324
53642.0237	81.918	−85.969	53689.0482	−91.170	78.088
53642.0356	82.378	−86.335	53689.9204	1.251	−10.010
53642.0459	82.620	−86.652	53689.9410	4.824	−13.054
53662.8936	−89.908	76.766	53691.9214	−29.991	20.295
53662.9089	−89.276	76.243	53691.9349	−31.690	22.054
53665.9391	−58.136	46.753	53720.9769	78.093	−82.528
53665.9516	−59.641	48.175	53888.2958	7.198	−14.864
53665.9631	−60.965	49.369	53888.3058	8.842	−16.800
53895.1108	−78.383	65.813	54014.9391	−71.435	59.257

Continued on next page

Table C.1 – continued from previous page

HJD (2400000+)	$V_{\rm rad,1}$ ($\rm km\,s^{-1}$)	$V_{\rm rad,2}$ ($\rm km\,s^{-1}$)	**HJD** (2400000+)	$V_{\rm rad,1}$ ($\rm km\,s^{-1}$)	$V_{\rm rad,2}$ ($\rm km\,s^{-1}$)
53895.1218	−77.371	64.866	54014.9480	−70.535	58.363
53929.0456	−51.387	40.388	54014.9869	−66.472	54.472
53929.1785	−33.485	23.549	54014.9959	−65.504	53.608
54001.0773	70.211	−74.895	54015.1134	−51.706	40.715
54001.0932	71.486	−76.069	54015.1252	−50.233	39.343
54001.1073	72.527	−77.078	54015.8955	55.776	−61.267
54001.1206	73.477	−77.996	54015.9083	57.149	−62.559
54012.9383	73.929	−78.383	54015.9501	61.664	−66.696
54012.9528	72.924	−77.385	54015.9615	62.773	−67.780
54014.0686	−69.252	57.135	54015.9727	63.741	−68.724
54014.0788	−70.264	58.136	54016.0756	72.400	−76.963
54014.0898	−71.350	59.178	54016.0868	73.246	−77.760
54014.1231	−74.467	62.196	54016.1357	76.448	−80.825
54014.1332	−75.268	62.985			

C.2 HD 77137

Table C.2: Radial velocities of HD 77137.

HJD (2400000+)	$V_{\rm rad,1}$ ($\rm km\,s^{-1}$)	$V_{\rm rad,2}$ ($\rm km\,s^{-1}$)	**HJD** (2400000+)	$V_{\rm rad,1}$ ($\rm km\,s^{-1}$)	$V_{\rm rad,2}$ ($\rm km\,s^{-1}$)
53304.1920	88.931	34.011	53405.0026	42.897	78.975
53377.0438	157.304	−34.413	53405.1053	66.182	–
53402.0315	87.707	34.943	53405.9109	157.299	−35.074
53402.1368	106.272	16.088	53406.1328	146.926	−24.106
53403.0281	137.261	−14.459	53424.9823	156.067	−33.399
53403.1174	125.657	−3.053	53425.0149	157.011	−34.347
53403.9863	−19.181	141.122	53451.8934	−10.649	133.208
53404.0988	−28.820	151.068	53451.9383	−16.033	138.610

Continued on next page

Table C.2 – continued from previous page

HJD (2400000+)	$V_{\mathrm{rad},1}$ ($\mathrm{km\,s^{-1}}$)	$V_{\mathrm{rad},2}$ ($\mathrm{km\,s^{-1}}$)	**HJD** (2400000+)	$V_{\mathrm{rad},1}$ ($\mathrm{km\,s^{-1}}$)	$V_{\mathrm{rad},2}$ ($\mathrm{km\,s^{-1}}$)
53452.9271	34.420	87.825	53779.0428	10.471	111.515
53452.9362	36.031	86.179	53829.9805	−21.053	143.862
53456.8962	152.598	−29.905	53829.9917	−19.806	142.728
53456.9562	155.603	−32.724	53835.8627	−25.586	147.903
53456.9669	156.110	−33.151	53835.8728	−26.513	148.824
53464.9270	−32.301	154.677	53835.8820	−27.261	149.482
53465.8636	62.972	–	53858.8352	−13.917	136.615
53466.8842	148.927	−26.454	53858.8464	−12.496	135.230
53486.7932	34.544	87.352	53858.8596	−10.767	133.643
53486.8039	32.664	89.349	53860.7971	80.167	42.733
53487.9089	0.672	121.981	53860.8054	78.976	44.047
53487.9199	2.298	120.338	53860.8152	77.605	45.737
53488.7759	143.592	−21.173	53860.8254	75.765	47.487
53488.7872	144.695	−22.223	53861.8111	−32.879	154.921
53490.7813	−32.527	154.953	53861.8197	−32.427	154.606
53490.7907	−32.070	154.484	53861.8305	−31.937	154.038
53490.7998	−31.599	153.954	53861.8383	−31.427	153.614
53741.0317	80.354	42.648	53887.7583	4.143	118.164
53741.0511	82.853	39.738	53887.7705	6.017	116.338
53741.0688	85.495	37.111	53890.8880	−5.715	128.469
53741.9967	145.414	−22.947	53891.7833	142.096	−19.825
53742.0124	144.001	−21.404	53891.7944	143.179	−20.922
53744.0105	36.752	85.228	53893.7809	−33.374	156.114
53744.0279	38.887	82.621	53894.7620	112.458	9.757
53779.0265	7.762	114.181	53894.7719	114.069	8.199

C.3 HD 155555

Table C.3: Radial velocities of HD 155555.

HJD (2400000+)	$V_{\mathrm{rad},1}$ ($\mathrm{km\,s^{-1}}$)	$V_{\mathrm{rad},2}$ ($\mathrm{km\,s^{-1}}$)	**HJD** (2400000+)	$V_{\mathrm{rad},1}$ ($\mathrm{km\,s^{-1}}$)	$V_{\mathrm{rad},2}$ ($\mathrm{km\,s^{-1}}$)
53253.8326	40.684	−39.090	53489.0559	−23.465	30.266
53253.8597	48.402	−46.841	53489.1899	18.428	−13.962
53254.0335	83.135	−83.932	53489.2006	22.192	−19.155
53254.0456	84.453	−85.166	53491.0448	66.863	−66.842
53254.9458	−84.745	92.992	53491.0563	69.168	−69.229
53255.8486	88.119	−88.847	53491.1855	87.141	−88.530
53255.8573	87.599	−88.310	53491.1968	87.890	−89.208
53255.8706	86.753	−87.525	53607.8056	−33.117	40.049
53256.9103	−47.962	53.998	53607.8334	−41.219	47.909
53303.8693	−74.532	83.070	53607.9147	−61.334	69.513
53304.0544	−31.695	38.099	53607.9416	−66.932	75.360
53304.8915	37.312	−35.894	53638.8563	17.304	−13.291
53320.8748	−30.457	36.690	53638.8652	20.225	−16.522
53423.9121	85.629	−88.106	53641.8455	−78.936	87.599
53456.1923	49.362	−47.969	53641.8549	−77.791	86.476
53456.2036	46.255	−44.822	53641.8933	−72.088	81.032
53456.2145	43.039	−42.014	53641.9046	−70.165	79.327
53457.1885	4.024	−0.927	53641.9928	−51.721	59.097
53457.1991	5.587	−1.030	53642.0028	−49.054	56.026
53465.1304	−83.534	92.794	53667.8670	87.042	−89.357
53466.0654	86.926	−88.793	53667.8791	86.189	−88.537
53466.0837	85.755	−87.480	53859.1466	16.323	−11.268
53487.1376	−78.336	86.897	53859.1580	20.714	−15.703
53487.8294	87.528	−89.116	53859.1693	24.515	−20.267
53488.0887	62.756	−61.946	53860.1079	−48.278	56.512
53488.1029	59.476	−58.568	53860.1193	−51.235	59.830
53488.2058	31.647	−27.979	53860.1303	−53.918	62.954
53488.2229	25.787	−21.447	53860.1412	−56.597	65.512
53489.0456	−26.940	33.668	53860.1531	−59.218	68.339

Continued on next page

Table C.3 – continued from previous page

HJD (2400000+)	$V_{\mathrm{rad},1}$ ($\mathrm{km\,s^{-1}}$)	$V_{\mathrm{rad},2}$ ($\mathrm{km\,s^{-1}}$)	**HJD** (2400000+)	$V_{\mathrm{rad},1}$ ($\mathrm{km\,s^{-1}}$)	$V_{\mathrm{rad},2}$ ($\mathrm{km\,s^{-1}}$)
53861.1433	86.351	−88.392	53894.9177	84.306	−85.612
53861.1503	86.808	−88.667	53894.9865	74.668	−75.363
53861.1574	87.333	−88.936	53894.9950	73.205	−73.681
53861.1979	88.571	−90.188	53895.0639	58.434	−57.761
53861.2050	88.620	−90.111	53895.0735	56.249	−55.139
53861.8905	−70.558	79.837	53895.1370	38.752	−37.886
53861.8975	−71.736	81.179	53895.2685	−2.496	4.136
53862.1702	−74.740	83.179	53927.9002	−43.122	49.158
53862.1803	−73.102	81.523	53927.9124	−40.107	45.584
53862.2241	−64.981	72.800	53927.9655	−23.143	29.194
53862.2346	−62.825	70.719	53927.9757	−20.217	25.984
53888.0288	84.767	−86.422	53927.9856	−17.151	23.582
53888.0380	85.569	−87.172	53928.9879	−30.152	36.442
53888.0470	86.330	−88.044	53929.0023	−34.806	40.916
53888.1707	86.168	−87.466	54000.8205	88.251	−89.084
53888.1795	85.326	−86.777	54000.8365	87.437	−88.278
53888.1876	84.730	−86.167	54013.8132	2.547	−4.590
53889.0432	−78.313	88.007	54013.8242	4.788	−4.075
53889.0544	−76.973	86.586	54013.8339	6.917	−6.037
53891.1362	29.312	−27.135	54013.8436	9.122	−7.955
53891.1487	33.344	−32.395	54013.8533	11.878	−11.054
53892.0701	−51.656	59.756	54013.8633	15.445	−15.673
53892.0817	−54.431	62.693	54013.8740	19.843	−18.293
53893.9600	−83.550	93.126	54013.8846	24.151	−21.693
53893.9678	−83.783	93.386	54013.8956	28.512	−25.728
53894.0605	−81.092	90.604	54014.8434	−53.454	62.541
53894.0710	−80.121	89.680	54014.8526	−55.717	64.907
53894.0804	−79.173	88.511	54014.8621	−57.957	67.603
53894.0890	−78.211	87.563	54014.8717	−60.057	69.668
53894.9082	85.268	−86.397	54014.8814	−62.308	71.977

Continued on next page

Table C.3 – continued from previous page

HJD (2400000+)	$V_{\mathrm{rad},1}$ ($\mathrm{km\,s^{-1}}$)	$V_{\mathrm{rad},2}$ ($\mathrm{km\,s^{-1}}$)	**HJD** (2400000+)	$V_{\mathrm{rad},1}$ ($\mathrm{km\,s^{-1}}$)	$V_{\mathrm{rad},2}$ ($\mathrm{km\,s^{-1}}$)
54014.8914	−64.424	74.137	54015.8253	83.632	−84.658
54014.9012	−66.481	76.423	54015.8386	85.135	−86.040
54015.8121	82.243	−83.052	54015.8522	86.381	−87.456

C.4 HD 197649

Table C.4: Radial velocities of HD 197649.

HJD (2400000+)	$V_{\mathrm{rad},1}$ ($\mathrm{km\,s^{-1}}$)	$V_{\mathrm{rad},2}$ ($\mathrm{km\,s^{-1}}$)	**HJD** (2400000+)	$V_{\mathrm{rad},1}$ ($\mathrm{km\,s^{-1}}$)	$V_{\mathrm{rad},2}$ ($\mathrm{km\,s^{-1}}$)
53251.8856	−32.531	7.639	53608.0487	−55.025	36.445
53253.8487	−2.361	−30.917	53608.0559	−55.081	36.512
53253.8708	−1.790	−31.293	53633.9654	14.020	−51.673
53254.9699	13.281	−50.690	53634.8853	23.480	−63.752
53254.9743	13.431	−50.726	53634.9694	24.111	−64.620
53255.9775	23.682	−64.119	53635.0296	24.560	−65.235
53255.9820	23.631	−64.140	53635.0430	24.704	−65.378
53256.9295	29.160	−71.169	53636.0284	29.661	−71.815
53300.9047	−51.697	32.472	53636.0377	29.653	−71.829
53303.9145	−55.773	37.387	53636.0478	29.709	−71.898
53304.9076	−46.849	26.068	53637.0920	29.179	−71.236
53466.1667	−56.713	38.581	53639.0138	13.829	−51.458
53491.1578	27.613	−69.300	53639.0225	13.775	−51.339
53491.1656	27.628	−69.347	53639.9354	1.596	−35.516
53491.1735	27.708	−69.392	53639.9430	1.509	−35.386
53607.8156	−53.242	34.074	53639.9494	1.397	−35.366
53607.8221	−53.295	34.165	53641.8656	−27.812	2.504
53607.9249	−54.102	35.239	53641.8724	−27.917	2.563
53607.9311	−54.115	35.316	53641.8800	−28.030	2.779

Continued on next page

Table C.4 – continued from previous page

HJD (2400000+)	$V_{\mathrm{rad},1}$ ($\mathrm{km\,s^{-1}}$)	$V_{\mathrm{rad},2}$ ($\mathrm{km\,s^{-1}}$)	**HJD** (2400000+)	$V_{\mathrm{rad},1}$ ($\mathrm{km\,s^{-1}}$)	$V_{\mathrm{rad},2}$ ($\mathrm{km\,s^{-1}}$)
53641.9173	−28.712	3.387	53862.1983	−59.812	42.712
53641.9252	−28.867	3.552	53862.2052	−59.840	42.648
53659.9591	−28.998	3.276	53862.2119	−59.810	42.644
53659.9690	−29.145	3.421	53888.0580	27.250	−68.757
53662.8552	−58.621	41.091	53888.0672	27.267	−68.813
53662.8656	−58.697	41.163	53888.0759	27.267	−68.925
53662.8750	−58.686	41.204	53888.0833	27.298	−68.933
53665.9048	−45.571	24.632	53891.1631	19.101	−58.409
53665.9207	−45.413	24.329	53891.1749	18.917	−58.290
53666.8833	−32.940	8.271	53892.0936	8.002	−44.081
53666.8935	−32.827	8.114	53892.1022	7.827	−43.969
53666.9023	−32.623	7.915	53892.1109	7.720	−43.852
53667.8937	−17.881	−11.876	53893.9780	−20.238	–
53667.9033	−17.678	−12.015	53893.9856	−20.424	–
53667.9129	−17.513	−12.205	53893.9924	−20.396	–
53830.1698	−19.479	–	53895.0842	−37.230	13.362
53830.1848	−19.355	–	53895.0920	−37.346	13.465
53859.1810	−39.349	16.429	53895.0992	−37.415	13.610
53859.1881	−39.463	16.547	53927.9350	11.107	−48.160
53859.1947	−39.491	16.693	53927.9457	10.932	−47.945
53859.2012	−39.621	16.835	53927.9538	10.916	−47.815
53860.1662	−50.591	30.961	53929.0187	−4.494	−28.659
53860.1764	−50.681	31.091	53929.0300	−4.678	−28.485
53860.1869	−50.792	31.200	53999.9989	12.718	−49.946
53860.1985	−50.918	31.344	54000.0117	12.512	−49.814
53861.1659	−57.898	40.089	54000.8549	1.026	−35.093
53861.1728	−57.915	40.164	54000.8827	0.611	−34.517
53861.1820	−57.976	40.212	54000.8961	0.407	−34.290
53861.1874	−57.990	40.263	54012.9031	14.104	−51.662
53862.1908	−59.864	42.700	54012.9131	14.276	−51.850

Continued on next page

Table C.4 – continued from previous page

HJD (2400000+)	$V_{\mathrm{rad},1}$ ($\mathrm{km\,s^{-1}}$)	$V_{\mathrm{rad},2}$ ($\mathrm{km\,s^{-1}}$)	**HJD** (2400000+)	$V_{\mathrm{rad},1}$ ($\mathrm{km\,s^{-1}}$)	$V_{\mathrm{rad},2}$ ($\mathrm{km\,s^{-1}}$)
54012.9228	14.366	−51.958	54014.9207	29.558	−71.636
54013.9104	24.096	−64.636	54014.9277	29.595	−71.661
54013.9188	24.241	−64.726	54015.8697	29.614	−71.719
54013.9274	24.267	−64.761	54015.8804	29.600	−71.772
54014.9136	29.525	−71.621			

APPENDIX D

Observed radial velocities and photometric data of GT Mus.

D.1 Radial velocity of GT Mus.

Table D.1: Radial velocities of GT Mus.

HJD (2400000+)	$V_{\rm rad}$ ($\rm km\,s^{-1}$)	**HJD** (2400000+)	$V_{\rm rad}$ ($\rm km\,s^{-1}$)	**HJD** (2400000+)	$V_{\rm rad}$ ($\rm km\,s^{-1}$)
53304.1054	14.893	53465.0117	−9.838	53779.1796	−3.842
53322.1640	1.617	53465.9375	−9.242	53779.1875	−3.807
53377.1289	9.489	53466.9531	−8.476	53836.0039	−8.143
53402.1015	−10.464	53486.9687	13.368	53859.0000	13.280
53402.1757	−10.508	53486.9765	13.367	53859.0117	13.271
53403.0859	−10.000	53486.9804	13.350	53859.0234	13.275
53403.1445	−10.035	53488.0039	13.865	53859.9687	13.207
53404.0156	−9.589	53488.0117	13.868	53859.9804	13.203
53404.0859	−9.557	53488.0234	13.867	53859.9960	13.196
53404.1367	−9.470	53488.9179	14.132	53861.0039	13.016
53405.0585	−8.634	53488.9257	14.133	53861.0078	13.031
53405.1367	−8.587	53488.9335	14.111	53861.0156	13.059
53406.0156	−7.674	53490.9335	14.324	53861.0234	13.026
53406.1210	−7.669	53490.9414	14.322	53862.0273	12.738
53423.9296	12.500	53490.9492	14.354	53862.0312	12.739
53423.9609	12.524	53742.1679	11.287	53862.0390	12.729
53424.9687	13.115	53744.1367	9.605	53862.0468	12.732
53457.0312	−10.842	53744.1445	9.574	53885.9648	−11.554
53457.0429	−10.852	53779.1757	−3.856	53885.9726	−11.570

Continued on next page

Table D.1 – continued from previous page

HJD (2400000+)	$V_{\rm rad}$ ($\rm km\,s^{-1}$)	**HJD** (2400000+)	$V_{\rm rad}$ ($\rm km\,s^{-1}$)	**HJD** (2400000+)	$V_{\rm rad}$ ($\rm km\,s^{-1}$)
53885.9804	−11.571	53891.9570	−11.724	53894.8906	−10.226
53885.9882	−11.571	53891.9648	−11.721	53894.8945	−10.234
53887.8828	−12.165	53891.9726	−11.730	53927.8320	9.865
53887.8906	−12.175	53893.8867	−10.885	53929.8398	7.896
53887.8945	−12.177	53893.8906	−10.873	53929.8515	7.895
53891.0000	−12.066	53893.8945	−10.883		
53891.0117	−12.066	53894.8828	−10.259		

D.2 Photometric data of GT Mus.

Table D.2: V, $U-B$, $B-V$, $(V-R)_C$, $(V-I)_C$ photometry of GT Mus.

HJD (2400000+)	$U-B$	$B-V$	V	$(V-R)_C$	$(V-I)_C$
50716.176	–	0.897	5.102	0.560	1.101
50716.177	–	0.896	5.098	0.563	1.103
50838.097	–	0.847	5.083	0.527	1.055
50838.101	–	0.850	5.052	0.546	1.076
50844.063	–	0.873	5.023	0.506	1.053
50844.066	–	0.871	5.023	0.520	1.051
50864.023	–	0.859	5.020	0.535	1.065
50864.027	–	0.858	5.020	0.530	1.068
50876.118	–	0.851	4.995	0.536	1.072
50876.122	–	0.861	4.983	0.522	1.055
50877.089	–	0.873	4.988	0.524	1.059
50877.092	–	0.878	4.974	0.503	1.036
50908.014	–	0.864	5.005	0.527	1.051
50908.018	–	0.872	4.999	0.524	1.044

Continued on next page

Table D.2 – continued from previous page

HJD (2400000+)	$U-B$	$B-V$	V	$(V-R)_C$	$(V-I)_C$
50949.980	–	0.878	4.980	0.528	1.052
50949.984	–	0.876	4.986	0.543	1.061
50960.913	–	0.861	5.002	0.538	1.067
50960.917	–	0.878	4.998	0.531	1.062
50961.912	–	0.822	5.016	0.491	0.834
50961.916	–	0.865	5.053	0.480	1.110
50967.950	–	0.858	4.999	0.537	1.060
50967.953	–	0.867	4.994	0.529	1.054
50968.890	–	0.848	4.998	0.534	1.055
50968.894	–	0.859	4.998	0.523	1.053
50973.983	–	0.859	4.990	0.526	1.054
50973.986	–	0.871	4.990	0.518	1.031
50978.964	–	0.860	5.008	0.527	1.058
50978.968	–	0.861	5.014	0.536	1.059
50980.885	–	0.869	5.009	0.522	1.050
50980.889	–	0.853	5.009	0.525	1.054
50983.916	–	0.859	5.015	0.534	1.062
50983.920	–	0.849	5.021	0.537	1.071
50991.877	–	0.845	4.998	0.536	1.060
50991.881	–	0.861	4.978	0.519	1.041
50992.894	–	0.854	5.051	0.498	1.066
50992.898	–	0.069	5.009	0.523	1.066
50992.862	–	–	–	–	–
50992.894	–	0.854	5.051	0.498	1.066
50992.825	–	–	–	–	–
50992.898	–	0.891	5.001	0.523	1.066
50992.894	–	0.854	5.051	0.551	1.066
50992.898	–	0.891	5.001	0.523	1.066
50996.957	–	0.865	4.990	0.537	1.056
50996.966	–	0.853	4.985	0.528	1.055

Continued on next page

Table D.2 – continued from previous page

HJD (2400000+)	$U-B$	$B-V$	V	$(V-R)_C$	$(V-I)_C$
51007.875	–	0.871	4.984	0.526	1.057
51007.879	–	0.871	4.977	0.518	1.042
51009.873	–	0.854	4.998	0.537	1.058
51009.877	–	0.861	4.994	0.535	1.062
51012.901	–	0.859	4.994	0.536	1.055
51012.904	–	0.863	4.995	0.540	1.054
51028.846	–	0.913	5.033	0.535	1.082
51028.849	–	0.913	5.035	0.540	1.087
51032.838	–	0.872	5.004	0.581	1.093
51032.842	–	0.873	4.998	0.624	1.145
51033.925	–	0.831	5.002	0.549	1.072
51033.928	–	0.853	4.996	0.547	1.070
51038.893	–	0.884	4.998	0.578	1.134
51038.896	–	0.983	4.991	0.539	1.086
51043.859	–	0.891	5.001	0.509	0.928
51043.862	–	0.889	5.006	0.533	1.052
51044.845	–	0.861	5.015	0.542	1.075
51044.848	–	0.868	5.012	0.552	1.077
51055.846	–	0.861	4.997	0.534	1.058
51055.849	–	0.870	5.005	0.540	1.054
51064.856	–	0.899	5.007	0.554	1.071
51064.858	–	0.868	4.996	0.548	1.063
51110.152	–	0.870	5.047	0.540	1.081
51110.156	–	0.877	5.038	0.530	1.066
51127.956	–	0.954	5.068	0.511	1.090
51127.960	–	0.915	5.097	0.561	1.112
51131.058	–	0.844	5.027	0.538	1.074
51131.062	–	0.858	5.018	0.529	1.061
51145.137	–	0.864	5.002	0.525	1.053
51145.141	–	0.867	4.998	0.521	1.059

Continued on next page

Table D.2 – continued from previous page

HJD (2400000+)	$U-B$	$B-V$	V	$(V-R)_C$	$(V-I)_C$
51204.135	–	0.860	5.011	0.527	1.054
51204.139	–	0.857	5.012	0.532	1.052
51211.148	–	0.854	5.000	0.540	1.062
51211.155	–	0.862	4.996	0.538	1.055
51214.048	–	0.865	4.981	0.528	1.048
51214.054	–	0.860	4.986	0.535	1.055
51221.159	–	0.881	4.993	0.528	1.057
51221.163	–	0.876	4.993	0.530	1.058
51227.191	–	0.911	5.029	0.542	1.074
51227.194	–	0.910	5.028	0.536	1.076
51227.191	–	0.911	5.029	0.542	1.074
51227.194	–	0.910	5.028	0.536	1.076
51231.077	–	0.879	5.009	0.527	1.058
51231.080	–	0.858	5.022	0.535	1.059
51231.878	–	0.866	5.019	0.541	1.064
51231.882	–	0.861	5.013	0.521	1.055
51239.081	–	0.858	5.027	0.540	1.070
51239.084	–	0.859	5.031	0.547	1.065
51247.201	–	0.873	5.034	0.527	1.062
51247.204	–	0.882	5.038	0.529	1.061
51252.061	–	0.863	5.042	0.527	1.055
51252.064	–	0.880	5.041	0.520	1.049
51262.062	–	0.858	5.053	0.539	1.080
51262.066	–	0.855	5.058	0.542	1.087
51258.045	–	0.882	5.056	0.522	1.056
51258.049	–	0.861	5.039	0.561	1.173
51258.053	–	0.848	5.060	0.543	1.081
51258.057	–	0.828	5.051	0.523	1.060
51269.053	–	0.865	5.033	0.535	1.061
51269.057	–	0.858	5.037	0.530	1.070

Continued on next page

Table D.2 – continued from previous page

HJD (2400000+)	$U-B$	$B-V$	V	$(V-R)_C$	$(V-I)_C$
51271.961	–	0.863	5.023	0.531	1.055
51271.964	–	0.868	5.025	0.538	1.050
51272.966	–	0.848	5.031	0.535	1.061
51272.970	–	0.851	5.028	0.537	1.064
51277.030	–	0.862	5.020	0.536	1.057
51277.033	–	0.864	5.015	0.525	1.055
51280.058	–	0.870	5.016	0.535	1.056
51280.062	–	0.872	5.010	0.529	1.052
51296.982	–	0.871	5.039	0.532	1.056
51296.986	–	0.862	5.040	0.529	1.050
51302.009	–	0.862	5.049	0.532	1.056
51302.012	–	0.861	5.053	0.531	1.055
51302.952	–	0.878	5.088	0.548	1.084
51302.957	–	0.889	5.076	0.542	1.070
51304.980	–	0.863	5.055	0.532	1.058
51304.985	–	0.857	5.062	0.532	1.063
51306.978	–	0.911	4.547	0.555	1.084
51306.983	–	0.881	3.447	0.512	0.961
51306.978	0.471	0.906	5.116	0.550	1.087
51306.983	0.484	0.868	5.150	0.495	0.965
51321.051	-0.224	0.349	2.890	0.198	0.328
51321.053	-0.183	0.333	2.898	0.197	0.336
51321.054	-0.203	0.343	2.914	0.232	0.348
51321.055	-0.188	0.328	2.893	0.223	0.337
51606.138	0.426	0.820	5.042	0.521	1.044
51606.144	0.425	0.819	5.060	0.533	1.057
51611.121	0.431	0.821	5.046	0.528	1.059
51611.126	0.453	0.824	5.044	0.519	1.058
51612.057	0.467	0.816	5.023	0.527	1.046
51612.064	0.470	0.816	5.036	0.528	1.051

Continued on next page

Table D.2 – continued from previous page

HJD (2400000+)	$U-B$	$B-V$	V	$(V-R)_C$	$(V-I)_C$
51613.978	0.429	0.820	5.042	0.530	1.054
51613.983	0.448	0.823	5.037	0.528	1.057
51620.034	0.438	0.825	5.023	0.509	1.050
51620.038	0.441	0.826	5.031	0.517	1.056
51623.009	0.440	0.818	5.026	0.521	1.054
51623.014	0.445	0.798	5.039	0.543	1.063
51665.007	0.434	0.828	5.056	0.516	1.054
51665.012	0.440	0.821	5.059	0.526	1.045
51667.979	0.446	0.816	5.052	0.528	1.047
51667.998	0.446	0.812	5.062	0.534	1.063
51669.996	0.422	0.821	5.057	0.524	1.072
51670.001	0.439	0.819	5.059	0.530	1.048
51673.917	0.458	0.805	5.058	0.531	1.068
51673.923	0.459	0.800	5.056	0.526	1.063
51690.916	0.445	0.813	5.013	0.536	1.058
51690.921	0.443	0.834	4.997	0.518	1.036
51714.938	0.426	0.826	4.993	0.530	1.058
51714.943	0.438	0.834	4.986	0.519	1.041
51720.909	0.420	0.822	5.003	0.533	1.047
51720.915	0.430	0.829	4.996	0.525	1.038
51721.878	0.430	0.833	4.996	0.503	1.035
51721.883	0.427	0.829	4.998	0.517	1.040
51726.885	0.421	0.812	5.022	0.528	1.061
51726.890	0.436	0.818	5.018	0.516	1.064
51729.934	0.464	0.843	5.034	0.518	1.050
51729.942	0.461	0.840	5.022	0.506	1.032
51731.885	0.441	0.829	5.026	0.518	1.071
51731.893	0.436	0.829	5.032	0.528	1.056
51741.893	0.433	0.824	5.036	0.536	1.059
51741.899	0.424	0.816	5.042	0.536	1.070

Continued on next page

Table D.2 – continued from previous page

HJD (2400000+)	$U-B$	$B-V$	V	$(V-R)_C$	$(V-I)_C$
51743.844	0.418	0.832	5.026	0.534	1.074
51743.849	0.435	0.827	5.029	0.529	1.065
51753.922	0.438	0.834	4.986	0.533	1.058
51753.929	0.441	0.830	5.004	0.529	1.057
51756.868	0.443	0.828	4.982	0.533	1.046
51756.873	0.447	0.829	4.991	0.537	1.048
51769.910	0.402	0.832	4.963	0.533	1.032
51769.917	0.405	0.840	4.966	0.544	1.046
51780.938	0.428	0.810	5.009	0.558	1.056
51780.946	0.423	0.826	5.000	0.536	1.047
51897.126	0.350	0.812	5.057	0.526	1.059
51897.131	0.379	0.805	5.072	0.534	1.070
51979.061	0.436	0.837	5.121	0.532	1.062
51979.066	0.451	0.836	5.123	0.543	1.088
51983.053	0.364	0.786	5.071	0.538	1.055
51983.058	0.358	0.768	5.092	0.565	1.069
51984.058	0.383	0.809	5.074	0.522	1.057
51984.064	0.397	0.795	5.078	0.523	1.077
51991.052	0.420	0.814	5.095	0.528	1.071
51991.060	0.418	0.816	5.089	0.519	1.038
51999.969	0.374	0.815	5.095	0.527	1.057
51999.977	0.370	0.823	5.090	0.535	1.061
52006.072	0.417	0.806	5.106	0.528	1.048
52006.079	0.433	0.799	5.106	0.526	1.062
52013.032	0.418	0.813	5.089	0.519	1.052
52013.039	0.423	0.819	5.083	0.508	1.054
52018.065	0.409	0.815	5.085	0.507	1.050
52018.072	0.408	0.818	5.080	0.525	1.057
52023.061	0.454	0.842	5.067	0.509	1.045
52023.068	0.541	0.845	5.048	0.494	1.037

Continued on next page

Table D.2 – continued from previous page

HJD (2400000+)	$U-B$	$B-V$	V	$(V-R)_C$	$(V-I)_C$
52052.967	0.475	0.812	5.082	0.523	1.038
52052.975	0.329	0.800	5.091	0.522	1.061
52056.057	0.377	0.807	5.104	0.549	1.070
52056.064	0.368	0.813	5.102	0.547	1.071
52059.973	0.382	0.839	5.093	0.507	1.060
52059.980	0.475	0.844	5.034	0.488	1.009
52059.988	0.437	0.803	5.351	0.458	0.929
52059.991	0.575	0.813	4.989	0.519	1.042
52062.994	0.408	0.812	5.107	0.537	1.057
52063.002	0.408	0.798	5.119	0.547	1.074
52065.942	0.484	0.854	5.153	0.534	1.070
52065.947	0.490	0.840	5.160	0.541	1.092
52078.865	0.393	0.810	5.088	0.531	1.064
52078.870	0.402	0.805	5.082	0.529	1.044
52115.958	0.336	0.818	5.081	0.536	1.063
52115.966	0.350	0.812	5.096	0.546	1.074
52114.908	0.377	0.830	5.061	0.505	1.041
52114.916	0.390	0.804	5.091	0.530	1.061
52121.876	0.348	0.809	5.101	0.519	1.072
52121.887	0.351	0.808	5.104	0.525	1.065
52221.059	0.346	0.847	5.079	0.500	1.042
52221.067	0.351	0.816	5.104	0.528	1.050
52313.012	0.379	0.794	5.112	0.532	1.056
52313.017	0.380	0.809	5.112	0.524	1.054
52320.087	0.364	0.816	5.087	0.517	1.060
52320.092	0.360	0.801	5.118	0.533	1.066
52321.054	0.380	0.793	5.105	0.534	1.058
52321.059	0.372	0.792	5.107	0.538	1.034
52322.081	0.410	0.869	5.161	0.560	1.103
52322.087	0.436	0.872	5.161	0.556	1.092

Continued on next page

Table D.2 – continued from previous page

HJD (2400000+)	$U-B$	$B-V$	V	$(V-R)_C$	$(V-I)_C$
52339.091	0.367	0.807	5.140	0.521	1.064
52339.099	0.386	0.799	5.141	0.520	1.054
52345.658	0.489	0.857	4.856	0.553	1.114
52345.119	0.378	0.790	5.159	0.522	1.058
52345.658	0.489	0.857	4.856	0.553	1.114
52345.119	0.378	0.790	5.159	0.522	1.058
52420.929	0.343	0.795	5.179	0.520	1.055
52420.934	0.352	0.783	5.175	0.513	1.053
52453.864	0.342	0.794	5.137	0.525	1.052
52453.869	0.357	0.802	5.127	0.504	1.043
52464.900	0.278	0.823	5.174	0.513	1.001
52464.905	0.323	0.802	5.145	0.516	0.839
52477.832	0.338	0.825	5.167	0.497	1.033
52477.837	0.349	0.774	5.192	0.525	1.073
52482.891	0.317	0.799	5.180	0.514	1.059
52482.895	0.351	0.815	5.170	0.507	1.008
52483.865	0.348	0.793	5.165	0.505	1.056
52483.870	0.343	0.804	5.170	0.502	1.042
52634.985	0.368	0.819	5.090	0.517	1.059
52634.990	0.387	0.798	5.108	0.543	1.078
52634.985	0.368	0.819	5.090	0.517	1.059
52634.990	0.387	0.798	5.108	0.543	1.078
52695.932	0.378	0.817	5.108	0.513	1.056
52695.939	0.373	0.820	5.100	0.519	1.020
52731.955	0.284	0.741	5.258	0.480	0.999
52731.987	0.362	0.785	5.074	0.485	1.031
52742.854	0.425	0.795	5.150	0.515	1.051
52742.860	0.399	0.773	5.167	0.544	1.076
52748.925	0.371	0.788	5.145	0.533	1.053
52748.932	0.364	0.795	5.136	0.532	1.057

Continued on next page

Table D.2 – continued from previous page

HJD (2400000+)	$U-B$	$B-V$	V	$(V-R)_C$	$(V-I)_C$
52758.890	0.354	0.834	5.135	0.523	1.046
52758.899	0.375	0.828	5.136	0.509	1.052
52764.020	0.361	0.839	5.131	0.510	1.052
52764.028	0.301	0.841	5.133	0.528	1.043
52764.847	0.379	0.824	5.151	0.521	1.073
52764.851	0.389	0.837	5.138	0.533	1.061
52770.894	0.369	0.831	5.137	0.519	1.057
52770.902	0.367	0.839	5.132	0.528	1.039
52772.900	0.349	0.840	5.139	0.513	1.048
52772.909	0.372	0.836	5.125	0.504	1.044
52800.858	0.357	0.825	5.167	0.514	1.051
52800.865	0.357	0.823	5.152	0.522	1.048
52807.844	0.349	0.828	5.151	0.519	1.046
52807.853	0.371	0.822	5.161	0.528	1.056
52815.977	0.351	0.824	5.160	0.525	1.067
52815.982	0.369	0.813	5.168	0.536	1.082
52816.836	0.359	0.824	5.159	0.509	1.047
52816.841	0.376	0.819	5.158	0.527	1.057
52855.829	0.356	0.834	5.138	0.516	1.044
52855.834	0.366	0.832	5.136	0.493	1.048
52858.877	0.352	0.813	5.167	0.514	1.056
52858.882	0.357	0.828	5.150	0.518	1.047
53006.997	0.348	0.851	5.152	0.482	1.028
53007.004	0.364	0.813	5.181	0.516	1.069
53009.970	0.254	0.807	5.141	0.538	1.053
53009.975	0.228	0.824	5.157	0.542	1.053
53010.949	0.310	0.822	5.168	0.502	1.049
53010.955	0.300	0.851	5.156	0.512	1.043
53004.011	0.356	0.829	5.170	0.534	1.057
53004.017	0.374	0.831	5.155	0.518	1.059

Continued on next page

Table D.2 – continued from previous page

HJD (2400000+)	$U-B$	$B-V$	V	$(V-R)_C$	$(V-I)_C$
53017.036	0.326	0.833	5.173	0.518	1.058
53017.041	0.346	0.842	5.154	0.518	1.065
53021.151	0.365	0.815	5.168	0.524	1.073
53021.156	0.349	0.817	5.168	0.541	1.071
53025.010	0.361	0.859	5.132	0.475	1.034
53025.015	0.377	0.848	5.156	0.514	1.051
53025.021	0.384	0.841	5.154	0.506	1.028
53025.027	0.361	0.839	5.157	0.504	1.047
53027.082	0.349	0.837	5.135	0.511	1.044
53027.086	0.362	0.834	5.160	0.518	1.047
53027.096	0.370	0.840	5.151	0.506	1.048
53071.013	0.358	0.818	5.173	0.511	1.064
53071.018	0.389	0.816	5.180	0.540	1.068
53075.935	0.327	0.809	5.208	0.531	1.061
53075.940	0.323	0.826	5.184	0.522	1.054
53085.893	0.354	0.832	5.169	0.505	1.043
53085.899	0.338	0.839	5.169	0.508	1.042
53088.928	0.374	0.833	5.167	0.534	1.051
53088.933	0.392	0.821	5.166	0.517	1.053
53099.911	0.281	0.818	5.156	0.516	1.046
53099.916	0.283	0.806	5.156	0.536	1.068
53107.973	0.360	0.829	5.169	0.525	1.062
53107.979	0.364	0.836	5.160	0.499	1.048
53151.922	0.371	0.802	5.217	0.527	1.070
53151.930	0.372	0.817	5.196	0.511	1.056
53151.941	0.343	0.827	5.195	0.512	1.049
53151.947	0.345	0.827	5.190	0.507	1.055
53167.905	0.341	0.829	5.209	0.507	1.044
53167.912	0.352	0.823	5.211	0.509	1.054
53172.855	0.341	0.810	5.209	0.527	1.068

Continued on next page

Table D.2 – continued from previous page

HJD (2400000+)	$U-B$	$B-V$	V	$(V-R)_C$	$(V-I)_C$
53172.860	0.344	0.822	5.188	0.529	1.037
53178.900	0.376	0.809	5.195	0.524	1.062
53178.905	0.377	0.800	5.206	0.551	1.085
53191.867	0.358	0.809	5.197	0.531	1.061
53191.875	0.353	0.810	5.200	0.519	1.044
53198.907	0.332	0.811	5.183	0.526	1.060
53198.916	0.326	0.813	5.199	0.531	1.078
53198.918	0.321	0.824	5.178	0.511	1.067
53206.823	0.328	0.797	5.274	0.555	1.170
53206.828	0.208	0.749	5.265	0.628	1.243
53219.850	0.329	0.817	5.217	0.515	1.054
53219.855	0.330	0.829	5.210	0.509	1.056
53246.808	0.353	0.826	5.180	0.516	1.062
53246.812	0.362	0.813	5.184	0.525	1.060
53327.131	0.368	0.787	5.225	0.532	1.060
53327.136	0.340	0.799	5.228	0.540	1.060
53399.010	0.303	0.816	5.232	0.521	1.077
53399.014	0.326	0.820	5.226	0.515	1.059
53399.060	0.339	0.810	5.249	0.521	1.058
53399.065	0.352	0.818	5.245	0.507	1.064
53399.130	0.347	0.839	5.312	0.549	1.113
53399.135	0.326	0.859	5.310	0.551	1.109
53399.170	0.342	0.879	5.292	0.552	1.097
53399.176	0.365	0.864	5.303	0.551	1.092
53402.939	0.280	0.810	5.238	0.524	1.073
53402.946	0.287	0.795	5.250	0.549	1.069
53403.030	0.288	0.802	5.244	0.529	1.070
53403.036	0.290	0.810	5.239	0.535	1.054
53457.021	0.387	0.863	5.303	0.554	1.107
53457.030	0.385	0.871	5.297	0.543	1.108

Continued on next page

Table D.2 – continued from previous page

HJD (2400000+)	$U-B$	$B-V$	V	$(V-R)_C$	$(V-I)_C$
53460.931	0.339	0.800	5.263	0.533	1.087
53460.941	0.350	0.810	5.251	0.520	1.073
53444.934	0.341	0.799	5.207	0.553	1.077
53444.939	0.368	0.813	5.202	0.531	1.074
53464.980	0.322	0.805	5.267	0.533	1.067
53464.985	0.312	0.796	5.262	0.523	1.065
53472.932	0.324	0.802	5.258	0.516	1.070
53472.937	0.314	0.822	5.246	0.515	1.066
53473.959	0.329	0.799	5.239	0.505	1.060
53473.964	0.325	0.799	5.245	0.514	1.072
53474.957	0.401	0.855	5.298	0.542	1.104
53474.962	0.398	0.828	5.304	0.546	1.115
53491.028	0.339	0.812	5.165	0.525	1.060
53491.044	0.358	0.809	5.165	0.519	1.064
53498.840	0.349	0.820	5.170	0.516	1.047
53498.846	0.336	0.835	5.146	0.496	1.036
53503.970	0.352	0.814	5.176	0.521	1.064
53503.980	0.360	0.815	5.185	0.524	1.062
53503.983	0.352	0.828	5.172	0.516	1.050
53534.839	0.361	0.789	5.246	0.516	1.074
53534.845	0.335	0.799	5.240	0.509	1.066
53561.840	0.357	0.827	5.140	0.486	1.051
53561.846	0.345	0.822	5.150	0.485	1.056
53563.917	0.354	0.839	5.138	0.516	1.061
53563.923	0.351	0.832	5.144	0.517	1.058
53566.958	0.350	0.842	5.142	0.520	1.066
53566.963	0.339	0.833	5.146	0.506	1.050
53600.846	0.366	0.829	5.175	0.496	1.038
53600.856	0.329	0.834	5.186	0.509	1.062
53606.827	0.341	0.824	5.175	0.540	1.074

Continued on next page

Table D.2 – continued from previous page

HJD (2400000+)	$U-B$	$B-V$	V	$(V-R)_C$	$(V-I)_C$
53606.834	0.362	0.819	5.159	0.508	1.036
53748.122	0.388	0.842	5.114	0.530	1.067
53748.127	0.387	0.847	5.097	0.512	1.046
53758.093	0.374	0.831	5.129	0.525	1.057
53758.098	0.376	0.820	5.128	0.540	1.069
53759.068	0.368	0.836	5.135	0.520	1.064
53759.073	0.382	0.819	5.138	0.535	1.067
53761.076	0.348	0.844	5.131	0.521	1.064
53761.081	0.329	0.830	5.133	0.524	1.073
53763.135	0.346	0.818	5.139	0.519	0.932
53763.141	0.334	0.812	5.150	0.538	0.991
53764.044	0.380	0.810	5.161	0.546	1.089
53764.049	0.374	0.843	5.139	0.531	1.064
53773.028	0.350	0.841	5.165	0.520	1.049
53773.033	0.363	0.821	5.185	0.542	1.055
53799.998	0.421	0.889	5.175	0.559	1.111
53800.003	0.434	0.901	5.161	0.561	1.099
53807.045	0.364	0.850	5.106	0.481	1.045
53807.050	0.389	0.835	5.103	0.524	1.062
53809.947	0.365	0.854	5.088	0.511	1.050
53809.952	0.374	0.836	5.101	0.530	1.069
53812.987	0.391	0.833	5.107	0.537	1.058
53812.993	0.420	0.837	5.097	0.547	1.055
53816.976	0.375	0.839	5.114	0.510	1.059
53816.981	0.391	0.835	5.104	0.518	1.043
53823.952	0.371	0.835	5.122	0.509	1.064
53823.957	0.369	0.829	5.118	0.528	1.069
53824.936	0.362	0.816	5.141	0.553	1.081
53824.941	0.367	0.840	5.110	0.519	1.051
53825.913	0.358	0.833	5.134	0.522	1.071

Continued on next page

Table D.2 – continued from previous page

HJD (2400000+)	$U-B$	$B-V$	V	$(V-R)_C$	$(V-I)_C$
53825.919	0.358	0.847	5.120	0.492	1.048
53830.099	0.361	0.851	5.143	0.506	1.065
53830.104	0.380	0.835	5.140	0.503	1.047
53887.970	0.361	0.828	5.152	0.492	1.079
53887.976	0.387	0.843	5.130	0.491	1.065
53891.923	0.348	0.825	5.154	0.517	1.065
53891.928	0.374	0.816	5.157	0.533	1.067
53895.017	0.421	0.885	5.241	0.549	1.114
53895.022	0.442	0.857	5.249	0.574	1.122
53938.931	0.357	0.842	5.125	0.477	1.047
53938.936	0.374	0.846	5.120	0.520	1.060
53941.884	0.412	0.871	5.174	0.538	1.095
53941.889	0.388	0.871	5.168	0.515	1.092
53942.842	0.367	0.823	5.153	0.538	1.078
53942.848	0.394	0.837	5.129	0.517	1.058

Bibliography

Abt, H. A. 1970, ApJS, 19, 387

—. 2006, ApJ, 651, 1151

Abt, H. A. 2007, in IAU Symposium, Vol. 240, IAU Symposium, ed. W. I. Hartkopf, E. F. Guinan, & P. Harmanec, 414–416

Adams, W. S., & Kohlschutter, A. 1914, ApJ, 40, 385

Adelman, S. J. 2000, IBVS, 4959, 1

Ake, T. B., & Parsons, S. B. 1987, IBVS, 3002, 1

Ake, III, T. B., & Parsons, S. B. 1988, in A Decade of UV Astronomy with the IUE Satellite, Volume 1, ed. E. J. Rolfe, Vol. 1, 213–215

Allen, W. H., Budding, E., Loudon, M., & Priestley, J. 1993, IBVS, 3838, 1

Andersen, J. 1983, The Observatory, 103, 165

Andersen, J., Clausen, J. V., Nordstrom, B., & Reipurth, B. 1981, A&Ap, 101, 7

Andersen, J., & Popper, D. M. 1975, A&Ap, 39, 131

Antonopoulou, E. 1983, A&Ap, 120, 85

Avni, Y. 1976, ApJ, 209, 574

Balona, L. A. 1987, SAAOC, 11, 1

Barry, D. C. 1970, ApJs, 19, 281

Barstow, M. A. 1987, MNRAS, 228, 251

Bassett, E. E. 1978, The Observatory, 98, 122

Batten, A. H. 1967, Publications of the Dominion Astrophysical Observatory Victoria, 13, 119

Batten, A. H., Fletcher, J. M., & MacCarthy, D. G. 1989, Publications of the Dominion Astrophysical Observatory Victoria, 17, 1

Beavers, W. I., & Eitter, J. J. 1986, ApJs, 62, 147

Beavers, W. I., & Salzer, J. J. 1985, PASP, 97, 355

Beech, M. 1985, Ap&SS, 117, 69

—. 1986a, Ap&SS, 122, 57

—. 1986b, Ap&SS, 125, 69

—. 1989, Ap&SS, 152, 329

Bennett, N. W. W., Evans, D. S., & Laing, J. D. 1963, RGOB, 78, 391

Bennett, N. W. W., Laing, J. D., & Evans, D. S. 1962, RGOB, 61, 91

Bidelman, W. P., & MacConnell, D. J. 1973, AJ, 78, 687

Bopp, B. W., Evans, D. S., Laing, J. D., & Deeming, T. J. 1970, MNRAS, 147, 355

Bozkurt, Z., & Değirmenci, Ö. L. 2007, MNRAS, 379, 370

Bradstreet, D. H., & Steelman, D. P. 2002, in Bulletin of the American Astronomical Society, Vol. 34, Bulletin of the American Astronomical Society, 1224

Brown, A., Bennett, P. D., Baade, R., Kirsch, T., Reimers, D., Hatzes, A. P., & Kürster, M. 2001, AJ, 122, 392

Burke, E. W., Baker, J. E., Fekel, F. C., Hall, D. S., & Henry, G. W. 1982, IBVS, 2111, 1

Buscombe, W., & Kennedy, P. M. 1968, MNRAS, 139, 341

Buscombe, W., & Morris, P. M. 1958, MNRAS, 118, 609

Busso, M., Scaltriti, F., Origlia, L., Ferrari-Toniolo, M., & Persi, P. 1990, Memorie della Societa Astronomica Italiana, 61, 77

Carpenter, E. F. 1930, ApJ, 72, 205

Christie, W. H. 1933, ApJ, 77, 310

Claret, A. 2005, in Astronomical Society of the Pacific Conference Series, Vol. 333, Tidal Evolution and Oscillations in Binary Stars, ed. A. Claret, A. Giménez, & J.-P. Zahn, 122

Claret, A., Gimenez, A., & Martin, E. L. 1995, A&Ap, 302, 741

Collier, A. C. 1982, PhD thesis, University of Canterbury

Collier, A. C., Haynes, R. F., Slee, O. B., Wright, A. E., & Hillier, D. J. 1982, MNRAS, 200, 869

Collier Cameron, A. 1987, SAAOC, 11, 13

Conti, P. S. 1970, PASP, 82, 781

Costa, E., & Loyola, P. 1990, A&Aps, 83, 235

Cowling, T. G. 1941, MNRAS, 101, 367

Cox, A. N. 2000, Allen's astrophysical quantities (Springer-Verlag New York)

Culhane, J. L., White, N. E., Parmar, A. N., & Shafer, R. A. 1990, MNRAS, 243, 424

Cutispoto, G., Pastori, L., Pasquini, L., de Medeiros, J. R., Tagliaferri, G., & Andersen, J. 2002, A&Ap, 384, 491

Cutri, R. M., Skrutskie, M. F., van Dyk, S., Beichman, C. A., Carpenter, J. M., Chester, T., Cambresy, L., Evans, T., Fowler, J., Gizis, J., Howard, E., Huchra, J., Jarrett, T., Kopan, E. L., Kirkpatrick, J. D., Light, R. M., Marsh, K. A., McCallon, H., Schneider, S., Stiening, R., Sykes, M., Weinberg, M., Wheaton, W. A., Wheelock, S., & Zacarias, N. 2003, 2MASS All Sky Catalog of point sources. (The IRSA 2MASS All-Sky Point Source Catalog, NASA/IPAC Infrared Science Archive. http://irsa.ipac.caltech.edu/applications/Gator/)

Darwin, G. H. 1879, The Observatory, 3, 79

Davidson, G. T., Claflin, E. S., & Haisch, B. M. 1987, AJ, 94, 771

De Medeiros, J. R., Udry, S., Burki, G., & Mayor, M. 2002, A&Ap, 395, 97

de Vaucouleurs, A. 1957, MNRAS, 117, 449

Dempsey, R. C., Bopp, B. W., Henry, G. W., & Hall, D. S. 1993, ApJs, 86, 293

Dempsey, R. C., Neff, J. E., & Lim, J. 2001, AJ, 122, 332

Duncan, J. C. 1921, ApJ, 54, 226

Duquennoy, A., & Mayor, M. 1992, Binaries as Tracers of Stellar Formation (Cambridge University Press)

Eaton, J. A., & Barden, S. C. 1986, IBVS, 2952, 1

—. 1988, Acta Astronomica, 38, 353

Eggen, O. J. 1994, AJ, 107, 594

Eggleton, P. 2006, Evolutionary Processes in Binary and Multiple Stars (Cambridge University Press)

Eggleton, P. P., & Kisseleva-Eggleton, L. 2006, Ap&SS, 304, 75

Etzel, P. B. 1981, in Photometric and Spectroscopic Binary Systems, ed. E. B. Carling & Z. Kopal, 111

Fabrycky, D., & Tremaine, S. 2007, ApJ, 669, 1298

Fekel, F. C., Hall, D. S., Africano, J. L., Gillies, K., Quigley, R., & Fried, R. E. 1985, AJ, 90, 2581

Fernandez-Figueroa, M. J., de Castro, E., & Gimenez, A. 1985, A&Aps, 60, 5

Fleming, T. A., Gioia, I. M., & Maccacaro, T. 1989, AJ, 98, 692

Fox, D. C., Linsky, J. L., Veale, A., Dempsey, R. C., Brown, A., Neff, J. E., Pagano, I., Rodono, M., Bromage, G. E., Kuerster, M., & Schmitt, J. H. M. M. 1994, A&Ap, 284, 91

Franciosini, E., Pallavicini, R., Maggio, A., Tagliaferri, G., & Covino, S. 2002, in Astronomical Society of the Pacific Conference Series, Vol. 277, Stellar Coronae in the Chandra and XMM-NEWTON Era, ed. F. Favata & J. J. Drake, 473

Franciosini, E., Pallavicini, R., & Tagliaferri, G. 2003, A&Ap, 399, 279

Frasca, A., Biazzo, K., Catalano, S., Marilli, E., Messina, S., & Rodonò, M. 2005, A&Ap, 432, 647

Garcia, M., Baliunas, S. L., Conroy, M., Ralph, E., Roberts, W., Schwartz, D. A., Tonry, J., & Johnston, M. D. 1980, ApJl, 240, L107

Gioia, I. M., Maccacaro, T., Schild, R. E., Wolter, A., Stocke, J. T., Morris, S. L., & Henry, J. P. 1990, ApJs, 72, 567

Gontcharov, G. A., Andronova, A. A., Titov, O. A., & Kornilov, E. V. 2001, A&Ap, 365, 222

Goodricke, J. 1783, Philosophical Transactions, Series I, 73, 474

Gould, A., & Chanamé, J. 2004, ApJs, 150, 455

Gray, D. 1992, The observation and analysis of stellar photopheres (Cambridge University Press)

Gunn, A. G. 1996, Irish Astronomical Journal, 23, 137

Gunn, A. G., Doyle, J. G., & Houdebine, E. R. 1997, A&Ap, 319, 211

Hadrava, P. 2004, Publications of the Astronomical Institute of the Czechoslovak Academy of Sciences, 92, 1

Hagen, W., & Stencel, R. E. 1985, AJ, 90, 120

Halbwachs, J. L. 1981, A&Aps, 44, 47

Hall, D. S. 1990, AJ, 100, 554

Hall, D. S., Kirkpatrick, J. D., Seufert, E. R., & Henry, G. W. 1986, International Amateur-Professional Photoelectric Photometry Communications, 25, 43

Harrington, R. S. 1968, AJ, 73, 190

—. 1969, Celestial Mechanics, 1, 200

Hatzes, A. P. 2002, Astronomische Nachrichten, 323, 392

Hatzes, A. P., & Kürster, M. 1999, A&Ap, 346, 432

Hearnshaw, J. B., Barnes, S. I., Kershaw, G. M., Frost, N., Graham, G., Ritchie, R., & Nankivell, G. R. 2002, Experimental Astronomy, 13, 59

Heck, A., & Mersch, G. 1980, A&Ap, 83, 287

Henry, T. J., Soderblom, D. R., Donahue, R. A., & Baliunas, S. L. 1996, AJ, 111, 439

Herschel, W. 1802, Philosophical Transactions, Series I, 92, 477

Hilditch, R. W. 2001, An Introduction to Close Binary Stars (Cambridge University Press)

Hoffleit, D., & Jaschek, C. 1991, The Bright Star Catalogue (New Haven, Conn.: Yale University Observatory)

Hoffmann, M. 1978, IBVS, 1489, 1

Houk, N., & Cowley, A. P. 1975, Michigan Catalogue of two-dimensional spectral types for the HD stars (Ann Arbor: University of Michigan, Department of Astronomy, 1975)

Huensch, M., Schmitt, J. H. M. M., & Voges, W. 1998, A&Aps, 132, 155

Ibukiyama, A., & Arimoto, N. 2002, A&Ap, 394, 927

Jancart, S., Jorissen, A., Babusiaux, C., & Pourbaix, D. 2005, A&Ap, 442, 365

Jasniewicz, G., & Mayor, M. 1988, A&Ap, 203, 329

Jones, H. S. 1928, Annals of the Cape Observatory, 10

Jones, K. L., Stewart, R. T., & Nelson, G. J. 1995, MNRAS, 274, 711

Kallrath, J., & Milone, E. 1998, Eclipsing binary stars: modelling and analysis (Springer-Verlag New York)

Karatas, Y., Bilir, S., Eker, Z., & Demircan, O. 2004, Monthly Notices of the Royal Astronomical Society, 349, 1069

Kaye, A. B., Hall, D. S., Henry, G. W., Eaton, J. A., Lines, R. D., Lines, H. C., Barksdale, W. S., Beck, S. J., Chambliss, C. R., Fried, R. E., Genet, R. M., Hopkins, J. L., Lovell, L. P., Louth, H. P., Montle, R. E., Renner, T. R., & Stelzer, H. J. 1995, AJ, 109, 2177

Keenan, P. C. 1983, Bulletin d'Information du Centre de Donnees Stellaires, 24, 19

King, J. R., Villarreal, A. R., Soderblom, D. R., Gulliver, A. F., & Adelman, S. J. 2003, AJ, 125, 1980

Kiseleva, L. G., Eggleton, P. P., & Mikkola, S. 1998, MNRAS, 300, 292

Komonjinda, S., Hearnshaw, J. B., & Ramm, D. J. 2007, in IAU Symposium, Vol. 240, IAU Symposium, ed. W. I. Hartkopf, E. F. Guinan, & P. Harmanec, 531–535

Kondo, Y., & McCluskey, Jr., G. E. 1969, ApJ, 156, 1007

Kopal, Z., ed. 1978, Astrophysics and Space Science Library, Vol. 68, Dynamics of Close Binary Systems

Kopal, Z. 1988, Ap&SS, 144, 557

Kozai, Y. 1962, AJ, 67, 591

Lada, C. J. 2006, ArXiv e-prints, 601

Landi Dessy, J., & Keenan, P. C. 1966, ApJ, 146, 587

Latham, D. W., Mathieu, R. D., Milone, A. A. E., & Davis, R. J. 1992a, in Workshop on Binaries as Tracers of Star Formation, p. 132 - 138, 132–138

Latham, D. W., Mathieu, R. D., Milone, A. A. E., & Davis, R. J. 1992b, in IAU Symposium, Vol. 151, Evolutionary Processes in Interacting Binary Stars, ed. Y. Kondo, R. Sistero, & R. S. Polidan, 471

Latham, D. W., Mazeh, T., Carney, B. W., McCrosky, R. E., Stefanik, R. P., & Davis, R. J. 1988, AJ, 96, 567

Lehmann-Filhés, R. 1894, Astronomische Nachrichten, 136, 17

Limber, D. N. 1963, ApJ, 138, 1112

Lindegren, L., & Dravins, D. 2003, A&A, 401, 1185

Lloyd Evans, T. 1986, South African Astronomical Observatory Circular, 10, 11

Lucke, P. B., & Mayor, M. 1982, A&Ap, 105, 318

Lucy, L. B. 2005, A&Ap, 439, 663

Lucy, L. B., & Sweeney, M. A. 1971, AJ, 76, 544

Lunt, J. 1919, ApJ, 50, 161

—. 1924, Annals of the Cape Observatory, 10, 1

Luyten, W. J. 1936, ApJ, 84, 85

MacConnell, D. J., & Bidelman, W. P. 1976, AJ, 81, 225

MacQueen, P. J. 1986, PhD thesis, University of Canterbury

Malaroda, S. 1973, PASP, 85, 328

—. 1975, AJ, 80, 637

Malaroda, S., Levato, H., & Galliani, S. 2006, VizieR Online Data Catalog, 3249, 0

Masana, E., Jordi, C., & Ribas, I. 2006, A&Ap, 450, 735

Mathieu, R. D., & Mazeh, T. 1988, ApJ, 326, 256

Mayor, M., & Mazeh, T. 1987, A&Ap, 171, 157

Mayor, M., & Mermilliod, J. C. 1984, in IAU Symposium, Vol. 105, Observational Tests of the Stellar Evolution Theory, ed. A. Maeder & A. Renzini, 411

Mazeh, T. 1990, A&A, 99, 675

Mazeh, T. 2008, in EAS Publications Series, Vol. 29, EAS Publications Series, 1

Mazeh, T., & Shaham, J. 1979, A&Ap, 77, 145

McAlister, H., Hartkopf, W. I., & Franz, O. G. 1990, AJ, 99, 965

McAlister, H. A., Hartkopf, W. I., Hutter, D. J., Shara, M. M., & Franz, O. G. 1987, AJ, 93, 183

McLaughlin, D. B. 1924, ApJ, 60, 22

Meibom, S., & Mathieu, R. D. 2005, ApJ, 620, 970

Mitrou, C. K., Mathioudakis, M., Doyle, J. G., & Antonopoulou, E. 1997, A&Ap, 317, 776

Montes, D., Fernandez-Figueroa, M. J., de Castro, E., & Cornide, M. 1995, A&Aps, 109, 135

Morris, D. H., & Mutel, R. L. 1988, AJ, 95, 204

Morris, S. L., & Naftilan, S. A. 1993, ApJ, 419, 344

Murdoch, K. A., Hearnshaw, J. B., Kilmartin, P. M., & Gilmore, A. C. 1995, MNRAS, 276, 836

Nordström, B., Mayor, M., Andersen, J., Holmberg, J., Pont, F., Jørgensen, B. R., Olsen, E. H., Udry, S., & Mowlavi, N. 2004, A&Ap, 418, 989

Ochsenbein, F., Bauer, P., & Marcout, J. 2000, A&Aps, 143, 23

Pasinetti-Fracassini, L. E., Pastori, L., Covino, S., & Pozzi, A. 2001, A&Ap, 367, 521

Pasquini, L., Cutispoto, G., Gratton, R., & Mayor, M. 1991, A&Ap, 248, 72

Perryman, M. A. C., ESA, Perryman, M. A. C., & ESA, eds. 1997, ESA Special Publication, Vol. 1200, The HIPPARCOS and TYCHO catalogues. Astrometric and photometric star catalogues derived from the ESA HIPPARCOS Space Astrometry Mission

Pickering, E. C., & Cannon, A. J. 1897, ApJ, 6, 349

Platais, I., Kozhurina-Platais, V., & van Leeuwen, F. 1998, AJ, 116, 2423

Popper, D. M. 1969, in Bulletin of the American Astronomical Society, Vol. 1, Bulletin of the American Astronomical Society, 257

Pourbaix, D., Tokovinin, A. A., Batten, A. H., Fekel, F. C., Hartkopf, W. I., Levato, H., Morrell, N. I., Torres, G., & Udry, S. 2004, A&Ap, 424, 727

Prés, P., Siarkowski, M., & Sylwester, J. 1995, MNRAS, 275, 43

Press, W. H., Teukolsky, S. A., Vetterling, W. T., & Flannery, B. P. 1994, Numerical recipes in C: the art of scientific computing (Cambridge University Press)

Radford, G. A., & Griffin, R. F. 1975, The Observatory, 95, 289

Ramm, D. J. 2004, PhD thesis, University of Canterbury

Reimers, D., Huensch, M., Schmitt, J. H. M. M., & Toussaint, F. 1996, A&Ap, 310, 813

Rossiter, R. A. 1924, ApJ, 60, 15

Saar, S. H., & Osten, R. A. 1997, MNRAS, 284, 803

Salzer, J. J., & Beavers, W. I. 1985, PASP, 97, 637

Samec, R. G., Fuller, R. E., Kaitchuck, R. H., Bookmyer, B. B., & Faulkner, D. R. 1989a, Space Science Reviews, 50, 359

Samec, R. G., van Hamme, W., & Bookmyer, B. B. 1989b, AJ, 98, 2287

Samus, N. N., Durlevich, O. V., & et al. 2004, VizieR Online Data Catalog, 2250, 0

Savedoff, M. P. 1951, AJ, 56, 1

Schreier, E., Levinson, R., Gursky, H., Kellogg, E., Tananbaum, H., & Giacconi, R. 1972, ApJL, 172, L79+

Schröder, K.-P. 1990, A&Ap, 236, 165

Schröder, K.-P., & Hünsch, M. 1992, A&Ap, 257, 219

Simon, T., & Fekel, Jr., F. C. 1987, ApJ, 316, 434

Skuljan, J. 1999, PhD thesis, University of Canterbury

Skuljan, J., Hearnshaw, J. B., & Barnes, S. I. 2003, in Astronomical Society of the Pacific Conference Series, Vol. 298, GAIA Spectroscopy: Science and Technology, ed. U. Munari, 473

Skuljan, J., Ramm, D. J., & Hearnshaw, J. B. 2004, MNRAS, 352, 975

Slee, O. B., Nelson, G. J., Stewart, R. T., Wright, A. E., Innis, J. L., Ryan, S. G., & Vaughan, A. E. 1987, MNRAS, 229, 659

Sowell, J. R., Bord, D. J., Hart, D. L., & Beletic, J. W. 2001, AJ, 122, 1981

Stefanik, R. P., Latham, D. W., & Torres, G. 1999, in Precise stellar radial velocities IAU Colloquium 170, ed. J. Hearnshaw & C. D. Scarfe (Astronomical Society of the Pacific)

Sterne, T. E. 1941a, Proceedings of the National Academy of Sciences, 27, 168

—. 1941b, Proceedings of the National Academy of Sciences, 27, 175

Stokes, N. R. 1972, MNRAS, 160, 155

Strassmeier, K. G., Hall, D. S., Boyd, L. J., & Genet, R. M. 1989, ApJs, 69, 141

Strassmeier, K. G., & Rice, J. B. 2000, A&Ap, 360, 1019

Strohmeier, W. 1967, IBVS, 217, 1

Tananbaum, H., Gursky, H., Kellogg, E. M., Levinson, R., Schreier, E., & Giacconi, R. 1972, ApJL, 174, L143+

Tassoul, J.-L. 1987, ApJ, 322, 856

—. 1988, ApJL, 324, L71

Tassoul, J.-L., & Tassoul, M. 1992, ApJ, 395, 259

Tokovinin, A., Thomas, S., Sterzik, M., & Udry, S. 2006, A&Ap, 450, 681

Tokovinin, A. A. 1997, A&Ap, 124, 75

Torres, G., Latham, D. W., & Stefanik, R. P. 2007, ApJ, 662, 602

Udalski, A., & Geyer, E. H. 1984, IBVS, 2593, 1

Udry, S., Mayor, M., Maurice, E., Andersen, J., Imbert, M., Lindgren, H., Mermilliod, J.-C., Nordström, B., & Prévot, L. 1999, in Precise stellar radial velocities IAU Colloquium 170, ed. J. Hearnshaw & C. D. Scarfe (Astronomical Society of the Pacific)

van der Sluys, M. 2006, http://hemel.waarnemen.com/Informatie/Sterren/hoofdstuk6.html

van Hamme, W., & Wilson, R. E. 1984, A&Ap, 141, 1

van Hamme, W., & Wilson, R. E. 2003, in Astronomical Society of the Pacific Conference Series, Vol. 298, GAIA Spectroscopy: Science and Technology, ed. U. Munari, 323–+

van Hamme, W., & Wilson, R. E. 2007, in IAU Symposium, Vol. 240, IAU Symposium, ed. W. I. Hartkopf, E. F. Guinan, & P. Harmanec, 211–+

Vansina, F., & de Grève, J. P. 1982, Ap&SS, 87, 377

Verma, R. P., Iyengar, K. V. K., & Rengarajan, T. N. 1987, A&Ap, 177, 346

Vivekananda Rao, P., & Sarma, M. B. K. 1981, Acta Astronomica, 31, 107

Walter, F. M., Cash, W., Charles, P. A., & Bowyer, C. S. 1980, ApJ, 236, 212

Wesselink, A. J. 1969, MNRAS, 144, 297

Wilson, R. E. 1979, ApJ, 234, 1054

—. 1990, ApJ, 356, 613

—. 1994, PASP, 106, 921

Wilson, R. E., & Devinney, E. J. 1971, ApJ, 166, 605

Wilson, R. E., & Huffer, C. M. 1918, Lick Observatory Bulletin, 10, 17

Wood, D. B. 1973, PASP, 85, 253

Wright, W. H. 1904, ApJ, 20, 140

—. 1905, ApJ, 21, 371

—. 1907, ApJ, 25, 56

Zahn, J.-P. 1975, A&Ap, 41, 329

—. 1977, A&Ap, 57, 383

—. 1978, A&Ap, 67, 162

Zahn, J.-P. 1992, in Binaries as Tracers of Stellar Formation. Proceedings of a Workshop held in Bettmeralp, Switzerland, Sept. 1991, in honor of Dr. Roger Griffin. University Press, Cambridge, England, New York, NY, 1992., ed. A. Duquennoy & M. Mayor, 253

Zahn, J.-P., & Bouchet, L. 1989, A&Ap, 223, 112

Zucker, S., & Mazeh, T. 1994, Astrophysical Journal, 420, 806

Zucker, S., Torres, G., & Mazeh, T. 1995, ApJ, 452, 863